

DEVELOPMENT OF COLLAGEN SCAFFOLDS TO ADDRESS BIOMECHANICAL
DESIGN CRITERIA FOR TENDON-TO-BONE REPAIR

BY

LAURA C. MOZDZEN

DISSERTATION

Submitted in partial fulfillment of the requirements
for the degree of Doctor of Philosophy in Chemical Engineering
in the Graduate College of the
University of Illinois at Urbana-Champaign, 2016

Urbana, Illinois

Doctoral Committee:

Associate Professor Brendan A. C. Harley, Chair
Professor Hyun Joon Kong
Professor Deborah Leckband
Associate Professor Amy Wagoner Johnson

ABSTRACT

The tendon-bone junction (TBJ) is a unique, mechanically dynamic and structurally graded anatomical zone which transmits tensile loads between tendon and bone. The TBJ repeatedly transmits high tensile loads to result in movement without failure by effectively dissipating stress concentrations which arise between mechanically dissimilar materials (*tendon, bone*). Upon injury, surgical repair techniques rely on mechanical fixation, and the local heterogeneities of the TBJ do not reform, causing poor functional outcomes (re-failure >90%). Biomaterial platforms and tissue engineering methods offer an alternative approach to address these injuries. Although current methods are moving towards multi-tissue regenerative approaches to address these injuries, it remains a challenge to fully characterize local mechanical and cellular heterogeneities within a single biomaterial using traditional techniques. Herein we describe a variety of collagen biomaterials which incorporate local changes and patterns in composition to create multi-compartment and composite scaffolds for the purpose of orthopedic regeneration. We demonstrate that these biomaterials exhibit enhanced, locally tunable mechanical properties, and are capable of providing mesenchymal stem cells (MSCs) signals in a spatially selective manner. We highlight tradeoffs and synergies in local cellular and mechanical behavior, which give rise to the mechanisms behind observed differences in bulk cellular and biomaterial behavior. This work provides key insights into design elements under consideration for mechanically competent, multi-tissue biomaterial platforms which drive MSCs towards spatially distinct lineages for orthopedic regeneration.

ACKNOWLEDGMENTS

I would like to start by thanking my family and my fiancé, Dan Reilly. They supported and encouraged me through the frustrations and triumphs of my Ph.D., which has taken more perseverance than I had originally expected, but has led to greater accomplishments as well. This program would have been much lonelier without you.

I would also like to thank my advisor, Prof. Brendan Harley, for his support and guidance over the last five years. I appreciate his mentorship as I refine all of the skills which create a successful chemical engineering scientist. I especially appreciate his understanding and implicit encouragement of personal development, which he has demonstrated throughout his lab group by allowing the pursuit of personal and professional activities which will further his trainee's careers, but also further a well-balanced life.

I would like to thank all of my colleagues and collaborators throughout the years, who assisted in the areas of research outside my expertise. I would like to acknowledge the efforts of my undergraduate researchers, Jaime Kelleher, Alan Vucetic, Shayta Roy, and Ryan Rodgers, who truly added to the volume of the research conducted within this thesis. I would like to thank the Bailey Group, especially Jessica Banks and Richard Graybill for assistance in polymer functionalization (**Chapter 2**) and Dan Reilly for assistance with MATLAB (**Chapters 3, 5**). I would like to express my appreciation of Dr. Michael Poellmann, as well as the Kong Lab, for assistance with initial mechanical techniques which later helped lay the foundation for much of this work (**Chapters 2-4**). I would also like to thank the Screen Lab and Oyen Lab for adopting me as a research assistant for the summer I spent in London and Cambridge, especially Dr.

Chavaunne Thorpe, who opened her home to me when I was abroad, and Oliver Armitage, who both showed me their hospitality in a foreign land and lab (**Chapter 5**). I would also like to acknowledge the support of the staff. Dr. Sandra McMasters provided culture media (**Chapter 2,5**), Dr. Matthew Wheeler for provided pASCs (**Chapter 2**) and Knight Lab (QMUL) provided hMSCs (**Chapter 5**).

Finally, I would also like to thank my current and former lab mates, especially Dr. Steven Caliari, who showed by example how to be an exceptional, independent scientist, but also Bill Grier, Rebecca Hortensius, Dan Weisgerber, Jackie Pence, Sunny Choi, Bhushan Mahadik, Sara Pedron, Emily Chen, Aiden Gillchrist, and Mai Ngo for all of their support, for sharing their ideas and knowledge, and for keeping my day interesting.

TABLE OF CONTENTS

LIST OF SYMBOLS AND ABBREVIATIONS	viii
CHAPTER 1: INTRODUCTION	1
1.1: Chapter Overview	1
1.2: The Rotator Cuff as an Orthopedic Interface	1
1.3: Functionalizing Porous Collagen-Glycosaminoglycan (CG) Biomaterials with Singular Factors	4
1.3.1 Pore structure.....	6
1.3.2 Stiffness	8
1.3.3 Composition	10
1.3.4 Mechanical Stimulation.....	11
1.3.5 Biomolecular cues	11
1.4: Spatially Selective and Combinatorial Approaches to Biomaterial Functionalization	13
1.4.1 Layered biomaterials.....	13
1.4.2 Spatially graded or patterned biomaterials	15
1.4.3 Improving the mechanical competence of compositionally graded biomaterials	16
1.4.4 Combinations of multiple signals	17
1.5: Summary	19
1.6: Thesis Overview	19
1.7: Figures	21
CHAPTER 2: INCREASING THE STRENGTH AND BIOACTIVITY OF COLLAGEN SCAFFOLDS USING CUSTOMIZABLE ARRAYS OF 3D-PRINTED POLYMER FIBERS	27
2.1: Chapter Overview	27
2.2: Introduction	28
2.3: Materials and Methods	31
2.3.1 Preparation of collagen-GAG precursor suspension	31
2.3.2 Fabrication of acrylonitrile butadiene styrene fiber arrays via 3D printing	32
2.3.3 Fabrication of ABS fiber reinforced CG scaffolds via lyophilization	32
2.3.4 SEM analysis of fiber-scaffold composite microstructure	33
2.3.5 Tensile testing of ABS-CG composites	33
2.3.6 Functionalizing ABS constructs with biomolecules.....	34
2.3.7 Cylindrical ABS-CG scaffolds to evaluate cell metabolic health	35
2.3.8 Culture of porcine adipose tissue derived stem cells (pASCs)	36
2.3.9 Statistics	38
2.4: Results	38
2.4.1 Incorporation of ABS fibers within the CG scaffold.....	38
2.4.2 The mechanical properties of the CG-ABS fiber array composites can be tuned via the fiber array design	39
2.4.3 Selective attachment of a model protein to the ABS fiber arrays via carbodiimide chemistry.....	40
2.4.4 Metabolic activity of pASCs on ABS substrates as a function of immobilized PDGF	40
2.4.5 The bioactivity of pASCs within CG scaffold-ABS fiber composites	41
2.5: Discussion	41
2.6: Conclusions	45
2.7: Figures	47
CHAPTER 3: INCREASING THE STRENGTH AND ALTERING STRESS CONCENTRATIONS IN COLLAGEN SCAFFOLDS VIA CUSTOMIZABLE ARRAYS OF POLY-LACTIC ACID FIBERS	54
3.1: Chapter Overview	54
3.2: Introduction	55
3.3: Materials and Methods	56
3.3.1 Preparation of collagen-GAG (CG) suspension	56
3.3.2 Fabrication of polylactic acid fiber arrays via 3D printing	57
3.3.3 Fabrication of PLA fiber reinforced CG scaffolds via lyophilization	58

3.3.4 Sample preparation for mechanical testing and digital image correlation (DIC)	58
3.3.5 Bulk mechanical characterization.....	58
3.3.6 Local mechanical characterization via Digital Image Correlation	59
3.3.7 Statistics	60
3.4: Results.....	60
3.4.1 Bulk mechanical characterization of PLA collagen composites	60
3.4.2 Termination of correlation	61
3.4.3 Failure modes (2 mm amp samples).....	61
3.4.4 Local mechanical characterization of PLA collagen composites.....	61
3.4.5 Local strain profiles	62
3.4.6 Local strain gradient maxima	62
3.5: Discussion	63
3.6: Conclusions	67
3.7: Figures	68
CHAPTER 4: THE INCORPORATION OF GEOMETRIC INTERDIGITATIONS TO DISSIPATE STRESS CONCENTRATIONS ACROSS THE INTERFACE OF A MULTI-COMPARTMENT COLLAGEN SCAFFOLD	77
4.1: Chapter Overview.....	77
4.2: Introduction	78
4.3: Materials and Methods.....	80
4.3.1 CG suspension preparation.....	80
4.3.2 CGCaP suspension preparation.....	80
4.3.3 3D printed dividers for multi-compartment scaffold creation.....	80
4.3.4 Geometrically interdigitated multi-compartment scaffold creation	81
4.3.5 Sample preparation for mechanical testing and digital image correlation (DIC)	82
4.3.6 Bulk mechanical characterization.....	82
4.3.7 Local mechanical characterization via Digital Image Correlation	83
4.3.8 Statistics	84
4.4: Results.....	84
4.4.1 Failure mode	84
4.4.2 Bulk mechanical characterization.....	84
4.4.3 Local mechanical characterization	85
4.4.4 Local strain profiles	86
4.4.5 Local strain gradient maxima	87
4.5: Discussion	87
4.6: Conclusions	93
4.7: Figures	95
CHAPTER 5: THE EFFECT OF GRADATIONS IN MINERAL CONTENT, MATRIX ALIGNMENT, AND APPLIED STRAIN ON HUMAN MESENCHYMAL STEM CELL MORPHOLOGY WITHIN COLLAGEN BIOMATERIALS	107
5.1: Chapter Overview.....	107
5.2: Introduction	108
5.3: Materials and Methods.....	111
5.3.1 Collagen-glycosaminoglycan (CG) suspension preparation.....	111
5.3.2 Mineralized CG suspension preparation.....	111
5.3.3 Layered scaffold creation.....	112
5.3.4 Osteotendinous scaffold creation	112
5.3.5 Carbodiimide crosslinking of multi-compartment scaffolds.....	113
5.3.6 Quantitative microstructural analysis of multi-compartment scaffolds	113
5.3.7 SEM analysis of multi-compartment scaffold microstructure	114
5.3.8 hMSC culture.....	114
5.3.9 Tensile strain.....	114
5.3.10 Nuclear and actin staining	115
5.3.11 Confocal imaging of cell-seeded scaffolds	115
5.3.12 Analysis of hMSC nuclear aspect ratio, orientation.....	116

5.3.13 Analysis of hMSC cytoskeletal orientation.....	116
5.3.14 Statistics	116
5.4: Results.....	117
5.4.1 Layered and osteotendinous scaffolds both show graded mineral content but only osteotendinous scaffolds display an aligned pore microstructure	117
5.4.2 Tracking MSC morphology within the scaffold in response to applied strain	118
5.4.3 hMSC nuclear aspect ratio is heightened and is sensitive to applied tensile strains in scaffolds that contain structural alignment	118
5.4.4 hMSC nuclear alignment is co-regulated by scaffold microstructural alignment and applied tensile strain	119
5.4.5 hMSC cytoskeletal response to tensile strain in multi-compartment scaffolds.....	120
5.5: Discussion	121
5.6: Conclusions	124
5.7: Figures and Tables.....	126
CHAPTER 6: CONCLUSIONS AND FUTURE WORK.....	132
6.1: Conclusions	132
6.2: Future Work	136
6.2.1 Combining multiple mechanically robust strategies	136
6.2.2 Characterizing cellular response at the microscale.....	138
6.2.3 Linking local cellular response to fundamentally different local mechanical profiles.....	139
6.3: Perspective.....	139
APPENDIX A: MATERIAL CREATION PROTOCOLS	141
A.1: CG Suspension Preparation Protocol	141
A.2: CGCaP Suspension Preparation	143
A.3: Layered and Interdigitated Scaffold Preparation.....	145
A.4: Osteotendinous Scaffold Preparation	147
A.5: Fabrication of ABS/PLA Constructs via 3D Printing.....	149
A.6: Fabrication of ABS/PLA-Scaffold Composite Scaffolds via Lyophilization.....	151
APPENDIX B: MATERIAL PROCESSING AND FUNCTIONALIZATION PROTOCOLS	153
B.1: EDC Cross-linking Protocol.....	153
B.2: Functionalization of ABS Constructs with Biomolecules	155
B.3: Sectioning Collagen-Based Scaffolds via Cryostat.....	157
B.4: Scaffold Glycolmethacrylate Embedding Protocol	158
APPENDIX C: MATERIAL VISUALIZATION, CHARACTERIZATION, AND ANALYSIS PROTOCOLS	159
C.1: Scanning Electron Microscope Imaging	159
C.2: Scaffold Pore Size Analysis: Aniline Blue Staining, Image Acquisition, and Linear Intercept Analysis Protocol.....	160
C.3: Bulk Mechanical Characterization	167
C.4: Local Mechanical Characterization via Digital Image Correlation	169
APPENDIX D: CELL CULTURE, ASSAYS, AND STAINING PROTOCOLS	175
D.1: hMSC and pMSC Culture Protocol	175
D.2: Cell Seeding on Scaffold Variants	179
D.3: AlamarBlue Metabolic Activity Protocol.....	181
D.4: DNA Quantification (Hoechst Dye) Protocol.....	183
D.5: BOSE System Multi-Compartment Scaffold Straining.....	185
D.6: Confocal Imaging Protocol	186
D.7: Nuclei and Actin Orientation Analysis	188
REFERENCES	194

LIST OF SYMBOLS AND ABBREVIATIONS

Abbreviation	Term, Definition
λ	Period
Θ	Angle of interdigitation
2D	Two-dimensional
3D	Three-dimensional
a	Minor axis (ellipsoid)
A	Amplitude
ABS	Acrylonitrile butadiene styrene
ANOVA	Analysis of variance
pASC	Porcine-derived adipose derived stem cell
ASC	Adipose derived stem cell
b	Major axis (ellipsoid)
BMP-2	Bone morphogenetic protein 2
BMP-7	Bone morphogenetic protein 7
BSA	Bovine serum albumin
CaP	Calcium phosphate
Ca(OH) ₂	Calcium hydroxide
Ca(NO ₃)·4H ₂ O	Calcium nitrate tetrahydrate
CG	Collagen-glycosaminoglycan co-precipitate
CGCaP	Collagen-glycosaminoglycan calcium phosphate triple co-precipitate
COOH	Carboxylic acid group
d	Mean pore size
DIC	Digital image correlation
DMEM	Dulbecco's modified Eagle's media
DMSO	Dimethyl sulfoxide
DNA	Deoxyribonucleic acid
ECM	Extracellular matrix
EDC	1-Ethyl-3-(3-dimethylaminopropyl) carbodiimide hydrochloride
EDTA	Ethylenediaminetetraacetic acid
FBS	Fetal bovine serum
FITC	Fluorescein isothiocyanate
g	Thickness
GAGs	Glycosaminoglycans
GDF-5	Growth/differentiation factor 5
GF	Growth factor
GFP	Green fluorescent protein
GUI	Graphical user interface
HCl	Hydrogen chloride
IGF-1	Insulin-like growth factor-1
<i>l</i>	Actual contact length
<i>l_o</i>	Minimum contact length
J	Energy (ellipsoid)
MSC	Mesenchymal stem cell
hMSC	Human-derived mesenchymal stem cell

Abbreviation	Term, Definition
NA	Numerical aperture
NHS	<i>N</i> -hydroxysulfosuccinimide
OH	Hydroxyl group
PBS	Phosphate-buffered saline
PC	Personal computer
PDGF	Platelet derived growth factor
PDGF-BB	Platelet derived growth factor BB
PDMS	Polydimethylsiloxane
Phi	Direction of orientation (ellipsoid)
PLA	Poly-lactic acid
PTFE	Polytetrafluoroethylene
PTgui	Panoramic Tools graphic user interface
QMUL	Queen Mary University of London
R	Any protein of interest
ROCK1	Rho-associated, coiled-coil-containing protein kinase 1
SCI	Suture complexity index
SEM	Scanning electron microscope
TBJ	Tendon-bone junction
TRITC	Tetramethylrhodamine
UV	Ultraviolet light

CHAPTER 1: INTRODUCTION

1.1: Chapter Overview

This chapter motivates the need for better strategies to repair and regenerate the tendon bone junction and introduces the topic of multi-tissue regeneration through tissue engineering approaches. Porous, collagen-based biomaterials for tendon and bone tissue engineering are first introduced separately, and individual contributing cues – specifically pore structure, biomolecules, composition, mechanical stimulation, and stiffness – and how they have been utilized to effect stem cell fate are reported (**Figure 1.1**). This chapter then reviews the challenges of both a multi-tissue engineering approach, as well as presenting combinations of cues together instead of separately. Finally, we summarize the work presented in this thesis and describe our goal of engineering a multi-compartment collagen biomaterial with spatial heterogeneities to impart biophysical and biochemical cues to mesenchymal stem cells through manipulating a series of biomaterial design criteria.

1.2: The Rotator Cuff as an Orthopedic Interface

The tendon-bone junction (TBJ) is a unique, mechanically dynamic anatomical zone that transmits force from aligned and highly elastic tendon tissue to mechanically stiffer and mineralized bone tissue without failure. Due to 100-fold differences in mechanical properties of tendon (0.4 GPa) and bone (20 GPa), the TBJ experiences high stress concentrations which it must dissipate without failure. It does this through local gradients and patterns in extracellular matrix (ECM) proteins, growth factors (GF), mineral content, and stiffness (**Figure 1.2**) [1-4]. However, TBJ injuries such as rotator cuff tears are common, with more than 4.5 million physician visits and 250,000 surgeries nationally each year [5]. In a rotator cuff tear, the tendon

typically tears away from the bone (humeral head), and to reattach the rotator cuff tendon to the humeral head, surgeons typically suture the tendon to holes drilled directly into the bone (**Figure 1.3**).

Current challenges in rotator cuff repair remain, as during the healing process the complex patterns of tissue composition across the interface are replaced by scar tissue, which lacks the functionality of the TBJ. This leads to extremely high (>90%) re-failure rates in certain demographics, especially older populations [1]. Although a surgical approach is successful for many patients, there is a large field of research being conducted to explore different methods and techniques of surgical anchoring and reattachment, as well as and pre- and post- operative physical therapy treatment [6-16]. One strategy to better address rotator cuff tears is a better tendon anchoring technique. *Barber and Drew* examined TBJ motion and cyclic loading to compare single-row, triple-loaded anchors with suture-tape, rip stop, double-row anchoring techniques. While the suture-tape, rip-stop, double-row rotator cuff repair technique outperformed the traditional single-row anchor, both methods typically failed at the suture in the tendon, where stresses were concentrated and the suture ripped through the softer tendon [6]. However, additional studies have often placed failure of double-row repair at the original failure site, resulting in mixed clinical results between these two techniques remain, and the best repair technique remains controversial [14]. Additionally, biomaterial, biochemical, and stem cell augmentation techniques provide evidence for better or less variable surgical outcomes [16-20]. Finally, a great deal of research has been conducted into the best biomechanical loading regiment post-surgery. Depending on the location of the repair, different immobilization positions have been shown to reduce stress at the tear site, potentially allowing for better healing [8], and

inducing paralysis in the shoulder has shown to enhance future mobility [7]. However, the shoulder must also remain mechanically dynamic during rehabilitation to prevent tendon and muscular degeneration and fatty infiltration of the rotator cuff [21, 22]. Return to overuse activity in rats, while not resulting in compromised function, does contribute to altered tendon properties which may result in a chronic condition [11, 23]. In the field of rotator cuff repair, unique injury sites surely require personalized medicine approaches to address the wide variability of clinical outcomes. However, all of these techniques have lower success rates as the patient's age increases, which is concerning as the United States population ages and life expectancies increase [24-26], some large and massive rotator cuff tears remain irreparable under current surgical techniques [13, 15, 27]. Considered together, this clearly demonstrates the need for a new approach to tendon-to-bone healing.

The challenges in rotator cuff repair, and more generally in multi-tissue orthopedic regeneration, can be met with biomaterial approaches which may offer the ability to engineer cellular microenvironments to better restore injured tissues. This approach may have the capability to provide better healing and regenerative capacity across the unique complexities of a multi-tissue healing approach, such as that required for the TBJ. To achieve this, we must develop biomaterial approaches which can utilize stem cells isolated from the patient's own body and direct them down distinct, spatially selective lineages. This biomaterial approach requires distinct regions for tendon, bone, and insertion regeneration while using compartment-specific chemical and biophysical cues to direct stem cell fate. Although many approaches have been developed for singular presentation of specific chemical or biophysical factors to direct stem cell fate, the complexities of multi-tissue regeneration must utilize multiple signals across a single

biomaterial, which remains a unique challenge. In this thesis, we examine five fundamental elements (*stiffness, composition, pore structure, mechanical stimulation, biomolecular cues*) of a successful biomaterial approach, basing our work off of individual cues first, but primarily focusing on multiple factor presentation as the biomaterial becomes more complex and mimics the native tissue microenvironment more fully.

1.3: Functionalizing Porous Collagen-Glycosaminoglycan (CG) Biomaterials with Singular Factors

Tendon and bone both consist of approximately 90% extracellular matrix (ECM), which is a complex combination of macromolecules and proteins, often arranged in a hierarchal structure (**Figures 1.4, 1.5**) [28]. The ECM is secreted by tissue-specific cells to provide structural support, biomolecular sequestration, and a microenvironment in which cells can live and interact [29, 30]. In tendon, the ECM is primarily composed of collagen (predominantly type I) and elastin and is notably structured in a complex hierarchy. Collagen molecules are the most basic unit of this hierarchy. Collagen molecules (~1.5 nm) come together to create collagen fibrils (~50-500 nm), which then make up tendon fascicles (~50-100 μm), which are crimped to form the macroscopic tendon structure (**Figure 1.4**) [3]. Although a large percent of bone is also composed of collagen, approximately 80% of bone by weight is also mineralized with calcium hydroxyapatite [30]. The mineral provides a much stiffer microenvironment compared to tendon, although both are highly structured. In compact bone, mineralized collagen fibrils are arranged into concentric rings called lamella, which are further arranged into osteons, which make up the bone (**Figure 1.5**) [31]. Most materials employed in tissue engineering are meant to mimic the properties or functionality of the native ECM [28].

Porous biomaterials are able to provide an initial substrate which mimics the native ECM and provides high specific surface area for initial cellular attachment and proliferation. Porous biomaterials can incorporate a wide range of microstructures into a construct which not only promotes cellular viability, but provides biophysical and microenvironmental cues to regenerate entire tissues. While there are many available biomaterials and techniques to create a porous construct, all with their (often application-specific) advantages and disadvantages, in this thesis we will focus on collagen-glycosaminoglycan (CG) variants which are popular as substrates for connective tissue engineering, including tendon and bone regeneration.

CG scaffolds are often created through a lyophilization process commonly known as freeze-drying. This technique requires an aqueous suspension, which can be adjusted for a specific application (mineral content to support bone formation [32]; GAG selection to encourage selective biomolecular sequestration [33]). Lyophilization consists of freezing, then sublimating the ice crystals through a drop in pressure, which leaves behind a dry, porous construct. Pore size is dependent on the size of ice crystal formation; it can be controlled by adjusting the freezing temperature and is typically between 50 μm and 300 μm [34-36]. Pore shape can also be controlled by using a directional solidification technique, creating highly aligned pores that can help drive stem cells down a tenogenic lineage [37-39]. These parameters will be discussed in further detail later in this chapter. Lyophilization is an extremely versatile technique that increases the shelf life of the construct and maintains biological and chemical activity [40].

(Figure 1.6)

1.3.1 Pore structure

Biomaterials must provide a microenvironment which can support and recruit tissue-specific cells, while also mimicking the mechanical and biophysical properties of the tissue as a whole. While the specifics of these criteria change depending on the tissue application, there are fundamental tradeoffs between pore size, permeability, and mechanical properties that are integral to any porous biomaterial scaffold. In order to be used as a template for cellular growth, pores should be large enough to allow for nutrient transport and cellular infiltration (approximately 50 to 400 μm depending on cell type [41]), while maintaining appropriate tissue-dependent mechanical integrity. Pore size also influences the specific surface area (total surface area per unit volume), permeability (the rate at which liquid can pass through a porous material), and elastic modulus of the material. These tradeoffs are expressed as

$$\frac{E^*}{E_s} = A' \left(\frac{\rho^*}{\rho_s} \right)^2 \quad \text{(Equation 1.1)}$$

where E^* is the elastic modulus of the porous construct, E_s is the elastic modulus of the solid, A' is specific surface area, ρ^* is the density of the porous construct, and ρ_s is the density of the solid [42]. Specific surface area is inversely related to pore size, while permeability increases proportionately with pore size. In general, initial cellular attachment increases with an increase in specific surface area [41]. Although initial cellular attachment influences all future cellular proliferation and activity, an increase in specific surface area decreases the permeability of the material. Permeability of tissue engineering scaffolds is on the order of 10^{-9} - 10^{-12} m^2 , and influences how nutrients diffuse through the scaffold and reach the cell for proliferation, differentiation, and waste removal [41, 43, 44]. This is expressed as Darcy's Law, and is given by

$$K = \frac{Ql\mu}{\Delta PA} \quad \text{(Equation 1.2)}$$

where Q is the resultant flow rate, μ is the viscosity, ΔP is the pressure drop across the material, and l (thickness) and A (cross-sectional area) are sample dimensions. These parameters can be easily measured in a laboratory setting, and the fluid flow rate (Q) and pressure drop (ΔP) are affected by the porosity of the material [41, 45]. With decreased permeability, there is a decrease in nutrient transport and autocrine signaling in addition to limited cell recruitment and mobility [41, 46-48]. Pore size must be carefully selected in order to balance the tradeoff between specific surface area and permeability. The optimal range of pore sizes for cellular applications is typically between 200 and 400 μm , which balances these parameters [41, 44, 48-51].

In addition to pore size, pore shape has been shown to influence cellular behavior in porous structures. Many tissues have an inherent architecture which can be described generally as a shape; these small microenvironmental cues can provide cells with powerful, tissue-specific behavioral information. For example, tendons and muscles are highly aligned, anisotropic tissues with a high aspect ratio, and the anisotropy of these native tissues has motivated efforts to develop biomaterials containing similar mechanical microenvironment to produce better cellular bioactivity. Tenocytes (tendon) and cardiomyocytes (muscle) both display higher degrees of tissue-specific bioactivity when cultured in three-dimensional (3D) materials with aligned pore geometry [35, 52]. In this thesis, we focus on using mesenchymal stem cells (MSCs), which have the ability to differentiate down both tenogenic and osteogenic lineages. In MSCs, anisotropic pores have shown to induce differentiation towards a tenogenic lineage [35, 53, 54], circular pores have been shown to steer mesenchymal stem cells towards an adipogenic lineage, and star-like pores have directed the same cells to produce osteogenic markers [53-55]. Cells have been shown to interact with their microenvironments through integrin and ligand interactions, which

can initiate cascades of signaling pathways which ultimately lead to gene expression, protein expression, stem cell differentiation, and other tissue-specific behaviors. Therefore, incorporating biophysical shapes into a cellular microenvironment is a powerful way to induce stem cell differentiation [53, 55, 56]. Moving forward, it still remains an open question as to how to best leverage these observations to create biomaterials for regenerative repair of orthopedic insertional tissues.

1.3.2 Stiffness

Different tissues throughout the body have very different stiffness and mechanical properties which provide cellular information, and stem cells are particularly sensitive to the mechanics of their local microenvironment [57-60]. The elastic modulus of the extracellular matrix ranges from approximately 0.1 kPa in the brain to approximately 20 GPa in cortical bone [57]. Cells can perceive their mechanical environment by generating contractile forces to sense their surroundings, and the stiffness of the matrix can influence stem cell fate decisions through the activation or hindrance of cytoskeletal organization and mechanotransduction pathways. This has been shown to drive stem cells down tissue-specific lineages (such as brain and muscle) via biomaterial surfaces that provide the corresponding elastic modulus of the tissue [57]. Recent advancements in biomaterials have led to increasingly complex emulation of the ECM, including these mechanical and biophysical properties. However, independent control of mechanical properties in a biologically relevant substrate has proven to be challenging, especially as biomaterials trend towards combining multiple compositions to regenerate mechanically distinct tissues. Traditional porous materials have inherent difficulty elucidating an independent response while simultaneously changing the stiffness of the material, since the pore structure is highly

inter-related with the elastic modulus of the material as given by **Equation 1.1**. Electrospun scaffolds typically increase mechanical stiffness (E^*) by increasing the thickness of each spun fiber, which concurrently decreases pore size [61], and this holds true across other porous biomaterials as well. Changing the stiffness of the overall material (E^*) by changing its composition, which changes the modulus of the overall solid (E_s) can also expose cells to a different and often undesirable microenvironment.

While porous, collagen-based biomaterials display advantageous bioactive characteristics, they also display sub-optimal mechanical strength. While pore size does specifically affect the mechanics of the biomaterial, the relative density of the construct (ρ^*) is directly related to the elastic modulus of the construct (E^*), given in **Equation 1.1**. Healthy tendon, trabecular bone, and the osteotendinous insertion each have elastic moduli well in excess of 10MPa [62-66], while CG scaffolds typically exhibit elastic moduli on the order of 20 – 200 kPa (dry) and 1 – 50 kPa (hydrated) [67-69]. While this stiffness can be increased through addition of mineral content (which changes the composition of the construct) or crosslinking (which is unknown whether this affects the porosity of the construct), the native stiffness of these scaffolds does not mimic that of native tissue [67]. Although tissue engineering constructs do not need to exactly match the tissue they are implanted into and cellular remodeling is expected to eventually increase the mechanical strength of the construct, the timescale for remodeling makes it impractical to rely on it as an initial stiffening strategy while scaffolds must still be able to withstand daily *in vivo* mechanical forces without failing [70].

1.3.3 Composition

Tendon and bone are both primarily composed of ECM, as briefly discussed earlier in this chapter. Collagen is the dominant ECM protein found in a wide variety of tissues, including the TBJ. Another group of compounds commonly found in connective tissues are proteoglycans, core proteins decorated with charged glycosaminoglycans. Collagen-glycosaminoglycan (CG) scaffolds are a versatile choice not only for tendon and bone tissue engineering, but also for many other collagen-containing tissues (i.e. tendon [2, 71, 72], bone [73-75], cartilage [32, 73, 76], eye, skin [77, 78], and vasculature [79]). A very successful CG scaffold, INTEGRA® Dermal Regeneration Template, uses a formulation of type I collagen and chondroitin sulfate and has already been approved by the FDA for dermal regeneration. Many CG scaffolds, such as the ones described within this thesis, are based off of the same FDA approved biomaterial, which lessens some of the hurdles in moving from bench top to clinical trials.

The basic composition of this CG scaffold can be modified slightly in order to include compositional cues to direct stem cell fate. As previously mentioned, bones primarily consist of a large percentage of calcium phosphate in the form of hydroxyapatite [80]. Calcium phosphate can easily be incorporated into a CG scaffold while creating the homogenized suspension later to be lyophilized, improves the mechanical properties of the CG scaffold, and has been shown to induce osteogenesis in mesenchymal stem cells [81]. Furthermore, hydroxyapatite has often been included in CG biomaterials used for bone tissue engineering [73, 82].

1.3.4 Mechanical Stimulation

Some tissues, such as those found in the musculoskeletal system, are mechanically dynamic. In order for these tissues to produce and maintain healthy cellular activity, they must provide the correct cellular cues through stretching and loading. For example, there is a balance between osteoblasts (bone forming cells) and osteoclasts (bone remodeling cells) in bone [83]. Bone formation via osteoblasts is triggered by active loading, such as exercise, while bone resorption via osteoclasts occurs after a period of lessened loading, such as bed rest. The musculoskeletal system (muscle, tendon, and cartilage) experiences similar dynamic mechanical cues [84]. Mechanical stimulation in the form of static or cyclic strain is a biologically relevant cue, and can also be used as a cue to drive stem cell response. *Hsieh et al.* established a method in which to create a gradient strain profile in which fibroblasts aligned themselves in the direction of strain, and both *Liang et al* and *Qiu et al* have shown that cyclic strain produces a tendon-like phenotype in MSCs [85, 86]. Chapter 2 of this thesis focuses on compartment-specific cellular responses to static strain on multi-compartment CG scaffold variants.

1.3.5 Biomolecular cues

Cells are constantly receiving and integrating a number of complex cues from a variety of biomolecules (i.e. growth factor, protein) *in vivo*. These biomolecules are generally classified as either solution phase or substrate supported. Solution phase signals mostly consist of growth factors, but can also consist of paracrine, endocrine, and other small bioactive molecules. In the field of tissue engineering, a common method of delivering growth factors to cells *in vitro* is to supplement the cellular media with soluble growth factors. However, cellular response to soluble factors is dependent on solution-phase dynamics, such as the diffusion rate of the factor, the

metabolic activity of the target cells, and the local concentration of the factor [87]. However, soluble factor supplementation has been successful in a variety of applications. Notably, in our research group, *Caliari et al.* demonstrated enhanced tenocyte chemotaxis (by insulin-like growth factor-1, or IGF-1 supplementation) and proliferation (by PDGF-BB supplementation) in a dose dependent manner [35], and went on to show that multiple growth factors could elicit synergistic cellular responses in proliferation and differentiation [88]. *Borselli et al.* showed a similar synergistic response in muscle cells with combined delivery of angiogenic and myogenic growth factors [89]. Critically, there are often trade-offs in stem cell proliferation and differentiation, which suggests that multiple cues may need to work in tandem to elicit the desired response. There have been a number of studies using growth factors as cues to direct human mesenchymal stem cell (hMSC) or adipose derived stem cell (ASC) fate. Notably, *Tan et al.* demonstrated that GDF-5 induced tenogenic differentiation in MSCs without negatively impacting proliferation [90], while other studies have looked at multiple cues to promote proliferation (i.e. PDGF) and tenogenesis simultaneously [91, 92].

While soluble factor presentation is an effective method of delivery *in vitro*, this method is limited *in vivo* by diffusion away from the target site. Lack of localization also increases the probability that the growth factor will affect unintended targets, such as other cell types or tissues. Furthermore, there is evidence immobilization of growth factors may even enhance activity, as this is how these signals are often presented in the native ECM [93, 94]. To this end, many research groups have immobilized growth factors to scaffolds using a variety of methods (carbodiimide cross-linking [78, 95, 96], biotin-avidin linkages [97], and “click” chemistries [98], photo-patterning [99-101], incorporation prior to lyophilization). The ability to present

biomolecular cues in a spatially controlled manner is particularly attractive for orthopedic interface repair applications, which require spatial heterogeneities for functionality. This thesis explores several immobilization strategies to control the spatial presentation of biomolecular cues.

1.4: Spatially Selective and Combinatorial Approaches to Biomaterial Functionalization

In order to effectively regenerate a spatially heterogeneous tissue such as the TBJ, the biomaterial scaffold must present cues in a spatially specific manner. These materials are often more challenging to fabricate than homogenous biomaterials, but have the potential to become more powerful tissue engineering tools.

1.4.1 Layered biomaterials

Perhaps the most straightforward approach to creating a biomaterial with spatial presentation of biophysical or chemical cues is to create a scaffold in layers. Collagen-based biomaterials are exceptionally versatile and minor modifications to the composition of the collagen starting material can produce subtle but powerful differences in cell response, especially within the musculoskeletal system. This section focuses on layered biomaterials for the purpose of regenerating bone and vasculature, bone and cartilage (osteocondral) and bone and tendon (osteotendinous) in parallel.

Sathy et al has developed a multi-layer collagen-based biomaterial to simultaneously regenerate bone tissue and vasculature, which is often lacking in critical-sized bone tissue engineering. *Sathy et al* used a collagen-fibronectin gel as the angiogenic layer and hydroxyapatite or

polycaprolactone with collagen nanospheres as the osteogenic layer, and built up a construct layer by layer which could effectively heal a critical sized bone defect in rats [102, 103].

Research efforts have also focused on developing an osteochondral scaffold for the purpose of dual cartilage and bone tissue regeneration. Cartilage alone has poor regenerative properties, and when a cartilage defect occurs in combination with a bone defect, a tissue engineering approach using a multi-layer scaffold has provided a reasonably successful platform to address poor functional outcomes. *Ghezzi et al* has developed a collage-silk multilayer scaffold capable of driving MSCs down distinct osteo- and chondro-genic lineages, although this approach is currently confined to *in vitro* techniques [104]. However, *Levingstone et al* has repeatedly demonstrated the ability of their multi-layer to regenerate osteochondral defects *in vivo* using rabbit animal models [73, 105, 106].

Similarly, previous work in our lab has developed an osteotendinous scaffold for tendon to bone regeneration via a layered approach, and has had high success incorporating alignment into the tendinous compartment while incorporating mineral into the osseous compartment [45]. Current work in our lab is focused on efforts to translate this scaffold from an *in vitro* platform to an *in vivo* model in mice, rats, and pigs. While many other researchers have incorporated a layered approach into a biomaterial platform, this section was meant to introduce collagen-based biomaterials specifically for musculoskeletal tissues, although the application of layered, multi-compartment scaffolds is not limited to these tissues.

1.4.2 Spatially graded or patterned biomaterials

Recent research has begun exploring methodologies in depth to produce gradations in both physical and chemical signals within biomaterials. One common way to mimic the native TBJ is by recreating the gradation in mineral content and stiffness within the biomaterial [107-111]. Notably, *Liu et al* developed a process in which to precipitate mineral content onto a biomaterial by slowly pumping a solution into a glass vial containing their electrospun scaffold, therefore exposing different portions of their scaffold to the mineralized solution for different periods of time. Another method of biomimicry is capturing the fiber (TBJ [112]) or cellular(tendon [113]) orientation gradient, moving from aligned to random across the interface. Similarly, gradation in biochemical presentation has been developed by multiple research groups independently [114-117], by methods ranging from simple diffusion (vasculature [112], TBJ [[114, 116]) to microfluidics (muscle [113], hematopoietic stem cell niche [115, 117]). Although a diffusive method to gradient creation is compatible with most porous biomaterials, microfluidic approaches are limited to liquids, and not homogenized suspensions typically used for lyophilized CG biomaterials.

Patterns of biomolecular signals can also be incorporated into biomaterials through a variety of means, although these signals are typically biochemical in nature and not physical. Patterning biomolecules using photo-sensitive chemistries are typically achieved by using photolithographic techniques [118-120]. Remarkably, *Almodovar et al* not only patterned multiple growth factors (BMP-2 and BMP-7) across a single 2D substrate which was capable of being both osteo- and myo-inductive simultaneously, but found synergistic effects when the two growth factors were present within the same substrate [118]. Two photon laser scanning lithography is another

technique, recently reported by *Culver et al* to create highly complex and structurally biomimetic patterns within hydrogels at micron resolutions [99]. The last major method of patterning we will discuss in this chapter is microcontact printing, which is exceptionally similar to making a pattern using a rubber stamp [121]. *Xu et al* reported a novel method of patterning dendrimers, proteins, and nanoparticles onto a biomaterial by using a porous stamp which first absorbed the biomolecular “ink”, and then in turn deposited it onto the surface. In the context of multi-tissue regeneration, patterning techniques are exceptionally powerful when the aim is to direct stem cells down a particular fate in a spatially selective manner. However, many of these techniques lose pattern fidelity or become complicated when translated from 2D to 3D substrates.

1.4.3 Improving the mechanical competence of compositionally graded biomaterials

Bioinspired designs offers an alternative paradigm for addressing current trade-offs between scaffold modulus and porosity. Core-shell composites, such as those found in the porcupine quills [122, 123] have inspired the work done by *Caliari et al*, integrating a high-density collagen membrane *shell* to the porous (low-density) collagen scaffold *core*, and have proven capable of increasing the overall elastic modulus by over 30-fold [72]. Further work used the addition of periodic perforations to the shell to improve biotransport and cell penetration into the scaffold [46]. While effective, the inherent shape of core-shell composite limits the ability to personalize this structure to individual injury dimensions. An additional bioinspired paradigm is found in plant stems, which use stiffer, longitudinal fibers to reinforce a porous construct, and **Chapters 2-3** focus on the translation of this paradigm into a tissue engineering biomaterial.

Another way to increase the overall mechanical properties of a material are to dissipate stress concentrations if they occur. Mechanical stresses are concentrated at the interface between any two mechanically mismatched materials; since our focus is on creating a multi-compartment scaffold where each compartment has unique mechanical properties, we expect stress concentrations to develop near the interfacial region. In nature, stress concentrations are often dissipated through interdigitation, such as those found in the scales of arapaima [124-126], turtle shells [127], and the native rotator cuff [1]. Although this general form of interdigitation has been considered and modeled in the design of structural materials [128], it has yet to be translated to biomaterial applications. Across a periodically repeating interdigitation, the amplitude (A), period (λ), interfacial thickness (g), minimum contact length (l_o), and actual contact length (l) can all impact interfacial shape. However, *Li et al.* demonstrated that these variables can all be reduced down to two components: the suture complexity index (SCI) and the angle of interdigitations (Θ). The SCI is a measure of contact length across the interface, l divided by l_o . Θ determines how many interdigitations, or “teeth” can fit across the interface. *Li et al.* also showed that there is an ideal Θ (approximately 12° in their model system) where tensile forces applied across the interface fundamentally shift to shear forces, which can be distributed over a larger area and thus minimized [128]. **Chapter 4** of this thesis explores ways in which we can translate this paradigm of interdigitation into a functional biomaterial.

1.4.4 Combinations of multiple signals

Within this chapter, we have primarily focused on single factor presentation to direct stem cell fate within a substrate, both homo- and heterogeneously. However, multiple classes of factors may elicit synergistic responses when presented together. For example, matrix stiffness has been

shown to sensitize cells to exogenous biomolecular cues. In the case of osteocytes, or bone cells, an increase in stiffness alone can produce osteogenic fate decisions. However, when provided with mechano-environmental signals in the form of a soft surrounding matrix in addition to a bone morphogenic protein (BMP-2), the protein has produced mixed effects [129, 130]. *Zouani et al* demonstrated that a stiffer substrate (>3.5 kPa) is required for BMP-2 to produce any effect on stem cell fate, but that this effect was not synergistic [129]. However, *Tan et al* found a synergetic effect of matrix stiffness and BMP-2 using a hydrogel-based platform. This result may be complicated by the fact that the stiffer hydrogels had a decreased porosity, and may provide an increased surface area for both BMP-2 and cells to adhere to. However, both of these studies support the conclusion that cells receive information through multiple sources and behave in a manner that is only consistent with all presented cues. However, many signals can produce synergistic responses. It has been shown that both alignment cues and mechanical stimulation can synergistically drive mesenchymal stem cells towards a tenogenic fate [131], while presenting multiple growth factors at once can induce simultaneous stem cell proliferation and differentiation, which is often difficult to achieve [116, 132, 133]. Biomaterials for complex musculoskeletal repair applications must incorporate a range of structural, biomolecular, compositional, mechanical, and stiffness cues to create a complex microenvironment which drives cellular behavior. By selecting and combining these signals, we may be able to develop a class of functional, synthetic biomaterials which can elicit a range of discrete responses from a single (stem) cell type. Our goal is to combine these physical and chemical attributes into a single construct for TBJ regeneration.

1.5: Summary

The purpose of this research project is to develop a mechanically strong, spatially distinct (biophysical and biomolecular) CG biomaterial to regenerate the TBJ. Our approach is unique in that it recognizes the complexity and heterogeneity of both microstructural and biomolecular cues across the native rotator cuff and uses strategies to prune these cues down to a fundamental set to regenerate the TBJ after failure (**Figure 1.1**). To create a mechanically robust biomaterial, we are exploring two bioinspired strategies. **1)** We have created a series of geometrically interdigitating scaffolds to show that we can translate the functionality and geometry of the native rotator cuff into a biomaterial for the first time and **2)** we have created a series of fiber-reinforced CG scaffolds to combine the bioactivity of the CG scaffold with the mechanical strength of the polymer support. Our platform also allows us to explore the fundamental mechanistic questions relevant to the design of biomaterials for orthopedic repair. While there is a wide field of research being conducted on how single cues influence cellular behavior, we have a unique platform on which we can vary a multitude of signals while simultaneously varying the substrate stiffness and pore architecture. By leveraging different strategies to combine multiple microenvironmental cues, we hypothesize that we will be able to synergistically direct stem cell fate across a large construct. We have the unique ability to control and monitor patterns of cues and cellular response across a biomaterial for orthopedic repair.

1.6: Thesis Overview

This thesis is aimed at developing a biomaterial platform to improve the regeneration of the tendon bone junction (TBJ) after injury. The TBJ is a unique, heterogeneous anatomical zone which connects highly elastic and aligned tendon tissue to mechanically stiff and mineralized bone tissue through a fibrocartilaginous interface. After injury, the unique gradations in matrix

proteins, mineral content, and structure do not regenerate, and re-failure often occurs. Our goal is to engineer a biomaterial to mimic these tissue heterogeneities and impart spatially selective cues to mesenchymal stem cells through manipulating a series of biomaterial design criteria (pore structure, biomolecular cues, composition, mechanical stimulation, stiffness).

Chapter 1 provides an overview of the current techniques that are used in rotator cuff repair, introduces our collagen-glycosaminoglycan (CG) biomaterial platform, and the techniques available to modify them to manipulate spatially selective differentiation cues to a stem cell population. Chapter 2 explores a model system of 3D printed, customizable fiber arrays embedded within a CG biomaterial to improve the mechanical properties of the system while maintaining the characteristic bioactivity of a highly porous material. Chapter 3 adapts the model system of fiber-composites to a more biocompatible system of PLA fibers. Chapter 4 discusses strategies to dissipate stress concentrations at the interface of two dissimilar materials through incorporating geometric interdigitations into the interface. Chapter 5 explores how mechanical cues in the form of static strain impact mesenchymal stem cell (MSC) morphology in the presence and absence of structural pore alignment. Finally, Chapter 7 will conclude with a summary and description of on-going work, as well as placing this work in the context of the field.

1.7: Figures

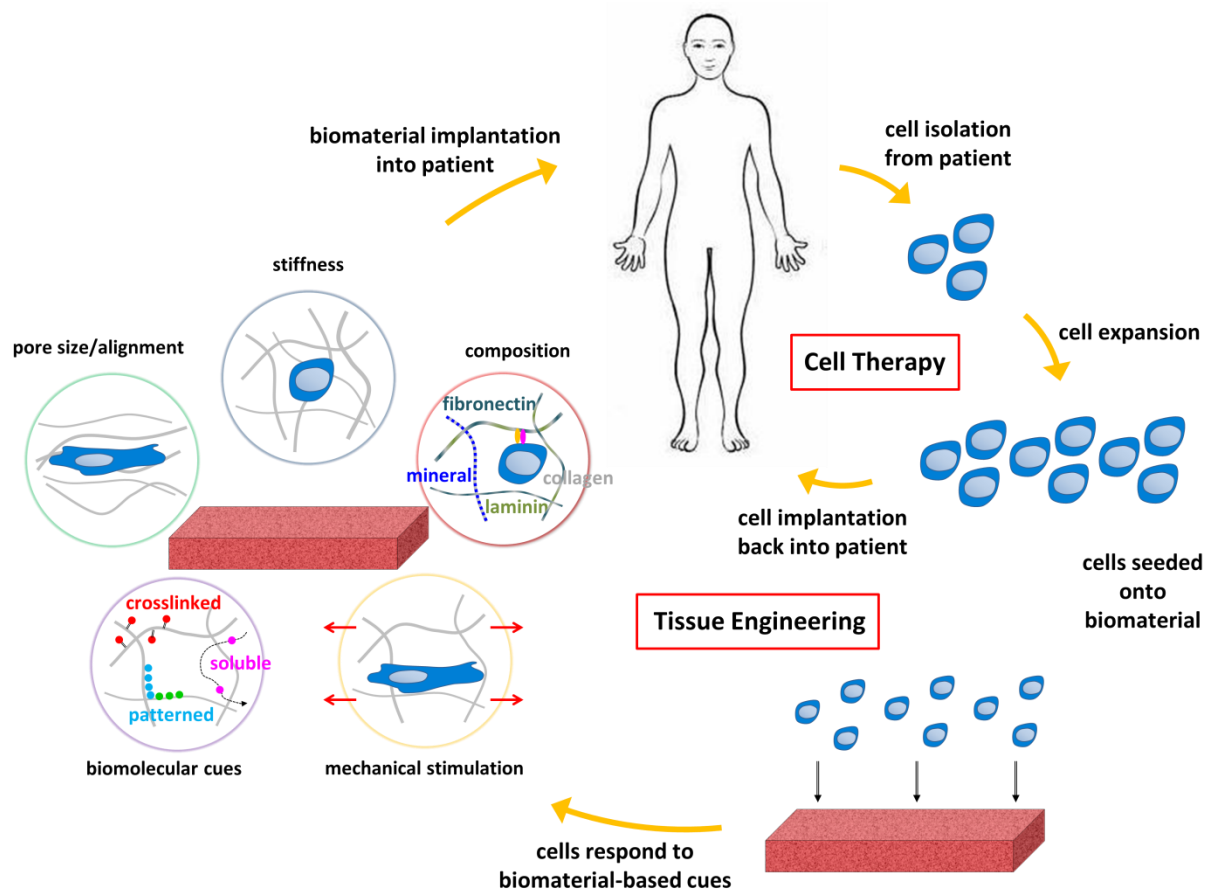
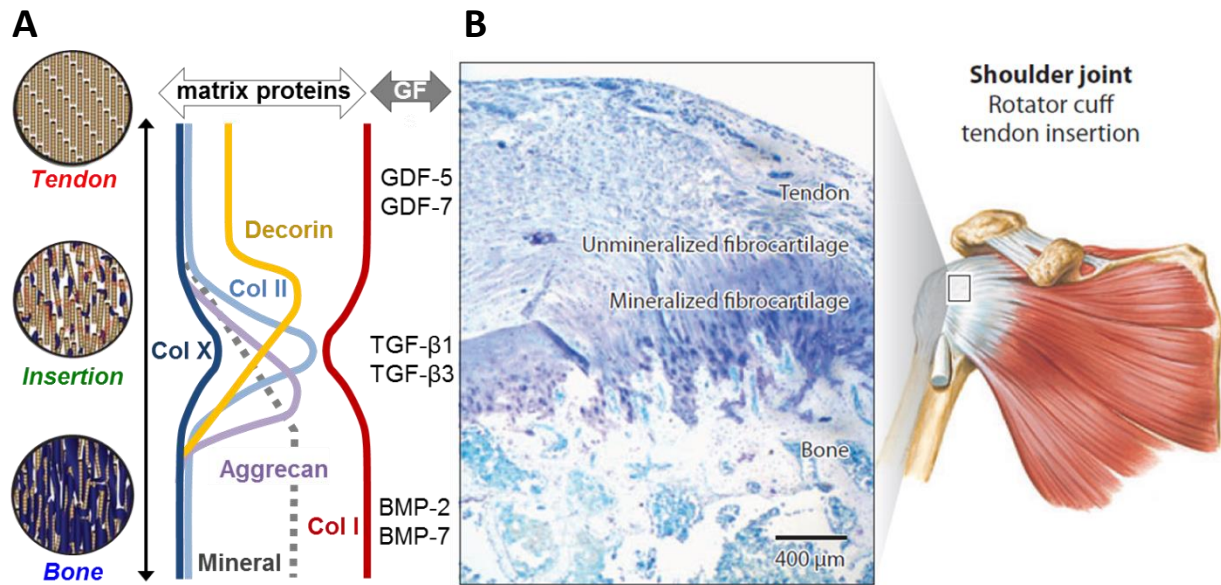


Figure 1.1 Biological cues to direct stem cell fate in tissue engineering approaches. Cells are isolated from the patient and expanded in culture. For cell therapy techniques, these cells are then placed back in the patient at the location of diseased tissue or injury. For tissue engineering techniques, the expanded cells are seeded onto a biomaterial, where they receive a variety of cues for further expansion, maintenance, or differentiation before the biomaterial is surgically implanted back into the patient, where it will continue to provide mechanical support and biological cues to the surrounding cellular environment [134].



*Figure 1.2 Visualization of the spatial heterogeneities across the TBJ. **A)** The TBJ consists of spatial patterns of matrix proteins, alignment, and growth factors. **B)** The structural anatomy of the TBJ at the rotator cuff consists of tendon and bone bound together by interdigitating unmineralized and mineralized fibrocartilage. Figure adapted from [1-3, 135].*

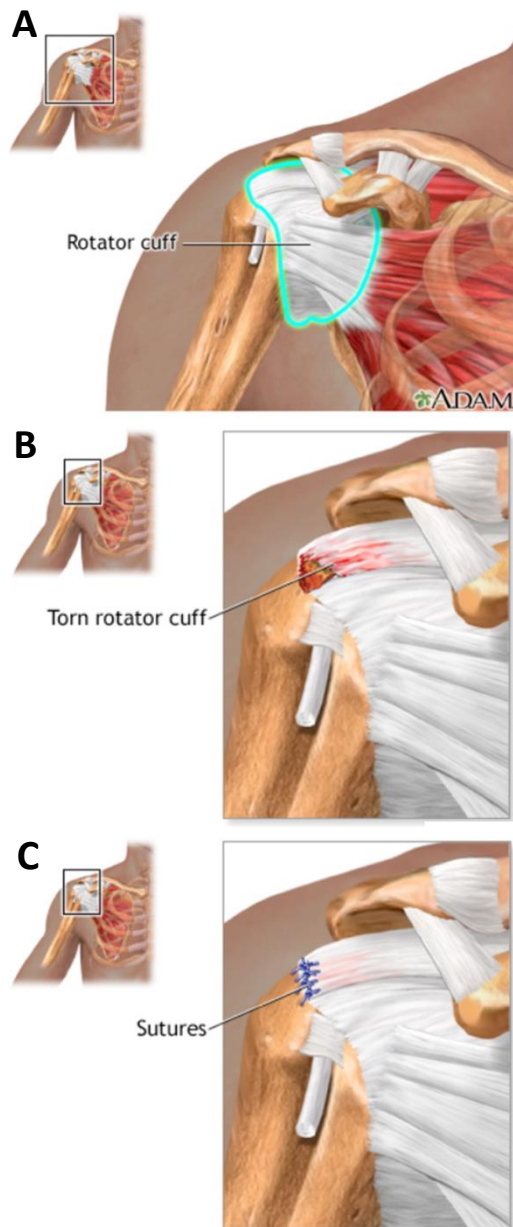


Figure 1.3 Typical surgical repair methods for a torn rotator cuff. A) The anatomy of a healthy rotator cuff, which is a portion of the shoulder. B) A torn rotator cuff is shown, where the tendon has ripped away from the bone after injury. C) A typical repair of the rotator cuff after injury. The sutures attach the tendon to holes which are drilled into the bone [10].

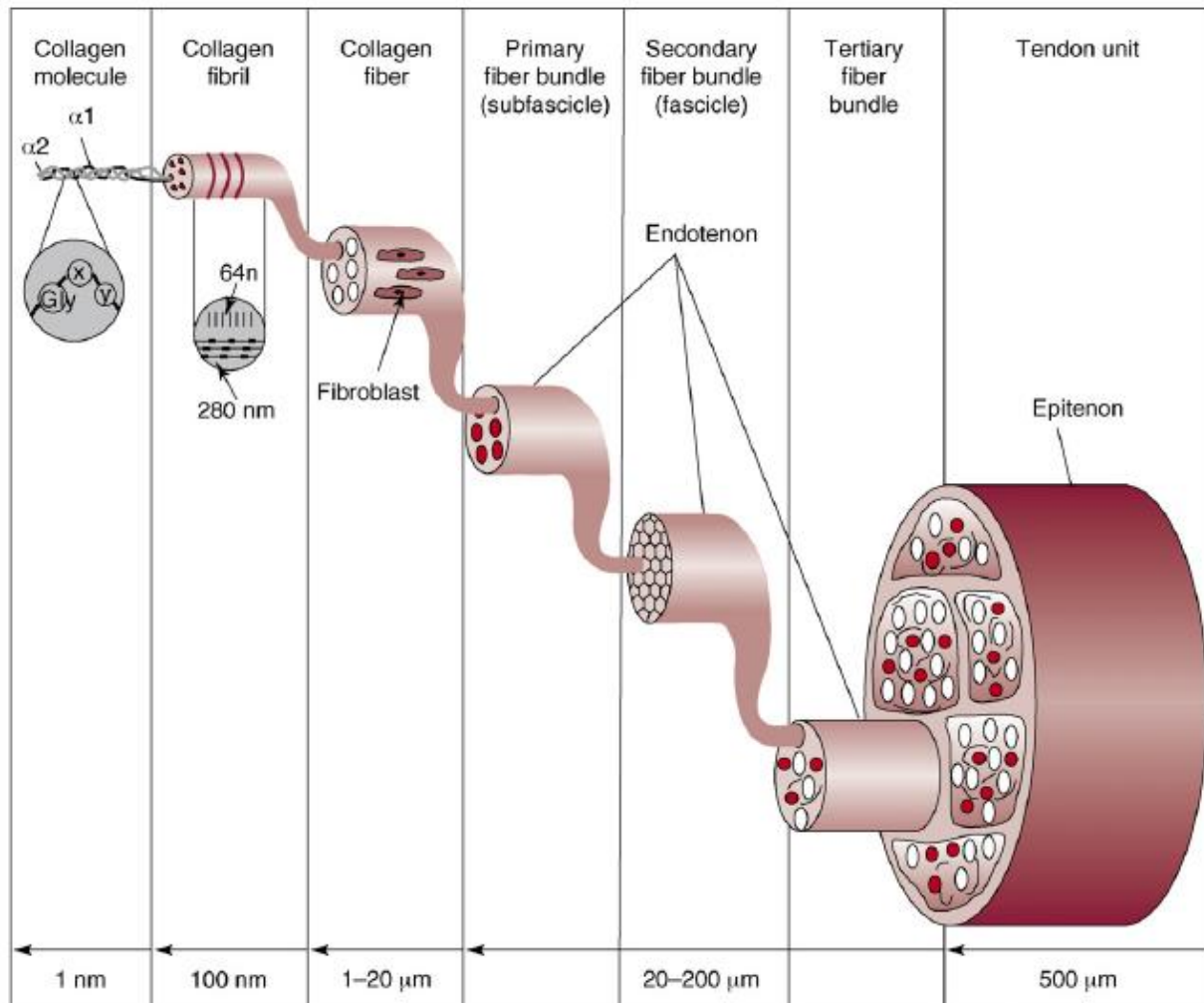


Figure 1.4 Hierarchal structure of tendon. Collagen molecules are arranged in a hierarchal structure which helps to impart mechanical bulk mechanical characteristics [3].

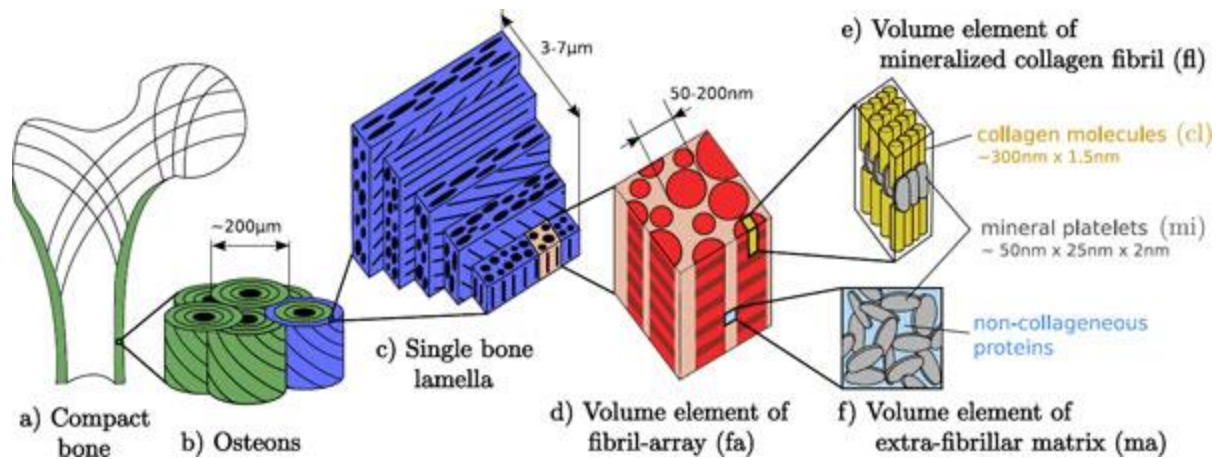


Figure 1.5 Hierarchal structure of bone. Mineralized collagen molecules are arranged in a hierarchal structure which culminates in osteons. The structured, mineralized collagen helps to impart bulk mechanical characteristics to the bone [31].

Collagen-GAG suspension:

Type I collagen
Chondroitin 6-sulfate
Acetic acid

CGCaP suspension:

Type I collagen
Chondroitin 6-sulfate
Calcium salts
Phosphoric acid

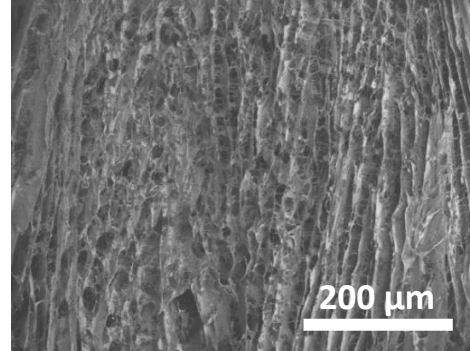
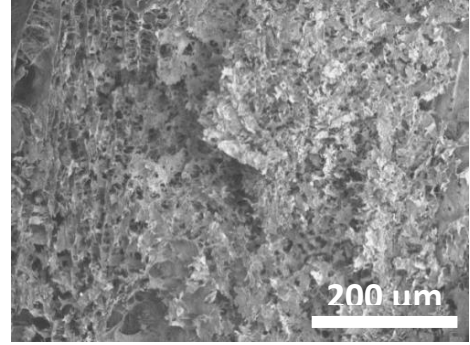
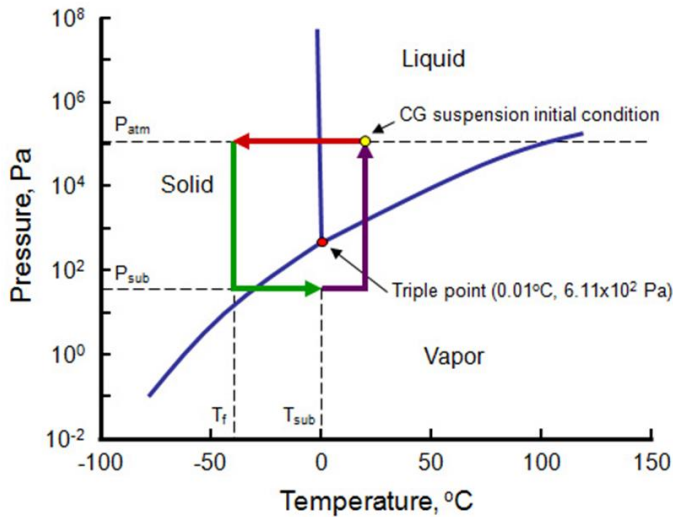


Figure 1.6 Fabrication schematic for CG and CGCaP scaffolds. Two suspensions, one consisting of type I collagen, chondroitin sulfate, and acetic acid and the other consisting of type I collagen, chondroitin sulfate, calcium salts, and phosphoric acid, are homogenized. The homogeneous suspensions can then be taken through a lyophilization process, which consists of a freezing step followed by sublimation. This leaves a dry, porous, sponge-like scaffold. SEM of a mineralized CG lyophilized scaffold (top, right) and anisotropic CG lyophilized scaffold (bottom, right) [136].

CHAPTER 2: INCREASING THE STRENGTH AND BIOACTIVITY OF COLLAGEN SCAFFOLDS USING CUSTOMIZABLE ARRAYS OF 3D-PRINTED POLYMER FIBERS¹

2.1: Chapter Overview

Tendon is a highly aligned connective tissue which transmits force from muscle to bone. Each year, people in the US sustain more than 32 million tendon injuries. To mitigate poor functional outcomes due to scar formation, current surgical techniques rely heavily on autografts. Biomaterial platforms and tissue engineering methods offer an alternative approach to address these injuries. Scaffolds incorporating aligned structural features can promote expansion of adult tenocytes and mesenchymal stem cells capable of tenogenic differentiation. However, appropriate balance between scaffold bioactivity and mechanical strength of these constructs remains challenging. The high porosity required to facilitate cell infiltration, nutrient and oxygen biotransport within three-dimensional constructs typically results in insufficient biomechanical strength. Here we describe the use of three-dimensional printing techniques to create customizable arrays of acrylonitrile butadiene styrene (ABS) fibers that can be incorporated into a collagen scaffold under development for tendon repair. Notably, mechanical performance of scaffold-fiber composites (elastic modulus, peak stress, strain at peak stress, and toughness) can be selectively manipulated by varying fiber-reinforcement geometry without affecting the native bioactivity of the collagen scaffold. Further, we report an approach to functionalize ABS fibers with activity-inducing growth factors via sequential oxygen plasma and carbodiimide crosslinking treatments. Together, we report an adaptable approach to control both mechanical

¹ This chapter is adapted from Mozdzen et al, Acta Biomaterialia 2016

strength and presence of biomolecular cues in a manner orthogonal to the architecture of the collagen scaffold itself.

2.2: Introduction

Tendons are highly aligned tissues made from a hierarchical alignment of type I collagen fibrils which transmit force from muscle to bone. Each year, chronic and acute tendon injuries account for more than 32 million injuries in the US alone [137]. Healing of these injuries can be complicated by the scale of the defect as well as the age and physical activity of the patient as well as resultant inflammatory response post-injury. While relatively minor tendon injuries may heal on their own, major tendon injuries result in scar formation which hinders mechanical performance and often results in pain and poor functionality. Current surgical techniques rely heavily on autografts and allografts [138]. Although these techniques are successful for some, they become problematic for recurrent injuries. Biomaterials for tissue engineering are becoming a popular approach to address these injuries and have a significant potential to replace allografts and autografts for many classes of complex tendon and ligament injuries. However, significant hurdles, particularly mechanical optimization, remain [139].

Collagen-glycosaminoglycan (CG) scaffolds belong to a versatile class of porous biomaterials that have been used for a wide range of tissue engineering applications. Fabricated via lyophilization from a suspension of extracellular matrix (ECM) derived proteins, these scaffolds present a porous network (typically greater than 95% porous) that supports cell invasion and metabolite biotransport [41, 140]. Here, individual pores of order 50 – 250 μ m in size are defined by fibers of collagen content, termed struts, which provide alignment, compositional, and stiffness cues to cells within the network. Originally developed to promote scarless healing in

dermis [77, 78] and peripheral nerves [141], the ability to precisely control microstructural features (pore size, shape) of these scaffolds has been exploited to examine mechanistic details regarding how scaffold biophysical properties affect cell adhesion, migration, and contraction [77, 140, 142, 143]. More recently, variants of these scaffolds have been developed towards promote healing of a wider range of tissues including tendon [2, 71, 72], bone [73-75], cartilage [32, 73, 76], and orthopedic insertions (tendon-bone; cartilage-bone) [144, 145].

Emerging efforts have focused on developing strategies that use the scaffold to provide instructive signals that selectively promote a desired cell behavior such as proliferation, migration, or functional phenotype. Mineral content and bioactive glass can be included into the scaffold to enhance mesenchymal stem cell (MSC) osteogenic differentiation and bone repair [144, 146-148]. Similarly, aligned networks of ellipsoidal pores generated via directional solidification have been exploited for applications in anisotropic tissue engineering (*e.g.*, cardiac, tendon) [35]. Biomolecular signals are particularly popular, and multiple strategies have been explored to incorporate growth factors within these collagen scaffolds. We and others have described the optimization of individual factors or combinations of soluble growth factors in the context of musculoskeletal repair [88, 149, 150]. In order to combat diffusive loss of these factors, additional efforts have described modifications to promote ubiquitous or spatially-patterned covalent immobilization of growth factors within the scaffold network [100, 151-153]. More recently, we have also described the use of scaffold proteoglycan chemistry to promote transient sequestration of growth factors within the CG scaffold via non-covalent interactions [33, 154].

Efforts in our lab have recently focused on the development of a new class of scaffold for regenerative repair of orthopedic insertions, notably the osteotendinous (tendon-bone) junction [144]. While CG scaffolds display advantageous bioactive characteristics particularly in the realm of promoting cell expansion and metabolic health, one particular disadvantage which has yet to be adequately addressed is the sub-optimal mechanical strength. Healthy tendon, trabecular bone, and the osteotendinous insertion each have elastic moduli well in excess of 10MPa [62-66]. CG scaffolds typically exhibit porosities in excess of 95% (relative density: <5%) in order to provide sufficient specific surface area for initial cell attachment as well as to facilitate nutrient biotransport [140, 155]. However, this high porosity leads to low mechanical strength, with typical elastic moduli of order 20 – 200 kPa (dry) and 1 – 50 kPa (hydrated) [67, 69, 144]. While this stiffness can be increased through the selective addition of mineral content or crosslinking, the native stiffness of these scaffolds is still more than two orders of magnitude too soft [67]. Although tissue engineering constructs do not need to exactly match the tissue they are implanted into, they do need to withstand daily *in vivo* mechanical forces without permanently deforming or failing. And while increasing the relative density of the scaffold leads to significant increases in the macroscopic scaffold modulus [67, 156], such increases come at a cost of reduced cell penetration and metabolic health. And while cellular remodeling can lead to significant increases in the mechanical strength of the construct, the timescale for remodeling makes it impractical to rely on it as an initial stiffening strategy [70].

Bioinspired designs offers an alternative paradigm for addressing current trade-offs between scaffold modulus and biotransport-influenced bioactivity. Inspired by core-shell composite structures such as those found in the porcupine quills and plant stems [122, 123], we recently

described the integration of a high-density collagen membrane *shell* to the porous (low-density) collagen scaffold *core* capable of increasing the overall construct elastic modulus by over 30-fold [72]. We added periodic perforations to the shell to improve biotransport and cell penetration into the scaffold [46]. While effective, the shell limited the capacity to rapidly produce constructs of arbitrary shape to address many osteotendinous injuries. So here we describe efforts to create a different reinforced scaffold composite inspired by the longitudinal fibers found as reinforcing structures in plant stems. This effort is enabled by the recent rapid proliferation of commercial three-dimensional printing tools. Here we report a prototype scaffold-fiber composite fabricated from a CG scaffold impregnated with arrays of acrylonitrile butadiene styrene (ABS) fibers generated using a commercial three-dimensional printing platform. This effort looks to combine the poor mechanical strength yet high biocompatibility of the CG scaffold with the superior mechanical properties but poor biocompatibility of ABS in a single composite. We explore the use of different fiber morphologies as a means to customize the composite mechanical behavior, as well as approaches to functionalize the fiber reinforcement array with biomolecules to enhance cellular bioactivity.

2.3: Materials and Methods

2.3.1 Preparation of collagen-GAG precursor suspension

A CG suspension was prepared from type I collagen (1.0% w/v) isolated from bovine Achilles tendon and chondroitin sulfate (0.1% w/v) derived from shark cartilage in 0.05 M acetic acid (Sigma-Aldrich, St. Louis, MO). The suspension was homogenized at 4 °C to prevent gelatinization during mixing and was degassed before use [157].

2.3.2 Fabrication of acrylonitrile butadiene styrene fiber arrays via 3D printing

A series of acrylonitrile butadiene styrene (ABS) fiber arrays were created then incorporated into CG scaffolds to evaluate the effect of ABS fiber reinforcement on scaffold mechanical properties. Each array consisted of 9 parallel 1mm diameter ABS fibers fixed together at either end with ABS end blocks (end blocks: 20 mm x 4 mm x 3 mm; complete fiber array: 20 mm x 76 mm x 3 mm) (**Figure 2.1**). Three different fiber geometries of theoretically decreasing elastic modulus were fabricated: a parallel array of 9 linear fibers (*straight fiber array*); a parallel array of 9 sinusoidal fibers with 1 mm amplitude (period: 11.3 mm; *1 mm sinusoidal fiber array*); a parallel array of 9 sinusoidal fibers with 2 mm amplitude (period: 11.3 mm; *2 mm sinusoidal fiber array*). Alternatively, ABS end blocks not connected by fibers were used as a negative control (*scaffold alone*). All constructs were printed using a MakerBot Replicator 2X (MakerBot Industries, Brooklyn, NY) at standard quality settings (10% infill, 2 shells, 200 μ m layered height) and an extruder speed of 90 mm/s. To ensure structural fidelity of the fiber arrays, ABS fibers were co-printed with polystyrene supports using dual nozzles (polystyrene: 250 °C; ABS: 230 °C) onto a temperature controlled build-plate (110 °C). The polystyrene supports were subsequently dissolved in D-Limonene (GreenTerpene, Miami, FL), leaving behind the final ABS fiber array. After all polystyrene was dissolved, ABS fiber arrays were washed multiple times with deionized water, and then dried before use.

2.3.3 Fabrication of ABS fiber reinforced CG scaffolds via lyophilization

ABS fiber arrays or ABS end blocks alone were placed into aluminum molds 7.6 cm (long) x 2 cm (wide). The CG suspension was then added to submerge the fiber array, with the final ABS-CG composite fabricated via a previously described lyophilization protocol [36]. Briefly, the

mold was placed on a freeze-dryer shelf (VirTis, Gardiner, NY) maintained initially at 20 °C. The shelf temperature was then ramped down to -40 °C at a rate of 1 °C/min, followed by a 1 hour hold at -40 °C to ensure complete solidification. Following freezing, the shelf temperature was ramped up to 0 °C at a rate of 1 °C/min, after which a 200 mTorr vacuum was maintained overnight to remove ice crystals via sublimation [36, 67], leaving behind the porous CG scaffold impregnated with ABS fibers (**Figure 2.1.A**). The CG-ABS fiber-reinforced scaffolds were dehydrothermally crosslinked at 105 °C for 24 hours under vacuum (<25 torr) in a vacuum oven (Welch, Niles, IL) [158]. After DHT crosslinking, scaffolds were stored under desiccation until use.

2.3.4 SEM analysis of fiber-scaffold composite microstructure

In order to visualize the degree of penetration of the CG scaffold into the ABS fiber array, transverse sections were cut through the CG-ABS composites with a razor blade in order to expose the interior structure of the composites. Transverse sections were subsequently imaged with scanning electron microscopy (SEM) on a JEOL JSM-6060LV (JEOL USA) to assess both the degree of CG scaffold penetration within the ABS fiber array as well as the presence of any voids between the ABS surface and the surrounding CG scaffold. A combination of secondary and backscatter electron detection were used under low vacuum to image the CG-ABS fiber array composite.

2.3.5 Tensile testing of ABS-CG composites

The elastic modulus of CG-ABS fiber array composites (7.6 cm x 2cm x 5 mm thick) were assessed via uniaxial tension tests. Tensile mechanical tests were performed on dry scaffold fiber

composite samples (5 cm gauge length) at a rate of 5.0 mm/min using an MTS Insight electromechanical load frame (Eden Prairie, MN), with tensile grips gripping the ABS end blocks embedded within each scaffold. Tests were performed on scaffolds ($n = 6/\text{group}$) containing: end blocks only (no connecting fibers; *scaffold alone*); a parallel array of 9 sinusoidal fibers with 2 mm amplitude (*2 mm sinusoidal fiber array*); a parallel array of 9 sinusoidal fibers with 1 mm amplitude (*1 mm sinusoidal fiber array*); a parallel array of 9 linear fibers (*straight fiber array*). The elastic modulus of each construct was calculated by taking the slope of the linear region (0.5% to 5% strain) of the stress-strain curve for each sample. Construct toughness was calculated analytically from the area under the stress-strain curve for each sample. Additionally, for each test overall peak stress (maximum load divided by sample cross-sectional area) and strain at peak stress were also calculated.

2.3.6 Functionalizing ABS constructs with biomolecules

In order to immobilize a biomolecule of interest to ABS constructs, the constructs were cleaned via oxygen plasma (no gas flow, high RF, <0.3 torr, 5 min per side; PDC-32G, Harrick Plasma, Ithaca, NY) in order to expose carboxylic acid groups on the ABS surface (**Figure 2.2**). Fibers were subsequently functionalized with either a model protein, bovine serum albumin (BSA), or platelet derived growth factor BB (PDGF-BB), known to enhance cell metabolic activity in CG scaffolds [88]. Plasma-cleaned ABS constructs were incubated with BSA (100 $\mu\text{g/mL}$) or PDGF (1 $\mu\text{g/mL}$) [159] in the presence of a solution of 1-ethyl-3-[3-dimethylaminopropyl] carbodiimide hydrochloride (EDC) and N-hydroxysulfosuccinimide (NHS) (5 mg/mL, 1 hr) to catalyze the formation of covalent crosslinks between the plasma cleaned ABS and the biomolecule of interest. Samples were washed in PBS and stored for future use. To quantify the

degree of biomolecular attachment, fluorescently labeled BSA (BSA-Alexafluor-594 conjugate, BSA-594, Fisher Scientific, Pittsburgh, PA, USA) was immobilized on two-dimensional ABS substrates. The supernatant was collected after biomolecular functionalization for each of 4 experimental groups (n = 3 per group): negative control (no BSA-594, plasma cleaning, or carbodiimide crosslinker); BSA-594 added with carbodiimide crosslinker without plasma cleaning; BSA-594 added after plasma cleaning but without the carbodiimide crosslinker; BSA-594 added with carbodiimide crosslinker after plasma cleaning. The amount of unattached BSA-594 remaining in the supernatant was quantified against a known standard via a fluorescence spectrophotometer (infinite M200 Pro, Tecan, Switzerland). Immobilized BSA-594 was calculated from the total BSA-594 added and the amount remaining in solution. Additionally, ABS fibers (1mm diameter) conjugated with BSA-594 were imaged with a fluorescent microscope (Leica DMI 4000B; excitation: 596; emission: 615) using an HCLImage camera (exposure time: 0.1 s) to assess the distribution of BSA-594 on the fiber surface (versus unconjugated ABS).

2.3.7 Cylindrical ABS-CG scaffolds to evaluate cell metabolic health

While large (7.6 cm x 2 cm x 5 mm) rectilinear constructs were used to demonstrate the efficacy of ABS-fiber reinforcement on the tensile properties of CG scaffolds, such large specimens were impractical for assays to evaluate the metabolic health of cells within the CG-ABS composites. In this case, 90,000 cells per construct would be required to match typical seeding densities of cells within CG scaffolds [160]. As a result, a second set of CG-ABS composites were generated to evaluate the impact of ABS-fiber incorporation on cell bioactivity. Here, a 10mm diameter scaffold disk (6mm thick) commonly-used by our laboratory for evaluating the effect of scaffold

properties on cell bioactivity [69] was used. Cylindrical ABS fiber cages (10mm dia.; 6mm thick) were fabricated from two parallel ABS fiber rings connected by 8 parallel ABS fibers (all fibers 1mm dia.) were incorporated into cylindrical CG scaffold disks via identical lyophilization steps as described in section 2.3. Importantly both the rectilinear (used for mechanical tests) and cylindrical (cell bioactivity) composites were designed such that the fiber volume remained relatively constant (cylindrical: 28%; rectilinear: 31%). Cylindrical CG-ABS composites were hydrated in ethanol followed by phosphate-buffered saline (PBS) then were crosslinked using carbodiimide chemistry for 1 hour in a solution EDC and NHS at a molar ratio of 5:2:1 EDC:NHS:COOH where COOH represents the amount of collagen in the scaffold [67, 78]. After crosslinking, cylindrical CG-ABS composites were rinsed and stored in PBS until further use.

2.3.8 Culture of porcine adipose tissue derived stem cells (pASCs)

Porcine adipose tissue derived stem cells (pASCs) were provided as a gift from Dr. Matthew Wheeler (U. Illinois at Urbana-Champaign) [161]. pASCs were expanded in standard tissue culture plastic in complete ASC growth medium (10% fetal bovine serum, 1% antibiotic-antimycotic in Dulbecco's Modified Eagle Medium) at 37 °C and 5% CO₂, fed every 3 days, and used at passage 7. For experiments evaluating the bioactivity of pASCs within CG-ABS composites (with or without immobilized PDGF), 9×10^4 pASCs in 20 μ L microliters of growth medium were seeded onto cylindrical (height: 6 mm; radius: 5 mm) scaffold specimens containing cylindrical fiber arrays using a previously described static seeding method [41]. After 30 minutes to allow initial cell attachment [35, 140], ABS-CG composites were transferred to complete ASC growth medium and then maintained for up to 7 days in a cell culture incubator (37 °C and 5% CO₂).

As a two-dimensional control, well plate inserts consisting of bare or PDGF-functionalized ABS disks (0.42 cm radius; height: 0.5 cm; 10% infill, 2 shells, 200 μ m layers; polystyrene extruder: 250 °C; ABS extruder: 230 °C; build plate: 110 °C; extruder speed: 90 mm/s) were generated via 3D printing. The inserts were placed into standard 24-well plates (Fisher Scientific,), seeded with porcine adipose derived stem cells (50,000 cells/well insert), and maintained for up to 7 days in a cell culture incubator (37 °C and 5% CO₂).

The mitochondrial metabolic activity of ASCs seeded in CG-ABS composites and on 2D ABS well plate inserts were quantified at day 1, 4 and 7 via alamarBlue® (Invitrogen, Carlsbad, CA). Viable, healthy cells reduce resazurin in alamarBlue solution to resorufin, which produces fluorescence. CG-ABS composites and 2D ABS well plate inserts were incubated in alamarBlue solution with gentle shaking for 1 hour, and fluorescence was then measured (excitation 540 nm, emission 580 nm) on a fluorescent spectrophotometer (Tecan, Switzerland). Results were compared to a prepared standard to compute equivalent cell number. Results (n = 5) were reported as the relative metabolic activity compared to the number of originally seeded cells [162]. The total number of pASCs attached to the CG-ABS fiber reinforced scaffold was also quantified at day 7 using Hoechst 33258 dye (Invitrogen, Carlsbad, CA) which fluorescently labels double-stranded DNA. Briefly, scaffolds were rinsed in PBS to remove unattached and/or dead cells, then placed in a papain solution at 60 °C overnight to digest the scaffold and lyse the cells. Total cell number was determined at day 7 using a fluorescence spectrophotometer (Tecan, Switzerland). Results (n = 5) were compared to a prepared standard to compute cell number and

were reported as the relative fold change as compared to the number of originally seeded cells [163].

2.3.9 Statistics

Significance was set at $p < 0.05$ and error is reported as standard error of the mean unless otherwise noted. The Levene test for equal variance was performed on all data sets to confirm validity of further statistical testing; If the Levene test showed unequal variance, the data was transformed by taking either the square root (toughness) or natural log (elastic modulus, 3D metabolic activity) and further statistical analysis was performed on the transformed data. One-way ANOVA was performed on mechanical (elastic modulus, peak stress, strain at peak stress, toughness), cell viability (alamarBlue), and proliferation (Hoescht) data followed by Tukey post-hoc tests. Mechanical tensile tests were performed with $n = 6$ samples per group, biomolecular functionalization experiments were performed with $n = 3$ samples per group, and all cell experiments were performed with $n = 5$ samples per group.

2.4: Results

2.4.1 Incorporation of ABS fibers within the CG scaffold

Following lyophilization, the CG scaffold fully incorporated the ABS fiber array (**Figure 2.1.B**). SEM analysis of transverse sections taken from the CG-ABS fiber array composite showed that the CG scaffold was directly opposed to the surface of the ABS fibers (**Figure 2.1.C**). Incorporation of the ABS fiber array was observed to add significant mechanical advantage relative to the scaffold alone; when strained to 20% strain, far in excess of the loading range of tissue engineering constructs for tendon applications (5% strain) [164] and the typical failure

strain of the CG scaffold (15%), the ABS fiber array – and hence the CG-ABS composite – remained competent.

2.4.2 The mechanical properties of the CG-ABS fiber array composites can be tuned via the fiber array design

The elastic modulus, peak stress, strain at peak stress, and toughness were calculated for a series of CG-ABS composites containing increasing degrees of mechanical reinforcement (*scaffold alone*; *2 mm sinusoidal fiber array*; *1 mm sinusoidal fiber array*; *straight fiber array*; **Figure 2.3**). The elastic modulus of the composites increased significantly ($p < 0.001$) with mechanical reinforcement, with the *straight fiber array* having the highest elastic modulus (15.05 ± 1.73 MPa), followed by *1 mm sinusoidal fiber array* (8.01 ± 0.51 MPa), *2 mm sinusoidal fiber array* (2.47 ± 0.32 MPa), and *scaffold alone* (0.22 ± 0.01 MPa). The peak stress also increased significantly ($p < 0.01$) following the same trend (*straight fiber array*: 0.91 ± 0.063 MPa; *1 mm sinusoidal fiber array*: 0.65 ± 0.075 MPa; *2 mm sinusoidal fiber array*: 0.30 ± 0.015 MPa; *scaffold alone*: 0.03 ± 0.001 MPa). The strain at peak stress was significantly ($p < 0.05$) higher for the *2 mm sinusoidal fiber array* (0.24 ± 0.03 mm/mm), though otherwise there was no significant differences between the strain at peak stress for any other groups ($0.10 - 0.15$ mm/mm). However, fiber reinforcement did significantly ($p < 0.01$) affect the overall toughness of the composites, with *straight fiber array* displaying highest toughness (151.9 ± 15.4 kJ/m²), followed by the *2 mm sinusoidal fiber array* (77.29 ± 6.3 kJ/m²), *1 mm sinusoidal fiber array* (75.4 ± 12.6 kJ/m²), and *scaffold alone* (2.77 ± 0.11 kJ/m²) (**Figure 2.4**). Overall, ABS-fiber reinforcement increased scaffold elastic modulus by up to 68-fold, peak stress by 30-fold, and toughness by 55-fold. Results for the CG-ABS fiber composites were compared to arrays of ABS

fibers alone; no significant differences were observed between the elastic modulus of the composites versus the ABS fibers alone (**Figure 2.5**), suggesting that processing steps for integrating the ABS fibers within the CG scaffold do not affect the mechanical stability of the fiber array itself.

2.4.3 Selective attachment of a model protein to the ABS fiber arrays via carbodiimide chemistry

Using fluorescently labeled BSA (BSA-594) as a model protein we confirmed that exposing plasma treated ABS to a protein of interest in the presence of EDC:NHS chemistry led to efficient covalent immobilization of the protein on the ABS fiber (**Figure 2.6**). No appreciable immobilization was observed when the BSA was simply exposed to the fiber or when either the plasma treatment or the EDC:NHS crosslinker were removed. However, significantly higher BSA attachment was observed when both plasma treatment and EDC:NHS crosslinking were employed, with PSA immobilization assessed via quantitative metrics (**Figure 2.6.A**) or fluorescent image analysis (**Figure 2.6.B**).

2.4.4 Metabolic activity of pASCs on ABS substrates as a function of immobilized PDGF

The metabolic activity of pASCs was measured at days 1, 4 and 7 on 2D ABS well plate inserts. Although metabolic activity increased at day 4 versus initial seeding conditions regardless of PDGF availability, it dropped to approximately initial seeding conditions by day 7. However, ABS substrates functionalized with PDGF promoted a significant increase in pASC metabolic activity compared to pASCs on ABS alone group at every time point ($p < 0.05$). (**Figure 2.7.A, B**).

2.4.5 The bioactivity of pASCs within CG scaffold-ABS fiber composites

The metabolic activity of pASCs maintained within the CG-ABS fiber array composites increased significantly in all groups with time (from day 1 to day 7; $p < 0.05$). While not significant ($p = 0.11$) the metabolic activity of pASCs in CG-ABS fiber array composites containing covalently attached PDGF was higher compared to composites containing bare ABS fibers (**Figure 2.7.C**). However, by day 7 there was a significant increase in the total number of pASCs within composites containing PDGF-functionalized ABS fiber arrays ($p < 0.05$) (**Figure 2.7.D**).

2.5: Discussion

Herein, we report an adaptable approach to mechanically reinforce a CG scaffold under development for tendon repair applications via incorporation of arrays of polymeric fibers created via three-dimensional printing methods. This approach led to significant (30- to 68-fold) increases in the overall mechanical performance of the CG composite in a manner that did not affect the metabolic health of cells within the matrix but which provides significant flexibility for tailoring overall construct mechanical properties. Additionally, we demonstrated the ability to functionalize the reinforcing fibers with activity-inducing biomolecules to further instruct cell response. Together, this approach offers a new avenue for designing high-porosity biomaterials for high-strength applications.

Increasingly, tissue engineering requires biomaterials with sufficient strength to match the mechanical properties of a healthy tissue while leaving the material porous enough and with high enough specific surface area to support cellular penetration, attachment, and sufficient nutrient biotransport. Composite designs offer a potential solution to this trade-off between sufficient

porosity and high mechanical strength. Previous work in our lab has demonstrated a core-shell composite design inspired by porcupine quills and plant stems [122, 123]. Here, a highly porous CG scaffold *core* was surrounded by a high density collagen membrane *shell* capable of increasing the composite modulus by over 30-fold [72]. To increase nutrient transport and cell penetration, periodic perforation could be added to the shell, but at the expense of strength [46]. While a useful demonstration of composite design, these constructs were difficult to adapt for the unique geometric needs of patient-specific defects. Work by *Mauck et al.* has explored the idea of using sacrificial chemistries for electrospun fibers to create fibrous mats for tissue engineering applications with enhanced permeability and cell infiltration [165]. However, these constructs are limited to relatively thin two-dimensional geometries and as such are difficult to individualize for personalized tissue engineering applications which require a unique, specifically shaped 3D biomaterial for patient-specific injuries.

The rapid growth of commercial 3D printing tools offers new potential to personalize biomaterials for tissue engineering applications. Advances in nozzle and ink design have allowed extrusion and printing of some cell containing hydrogels, yet the resolution of many commercial 3D printing tools is limited to millimeter-scale features [166]. However, the ability to generate customizable reinforcement structures to be integrated into more traditional tissue engineering biomaterials have been explored in only a limited manner [167]. The goal of this work therefore was to integrate the high strength, yet low spatial resolution of 3D printing techniques with a biomaterial with micrometer-scale features to create a composite with the best attributes of both, and was inspired by the longitudinal fibers found as reinforcing structures in plant stems [168]. Our novel CG-ABS composites described here are an example of multi-functional biomaterials,

using the ABS fiber array to selectively modify both mechanical strength and the incorporation of a biomolecule of interest independent of the CG scaffold design. Native tendon *in vivo* typically experiences strain profiles ranging from relatively small for position tendons (max. strain: 3.1%) [169] to significantly larger for energy storing tendons (e.g., Achilles tendon; max strain: 10.3%) [170], with a peak stresses of approximately 15-30 MPa, as well as a range of elastic moduli (0.45 GPa to 1.2 GPa) [63, 171, 172]. Although our composites fall short of matching these mechanical properties (especially at maximum loads which are typically avoided after injury) they are mechanically competent within the physiologically relevant range of strain, and have drastically improved properties compared to the collagen scaffold alone. As the composite is meant to be a regenerative template which provides a microenvironment to enable cell recruitment, proliferation, and matrix deposition, our focus here is to validate the fiber-reinforced biomimetic scaffold design paradigm. These composites show significantly improved and tunable mechanical properties compared to CG scaffolds alone, improved bioactivity when compared to ABS constructs alone, and lose neither mechanical integrity nor bioactivity when combined.

A significant concern for many biomaterials is the inability to orthogonally tune mechanics and bioactivity over a desired, functional range. Critically, the stress a biomaterial scaffold may experience *in vivo* often exceeds the amount of stress the scaffold alone can withstand before failure. This work demonstrates an approach to design a composite with a heightened modulus to result in desired levels of strain when exposed to a physiologically relevant load (or stress). Incorporating the ABS fiber arrays within a collagen composite allows the cells to experience a defined amount of strain, while withstanding an increased amount of stress. This approach also

suggests the capability to tune the elastic modulus, toughness, and peak stress/strain to meet patient-specific criteria. Ongoing efforts are exploring selective modification of the total number of ABS fibers, the thickness of the fibers, and the longitudinal changes in fiber architecture (*e.g.*, sinusoidal amplitude, period) along the fibers in order to regionally manipulate the local stress-strain fields during loading.

ABS was chosen as a model system for its ease of printing via commercially available 3D printing tools, its strength, and the potential for surface modification to facilitate covalent immobilization of biomolecules. However, long-term development of fiber-reinforced composites will likely require a different polymer that would support a wider range of functionality (*e.g.*, cell-adhesion, growth factor release, degradability). Given the low specific surface area of the ABS within the CG-ABS composite, cells likely primarily interact with the CG scaffold in the full composite. However, examining the role of PDGF-immobilization on 2D ABS substrates (**Figure 2.7**), pASCs were forced to interact directly with the ABS. While pASC metabolic activity was higher at all timepoints on ABS substrates containing surface immobilized PDGF versus ABS alone, an observation consistent with previous efforts in our group showing the efficacy of covalently-tethered PDGF [88], ABS itself did not support pASC expansion. Translated to the ABS-fiber reinforced CG composite, pASC metabolism increased significantly ($p<0.05$) over the 7 day culture period and total cell expansion was significantly higher ($p<0.05$) for CG-ABS composites containing covalently-immobilized PDGF (**Figure 2.7.C, 2.7.D**). This suggests construct mechanical behavior can be defined by the ABS fiber arrays, while cell response is likely dominated by the porous CG scaffold material. Given the surface area of ABS within the current composite design, effective use of the ABS fibers to

present activity-inducing growth factors while maximizing cellular activity within the collagen scaffold composite will require new methodological development. As there is a tradeoff between mechanics and bioactivity, even in our composite constructs, ongoing efforts are looking to solve a new optimization problem: minimizing the volume fraction of the ABS fibers while maximizing the enhancement in mechanics seen for the composite as a whole. To this end we are exploring more complex fiber designs, both increasing the number of ABS fibers as well as exploring the use of enzymatically cleavable linkers to provide temporal control over the bioavailability of immobilized biomolecules.

2.6: Conclusions

The need to balance biomechanical and bioactivity requirements in the design of tissue engineering biomaterials for musculoskeletal applications requires a new design toolbox. While typically incapable of generating biomaterials with micrometer-scale features, three-dimensional printing offers a unique way to generate composite biomaterials. Herein we demonstrate a composite design that integrates arrays of ABS fibers with tailorable mechanical properties generated via 3D printing into a collagen-GAG scaffold with high bioactivity under development for tendon repair applications. In addition to mechanical reinforcement, we also show that the fiber array offers a platform to integrate activity-inducing doses of growth factors into the construct in a manner orthogonal to the design of the collagen scaffold itself. The paradigm described here represents a novel departure from current methods to address bioactivity-biomechanical trade-offs in biomaterial design. This approach also offers the potential to integrate patient-customizable reinforcement elements into a standardized scaffold as well as the ability to locally tune the permissible stress-strain behavior of the composite in order to meet the

needs of a variety of musculoskeletal tissues including insertional zones between disparate tissues such as tendon and bone.

2.7: Figures

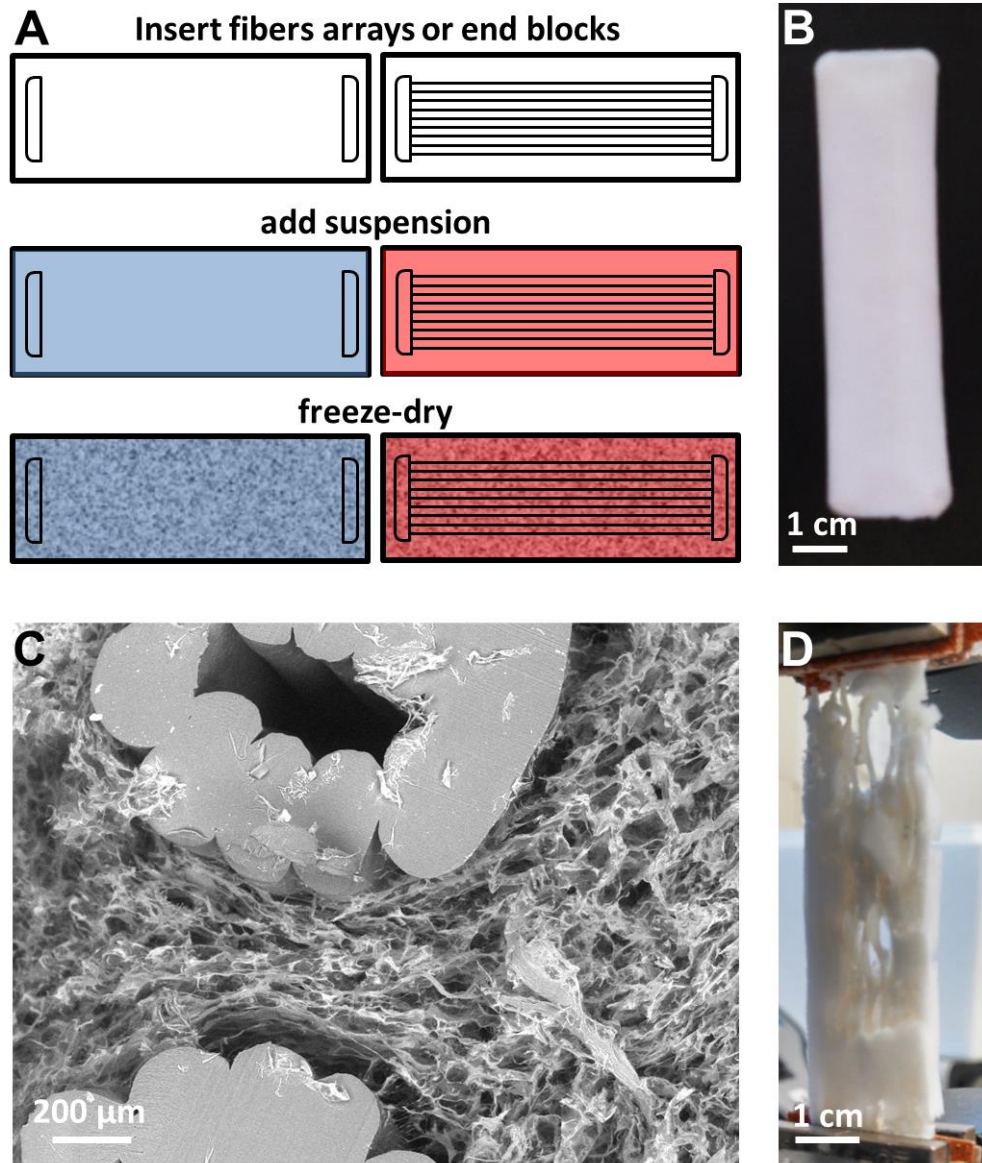


Figure 2.1 Structurally reinforced scaffold-fiber composite. **A)** Schematic for creating CG scaffolds without (left) and with (right) ABS polymeric fibers embedded within. Both contain ABS polymer end blocks to facilitate mechanical testing. **B)** ABS-fiber reinforced scaffold; fibers are completely incorporated within the scaffold. **C)** Representative scanning electron microscopy (SEM) image of transverse section through fiber-reinforced scaffold showing cross-section of ABS fibers and CG scaffold. Scale bar: 200 μ m. **D)** ABS-fiber reinforced scaffold strained to 20% strain in tension; although the scaffold would have failed, fiber reinforcement holds the composite together well past physiological strains.

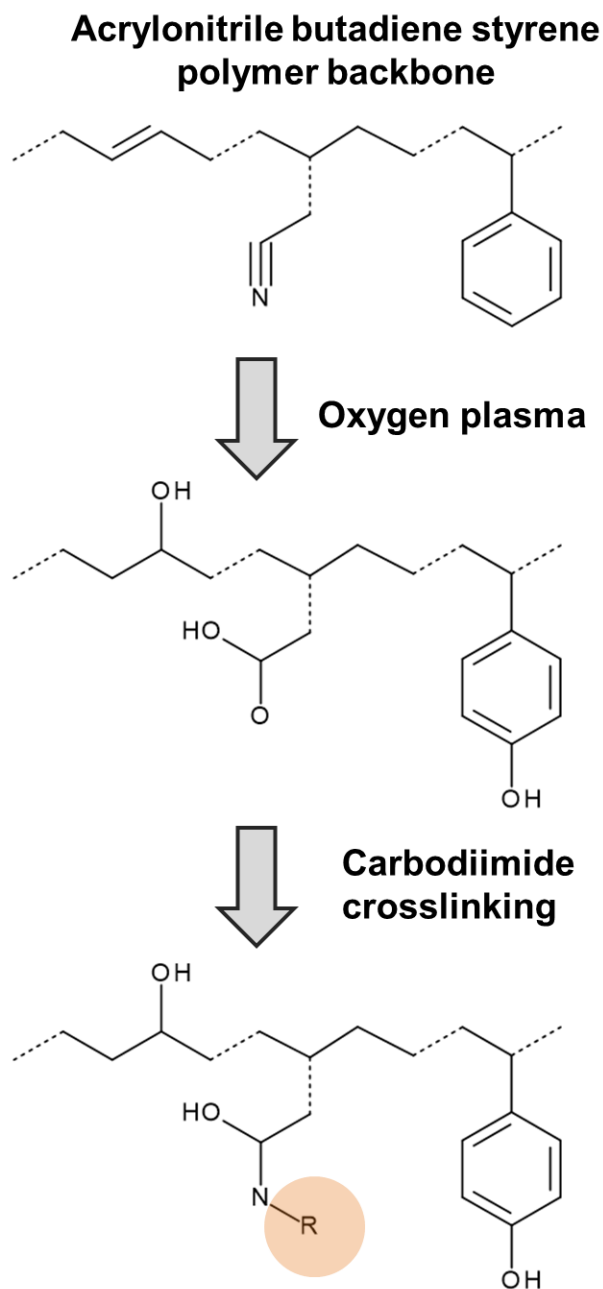


Figure 2.2 Schematic depicting sequential oxygen plasma treatment followed by carbodiimide crosslinking to immobilize a biomolecule of interest to the ABS. Oxygen plasma treatment bombards ABS with oxygen radicals, which introduces phenol, hydroxyl (OH) and carboxylic acid (COOH) groups into the polymer. EDC/NHS crosslinking can then attach any protein (R; orange highlight) via a primary amine to the ABS fiber backbone through the carboxylic acid functional group.

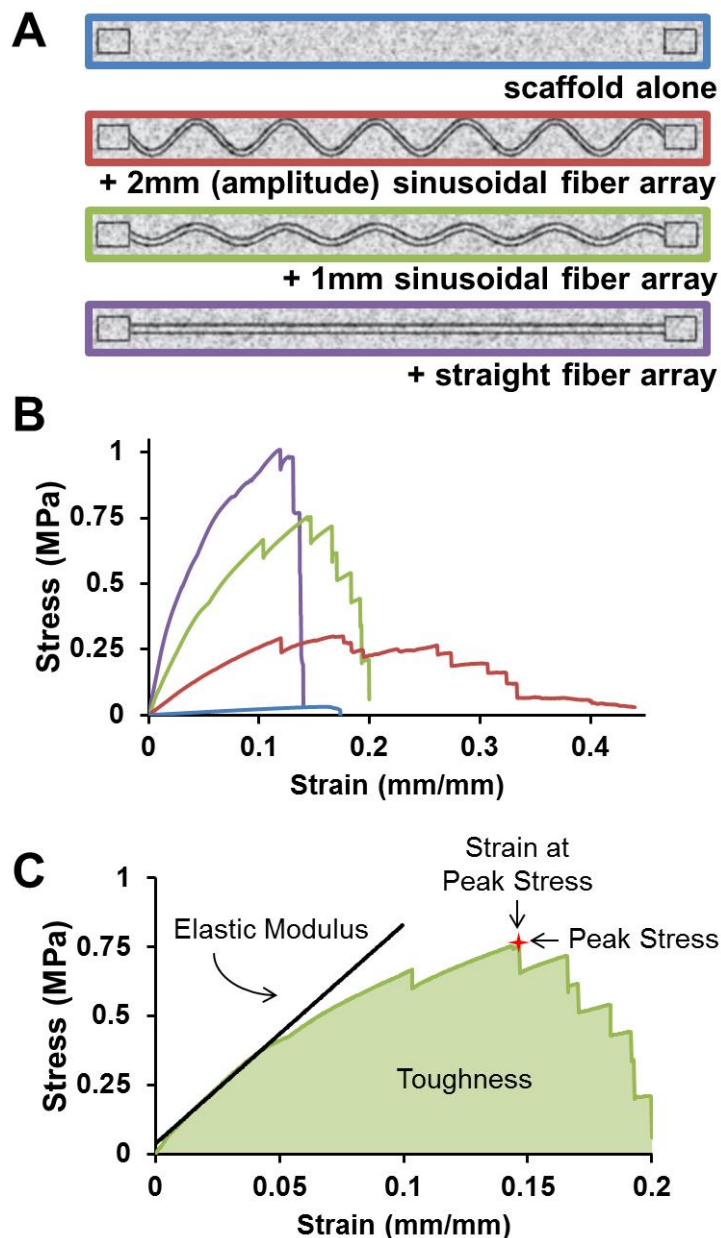
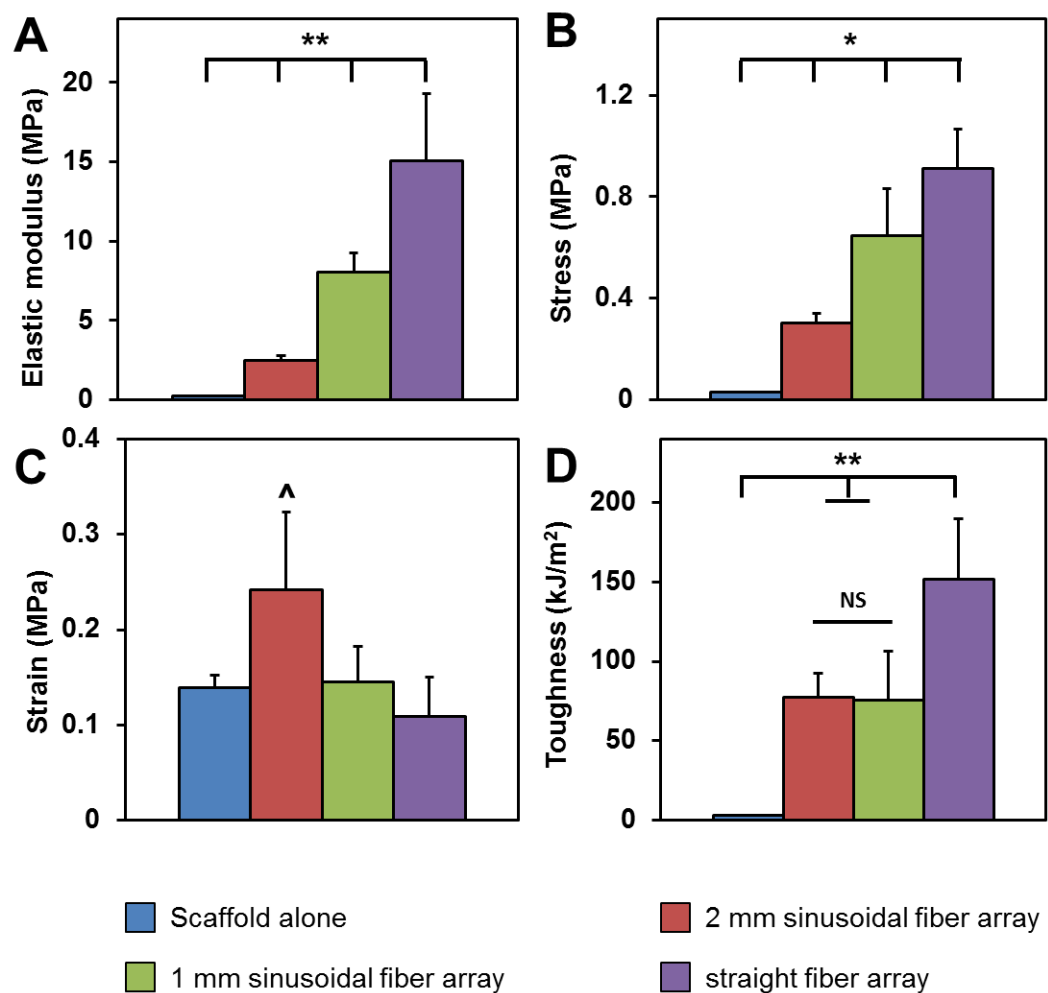


Figure 2.3 Mechanical behavior of fiber-reinforced scaffolds. **A)** The tensile behavior of ABS-CG composites was assessed for four discrete: scaffold alone; 2mm sinusoidal fiber array; 1mm sinusoidal fiber array; straight fiber array. All fiber-reinforced variants were contained 9 parallel fibers (each 1 mm diameter) connecting ABS end blocks to facilitate clamping during tensile tests. The scaffold alone variants also contained ABS end blocks to facilitate clamping. **B)** Representative stress-strain curves of all four variants. **C)** Diagram depicting how the mechanical properties for each sample were measured. Elastic modulus was taken as the slope of the linear elastic region of the curve. Peak stress was taken as the maximum stress the sample reached, and strain at peak stress was taken as the strain (extension divided by cross-sectional area) at this same point. Finally, toughness was taken as the area under the stress-strain curve before failure.



*Figure 2.4 Mechanical properties of ABS-fiber reinforced CG scaffold. Elastic modulus (A) and peak stress (B) increased significantly with increasing degree of fiber reinforcement. C) Strain at peak stress remained unchanged with the exception of the most compliant fiber-reinforcement variant. D) The toughness of the fiber-reinforced composites was significantly greater than the scaffold alone and increased with degree of fiber reinforcement. ^: $p < 0.05$; *: $p < 0.01$; **: $p < 0.001$.*

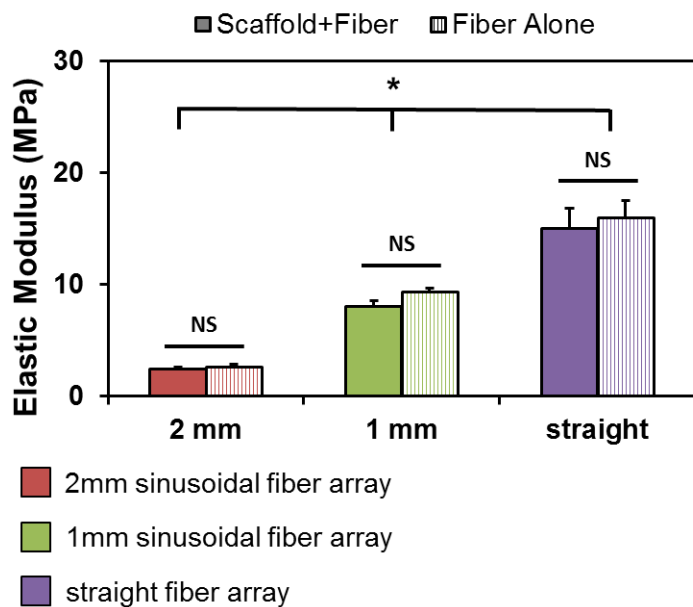


Figure 2.5 Mechanical properties of ABS-fiber reinforced CG scaffolds compared to ABS-fibers alone. There is no significant difference in the elastic modulus of fibers embedded in a CG scaffold and the fibers alone (modulus calculated via the same cross-sectional area), suggesting the fiber is the dominant mechanical contributor in the mechanical performance of the composite and it does not lose mechanical integrity during scaffold fabrication. *: $p < 0.05$ between fiber variants.

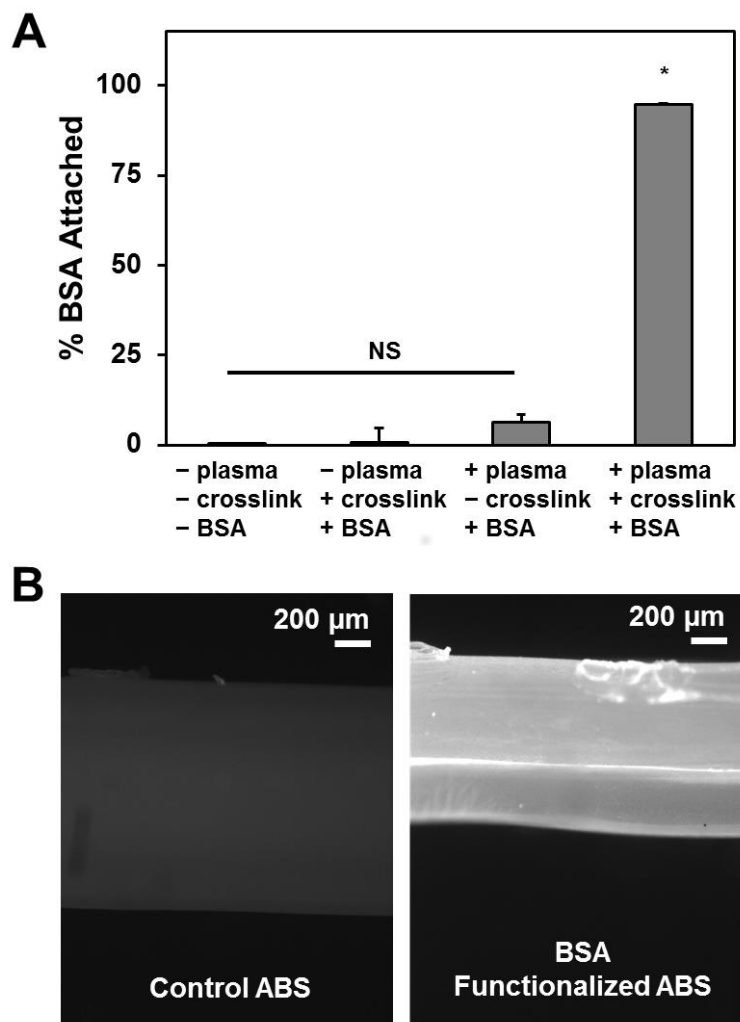


Figure 2.6 Covalent attachment of biomolecular cues via ABS-fibers. A) Attachment of a model protein (BSA) to ABS substrates via sequential oxygen plasma treatment followed by carbodiimide crosslinking in the presence of fluorescently labeled BSA. Both plasma treatment then carbodiimide crosslinking are required to facilitate covalent biomolecule incorporation. **B)** Representative fluorescent images of control ABS fibers (left) and BSA-functionalized ABS fibers (right). *: $p < 0.001$.

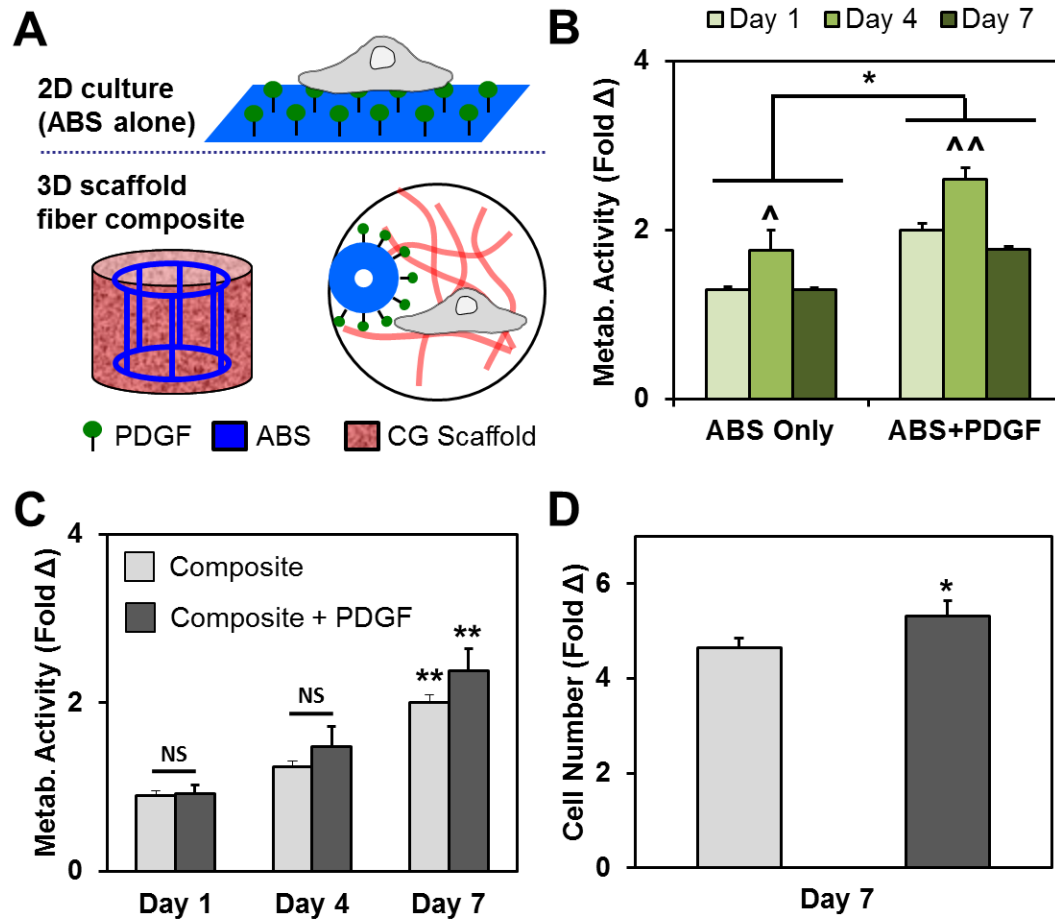


Figure 2.7 Covalent presentation of PDGF promotes changes in cell number and metabolic activity. A) pASCs were cultured on ABS or PDGF-functionalized ABS substrates (2D); pASCs were subsequently cultured in CG scaffolds containing ABS fiber reinforcement or PDGF-functionalized ABS fiber reinforcement. B) The metabolic activity of pASCs was higher when cultured on PDGF-decorated ABS substrates than ABS substrate controls at each time point. In both cases, the highest metabolic activity was observed at day 4. C) The metabolic activity of pASCs significantly increased over 7 day culture in CG scaffolds containing either ABS fibers (composite) or PDGF-decorated ABS fibers (composite + PDGF). D) Additionally, the overall cell number was significantly higher after 7 days in CG scaffolds containing PDGF-decorated fibers. *: $p < 0.05$; ^: $p < 0.01$ compared to other timepoints for the same ABS group; ^^: $p < 0.001$ compared to other timepoints for the same ABS group; ** $p < 0.05$ compared to days 1 and 4.

CHAPTER 3: INCREASING THE STRENGTH AND ALTERING STRESS CONCENTRATIONS IN COLLAGEN SCAFFOLDS VIA CUSTOMIZABLE ARRAYS OF POLY-LACTIC ACID FIBERS²

3.1: Chapter Overview

The tendon bone junction is a highly specialized tissue which dissipates stress concentrations between mechanically dissimilar tendon and bone. Upon injury, the local heterogeneities of the TBJ do not reform, causing poor functional outcomes with re-failure rates exceeding 90%. Although current tissue engineering methods are moving towards the development of spatially-graded biomaterials as regenerative approaches to address these injuries, many opportunities remain to characterize the (often complex) local mechanical properties of combined multi-compartment and composite materials in the field of orthopedic tissue engineering. Here, we describe the use of three-dimensional printing techniques to create customizable arrays of polylactic acid (PLA) fibers that can be incorporated into a collagen scaffold for tendon bone junction repair. This work builds upon previous work which demonstrated a model fiber-scaffold composite system as a mechanically tunable platform for tendon engineering constructs. This work incorporates fabrication methods to generate composites with regionally different mechanical properties from biodegradable PLA. We demonstrate a similar ability to tune the mechanical performance of the fiber-scaffold composite at the bulk scale. Additionally, we demonstrate the use of heterogeneous fiber designs to create complex, non-uniform local mechanical performance under loading, an important precursor to successful multi-compartment biomaterials. We highlight tradeoffs in local and bulk mechanical properties, which provide key

² This chapter is adapted from Mozdzen et al, *In Preparation*, 2016

insights into design elements under consideration for mechanically competent, multi-tissue regeneration platforms.

3.2: Introduction

The tendon bone junction (TBJ) is a highly specialized transition region which connects elastic tendon to stiff, mineralized bone for the purpose of movement through the translation of high tensile forces. The TBJ effectively transmits these loads and dissipates stress concentrations (found between mechanically mismatched materials or tissues [1, 173, 174]) without failure through local gradients and interdigitations at the interface between tendon and bone. The TBJ is often injured in rotator cuff tears, which require more than 4.5 million physician visits and more than 250,000 surgeries each year in the US alone [5]. Despite the high prevalence of this injury, surgical outcomes are poor and re-failure rates are quite high (>90%) because the insertion is not regenerated during the healing process and local heterogeneities are not reformed [1]. This poor functional outcome motivates the development of tissue engineering solutions to improve the regenerative healing capacity of the osteotendinous enthesis.

Emerging efforts have begun to shift focus from the development of homogenous biomaterials for the purpose of regenerating a single tissue [2, 71-75] to multi-compartment and spatially graded biomaterials for the express purpose of multi-tissue regeneration [45, 81, 107, 108, 144, 145, 175]. Efforts in our lab have recently focused on the development of two types of biomaterial scaffolds, a multi-compartment osteotendinous scaffold with distinct regions of mineralized and nonmineralized collagen for multi-tissue regeneration [68, 136], and a model ABS fiber reinforced scaffold composite which displays tunable mechanical properties and addresses the sub-optimal mechanical strength typically found in porous biomaterials [176]. This

work combines and expands upon these previous biomaterial designs and describes the development of a biocompatible PLA fiber reinforced composite with discrete (*discontinuous*) and gradual (*gradient*) transitions in mechanical properties for the purpose of tendon-bone regeneration.

We have previously characterized the bulk mechanical properties and cellular viability within a model ABS fiber reinforced composite [176]. This work moves from using a model polymer (ABS) to using a PLA fiber array, which is stiffer, more easily functionalized with biomolecules, and commonly used in tissue engineering applications for its biodegradable properties. However, heterogeneous materials are difficult to characterize through traditional mechanical techniques, and local mechanical deviations (often extremely influential to mechanically sensitive cellular behavior) are lost within bulk measurements. Here we report the unique and tunable bulk and local mechanical properties of a single CG scaffold design incorporating different PLA fiber array geometries (*continuous, discontinuous, gradient*) into a fiber-scaffold composite structure.

3.3: Materials and Methods

3.3.1 Preparation of collagen-GAG (CG) suspension

A CG suspension was prepared from type I collagen (1.0% w/v) isolated from bovine Achilles tendon and chondroitin sulfate (0.1% w/v) derived from shark cartilage in 0.05 M acetic acid (Sigma-Aldrich, St. Louis, MO) [157]. The suspension was homogenized at 4 °C to prevent gelatinization during mixing and was degassed before use [157].

3.3.2 Fabrication of polylactic acid fiber arrays via 3D printing

A series of polylactic acid (PLA) fiber arrays were created and incorporated into CG scaffolds as previously described [176]. Each PLA fiber array consisted of 9 parallel 1 mm diameter PLA fibers fixed together at either end with PLA end blocks (end blocks: 20 mm x 4 mm x 3 mm; complete fiber array: 20 mm x 76 mm x 3 mm). All constructs were printed using a MakerBot Replicator 2X (MakerBot Industries, Brooklyn, NY) at standard quality settings (10% infill, 2 shells, 200 μ m layered height) and an extruder speed of 25 mm/s. To ensure structural fidelity of the fiber arrays, PLA fibers were co-printed with polystyrene supports and rafts (base layer) using dual nozzles (polystyrene: 250 °C; PLA: 210 °C) onto a temperature controlled build-plate (55°C), with the chamber doors raised to increase the cooling rate. The polystyrene supports were subsequently dissolved in D-Limonene (GreenTerpene, Miami, FL), leaving behind the final PLA fiber array. After all polystyrene was dissolved, PLA fiber arrays were washed multiple times with deionized water, and then dried before use.

A homologous series of reinforcing arrays were created to explore the effect of local fiber geometry on mechanical performance. One set of fiber arrays was comprised of a uniform fiber architecture along the length of the fibers; these arrays were created using a sinusoidal fiber architecture with either a 1mm or a 2mm sinusoidal amplitude. The first group (*continuous*) displayed the same geometries reported in our previous work, which were based on sin waves of varying amplitudes (straight fiber array (*straight*), 1 mm sinusoidal fiber array (*1 mm amp*), 2 mm sinusoidal fiber array (*2 mm amp*); period: 11.3 mm) [176]. The second group of fiber arrays displays a discontinuous fiber geometry (*discontinuous*), with the length of the fiber divided into two geometries – one side a straight fiber joined to either a 1 mm or a 2 mm sinusoidal fiber on

the other side (*discontinuous: 1 mm amp, 2 mm amp*). The final group of fibers also displays discontinuous geometries, but with a gradual transition region at the discontinuity (*gradient*); one side contains a straight fiber which gradually transitions (straight; $\frac{1}{4}$ amplitude, $\frac{1}{2}$ amplitude, full amplitude) to either a 1 mm or a 2 mm sinusoidal fiber array (*gradient: 1 mm amp, 2 mm amp*)

3.3.3 Fabrication of PLA fiber reinforced CG scaffolds via lyophilization

After printing, PLA fiber arrays were placed into aluminum molds 7.6 cm (long) x 2 cm (wide) and 8.7 mL of CG suspension was added to submerge the fiber array. The final PLA-CG composite was fabricated via a previously described lyophilization protocol (-40 °C, 200 mTorr) [36, 176], leaving behind the porous CG scaffold impregnated with PLA fibers (**Figure 3.1.A**). Scaffold composites (7.6 cm x 2 cm x 0.5 cm) were stored under desiccation until use.

3.3.4 Sample preparation for mechanical testing and digital image correlation (DIC)

Scaffold composites were speckle patterned using an airbrush (nozzle: 0.3mm; gravity feed; GotHobby, South El Monte, CA) filled with waterproof india ink (Blick Art Materials, Galesburg, Illinois) attached to house air before use [177].

3.3.5 Bulk mechanical characterization

Fiber-scaffold composites (20 mm width, 5 mm thickness, 60 mm gauge length) underwent mechanical tensile testing in an Instron 5943 Mechanical Testing System with a 100 N electromechanical load frame. Samples were held in place at their end-blocks with pneumatic grips (60 psi). Composites were strained at a rate of 6 mm/min (0.167% strain/s) until failure,

with full-sample images captured using a high definition digital camera (Canon EOS E5) with a 100 mm lens (Canon 100 mm macro lens) and a time lapse remote (Canon Timer Remote Controller TC-80N3) at a rate of 1 image every 2 seconds. Elastic modulus was calculated from the slope of the linear elastic region of the stress-strain curve [172], peak stress was taken as the maximum stress the sample experienced before failure, toughness was calculated as the area under the stress-strain curve after failure (**Figure 3.2**)[178], and failure mode was recorded by taking the final image captured after failure (**Figures 3.3, 3.4**).

3.3.6 Local mechanical characterization via Digital Image Correlation

Images were correlated using the Improved Digital Image Correlation code (Improved Digital Image Correlation version 4 – Copyright © 2013, 2014, 2015 by Elizabeth Jones)[179] to calculate local strain profiles across the specimen. Reduced images were correlated first, with individual correlation settings optimized for each sample (typical settings: image reduction factor: 7, subset size: 35; threshold: 0.3; search zone: 4, grid step size: 15). Reduced correlations were iterated up to 6 times due to high strain. Full images were then correlated using the reduced data (typical settings: subset size: 21; threshold 0.3; search zone: 3; grid step size: 23). Finally, correlated data was smoothed and missing data (applicable at higher strains not included in the visual representations shown in **Figures 3.5-3.8**) was interpolated (Gaussian distribution of weights; kernel size: 11; number of smoothing passes: 3; maximum size of contiguous non-correlated points to smooth over: 35) and local strain profiles were calculated using a cubic (16-node) strain algorithm [180, 181]. The “visualize data” feature of the Improved Digital Image Correlation code was utilized in order to generate contour plots and line scans (**Figures 3.5-3.8**) [179]. This data was exported to excel to perform maximum strain gradient calculations. Strain

gradients were calculated by extracting 9 line scans (evenly spaced along the sample, perpendicular to strain) of local strain and calculating the maximum slope of each line [182-184].

3.3.7 Statistics

One-way analysis of variance (ANOVA) was performed on elastic modulus, peak stress, and toughness, and maximum strain gradient calculations (n=6), followed by Tukey post-hoc tests. Significance was set at $p < 0.05$. Error is reported as standard error of the mean unless otherwise noted.

3.4: Results

3.4.1 Bulk mechanical characterization of PLA collagen composites

Elastic modulus was found to significantly vary among each sample group (*continuous: straight, 1 mm amp, 2 mm amp; discontinuous: 1 mm amp, 2 mm amp; gradient: 1 mm amp, 2 mm amp*). As expected, the elastic modulus was found to significantly increase as the PLA fiber array sinusoidal amplitude decreased (*straight > 1 mm amp > 2 mm amp*). The elastic modulus was also found to significantly increase across sample groups (*gradient > discontinuous > continuous*). Moving forward, this work focused on the 2 mm amp group, instead changing the spatial properties of the fiber (*continuous, discontinuous, gradient*) to explore the effect on bulk mechanical characterization. Toughness was found to remain constant among the 2 mm amplitude continuous, discontinuous, and gradient transition samples while peak stress was found to be significantly increased in the gradient transition samples with 2 mm amplitude (**Figure 3.2**).

3.4.2 Termination of correlation

Images were correlated using digital image correlation to 3.7% applied (bulk) strain, at which point all samples still retained composite mechanical fidelity (**Figure 3.3**).

3.4.3 Failure modes (2 mm amp samples)

Moving forward, this work focused on the 2 mm amp group to explore the effects of continuous, discontinuous, and gradient fiber geometries on local mechanical characterization. Failure occurred randomly in the continuous samples, and occurred in the sinusoidal region of the discontinuous and gradient samples (**Figure 3.4**).

3.4.4 Local mechanical characterization of PLA collagen composites

After images were correlated, local strain contour plots were compared to examine patterns in strain concentrations. The continuous samples displayed periodic areas of high strain, which correspond to the geometry of the sinusoidal fiber embedded in the scaffold composite. These areas of local strain were more pronounced within the 1 mm amp sample. In the discontinuous sample groups, high areas of periodic strain appeared primarily on one half, which corresponds to the sinusoidal part of the discontinuous fiber composite. In the 1 mm amp group, these areas of local strain appeared sharper when compared to the 2 mm amp group, which were spread out over a greater distance. Similar to the discontinuous sample groups, the gradient sample groups had high levels of local strain confined to one region of the sample, corresponding to the location of the sinusoidal PLA fibers. Although there appears to be a gradual region of increasing strain, the local strain increased more sharply when the gradient transition reached the full amplitude of the fiber (**Figure 3.5**).

3.4.5 Local strain profiles

Line scans were taken from evenly spaced regions of each sample at multiple strains, perpendicular to the direction of strain in order to calculate maximum strain gradients for individual line scans (**Figure 3.6**). With increasing strain, the continuous samples both displayed increasingly high areas of local strain. Local strain was more evenly spread along the 2 mm sample, with less sharp periodicity, while in the 1 mm sample local strain was more sharply periodic, which was especially apparent at 3.7% strain. In the discontinuous and gradient sample groups, high areas of periodic strain appeared primarily on one half, which corresponds to the sinusoidal part of the discontinuous or gradient fiber composite. Again, local areas of strain appeared sharper in the 1 mm amp group compared to the 2 mm amp group, which were spread out over a greater distance. However, when compared to the discontinuous groups, the gradient sample groups appear to display more sharply increased local strain (**Figure 3.7, 3.8**).

3.4.6 Local strain gradient maxima

Maximum changes in local strain profiles were taken from individual line scans in order to obtain local strain gradient maxima for each group. The 1 mm group had significantly increased strain gradients compared to the 2 mm group in both continuous and discontinuous samples. Strain gradients were significantly increased in the gradient transition groups compared to the continuous and discontinuous groups as well (**Figure 3.9**).

3.5: Discussion

Orthopedic tissue engineering often requires the ability to regenerate multiple tissues at once, using biomaterials which have tunable strength and toughness to match local mechanical properties of not just one, but multiple healthy tissues. However, high mechanical properties are often traded for porosity and high specific surface area, which better support cellular penetration, attachment, and nutrient biotransport. We have previously described a composite design, originally inspired by the longitudinal fibers found as reinforcing structures in plant stems [168], as a potential solution to this trade-off, which incorporates ABS as a high strength fiber support within a highly porous collagen scaffold to create a composite with the best attributes of both [176]. Although successful as a model system, ABS is not an ideal polymer for long-term development of fiber-reinforced composites, which must allow incorporating of a wider range of functionality such as cell-adhesion and biodegradability *in vivo*.

This chapter reports an adaptable approach to mechanically reinforce a collagen scaffold under development for tendon-bone junction (TBJ) repair applications. This work expands upon the previous chapter's work of the incorporation of ABS fibers arrays as a model polymer [176] by replacing ABS with more biologically suitable poly-lactic acid (PLA), which is biodegradable, commonly used in biomaterial applications, and is approximately twice as stiff as ABS [185, 186]. Previous work focused on homogenous fiber designs, while this chapter explores more complex fiber designs with discrete regions created by distinct fiber geometries with variable mechanical properties for the purpose of supporting multi-tissue regeneration. This work further explores not only the bulk mechanical properties of heterogeneous fiber arrays, but examines

local strain profiles to further define the design parameters required to tailor composite construct bulk mechanical properties.

Homogenous biomaterials are relatively simple to characterize mechanically, but heterogeneous materials contain complex mechanical interactions, especially at the interface between discrete compartments (*tendon, bone*) or between distinct composite materials (CG, *PLA*), and require the correlation of local mechanical properties to properly describe the complete system. While the overall bulk mechanics performed as expected (elastic modulus: *straight* > *1 mm amp* > *2 mm amp*; elastic modulus and peak stress: *gradient* > *discontinuous* > *continuous*; toughness: *no change*) (**Figure 3.2**), local mechanical properties in our heterogeneous samples were more complex.

Although we observed higher elasticity, which corresponds to a lower elastic modulus and higher strain at failure in the 2 mm sample groups compared to the 1 mm sample groups on a bulk scale (**Figure 3.2**), local profiles demonstrated significantly higher strain gradients in 1 mm sample groups than 2 mm sample groups (**Figures 3.5, 3.7, 3.8, 3.9**) regardless of sample group (*continuous, discontinuous, gradient*). We have previously shown that CG scaffolds without fiber reinforcements exhibit cracking at somewhat regular intervals along the construct at high strains [187]. However, when PLA fibers are incorporated into a composite construct, stresses are redistributed within the composite such that the more elastic CG scaffold does not experience an even distribution of strain. We hypothesize that the higher degree of mechanical mismatch between the 1 mm amplitude sinusoidal fiber and the collagen scaffold results in higher local strain gradients in the softer and more compliant CG scaffold. We have previously demonstrated

that 1mm amplitude fiber-arrays display a significantly higher elastic modulus compared to both 2mm amplitude fiber-arrays and the scaffold alone. Here, we observe local, pre-failure cracks which propagate throughout the CG scaffold in the 1 mm amplitude composites and suggest that a mechanical mismatch between the 1mm amplitude fibers and the CGs scaffold allows a less even distribution of local strain between the two materials, which ultimately results in higher local strain gradients. Comparatively, local areas of high strain in scaffolds containing 2mm amplitude fibers were reduced compared to those seen in scaffolds containing 1mm amplitude fibers, suggesting that the 2mm amplitude fibers distribute strain throughout the CG scaffold more evenly, and that the choice in reinforcing fiber can significantly alter the strain experienced by cells within the scaffold compartment (**Figures 3.8, 3.9**). When engineering composite materials for increased strength in tissue engineering, the distribution of strain between composite materials remains an important design criterion, both due to concerns of failure and local cell mechanotransduction-based responses.

One of the challenges in the field of orthopedic tissue regeneration is to effectively dissipate stress concentrations between mechanically mismatched materials and move local regions of high strain gradients away from the interface between discrete compartments. *In vivo*, rotator cuff repairs often fail at the interface between tendon and bone due to these high stress concentrations [1]. We have demonstrated a fiber reinforced collagen composite with a gradual transition (*gradient*) in fiber geometry from straight to sinusoidal to address this need. Not surprisingly, this composite effectively alters the local strain profiles across the scaffold in a manner different from those seen for a fiber design that contained a discontinuous geometry (straight-sinusoidal transition). Notably, for a given bulk strain, larger strain gradients were

observed in the gradient fiber architecture, likely an effect of increased strain across a region of the fiber architecture with the highest extensibility (greatest sinusoidal amplitude) (**Figure 3.2, Figure 3.9**). This result provides a cautionary insight into the cost of shifting the location of high strain gradients. Although the overall elastic modulus and peak stress are significantly higher in the fiber composite containing a gradual transition region (*gradient*), this is at the expense of high regions of local strain in the sinusoidal region, which may ultimately result in collagen scaffold failure and increased local mechanical signals that can affect cells within the scaffold network.

Current studies in multi-tissue regeneration are exploring a wide range of design strategies to combine multiple materials into a single construct [115, 188-190]. However, the field of research exploring how these multi-material constructs behave on a local scale under mechanical load is extremely important for the dynamically active tissues found in the musculoskeletal system. The knowledge of local mechanical behavior is extremely vital as mechanically-sensitive cells are integrated into the biomaterial to ensure that proper loading conditions are met, but not exceeded [191, 192]. Incorporating PLA fiber arrays within a collagen composite allows the ability to increase and tune bulk mechanical properties, but also highlights the need to carefully consider local strain fields in composite biomaterials that integrate multiple mechanically dissimilar materials into a single construct. This work clearly illustrates opportunities and challenges associated with complex composite design. We have demonstrated a trade off in increased overall stiffness with allowing higher areas of local strain to form, as well as showing that shifting regions of high strain gradients from a discontinuity at the transition between fiber

geometries (*discontinuous v. gradient*) allows larger strain gradients to form in a region of the sample further removed from the graded transition zone between fiber geometries.

3.6: Conclusions

The need to balance multiple requirements in the design of multi-compartment tissue engineering composites for musculoskeletal applications requires a new design toolbox. We have previously reported a unique technique to generate composite biomaterials through the combination of model 3D printed ABS fibers and CG scaffolds. Herein we demonstrate a composite design that integrates more complex arrays of PLA fibers with tunable local mechanical properties into a CG scaffold for multi-tissue regeneration. This work further expands the toolbox of multi-tissue biomaterials by providing key insights into previously undemonstrated tradeoffs in bulk mechanical strength and local competence.

3.7: Figures

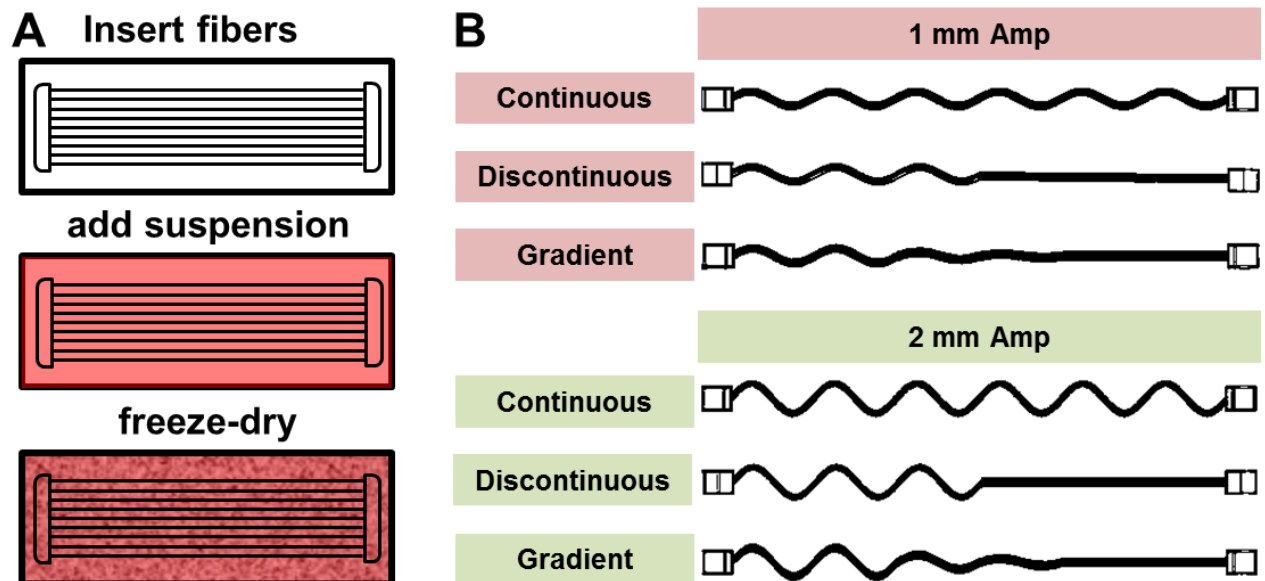


Figure 3.1 Fabrication of PLA fiber reinforced composites. A) PLA fiber reinforced composites are fabricated by incorporating the fiber within the liquid collagen suspension prior to lyophilization. **B)** Distinct fiber geometries with either 1 mm or 2 mm sinusoidal amplitudes and either continuous, discontinuous, or gradient transitions were fabricated.

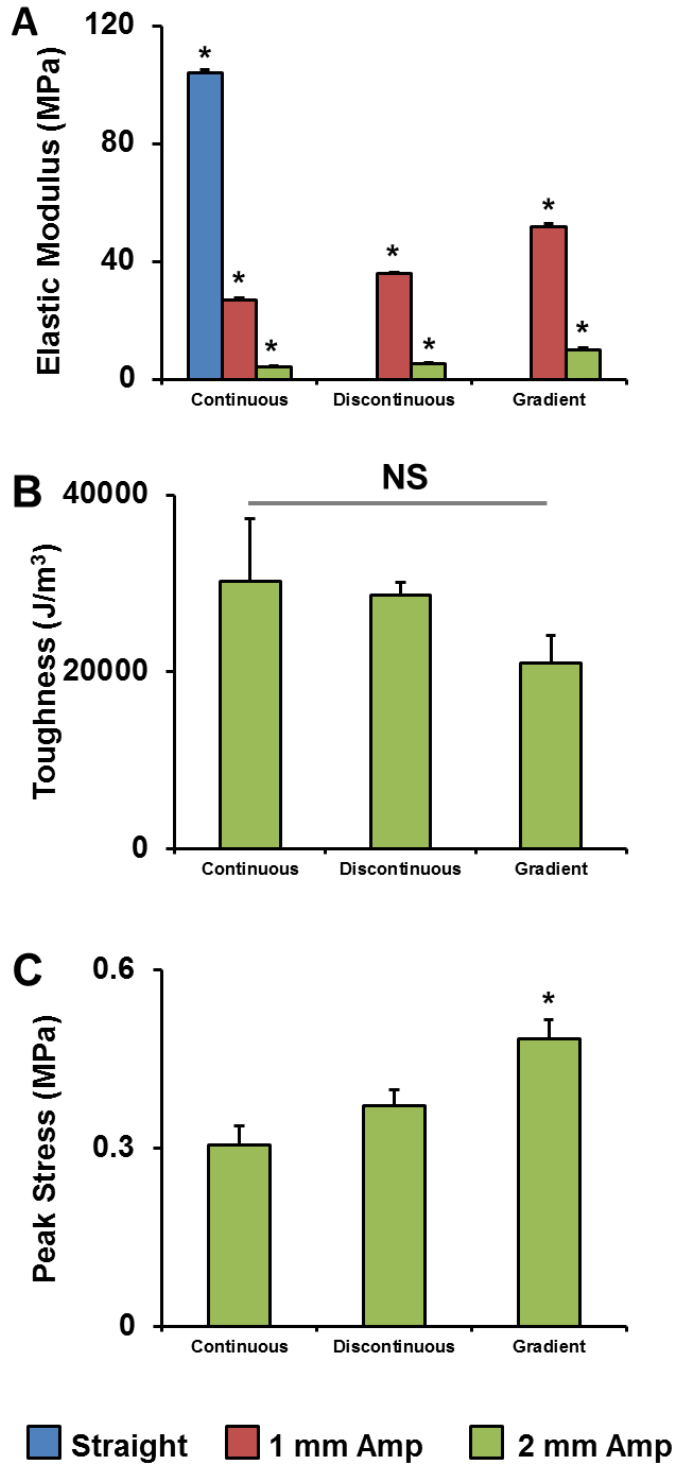


Figure 3.2 Bulk mechanical characterization. **A)** Elastic modulus was found to significantly increase as the PLA fiber array sinusoidal amplitude decreased (*straight* > *1 mm amp* > *2 mm amp*) and increase across sample groups (*gradient* > *discontinuous* > *continuous*). **B)** Toughness was found to remain constant among all the 2 mm amplitude groups. **C)** Peak stress was found to be significantly increased in the gradient transition group with 2 mm amplitude. *: $p < 0.05$ versus all other samples.

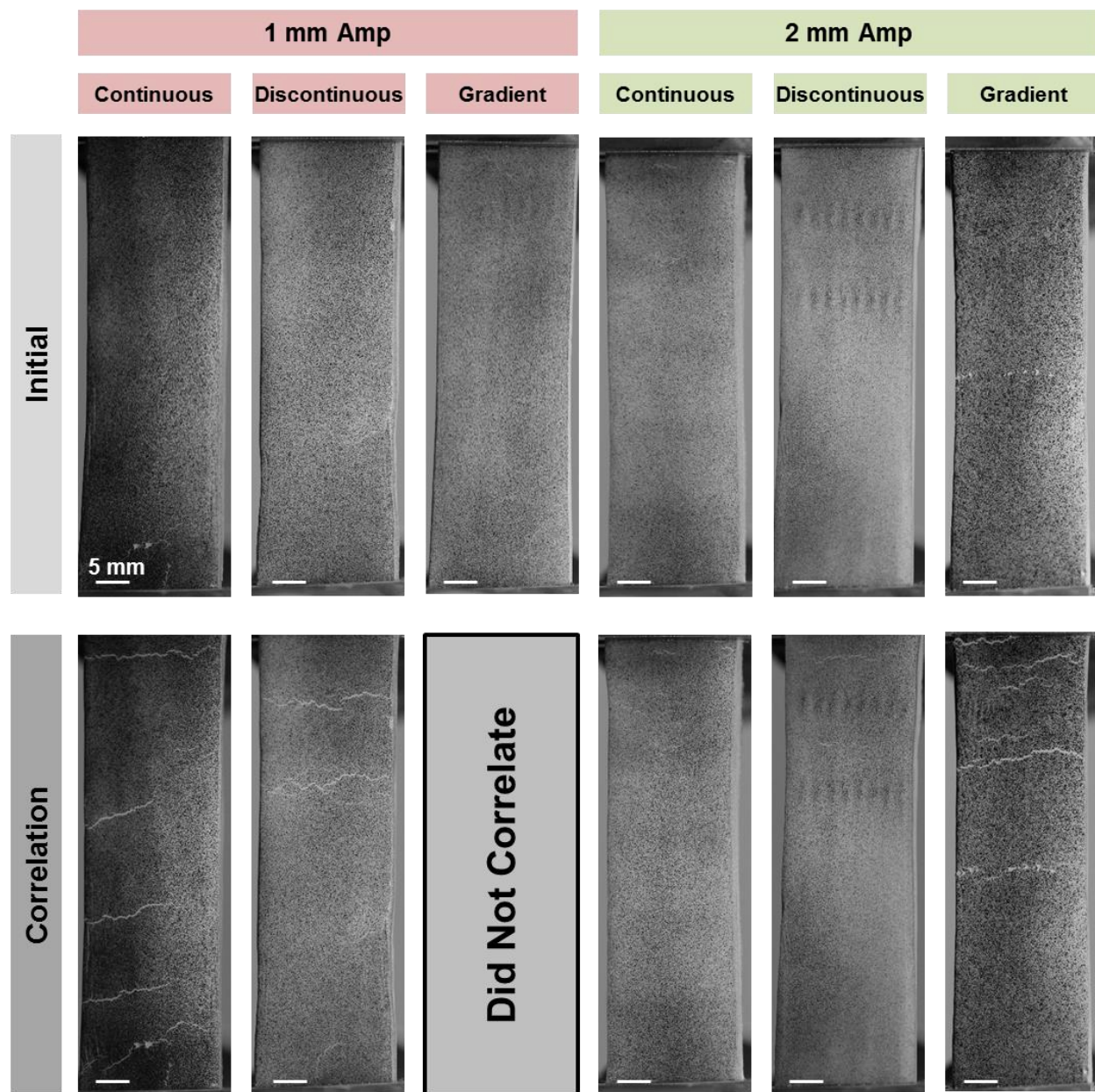


Figure 3.3 Termination of correlation. Images were correlated using digital image correlation to 3.7% strain (Image 11), at which point all samples still retained composite mechanical fidelity.

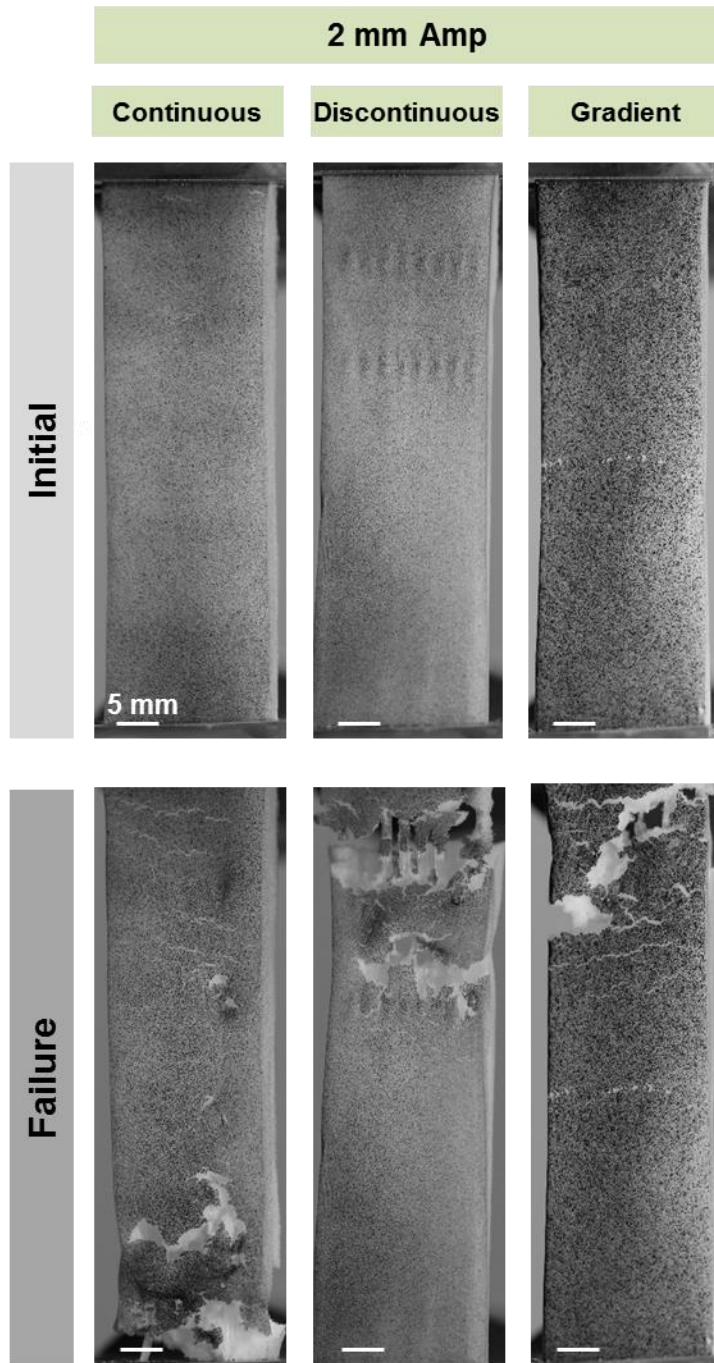


Figure 3.4 Failure modes (2 mm amp samples). Failure occurred randomly in the continuous samples, and occurred in the sinusoidal region of the discontinuous and gradient transition samples.

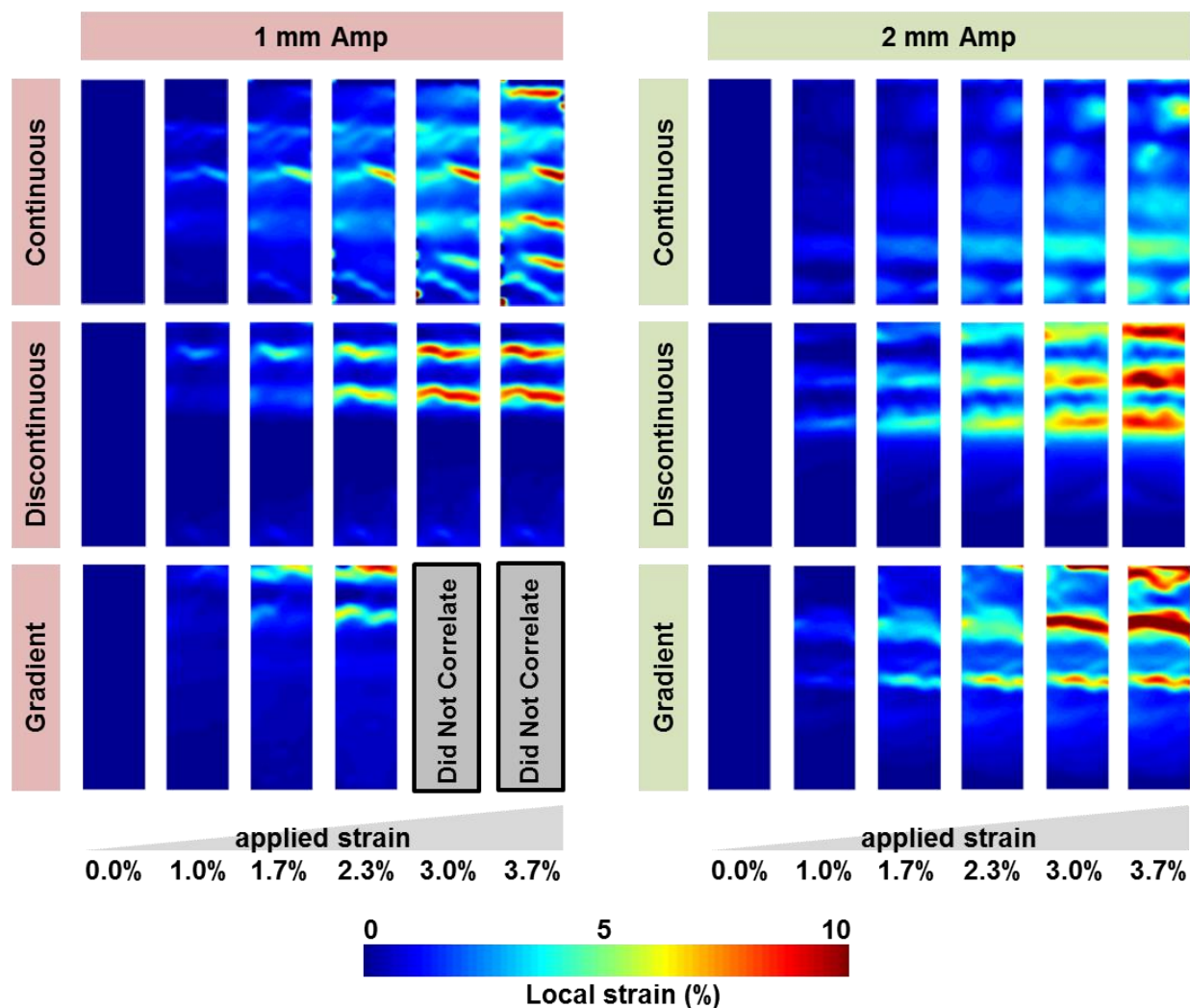


Figure 3.5 Local mechanical characterization of PLA collagen composites. Continuous samples displayed periodic areas of high strain, which correspond to the sinusoidal fiber embedded within the scaffold composite. Discontinuous and gradient sample groups contained high areas of periodic strain which appeared primarily on one half, which corresponds to the sinusoidal compartment of the fiber composite. In all 1 mm sample groups, areas of local strain appeared sharper when compared to the 2 mm amp group.

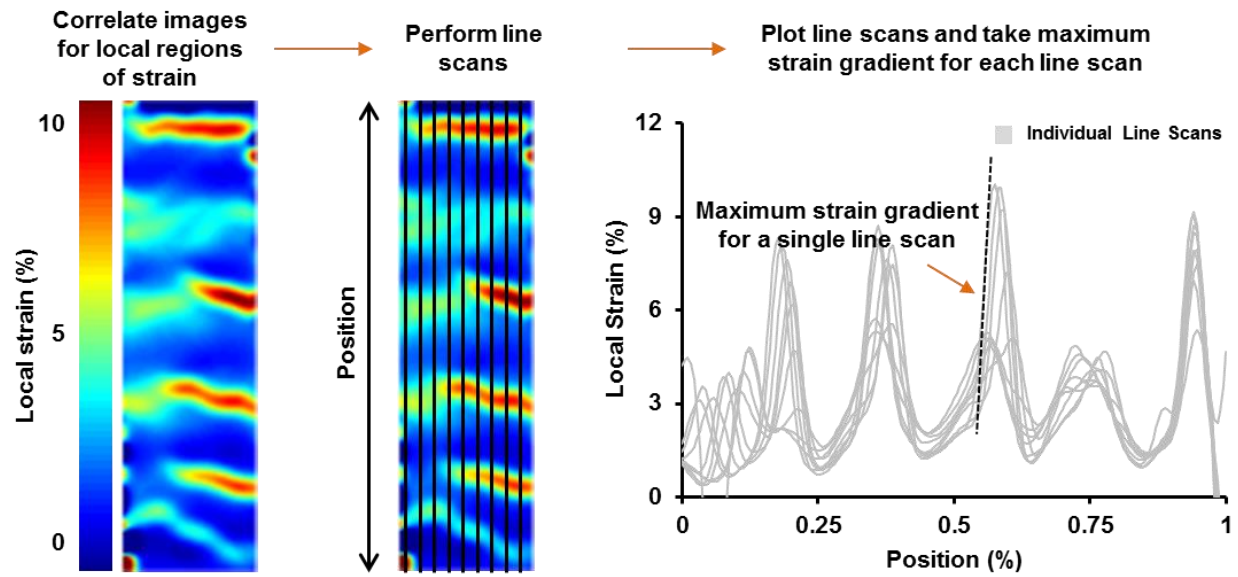


Figure 3.6 Digital image correlation and line scan analysis. Line scans were taken from evenly spaced regions of each sample at multiple strains, perpendicular to the direction of strain in order to calculate maximum strain gradients for individual line scans.

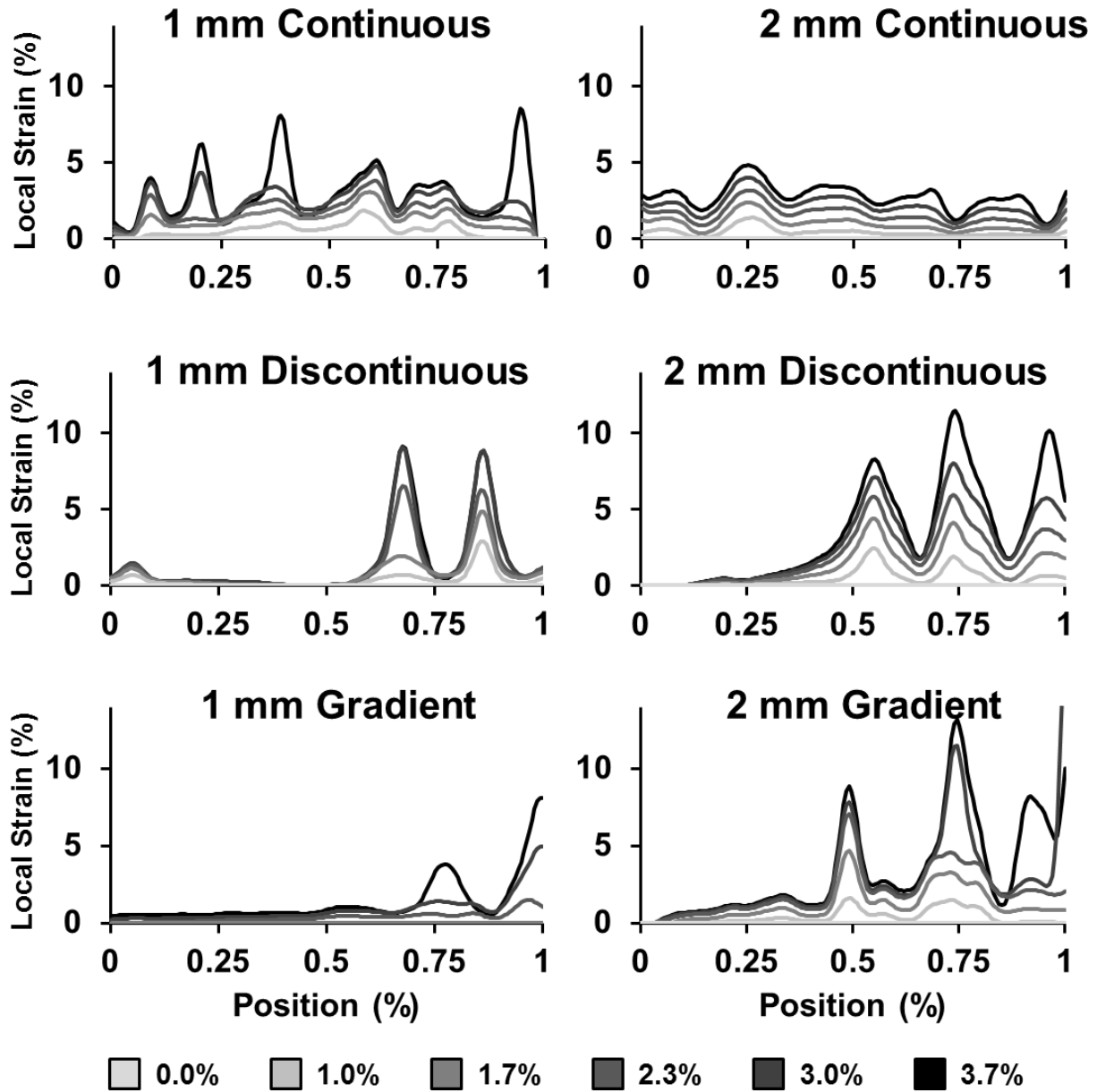


Figure 3.7 Local stress concentrations with increasing strain. Continuous samples displayed local areas of high periodic strain, with local strain was more evenly spread along the 2 mm sample (containing less sharp periodicity), while in the 1 mm sample local strain was more sharply periodic. This was especially apparent at the highest strain (3.7%). In the discontinuous and gradient sample groups, high areas of periodic strain appeared primarily on one half, which corresponds to the sinusoidal part of the discontinuous or gradient fiber composite. Local areas of strain appeared sharper in either the 1 mm amp group compared to the 2 mm amp group and the gradient group compared to the discontinuous group.

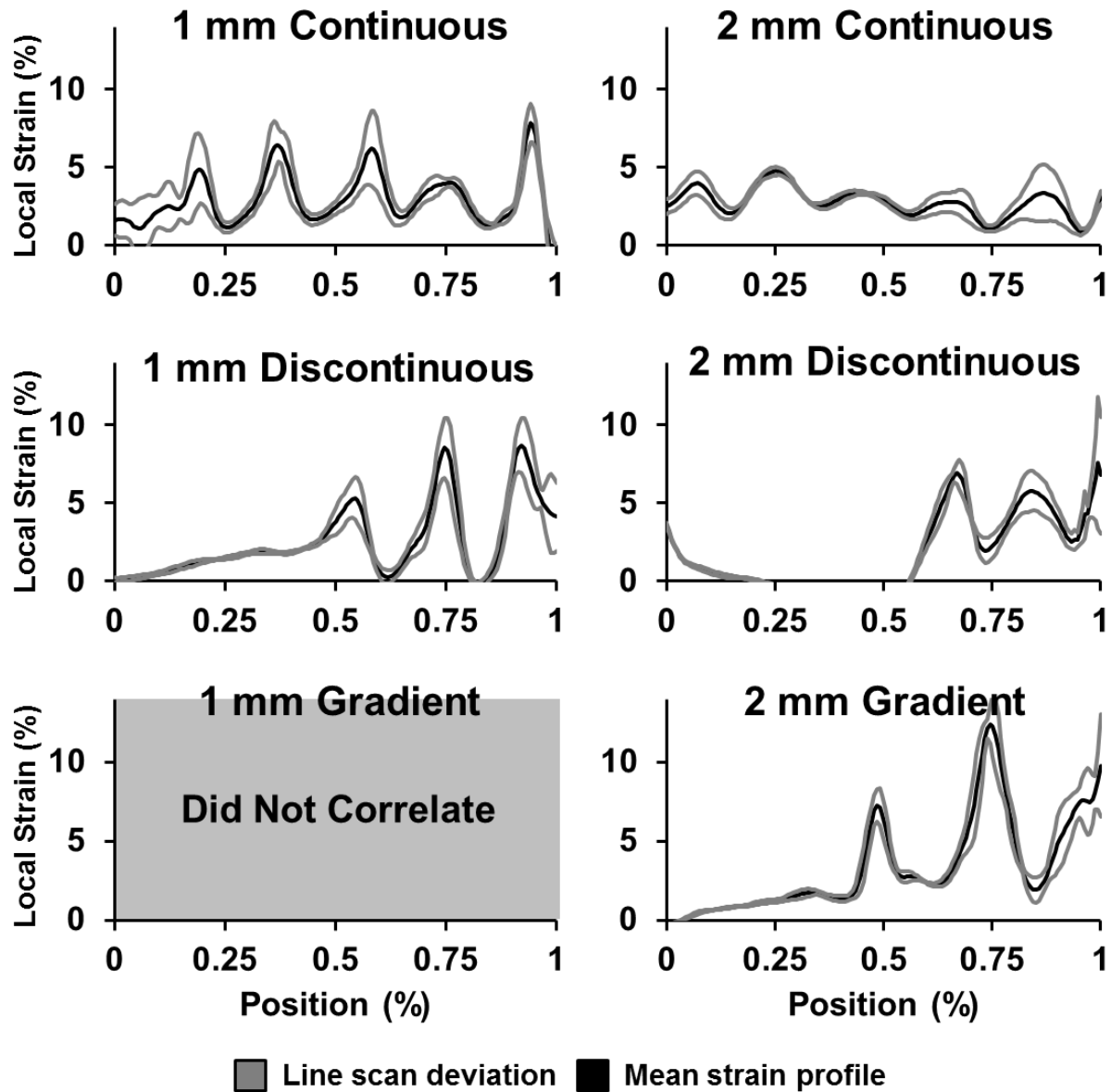


Figure 3.8 Local stress concentrations at 3.7% strain. Continuous samples displayed local areas of high periodic strain, with local strain was more evenly spread along the 2 mm sample (containing less sharp periodicity), while in the 1 mm sample local strain was more sharply periodic. In the discontinuous and gradient sample groups, high areas of periodic strain appeared primarily on one half, which corresponds to the sinusoidal part of the discontinuous or gradient fiber composite. Local areas of strain appeared sharper in either the 1 mm amp group compared to the 2 mm amp group and the gradient group compared to the discontinuous group.

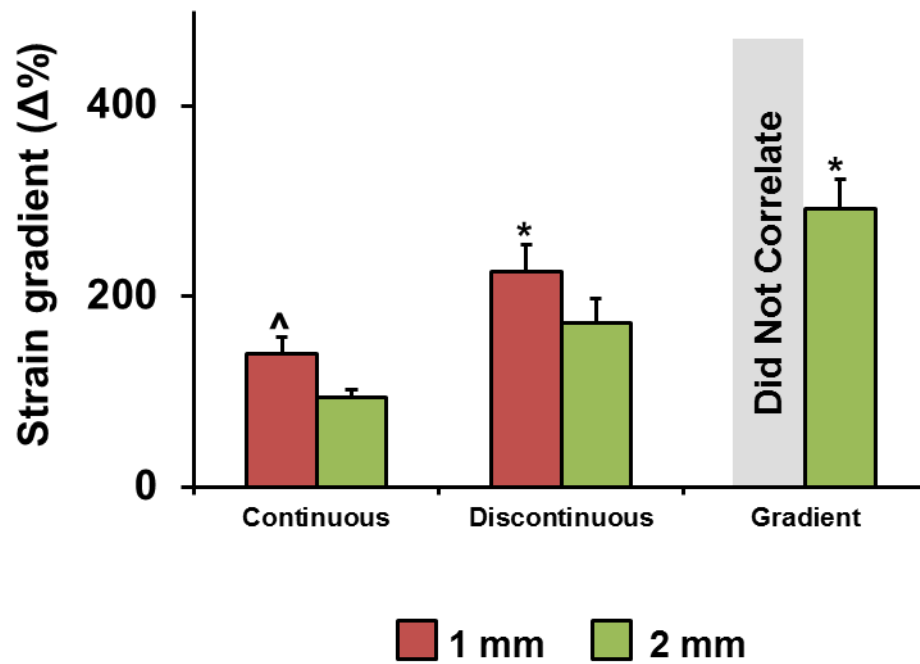


Figure 3.9 Local strain gradient maxima. Maximum changes in local strain profiles were significantly increased in the 1 mm group compared to the 2 mm group in both continuous and discontinuous samples. Strain gradients were significantly increased in the gradient groups compared to the continuous and discontinuous groups as well. *: $p < 0.05$ versus samples with the same amplitude. ^: $p < 0.05$ versus samples with the same fiber geometry.

CHAPTER 4: THE INCORPORATION OF GEOMETRIC INTERDIGITATIONS TO DISSIPATE STRESS CONCENTRATIONS ACROSS THE INTERFACE OF A MULTI-COMPARTMENT COLLAGEN SCAFFOLD ³

4.1: Chapter Overview

This chapter focuses on the mechanical properties of a biomaterial under development for repair of the tendon-bone junction (TBJ). To improve the regenerative healing of the TBJ, it is essential to develop approaches to address mechanical response at the interface between regions of a biomaterial with dissimilar mechanical properties. At such an interface, physical stresses are concentrated due to a mismatch in mechanical properties. We are developing a collagen-glycosaminoglycan (CG) scaffold which mimics elements of the biophysical heterogeneities of the native TBJ *in vitro*. To improve the mechanical competence of the interface between non-mineralized (CG) and mineralized (CGCaP) scaffold zones, we used triangular, interpenetrating and interdigitated geometries between compartments inspired by the plates of turtle shells and armored fish to increase the elastic modulus, toughness, and peak stress of the overall construct. Multi-compartment scaffolds were created with increasing angles of interdigitation (flat, 27°, 18°, 14°, 9°, 7°), tested under mechanical tension, and analyzed using digital image correlation to find local areas of increased strain. The best performing constructs ranged from 27° to 14° at the interface, and had significantly increased bulk mechanical properties when compared to a traditional flat interface. A mechanism by which these groups displayed increases in bulk mechanics appears linked to an ability to effectively dissipate strain concentrations at the interface and spread them across the entire construct. This work describes the first use of

³ This chapter is adapted from Mozdzen et al, *In Preparation*, 2016

geometric interdigitations in biomaterial design in order to modify the mechanical performance of the interface between dissimilar biomaterial constructs at the bulk scale.

4.2: Introduction

The tendon bone junction (TBJ) is a highly specialized and mechanically dynamic anatomical zone which connects mechanically dissimilar tissues, and can transmit high tensile loads without failure. The native rotator cuff demonstrates this junction between tendon and bone, gradually transitioning from tendon to bone through four anatomically definable zones (tendon, fibrocartilage, mineralized fibrocartilage, and bone). This gradual transition, together with an interdigitating interfacial structure, dissipates stress concentrations that are typical at the interface of mechanically dissimilar materials (0.4 GPa, tendon; 20 GPa, bone [1, 173, 174]). In a rotator cuff tear, the tendon typically tears away from the bone at the insertion, where stress concentrations are the highest; the insertion is not regenerated during the healing process and scar formation replaces the heterogeneities found in healthy tissue. Rotator cuff injuries are quite common, with more than 4.5 million physician visits and 250,000 surgeries in the US annually [5]. Despite this, rotator cuffs tears are typically managed through surgical fixation of the torn tendon to bone, which does little to remedy the loss of characteristic gradients and structure at the junction. This loss of structural specialization is a primary factor responsible for high (>90%) re-failure rates [1], motivating the development of tissue engineering solutions to improve regenerative healing of the osteotendinous enthesis.

Mechanical stresses are concentrated at the interface between any two mechanically mismatched materials. In nature, stress concentrations are often dissipated through interdigitation, such as those found in arapaima [124-126], turtle shells [127], and the native rotator cuff [1] (**Figure**

4.1). Although this general form of interdigitation has been considered and modeled in the design of structural materials [128], it has yet to be translated to biomaterial applications. Across a periodically repeating interdigitation, the amplitude (A), period (λ), interfacial thickness (g), minimum contact length (l_o), and actual contact length (l) can all impact interfacial shape. However, *Li et al.* demonstrated that these variables can all be reduced down to two components: the suture complexity index (SCI) and the angle of interdigitations (Θ). The SCI is a measure of contact length across the interface, l divided by l_o and mechanical strength generally increases with an increased SCI up to a certain physical limit, where Θ more appropriately describes the physical mechanistic behavior. Θ determines how many interdigitations, or “teeth” can fit across the interface, and *Li et al.* demonstrated that there is an ideal Θ (approximately 12° in their model system) where tensile forces applied across the interface fundamentally shift to shear forces, which can be distributed over a larger area and thus minimized (**Figure 4.2**) [128].

We are developing a multi-compartment, collagen-based biomaterial to drive mesenchymal stem cell (MSC) differentiation in a spatially selective manner towards osteogenesis and tenogenesis within a single construct [136, 193]. Although we have observed strong osteogenic and tenogenic markers in discrete compartments within a model graded biomaterial, the osseous-compartment of the biomaterial has distinctly stiffer mechanical properties than the more elastic tendinous compartment of our biomaterial scaffold. Under tensile strain, the mechanically dissimilar compartments of our biomaterial exhibit stress concentrations, similar to those found at the repaired junction in the native rotator cuff after injury, and ultimately fail at the interface [194-197]. Our goal is to demonstrate the incorporation of a geometrically interdigitated, mechanically stable interface into this biomaterial design for TBJ repair. This work describes the

creation and mechanical characterization of bulk and local properties within a multi-compartment scaffold with an increasingly interdigitated interface for the purpose of reducing stress concentrations between compartments.

4.3: Materials and Methods

4.3.1 CG suspension preparation

A CG suspension was prepared from type I collagen (1.0% w/v) isolated from bovine tendon (Sigma-Aldrich, St. Louis, MO) and chondroitin sulfate (0.1% w/v) derived from shark cartilage in 0.05 M acetic acid [157]. The suspension was homogenized at 4 °C to prevent collagen gelatinization during mixing and was degassed before use.

4.3.2 CGCaP suspension preparation

A CGCaP suspension was prepared from type I collagen (1.93% w/v) isolated from bovine tendon (Sigma-Aldrich, St. Louis, MO) and chondroitin sulfate (0.84% w/v) derived from shark cartilage in 0.1456M phosphoric acid / 0.037M calcium hydroxide buffer solution [198]. The suspension was homogenized at 4 °C to prevent collagen gelatinization during mixing. Calcium salts ($\text{Ca}(\text{OH})_2$) and $\text{Ca}(\text{NO}_3)_2 \cdot 4\text{H}_2\text{O}$ were added during homogenization and suspension was degassed before use. This suspension has previously been shown to produce 40 wt% mineral scaffolds by a titrant-free concurrent mapping method [198].

4.3.3 3D printed dividers for multi-compartment scaffold creation

A series of acrylonitrile butadiene styrene (ABS) dividers were printed using a MakerBot Replicator 2X (MakerBot Industries, Brooklyn, NY) at standard quality settings (10% infill, 2

shells, 200µm layered height), an extruder speed of 90 mm/s, and a nozzle temperature of 230 °C) onto a temperature controlled build-plate (110 °C). Six different ABS dividers (10mm x 10mm x 20mm) were fabricated with increasing degrees of interdigitation and therefore, increasing SCIs: a straight divider (*flat*, *SCI: 1.0*), a divider with two interdigitations (27° *interdigitation angle*, *SCI: 4.5*), a divider with three interdigitations (18° *interdigitation angle*, *SCI: 6.3*), a divider with four interdigitations (14° *interdigitation angle*, *SCI: 8.2*), a divider with six interdigitations (9° *interdigitation angle*, *SCI: 12.2*), and a divider with eight interdigitations (7° *interdigitation angle*, *SCI: 16.1*). Dividers were printed with a wall thickness of 600 µm to maintain high print fidelity. End-blocks were 3D printed using the same print settings (**Figure 4.3**).

4.3.4 Geometrically interdigitated multi-compartment scaffold creation

Scaffolds were fabricated within a custom aluminum mold (20mm x 76mm x 15mm) designed to accommodate the removable dividers with varying degrees of interdigitation (pattern: *flat*, 27° , 18° , 14° , 9° , and 7° ; 600µm divider: 20mm x 10mm x 10mm). After the divider was placed into the mold, separate halves of the mold were filled with CG and CGCaP suspensions (4.4 mL/region). Homogeneous samples of CG (*non-mineral*) or CGCaP (*mineral*) suspensions were prepared by loading 8.8 mL of one suspension into the same mold without any divider, but otherwise treated in the same manner. The suspension-loaded mold was placed into the freeze-dryer (VirTis, Gardiner, NY) at 20 °C, and the divider was then removed. The shelf temperature was then ramped down to -40 °C at a rate of 1 °C/min and held at -40 °C for 1 hour to ensure complete freezing. Following freezing, the shelf temperature was ramped up to 0 °C at a rate of 1 °C/min while pulling a 200 mTorr vacuum to remove ice crystals via sublimation (**Figure 4.3**).

4.3.5 Sample preparation for mechanical testing and digital image correlation (DIC)

Samples were first embedded into 3D printed end-blocks to prevent the grips during mechanical testing from unduly crushing, and damaging, the sample. PDMS was prepared in a 4:1 (monomer: catalyst) ratio, poured into 3D printed end-blocks (10mm height x 20mm width x 30mm length), and allowed to cure at room temperature for 60 minutes before scaffolds were placed within the end-blocks (Hisco-Schaumburg Incorporated, Schaumburg, Illinois). If necessary, additional PDMS was added to the end-block to ensure the scaffold would not pull out of the end-block during mechanical testing. Embedded scaffolds were then speckle patterned using an airbrush (nozzle: 0.3mm; gravity feed; GotHobby, South El Monte, CA) filled with waterproof india ink (Blick Art Materials, Galesburg, Illinois) attached to house air.

4.3.6 Bulk mechanical characterization

Multi-compartment scaffolds (20 mm width, 5 mm thickness, 40 mm gauge length) with varying interdigitated interfaces (*flat*, 27° , 18° , 14° , 9° , and 7°) as well as the homogenous controls (*mineral*, *non-mineral* only) underwent mechanical tensile testing in an Instron 5943 Mechanical Testing System with a 100 N electromechanical load cell. Samples were held in place at the 3D printed ABS end-blocks with pneumatic grips (60 psi) to prevent slippage. Scaffolds were strained at a rate of 1 mm/min until failure while images were captured using a high definition digital camera (Canon EOS E5) with a 100mm lens (Canon 100mm macro lens) and a time lapse remote (type here) at a rate of 1 image every 2 seconds. Failure mode was recorded by taking the final image captured after failure (**Figures 4.3**), elastic modulus was calculated as the slope of the linear elastic region of the stress-strain curve (**Figure 4.4**) [172], toughness was calculated as

the area under the stress-strain curve after failure (**Figure 4.5**) [178], and peak stress was taken as the maximum stress the sample experienced before failure (**Figure 4.6**) [178].

4.3.7 Local mechanical characterization via Digital Image Correlation

Images were correlated using the Improved Digital Image Correlation code (Improved Digital Image Correlation version 4 – Copyright © 2013, 2014, 2015 by Elizabeth Jones)[179] to calculate local strain profiles across the specimen. Reduced images were correlated first, with individual correlation settings optimized for each sample (typical settings: image reduction factor: 7, subset size: 35; threshold: 0.3; search zone: 4, grid step size: 15). Reduced correlations were iterated up to 6 times due to high strain. Full images were then correlated using the reduced data (typical settings: subset size: 21; threshold 0.3; search zone: 3; grid step size: 23). Finally, correlated data was smoothed and missing data (applicable at higher strains not included in the visual representations shown in **Figures 4.7-4.10**) was interpolated (Gaussian distribution of weights; kernel size: 11; number of smoothing passes: 3; maximum size of contiguous non-correlated points to smooth over: 35) and local strain profiles were calculated using a cubic (16-node) strain algorithm [180, 181]. The “visualize data” feature of the Improved Digital Image Correlation code was utilized in order to generate contour plots and line scans (**Figures 4.7-4.10**) [179]. This data was exported to excel to perform maximum strain gradient calculations. Strain gradients were calculated by extracting 9 line scans (evenly spaced along the sample, perpendicular to strain) of local strain and calculating the maximum slope of each line [182-184].

4.3.8 Statistics

One-way analysis of variance (ANOVA) was performed on elastic modulus, peak stress, and toughness, and maximum strain gradient calculations ($n=5$), followed by Tukey post-hoc tests. Significance was set at $p<0.05$. Error is reported as standard error of the mean unless otherwise noted.

4.4: Results

4.4.1 Failure mode

While failure occurred randomly in the homogenous (*mineral*, *non-mineral*) samples, failure typically occurred at the interface in multi-compartment scaffolds containing a flat interface as well as interdigitated interfaces with small angles of interdigitation (9° and 7°). However, within a subset of the interdigitated groups (27° , 18° , and 14°), failure was shifted away from the interface and occurred consistently in the CGCaP compartment (**Figure 4.4**).

4.4.2 Bulk mechanical characterization

Bulk mechanics (elastic modulus, peak stress, toughness, failure mode) were found to vary depending upon the degree of interdigitation at the interface. Generally, samples containing interdigitations at 27° , 18° , and 14° had a higher elastic modulus, peak stress, and toughness than other multi-compartment scaffolds. The elastic modulus of homogenous scaffolds was significantly higher (*mineral*) and lower (*non-mineral*) than multi-compartment scaffolds, consistent with previous findings in our laboratory [45]. As expected, multi-compartment scaffolds had elastic moduli which fell between the homogenous mineral or non-mineral samples. Interestingly, the 27° interdigitation group displayed a significantly ($p < 0.05$) higher

elastic modulus than 18°, 9°, and 7° groups (**Figure 4.5**). Not surprisingly, the toughness of the non-mineral (homogeneous) scaffold was superior to the mineral (homogenous) scaffold and the multi-compartment scaffold with a flat interface. However the incorporation of interdigitations significantly altered the toughness of the scaffolds, with the 27°, 18°, and 14° groups showing significantly ($p < 0.05$) increased toughness compared to the 7° interface, with the 14° groups also significantly tougher than the 9° group (**Figure 4.6**). Finally, the peak stress achieved by each scaffold also depended on interdigitations. Mineral (homogeneous) scaffolds showed significantly ($p < 0.05$) increased peak stress versus the non-mineral (homogenous) scaffold and the flat interface. Again, incorporation of an interdigitated interface improved overall peak stress, with 14°, 18° and 27° groups showing significantly ($p < 0.05$) enhanced peak stress compared to the 7° group. Further, the 27° and 14° interdigitation groups sustained peak stresses equivalent to the best-performing homogenous group (mineral), effectively removing any deleterious effect of the presence of an interface (**Figure 4.7**).

4.4.3 Local mechanical characterization

To better understand these bulk mechanical responses, local strain contour plots and line scans generated from DIC were examined to identify patterns in strain and stress concentrations. The homogeneous mineral sample had smooth strain fields across the entire sample. In the non-mineral samples, local regions of high strain (strain bands) developed and propagated along the width of the sample perpendicular to applied strain. In the multi-compartment scaffold groups, strain bands also developed and propagated in regions near the interface between compartments. However, in the flat interface group as well as the smallest angle of interdigitation groups (14°, 9°, and 7°), local strain concentrations developed at the interface preceding failure at the

interface, suggesting stress concentrations occur primarily at the interface of mechanically mismatched materials. However, in the 27° and 18° interface groups that displayed improved bulk mechanical performance, such strain bands did not develop at the interface. Instead, the strain was dissipated throughout the CG compartment, with failure occurring primarily in the CGCaP compartment away from the interface (**Figure 4.8**).

4.4.4 Local strain profiles

We next examined the presence of stain bands through the use of analysis of line scans taken from the strain mapping data. Line scans were acquired from the midpoint of specimens in the direction parallel to applied strain at discrete levels of overall bulk applied strain to the specimen (0%, 1.8%, 3.4%, 5.1%; **Figure 4.9**). In the multi-compartment samples, local areas of high strain initiate at relatively small bulk strain levels (by 1.8% strain) and then increase in magnitude as the overall bulk strain applied to the construct increases. This phenomenon is particularly notable for large strain concentrations precisely at the interface for scaffolds containing a flat interface as well as those with the smallest interdigitation angles (7 – 14°) that also showed poor bulk mechanical behavior. However, for the interdigitated specimens with enhanced bulk mechanical properties (27° and 18° groups), local strain concentrations are not seen at the interface. Instead, broader regions of increased strain were more evenly distributed throughout the sample as overall strain increases. As comparison, in the uniform non-mineral control specimens, local strain is evenly distributed throughout the sample until higher levels of bulk strain where regional strain bands begin to form. Interestingly this pattern is also observed in the CG region of the multi-compartment scaffold variants as well (**Figure 4.10**).

Additionally, a series of 9 line scans were acquired at equally spaced intervals across the specimen at 5.1% overall bulk applied strain to the specimen. In the homogenous non-mineral scaffold group, local areas of high strain (strain bands) are seen at regular intervals along the specimen. In the multi-compartment samples, local areas of high strain are again concentrated at the interface between CGCaP and CG compartments for the flat interface as well as for the interdigitated samples with poor bulk mechanical behavior (14°, 9°, and 7°). However, in interdigitated samples with interdigitation angles that displayed improved bulk mechanical performance (27° and 18°), there is a minimal increase in local strain at the interface, and the CG compartment does not display the characteristic full-width strain bands at 5.1% overall strain (**Figure 4.11**).

4.4.5 Local strain gradient maxima

We subsequently examined the maximum change in local strain from the individual line scans in order to obtain local strain gradient maxima for each experimental group. The flat interface group, along with the subset of interdigitated variants that displayed the poorest bulk mechanical behavior (14°, 9°, and 7°), exhibited strain gradient maxima equivalent to those seen in the uniform non-mineral group. However, the subset of interdigitated variants that displayed the best bulk mechanical behavior (27° and 18°) showed reduced local strain gradient maximums, with the 18° interface group having a significantly decreased value ($p < 0.05$) (**Figure 4.12**).

4.5: Discussion

A major necessity in the field of orthopedic tissue regeneration is to develop technologies that enable regenerative repair of transitional tissues in the body [188-190, 199]. Although a great deal of progress has been made in developing homogenous biomaterials for the regeneration of a

single tissue, the difficulty of incorporating heterogeneities into a single biomaterial construct remain [104, 188, 200]. One of these difficulties lies in the complex interactions at the interface of mechanically dissimilar materials, especially when this dual construct must remain competent at the interface in response to mechanical loading [194]. *In vivo*, rotator cuff repairs often fail at the interface between tendon and bone. Although tendon and bone can be repaired individually, repair of the insertion itself remains largely neglected [1]. Previous efforts in our laboratory have described a model collagen biomaterial for tendon-to-bone repair that contains discrete non-mineral (CG) and mineral (CGCaP) collagen scaffold regions joined by a continuous interface (order: 250 μ m) [72, 136, 193]. However, the interfacial zone of this material remains susceptible to failure under applied strains. As a result, here we describe the ability to effectively dissipate stresses at the interface of this multi-compartment scaffold via the incorporation of a biomimetic toughening strategy: the addition of interdigitations at the interface between two materials that differ in elastic modulus by orders of magnitude [196, 201]. While this toughening strategy has been observed in the protective shells and scales of animals [1, 124-127], and incorporated into materials such as body armor [126], such a strategy remains to be fully realized in the field of biomaterials and tissue engineering.

This manuscript reports the bulk and local mechanical properties observed within a range of multi-compartment collagen scaffolds with varying interfacial geometries for the purpose of creating a mechanically robust interface for orthopedic insertion tissue engineering applications. In homogenous scaffolds (*mineral*, *non-mineral*), failure was consistent with previous findings and occurred randomly throughout the sample. However, as two distinct compartments were incorporated into the sample with a linear insertional zone (*flat*), strains were concentrated at the

interface leading to failure (**Figures 4.4, 4.8**). This paradigm is commonly found in materials and tissues which contain distinct regions of varying composition which result in a mechanical mismatch, even when a small, graded transition region is present [108, 136, 196]. *In vivo*, repaired rotator cuffs lack the native toughening of the interfacial zone and fail at the interface due to similar stress concentrations found in our multi-compartment (*flat*) biomaterials lacking an interfacial toughening strategy[184]. However, when an interdigitated interface was incorporated (27° , 18° , 14°) between distinct compositions, failure shifted away from the interface and occurred consistently in the stiffer, CGCaP compartment of the scaffold. While the native, healthy rotator cuff has been shown to possess an insertional zone containing local regions of interdigitation [14, 36], such a paradigm has not previously been incorporated within a multi-compartment biomaterial. However, for low angle of interdigitation designs (9° , 7°) the interface fidelity was lost likely due to mixing along the interface prior to freeze-drying. In these samples, high areas of local strain returned to the interface and the failure mode reverted to a paradigm consistent with samples (*flat*) lacking an interfacial toughening strategy (**Figures 4.4, 4.8**).

Previous research, both in and outside of our lab, has characterized the bulk mechanical properties of homogenous mineral and non-mineral collagen scaffolds, as well as multi-compartment samples which lacked an interfacial toughening strategy (created with the same composition as the homogenous materials) [45, 198, 202]. The bulk mechanical properties of our homogenous materials were consistent with previous findings. As expected, mineral scaffolds displayed a significantly higher elastic modulus (**Figure 4.5**) and peak stress (**Figure 4.7**), and significantly lower toughness (**Figure 4.6**) than the non-mineral samples. Similarly, multi-

compartment materials lacking an interfacial toughening strategy (*flat*) displayed bulk mechanical properties similar to or matching the lowest value of the homogenous material (low elastic modulus, **Figure 4.5**; low toughness, **Figure 4.6**; low peak stress **Figure 4.7**). We propose that these bulk mechanical properties were observed due to stresses concentrating in the weakest material, and thus multi-compartment materials and tissues regularly display properties consistent with the weakest material or tissue. This is a major challenge in the field of orthopedic tissue regeneration, where multiple tissues with distinct mechanical properties are intended to be regenerated in parallel, but biomaterials with multiple compositions lack the mechanical competence of a single homogenous biomaterial.

The multi-compartment collagen scaffolds which successfully incorporate this toughening strategy (27° , 18° , 14°) regularly displayed bulk mechanical properties consistent with the strongest material from which it was comprised (27° : moderate elastic modulus, **Figure 4.5**; 27° , 18° , 14° : high toughness, **Figure 4.6**; 27° , 18° , 14° : high peak stress **Figure 4.7**), which implies a fundamentally different local mechanical mechanism at the interface. This strategy greatly improves the bulk mechanical properties of the entire construct and has great implications for the design of biomaterials with mechanically dissimilar compositions used for orthopedic tissue regeneration. However, this trend disappeared as the geometric interdigitations at the interface became smaller, the pattern fidelity decreased, and the observed length of the interfacial zone decreased (7° , 9°). These samples exhibited the same behavior as multi-compartment scaffolds which lacked the interfacial toughening strategy (*flat*) and returned to a paradigm consistent with the weakest mechanical properties of the homogenous samples (low elastic modulus, **Figure 4.5**; low toughness, **Figure 4.6**; low peak stress **Figure 4.7**). In order to further examine this

phenomenon, we analyzed local patterns of strain, which are imperative but often neglected in the characterization of heterogeneous materials.

Digital image correlation was used to examine strain patterns to find local regions of high strain gradients, which correspond to high stress concentrations, to elucidate the mechanisms behind the fundamental differences we observed in the bulk mechanical behavior of these materials. We visualized data from representative samples both as contour plots, which display full strain correlation data (**Figure 4.8**), and as line scans taken from these contour plots, which more easily display the regional changes in local strain gradient behavior (increasing strain from the central region: **Figure 4.10**; multiple regions at 5.1% strain: **Figure 4.11**). For comparison purposes, homogenous samples (*mineral, non-mineral*) were correlated in addition to the heterogeneous samples (*flat, 27°, 18°, 14°, 7°, 9°*). Mineral samples had smooth strain fields until failure (**Figures 4.8**) while non-mineral samples displayed small, regularly spaced (~8-10 mm) cracks which propagated along the width of the sample perpendicular to strain, yielding high local strain gradients which ultimately led to failure (**Figures 4.8, 4.10-12**). This local behavior was also found in the discrete bulk compartments of multi-compartment scaffolds which lacked interfacial toughening (*flat, 14°, 7°, 9°*), with the first area of high local strain appearing at the interface between compartments by 1.8% strain (**Figures 4.8, 4.10**). This local behavior is consistent with the knowledge that stresses concentrate at the interface of mechanically mismatched materials, and remains a leading challenge in the creation of mechanically robust biomaterials for multi-tissue regeneration.

Interestingly, a unique strain pattern emerges in samples which successfully incorporated an interfacial toughening strategy (27° , 18°) (**Figures 4.8, 4.10-11**). In these samples, local regions of high strain as well as large strain gradients were *not* localized at the interface, but were dissipated more evenly throughout the sample (**Figure 4.12**). Here, scaffolds containing interdigitation angles of 27° and 18° showed significantly reduced maximum strain gradients. Further, regions of increased strain as observed via DIC were incorporated more evenly within the CGCaP compartment compared to samples without a successful geometric interface (*flat*, 14° , 7° , 9°) (**Figures 4.8, 4.10-11**). These shifts are consistent with predictions regarding engineering materials containing interdigitated interfacial zones [128], and for the collagen biomaterial described here, likely contributes to the shift in failure mode and increase in interfacial toughness.

Examining the strain profiles via DIC, although periodic regions of increased strain were observed in scaffold variants that displayed improved toughness (27° , 18°), these samples did not display large strain bands like those seen in interfacial variants with poor toughness (*non-mineral*, *flat*, 14° , 7° , 9°). Instead periodic, local increases in strain were observed (**Figure 4.8**), and tended to lead to a more constant local strain value in the CG compartment (**Figure 4.11**), and lower maximum strain gradients (**Figure 4.12**). This phenomena resulted in a more even distribution of strain throughout the entire sample (both at the interface and throughout the discrete CGCaP compartment), and ultimately provides a local mechanism by which these samples display an increase in toughness under tensile loading. However, as the interfacial region became smaller (14° , 7° , 9°) strain band phenomena returned, ultimately resulting in

higher strain gradient maxima (**Figure 4.12**) resulting in reduced toughness similar to that observed for scaffolds containing a linear (*flat*) interface (**Figures 4.8, 4.10-11**).

Our findings, that constructs containing interdigitated interfaces with interdigitation angles ranging from 27° to 14° outperformed a traditional (*flat*) interface, are consistent with the theoretical work of *Li et al.* who modeled a system where two stiff materials were connected by a thin, soft material. In that work, specimens containing an optimal angle of interdigitation ($\sim 12^\circ$) led to superior bulk mechanical behavior where tensile forces were resolved as shear forces distributed over a larger area along the interface, and were thus minimized [128]. Here, we have experimentally demonstrated a low-density open-cell foam based collagen biomaterial system with a similar range of interdigitation angles (14° to 27°) that contains improved composite toughness. However, samples with smaller angles of interdigitation (7° , 9°) at the interface suffered from reduced fidelity of the fabricated pattern, leading to a smaller interfacial zone than intended, and possibly reduced the mechanical performance of those designs. Future work will focus on creating patterns with higher fidelity to further increase the size scale on which this paradigm can be applied in the field of orthopedic tissue engineering.

4.6: Conclusions

This chapter demonstrates a novel method to create multi-compartment scaffolds for musculoskeletal repair, incorporating bioinspired interdigitations at the interface between mechanically dissimilar compartments. We showed that adding an interdigitated interface between CG and CGCaP scaffolds, particularly for interdigitation angles between 14° to 27° , leads to significant increases in bulk elastic modulus, peak stress, and toughness. Examining strain profiles within these constructs, we find these increases are associated with effective

dissipation of local regions of high strain concentration. Together, this work demonstrated that interdigitation is a viable strategy to increase the bulk mechanical properties of a multi-compartment biomaterial by fundamentally changing the local strain profiles at and near the interface. This paradigm offers potential advantages to address challenges for tissue engineering applications for insertional tissues in the musculoskeletal system related to stress concentrations that can arise at the interface between mechanically mismatched biomaterials.

4.7: Figures

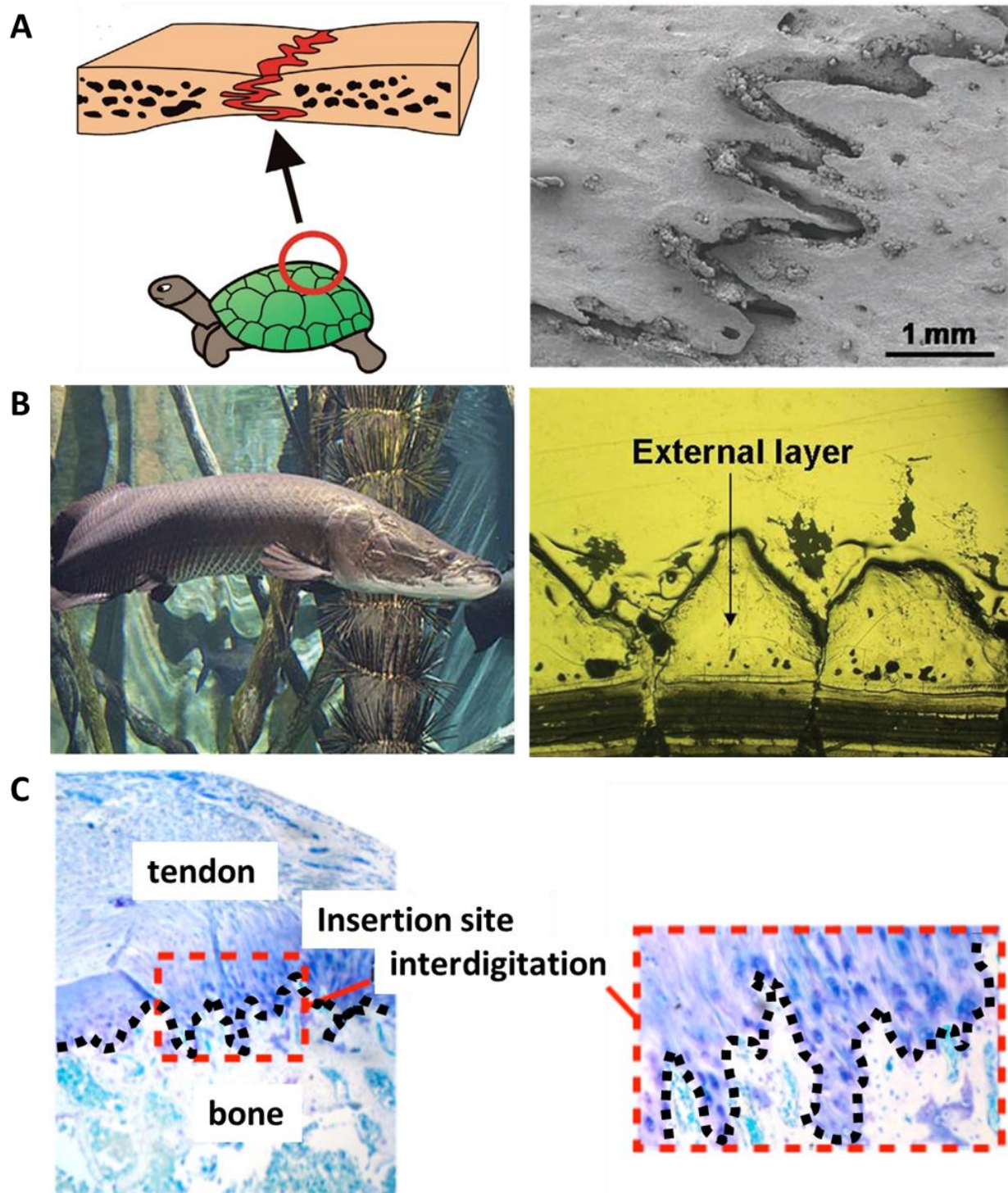


Figure 4.1 Naturally occurring interdigitation. A) The plates between a turtle shell and B) in the scales of an arapaima are interdigitated to maximize protection while allowing for movement and respiration. C) This same paradigm is found at the interface between bone and tendon to minimize stress concentrations at the rotator cuff [126, 127, 196, 203].

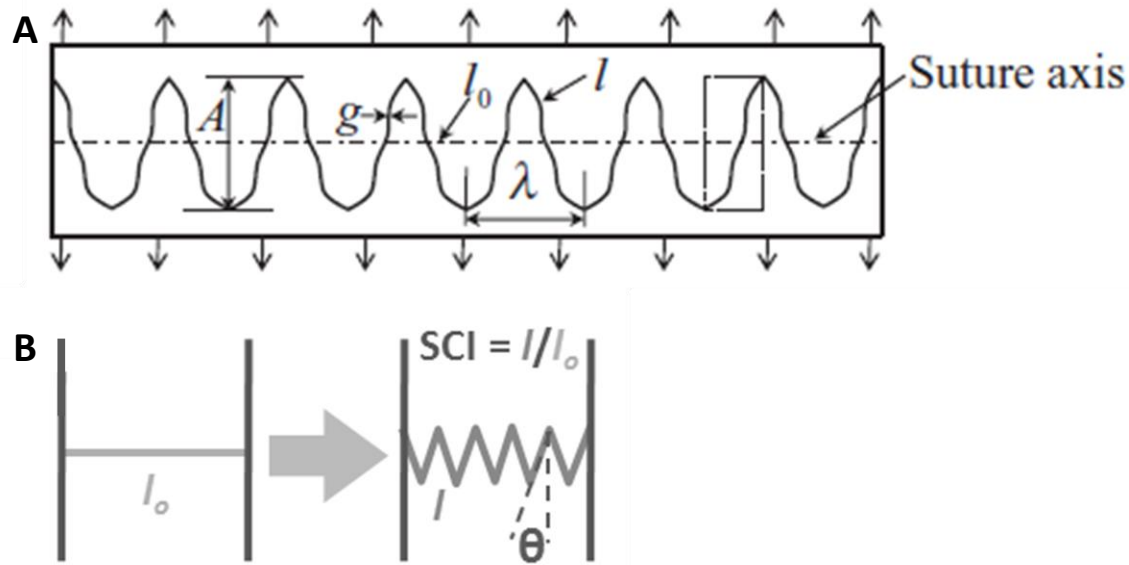


Figure 4.2 Key components in theoretical modeling of interdigitated interfaces. **A)** There are many components that can be measured across the interface to describe its degree of interdigitation, including the amplitude (A), period (λ), thickness (g), minimum contact length (l_0), and actual contact length (l). **B)** However, the strength of interdigitated interfaces can be simplified to just two components, the suture complexity index (SCI) and the angle of interdigitations. The SCI is a measure of contact length across the interface, l divided by l_0 . The angle of interdigitation (Θ) is important for two reasons. First, Θ determines how many interdigitations, or “teeth” can fit across the interface. There also exists an ideal Θ where tensile forces applied across the interface fundamentally shift to shear forces, which can be distributed over a larger area and thus minimized [128].

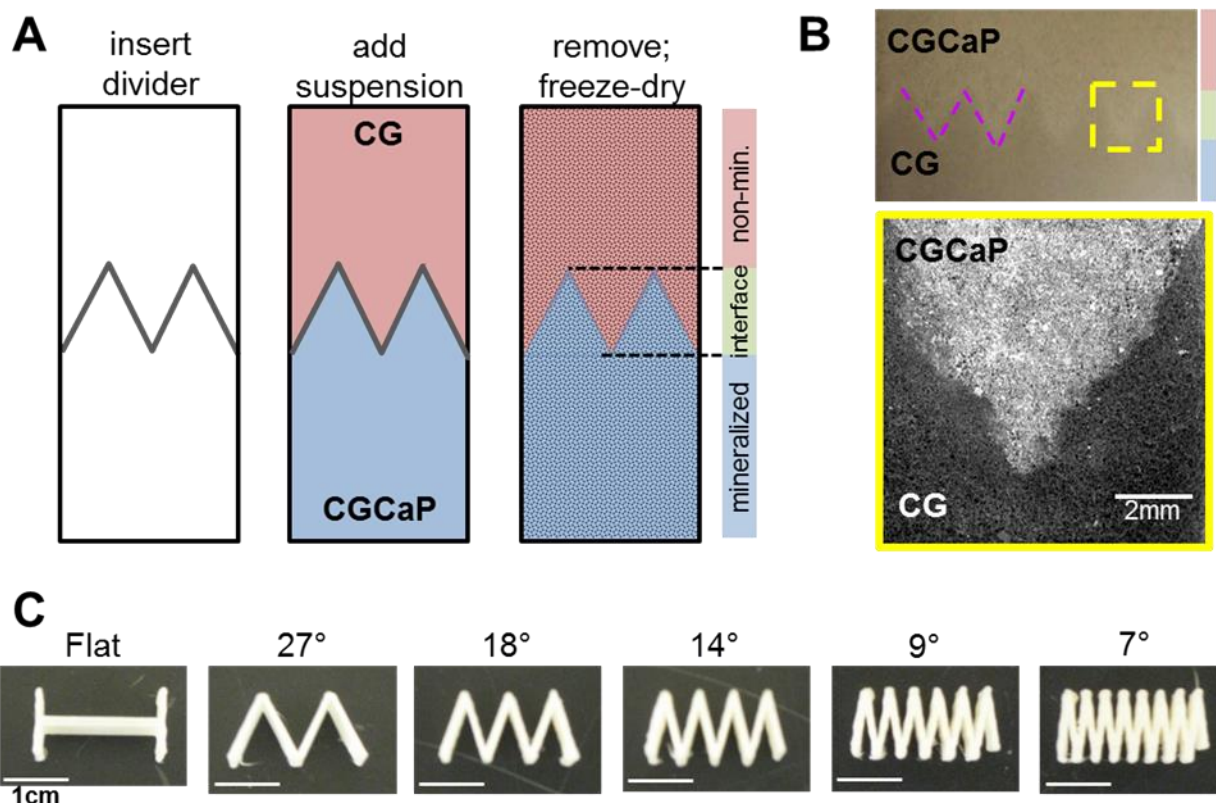


Figure 4.3 Fabrication of interdigitated CG scaffolds. A) Multi-compartment scaffolds are fabricated using a custom mold with a removable, interdigitated divider. Each compartment was filled with either a CG or a CGCaP suspension. The divider was removed immediately prior to lyophilization. *B)* Distinct geometries can be seen post fabrication. *C)* Representatives images of 3D printed ABS dividers with angle of interdigitation displayed above the image.

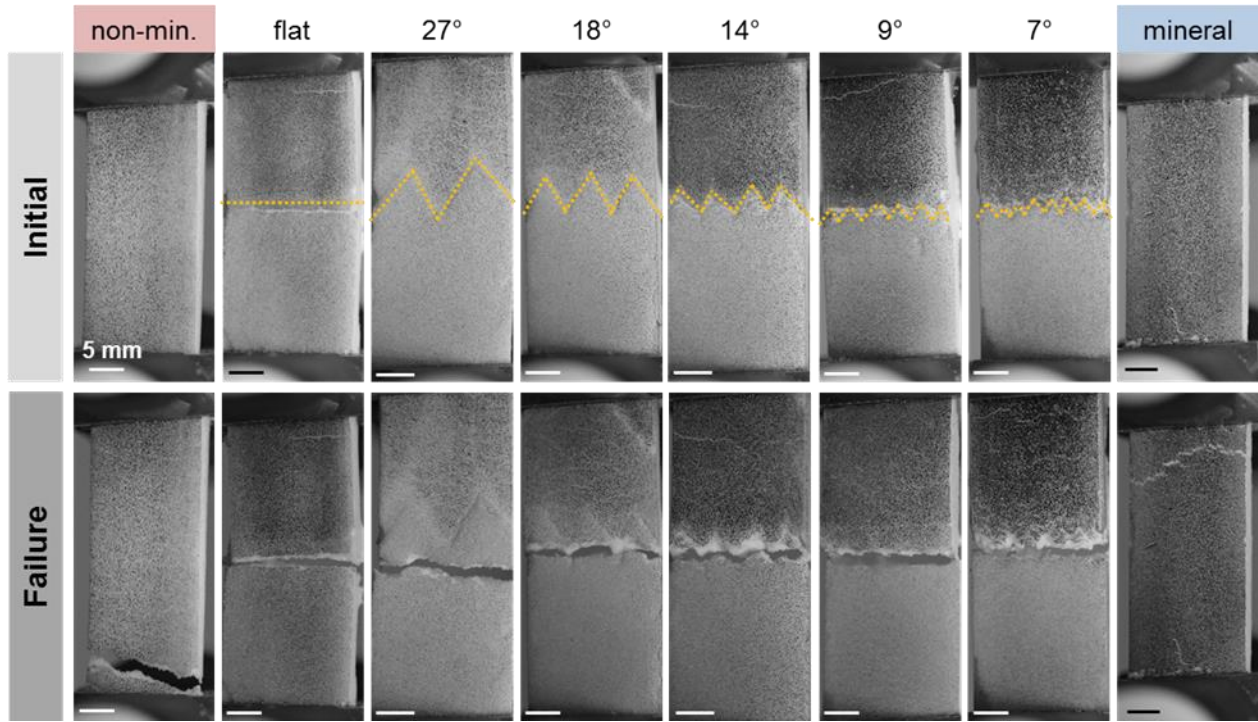


Figure 4.4 Interdigitated scaffolds before and after mechanical testing. (Top) All scaffolds were speckle patterned, with the CG side retaining more india ink for an overall darker appearance. Interdigitations can clearly be seen at the interface. (Bottom) Representative mechanical failures from each group are shown. When the interdigitations are large and pronounced, strain is dissipated away from the interface. As interdigitation angles become smaller, the failure mode returns to that of the flat interface.

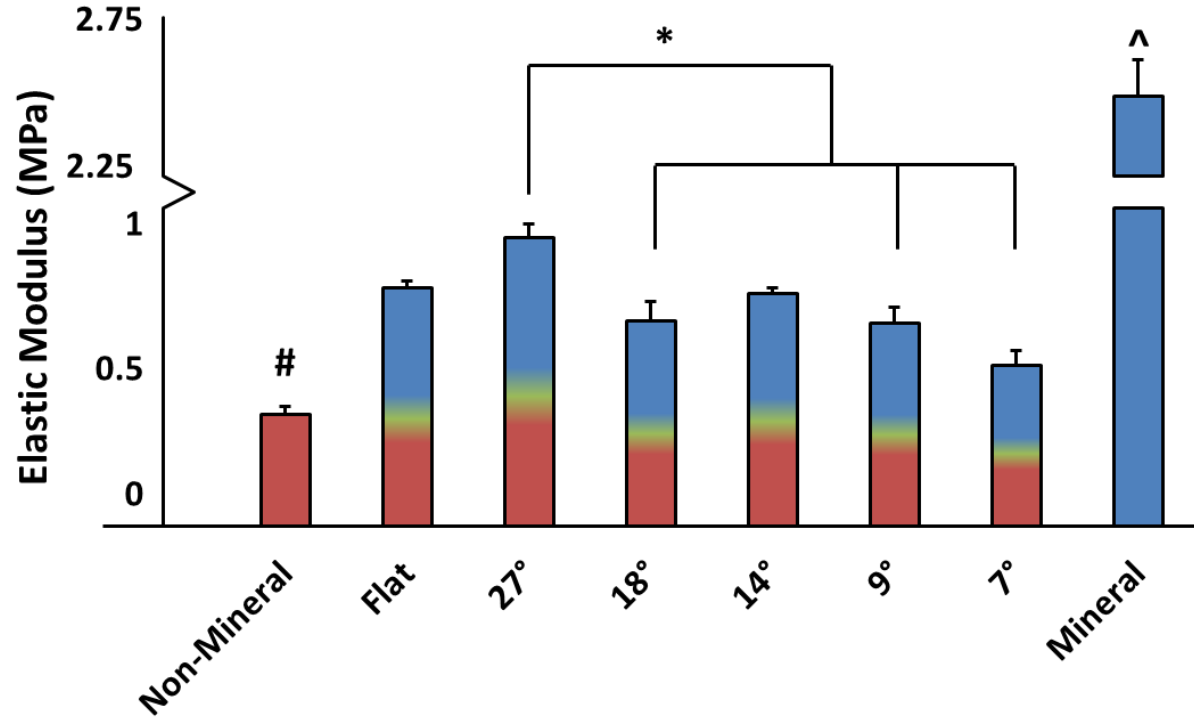


Figure 4.5 The elastic moduli of homogenous and interdigitated groups. While it was previously known that mineral scaffolds had significantly higher elastic moduli than non-mineral scaffolds, the multi-compartment scaffold with 27° interdigitation was found to have a significantly higher elastic modulus than most of the other multi-compartment scaffolds. *: $p < 0.05$. ^: $p < 0.05$ versus all other samples. #: $p < 0.05$ versus all other samples (except 7°).

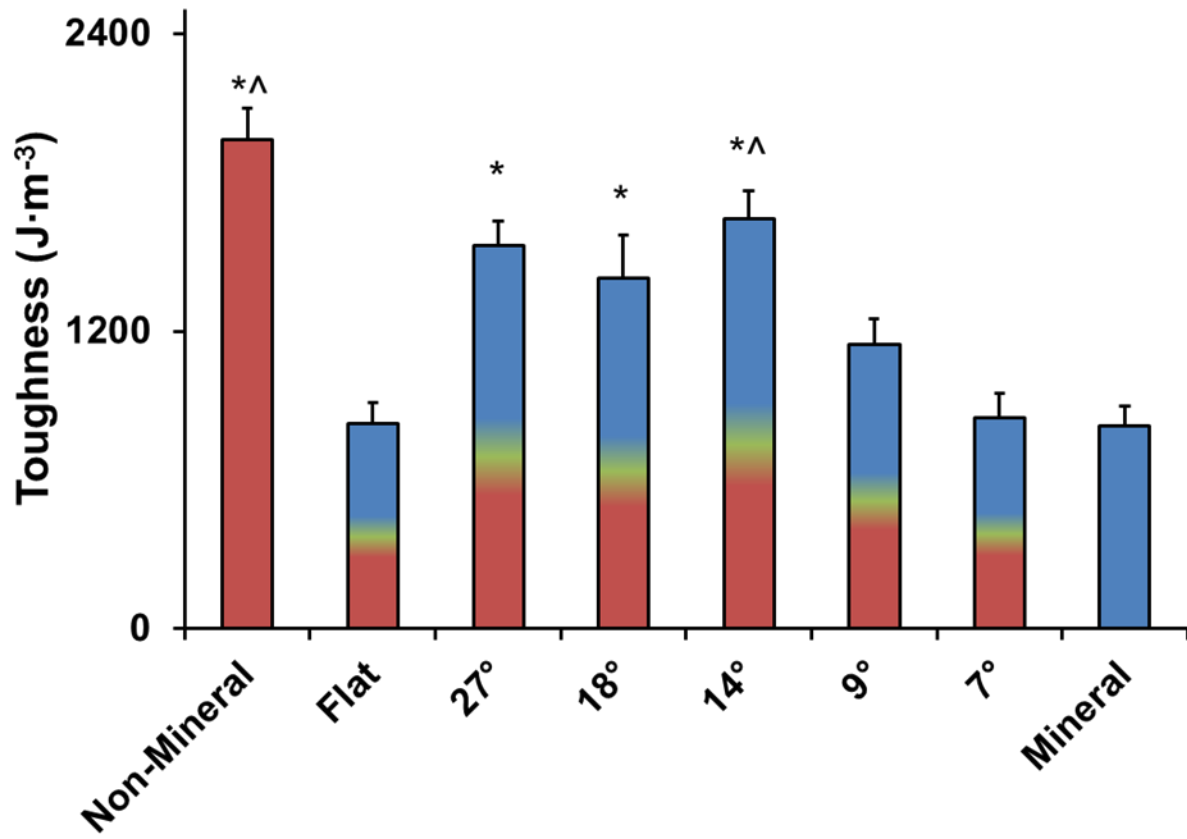


Figure 4.6 Toughness of homogenous and multi-compartment scaffolds. As previously reported, the non-mineral scaffold group had a significantly higher toughness than the mineral scaffold group. The interdigitating scaffolds displayed significantly higher toughness at larger degrees of interdigitation (27°, 18°, 14°), which returned to values not significantly different than the flat and mineral groups at higher degrees of interdigitation (9°, 7°). *: $p < 0.05$ versus mineral, 7°, and flat. ^: $p < 0.05$ versus 9°

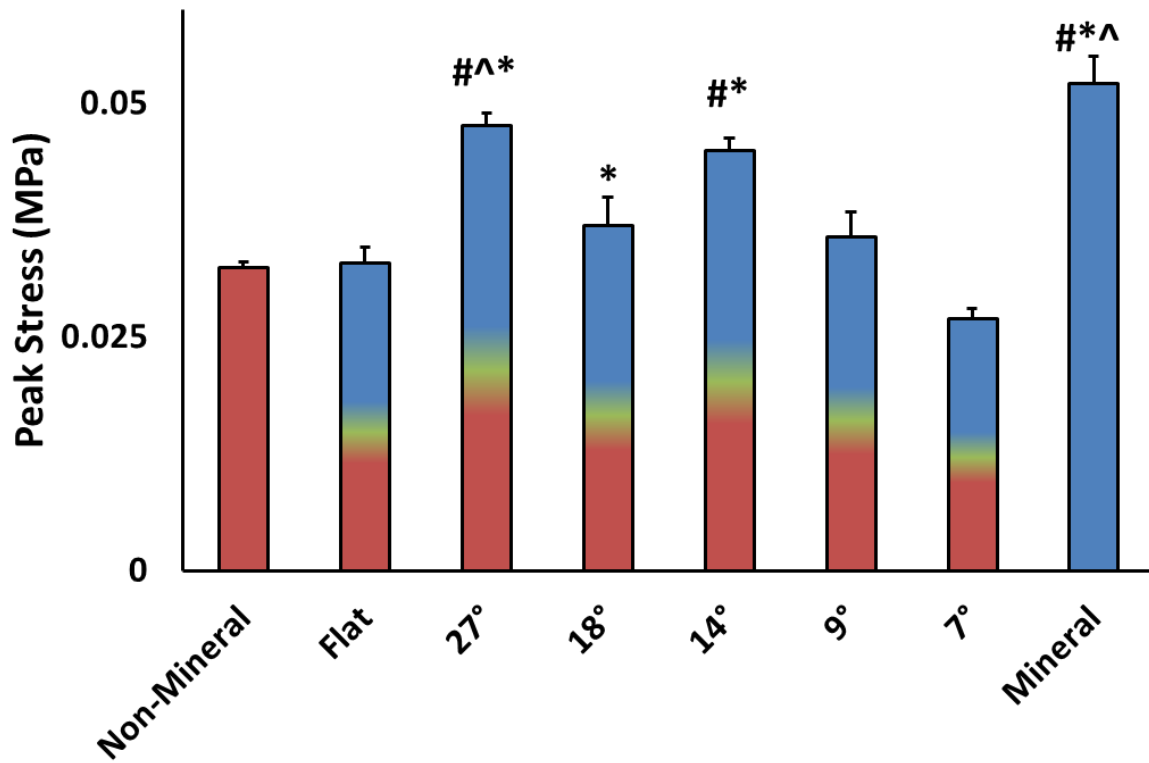


Figure 4.7 Peak stress of homogenous and multi-compartment scaffolds. As previously reported, the mineral scaffold group had a significantly higher peak stress than the non-mineral scaffold group. The interdigitating scaffolds displayed significantly higher peak stress at larger degrees of interdigitation (27°, 18°, 14°), which returned to values not significantly different than the flat and non-mineral groups at higher degrees of interdigitation (9°, 7°). #: $p < 0.05$ versus non-mineral, flat, and 9°. *: $p < 0.05$ versus 7°. ^: $p < 0.05$ versus 18°

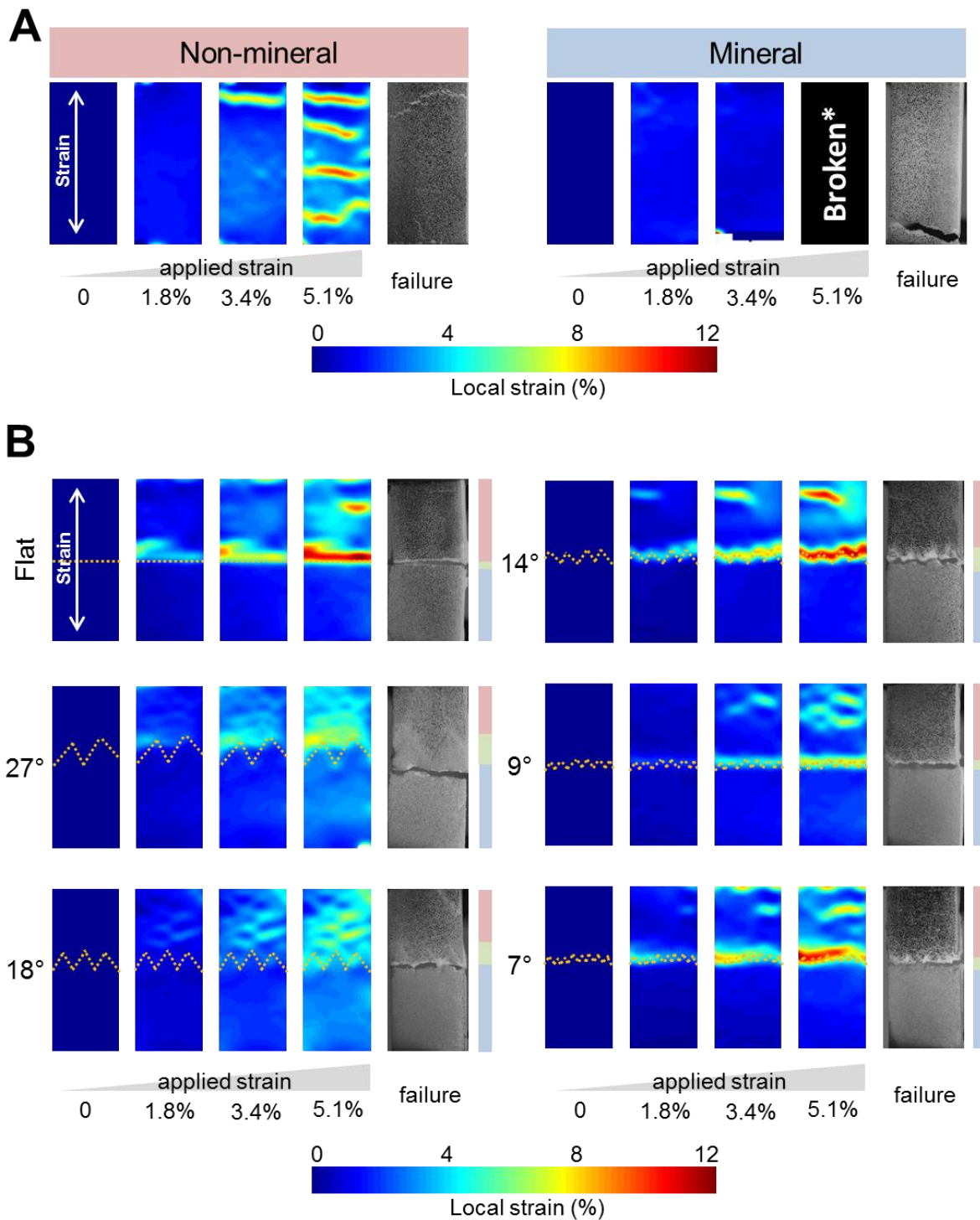


Figure 4.8 Local strain maps. A) Homogeneous samples: The mineral sample had smooth strain fields across the entire sample while in the non-mineral sample, small cracks propagated along the width of the sample at regularly spaced intervals and perpendicular to strain. *B) Multi-compartment samples:* Strain was typically concentrated at the interface between compartments with the exception of the 27° and 18° interface groups, where local strain was dissipated throughout the CG compartment before breaking in the CGCaP compartment.

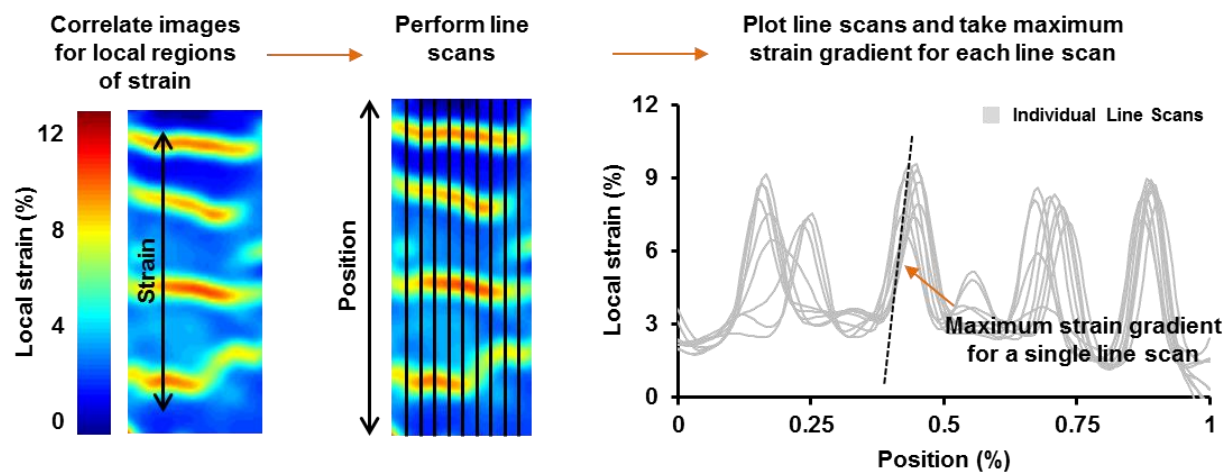


Figure 4.9 Digital image correlation and line scan analysis. Line scans were taken at regularly spaced intervals from each sample at multiple strains, in the direction perpendicular to the interface. These were then used to generate local strain profiles and maximum strain gradients.

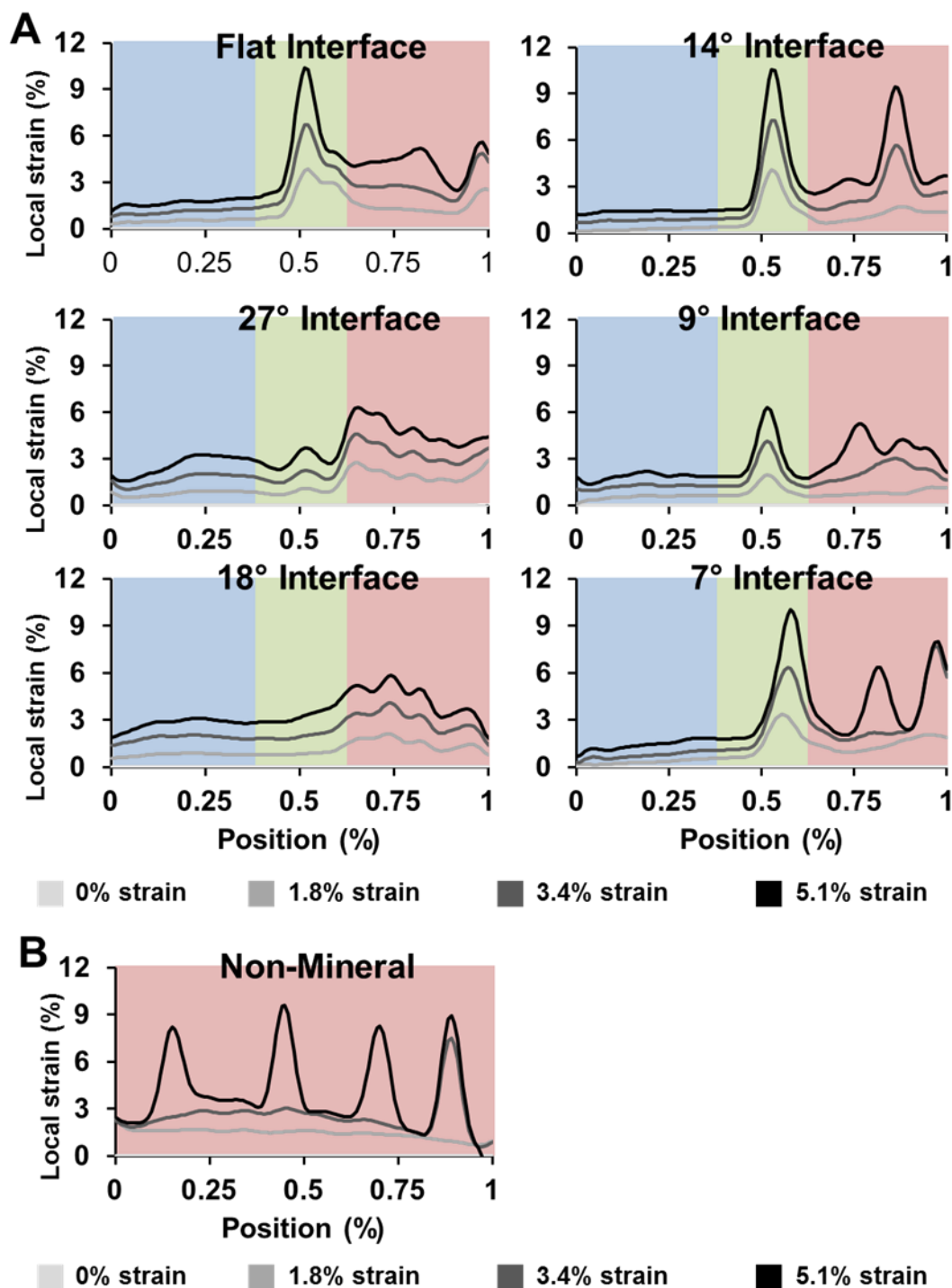


Figure 4.10 Local stress concentrations with increasing strain. A) Local areas of high strain originate at the interface at relatively low overall strain and continue to increase as the overall strain increases. Local strain rates are much smaller in the 27° and 18° groups. B) Local strain is evenly distributed throughout the sample until large levels of overall strain, where small cracks begin to form within the sample. These cracks then propagate at even intervals, yielding local regions of high strain.

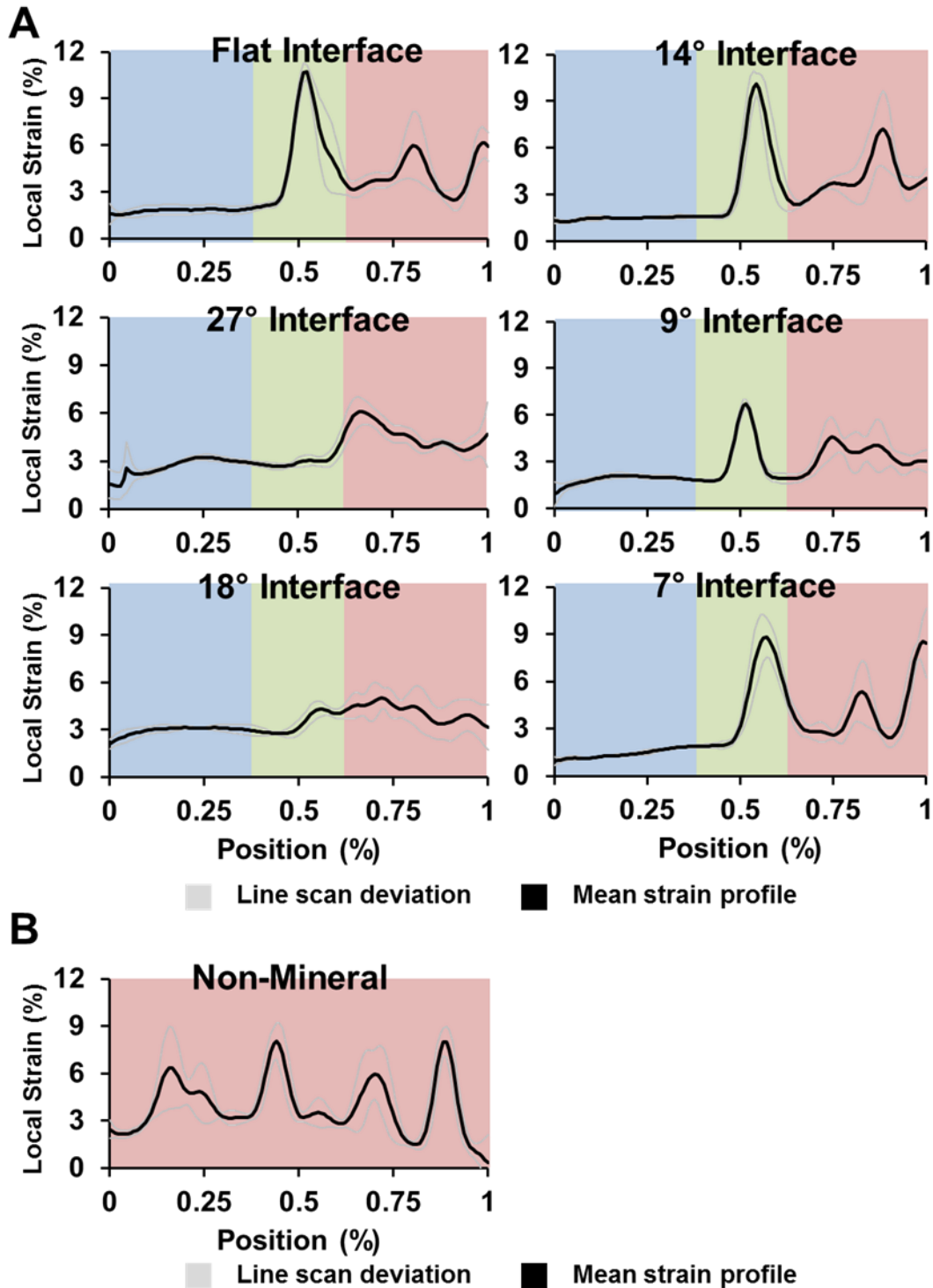


Figure 4.11 Local stress concentrations at 5.1% strain. A) Local areas of high strain are concentrated at the interface of multi-compartment samples. Multi-compartment samples display distinct regions that mimic the local strain profiles of homogenous mineral and non-mineral samples with a region of high local strain at the interface. However, the 27° and 18° groups have minimal local strain increases at the interface. B) Local areas of high strain are seen at regular intervals, which represents crack formation and propagation throughout the sample.

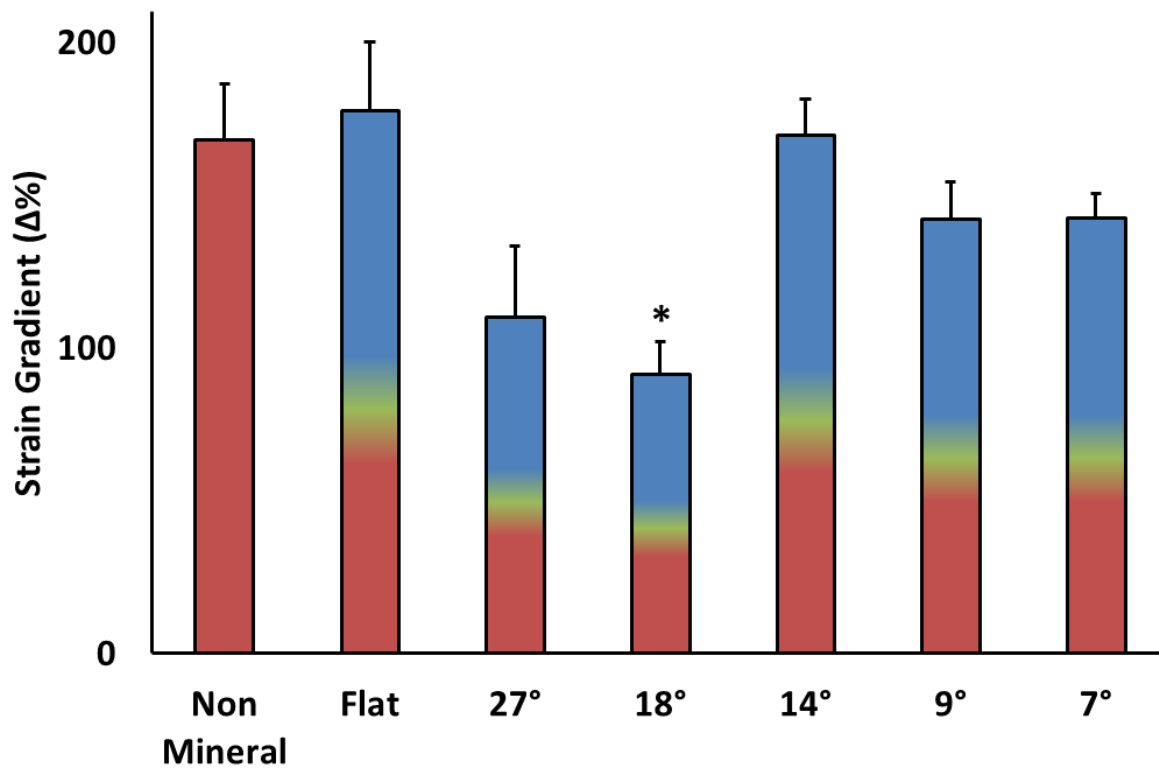


Figure 4.12 Maximum strain gradient across multi-compartment scaffolds. The flat interface group exhibits similar strain gradient maxima to the non-mineral group, with a similar trend in the 14°, 9°, and 7° interface groups. However, the 27° and 18° interface groups trended towards decreased local strain gradient maximums. *: $p < 0.05$ versus flat interface

CHAPTER 5: THE EFFECT OF GRADATIONS IN MINERAL CONTENT, MATRIX ALIGNMENT, AND APPLIED STRAIN ON HUMAN MESENCHYMAL STEM CELL MORPHOLOGY WITHIN COLLAGEN BIOMATERIALS⁴

5.1: Chapter Overview

The tendon-bone junction (TBJ) is a unique, mechanically dynamic, structurally graded anatomical zone which transmits tensile loads between tendon and bone. Current surgical repair techniques rely on mechanical fixation and can result in high re-failure rates. We have recently described a new class of collagen biomaterial that contains discrete mineralized and structurally aligned regions linked by a continuous interface to mimic the graded osteotendinous insertion. Here we report the combined influence of graded biomaterial environment and increasing levels of applied strain (0 – 20%) on MSC orientation and alignment. In *osteotendinous* scaffolds, which contain opposing gradients of mineral content and structural alignment characteristic of the native osteotendinous interface, MSC nuclear and actin alignment was initially dictated by the local pore architecture, while applied tensile strain enhanced cell alignment in the direction of strain. Comparatively, in *layered* scaffolds that did not contain any structural alignment cues, MSCs were randomly oriented in the unstrained condition, then became oriented in a direction perpendicular to applied strain. These findings provide an initial understanding of how scaffold architecture can provide significant, potentially competitive, feedback influencing MSC orientation under applied strain, and forms the basis for future tissue engineering efforts to regenerate the osteotendinous enthesis.

⁴ This chapter is adapted from Mozdzen et al, *Advanced Healthcare Materials*, 2016

5.2: Introduction

The tendon-to-bone junction (TBJ) is a unique anatomical zone connecting aligned, elastic tendon to stiff, mineralized bone. TBJ injuries such as in the case of rotator cuff tears are common, with more than 4.5 million physician visits and 250,000 surgeries annually in the US [5]. In a rotator cuff tear, the tendon typically tears away from the bone at the insertion. Surgical fixation is usually via direct anastomosis of the avulsed tendon to bone, resulting in the loss of the characteristic gradients in extracellular matrix proteins, growth factors and mineral content across the insertion. This loss of structural specialization is a primary factor responsible for high (>50%) re-failure rates [1], motivating development of tissue engineering solutions to improve regenerative healing of the osteotendinous enthesis.

Current technologies for osteotendinous interface repair are inspired by structural and compositional features of the native tissue. Tendons are highly aligned, anisotropic tissues. Like early efforts developing biomaterials for nerve [204, 205] and cardiac [52] tissue repair, the anisotropy of tendon motivated efforts to develop aligned biomaterials for tendon repair, to increase cell proliferation, enhance the maintenance of a tendon phenotype, and improve extracellular matrix production. Aligned biomaterials, with or without the application of tensile strain, have been shown to provide strong structural cues to direct tenocyte alignment and collagen synthesis [206, 207], increase MSC proliferation and alignment [131], and even increased expression levels of tenogenic markers in MSCs and adipose derived stem cells [91, 208]. Similarly, the increased stiffness and mineral content of bone have motivated development of a wide range of mineralized biomaterials with the goal of enhancing MSC osteogenic differentiation [73, 82].

Regenerative medicine solutions for the TBJ are increasingly turning to the development of biomaterials with complex structural (*e.g.*, pore architecture, alignment), mechanical (*e.g.*, elastic modulus, applied strain), and biomolecular (*e.g.*, mineral content, growth factors) properties, to replicate the complex gradient structure of the junction and subsequently ensure the appropriate guidance of cell bioactivity. Furthermore, given clinical concerns regarding limited expansion of terminally-differentiated cells as well as secondary wound site creation, many efforts are beginning to develop biomaterials to drive mesenchymal stem cell (MSC) differentiation down osteotendinous lineages in a spatially-selective manner [144]. However, in addition to biomaterial-based cues, the function of the native osteotendinous insertion suggests applied tensile strain may be a particularly important instructional signal. Applied strain has previously been shown to alter cell alignment within biomaterials [209], and in the TBJ is known to underlie initial development of the enthesis [210]. Indeed, while cyclic strain is more commonly used in the context of long-term culture [84, 86, 178, 211-213], static strain alone has been shown to induce cellular responses (morphology, alignment) [209, 214, 215]. Notably, *Subramony et al.* demonstrated that while mechanical stimulation can alter MSC integrin expression, fibroblast differentiation, and matrix deposition profiles, synergies between mechanical stimulation and alignment can preferentially induce a pro-tenogenic fate [131].

Unraveling how transitions in biomaterial properties and the application of tensile strain co-regulate MSC activity require the coordination of biomaterial science and imaging. Our lab has recently described a lyophilization approach to generate three-dimensional collagen-GAG (CG) scaffolds for tendon-to-bone healing applications. We showed anisotropic scaffolds containing

structural alignment cues can enhance alignment, proliferation and transcriptomic stability of equine tenocytes [160, 216], while also selectively activating mechanotransduction paths and MSC tenogenic differentiation in the absence of growth factors supplementation [144, 217, 218]. We have separately demonstrated a hydroxyapatite mineralized CG scaffold that enhanced MSC differentiation towards an osteogenic lineage, again in the absence of conventional osteogenic supplements [148, 218-220]. We have recently described a method to generate multi-compartment scaffolds that contain discrete scaffold regions connected by a continuous interface [144]. This approach provides orthogonal means to control both the degree of mineralization across the scaffold but also the degree of structural alignment (aligned, non-aligned). This capacity inspires significant questions regarding how cells within a graded scaffold architecture respond to applied strain. Given the graded native osteotendinous insertion, it is critical to establish an approach to examine the coordinated effect of exogenous physical cues such as applied strain and local biomaterial structural cues (pore size, shape) on cell bioactivity.

In this study, we report the collective effect of scaffold structural alignment and applied strain on the alignment and orientation of MSCs within a series of multi-compartment scaffolds inspired by the native tendon-to-bone insertion. The *layered* scaffold variant contained discrete mineralized and non-mineralized compartments, but with an isotropic (non-aligned) pore structure throughout. Comparatively, the *osteotendinous* scaffold also contained discrete mineralized and non-mineralized compartments; however the non-mineralized (tendon) region contained aligned tracks of ellipsoidal pores while the mineralized (bone) compartment contained isotropic pores. Previous work in our lab has shown that aligned, non-aligned, and mineralized scaffold variants all support cell growth and promote long-term (order: weeks)

changes in MSC differentiation [218], but that matrix anisotropy can influence initial cell alignment within the matrix in the absence of mechanical loading [160]. Given the likely need for tensile stimulation of biomaterials for osteotendinous repair applications, here we evaluate changes in MSC nuclear aspect ratio, nuclear orientation and actin alignment in response to applied tensile stain (0 – 20%) as a function of local scaffold microstructural properties, principally microstructural alignment. We seek to establish a relationship between structural features of *layered* vs. *osteotendinous* scaffolds and initial MSC response to applied stain as the basis for future studies profiling MSC bioactivity in response to long-term bioreactor cultures.

5.3: Materials and Methods

5.3.1 Collagen-glycosaminoglycan (CG) suspension preparation

A CG suspension was prepared from type I collagen (1.0% w/v) isolated from bovine Achilles tendon and chondroitin sulfate (0.1% w/v) derived from shark cartilage in 0.05 M acetic acid (Sigma-Aldrich, St. Louis, MO). The suspension was homogenized at 4 °C to prevent collagen gelatinization during mixing and was degassed before use [157].

5.3.2 Mineralized CG suspension preparation

A mineralized collagen suspension was prepared from type I collagen (1.93% w/v) isolated from bovine Achilles tendon and chondroitin sulfate (0.84% w/v) derived from shark cartilage in 0.1456M phosphoric acid / 0.037M calcium hydroxide buffer solution (Sigma-Aldrich, St. Louis, MO). The suspension was homogenized at 4 °C to prevent collagen gelatinization during mixing. Calcium salts (Ca(OH)_2 and $\text{Ca(NO}_3)_3 \cdot 4\text{H}_2\text{O}$) were added during homogenization and the suspension was degassed before use. This suspension has previously been shown to produce 40 wt% mineral scaffolds by a titrant-free concurrent mapping method [45, 198].

5.3.3 Layered scaffold creation

Custom aluminum molds (20 mm x 76 mm) with a removable, flat divider were filled with CG suspension (4.4 mL) in one compartment and mineralized CG suspension (4.4 mL) in the other. The suspension-loaded mold was placed on a freeze-dryer shelf (VirTis, Gardiner, NY) at 20 °C and the divider was removed. The shelf temperature was then ramped down to -40 °C at a rate of 1 °C min⁻¹ and held at -40 °C for 1 hour to ensure complete freezing. Following freezing, the shelf temperature was ramped up to 0 °C at a rate of 1 °C min⁻¹ while pulling a 200 mTorr vacuum to remove ice crystals via sublimation [36, 67].

5.3.4 Osteotendinous scaffold creation

Osteotendinous multi-compartment scaffolds were fabricated via lyophilization from a directional solidification method, which has previously been shown to create anisotropic pores [35]. Briefly, the CG suspension was pipetted into a custom polytetrafluoroethylene (PTFE) mold with a copper bottom (wells: 6 mm diameter, 15 mm deep; copper base plate: 1/16" thick), using the thermal mismatch to establish unidirectional heat transfer through the copper bottom, resulting in directionally-aligned ice crystals, and after sublimation directionally-aligned pores. The CG suspension was first pipetted into the PTFE-copper mold, followed by the mineralized CG suspension at a 2:1 volumetric ratio. Both suspensions were allowed to diffuse for approximately 20 minutes and were then placed onto a pre-cooled freeze-dryer shelf (-40 °C). The suspension was then held at -40 °C for 1 hour to ensure complete solidification, and then sublimated at 200 mTorr [35].

5.3.5 Carbodiimide crosslinking of multi-compartment scaffolds

Prior to use, all scaffolds were hydrated in ethanol followed by phosphate-buffered saline (PBS). They were subsequently crosslinked using carbodiimide chemistry for 1 hour in a solution of 1-ethyl-3-[3-dimethylaminopropyl]carbodiimide hydrochloride (EDC) and N-hydroxysulfosuccinimide (NHS) at a molar ratio of 5:2:1 EDC:NHS:COOH where COOH represents the amount of collagen in the scaffold [59, 221]. After crosslinking, scaffolds were rinsed and stored in PBS until further use.

5.3.6 Quantitative microstructural analysis of multi-compartment scaffolds

Multi-compartment scaffolds (layered and osteotendinous) were cut into pieces no larger than 6 x 10 mm and embedded in glycolmethacrylate. Longitudinal and transverse scaffold sections (5 μ m thick) were serially cut via microtome and stained with aniline blue to allow visualization of the collagen-GAG pore structure as previously described [222]. Serial images were then acquired at 10x magnification on an optical microscope (Leica Microsystems, Germany) and mosaically stitched together using Panoramic Tools graphical user interface (PTgui) software to produce a single high resolution image of each scaffold section. Sections from these images were taken depending on image size to ensure at least 10% of the sample was represented. Grayscale image sections were converted to binary images using Ostu's method, which minimizes intra-class variance and is a built-in function in MATLAB. These binary images were further analyzed using a linear intercept script in MATLAB. The script calculated a best-fit ellipse representation of the average pore in each histology section and gave fitting parameters to determine pore size and aspect ratio, the ratio of the major and minor axes of the best-fit ellipse [36].

5.3.7 SEM analysis of multi-compartment scaffold microstructure

In order to visualize pore elongation within the scaffold variants, longitudinal sections were cut through the scaffolds with a razor blade to expose the interior structure. Scanning electron microscopy (SEM) images of the exposed scaffold face was acquired with a JEOL JSM-6060LV (JEOL, USA) to visualize pore shape within the mineralized, non-mineralized, and interfacial zones of each scaffold variant using a combination of secondary and backscatter electron detection [216].

5.3.8 HMSC culture

hMSCs used in this experiment were provided by the Knight Group (Queen Mary University of London). They were expanded in complete MSC growth medium at 37 °C and 5% CO₂, and were used prior to passage 6 for all experiments. Multi-compartment scaffolds (layered: 4 mm width, 4 mm thickness, 16 mm length; osteotendinous: 6 mm diameter, 15 mm length) were seeded using a previously established seeding method [41]. Briefly, scaffolds were partially dried with Kimwipes and seeded with 6×10^4 MSCs in 60 μ L of complete MSC media on the top and bottom of each construct (3 aliquots of 20 μ L along the length of the scaffold) in six-well plates with 1% agarose gel to prevent cell attachment. Scaffolds were transferred to complete MSC media after a 30 minute attachment period [35, 49].

5.3.9 Tensile strain

hMSC seeded scaffolds were clamped into a custom tensile stimulation rig, previous described by *Screen* and colleagues [223-225]. Clamps were positioned to hold the scaffold securely while maintaining a 10 mm gauge-length between clamps at rest [211]. Samples were loaded while the

clamps were maintained at 10 mm, being careful not to impart strain to the sample while loading. The chamber was filled with complete MSC medium, with spacers (0 mm, 0.4 mm, 0.7 mm) subsequently inserted to generate the desired degree of static strain (0%, 11%, 20%). Strained scaffolds were maintained at 37 °C and 5% CO₂ for 16 hours prior to analysis [211].

5.3.10 Nuclear and actin staining

After tensile stimulation, cell-seeded scaffolds were briefly rinsed in PBS then transferred to formalin (Polysciences) overnight at 4 °C. Scaffolds were subsequently rinsed three times in PBS for 1 minute, and then incubated in 0.1% triton X100 for 15 minutes. Scaffolds were rinsed three times in PBS for 1 minute. To resolve actin morphology, scaffolds were incubated in AlexaFluor® 555-phalloidin (Invitrogen) dye methanolic stock solution (25 µL in 1 mL PBS) for 30 minutes. Scaffolds were rinsed three times in PBS for 1 minute, and then transferred to a Hoechst (Invitrogen) stock (1 µL in 800 µL PBS) for 5 minutes to label nuclei. Scaffolds were rinsed three times in PBS for 1 minute, transferred to fresh PBS, and stored in the dark at 4°C until imaging.

5.3.11 Confocal imaging of cell-seeded scaffolds

Stained, cell-seeded scaffolds were imaged within 48 hours of fixation using a Leica TCS SP2 laser scanning confocal microscope (Leica Microsystems GmbH, Wetzlar, Germany). Images were acquired using a 20X objective with a 40X lens immersed in oil using HeNe laser (excitation: 543 nm, collection: 560-700 nm) and UV (collection: 370-535 nm, filter ND50) to image actin and nuclei, respectively. The orientation of the scaffold was maintained so as to generate a series of images (same imaging plane throughout) from the mineralized and non-

mineralized regions of the scaffold with a known orientation for applied strain and or scaffold microstructural alignment.

5.3.12 Analysis of hMSC nuclear aspect ratio, orientation

Nuclear aspect ratio and alignment were analyzed from each image using Ovuscul in ImageJ, a macro previously shown to measure the orientation and aspect ratio of elliptical shapes [226]. Ovuscul fits an ellipse to each nucleus, which was then parameterized by three xy-coordinates to define an ellipse function. Ovuscul returns these three xy-coordinates (x1, x2, x3, y1, y2, y3) along with the energy (J), the major and minor axes, and orientation (phi) of the ellipse. Nuclear aspect ratio was determined as ellipsoidal major/minor axis ratio, with nuclear orientation described directly by the ellipsoidal orientation (phi). Nuclear orientation was then compared to the known orientation of applied strain and scaffold alignment.

5.3.13 Analysis of hMSC cytoskeletal orientation

Fluorescent images of the actin cytoskeleton were analyzed via a previously described MATLAB code to determine the location of actin fibers within the image, followed by localized analysis of the orientation (dominant angle) of that actin fiber [227]. Actin orientation was then compared to the known orientation of applied strain and scaffold alignment.

5.3.14 Statistics

All numerical ratios were logarithmically transformed before analysis by one-way ANOVA followed by Tukey post-hoc tests. V-tests were performed on orientation data using the Circular Statistics Toolbox in MATLAB [228]. Significance was set at $p < 0.05$ and error is reported as

standard deviation unless otherwise noted. For actin orientation experiments, $n = 3$ scaffolds comprising a total of $n = 12 - 16$ images were analyzed per group. For cell nuclei experiments, $n = 3 - 7$ independent images were analyzed for each group (60 – 400 cells/group).

5.4: Results

5.4.1 Layered and osteotendinous scaffolds both show graded mineral content but only osteotendinous scaffolds display an aligned pore microstructure

Mean pore size and shape were quantified from both the transverse and longitudinal planes of the *osteotendinous* and *layered* scaffolds (**Figure 5.1.A**) using a previously developed stereology approach in MATLAB [36]. Pore size (**Table 5.1**) and aspect ratio (**Figure 5.1.B**) varied as a function of mineralized vs. non-mineralized compartment as well as between *layered* and *osteotendinous* scaffold variants. Layered scaffold showed pore sizes in the range of 160 – 230 μm while osteotendinous variants showed pore sizes in the range of 120 – 180 μm , both significantly larger than individual MSCs. Further, both variants displayed an interfacial zone that lacked evidence of voids or areas of delamination (**Figure 5.1.C**), consistent with previous efforts developing these scaffolds [144]. Critical for this work, the *layered* scaffold variant showed no evidence of pore anisotropy in either scaffold compartment. Further, only the non-mineral compartment of the *osteotendinous* scaffold displayed a significant ($p < 0.05$) degree of pore anisotropy (alignment) (**Figure 5.1.B**). Together, these findings confirmed the successful fabrication of two distinct multi-compartment scaffold variants, one that showed a transition in mineral content (*layered*) and the second that showed a transition from a mineralized, isotropic region to non-mineralized, anisotropic (aligned) region (*osteotendinous*).

5.4.2 Tracking MSC morphology within the scaffold in response to applied strain

Layered and *osteotendinous* scaffolds were seeded with 6×10^4 human mesenchymal stem cells (hMSC; passage 6 or less) using a previously defined static seeding method [41]. After which, cell-seeded scaffolds were transferred to custom-made loading chambers fitted to a Leica TCS SP2 laser scanning confocal microscope [229]. This device allowed cell-seeded scaffolds to be maintained in culture media at 37 °C and 5% CO₂ while simultaneously applying defined tensile strain to the entire scaffold (0, 11, 20% strain) for a period of 16 hours, at which cells were fixed and stained for Hoescht (nucleus) and phalloidin (actin) [211]. Laser scanning confocal microscopy was used to gather longitudinal image planes from within each scaffold at defined positions, allowing us to examine hMSC nuclear morphology (aspect ratio, orientation) and actin orientation/alignment as a function of scaffold type (*layered* vs. *osteotendinous*), position in the scaffold (mineralized vs. non-mineralized zone) and applied tensile strain (0 vs. 11% vs. 20%) (**Figure 5.2**).

5.4.3 hMSC nuclear aspect ratio is heightened and is sensitive to applied tensile strains in scaffolds that contain structural alignment

hMSC nuclear aspect ratio was significantly affected by both the initial scaffold microstructure and applied strain (**Figure 5.3**). Notably, while hMSC nuclei were slightly ellipsoidal for all conditions, there was no significant difference in hMSC nuclear aspect ratio in the *layered* scaffold variants as a function of either compartment (mineralized vs. non-mineralized) or applied strain (0 vs. 11% vs. 20%) (**Figure 5.3.A**). However, hMSCs within the *osteotendinous* scaffold showed significant changes in hMSC nuclear aspect ratio as a function of both compartment and applied strain. In the absence of strain, hMSCs in the (non-aligned)

mineralized compartment showed nuclear aspect ratios similar to those seen in the *layered* scaffold, while hMSCs in the (aligned) non-mineralized compartment showed significantly ($p < 0.05$) higher nuclear aspect ratios, a result consistent with previous reports from our group that anisotropic scaffolds induce cell alignment in the absence of strain [136]. However, as strain increased (11, 20%) a more complex behavior emerged. At 11% and 20% strain, both mineralized and non-mineralized compartments of the *osteotendinous* scaffold display higher nuclear aspect ratios than the *layered* scaffolds ($p < 0.01$). Interestingly, at 20% strain, hMSCs in the mineralized compartment of the *osteotendinous* scaffold displayed the highest nuclear aspect ratio (53.7% greater than cells in the same compartment at 0% strain). While not increasing with applied strain, hMSCs in the aligned, non-mineralized compartment still displayed significantly ($p < 0.01$) greater nuclear aspect ratio than hMSCs in the *layered* scaffolds for all strain levels (**Figure 5.3.A**).

5.4.4 hMSC nuclear alignment is co-regulated by scaffold microstructural alignment and applied tensile strain

Having established changes in the aspect ratio of the nucleus, we next examined whether the alignment of the nuclei was sensitive to the direction of the applied strain or the scaffold microstructure. Here, data are represented as a half Wind-Rose plot with nuclear alignment histograms generated for angles between -90° and $+90^\circ$ (**Figure 5.3.B**). In this representation, 0° corresponds to the direction of applied strain and the direction of the aligned scaffold microstructure in the non-mineralized compartment of the *osteotendinous* scaffold. Interestingly, hMSCs in the *layered* scaffolds predominantly displayed a significant degree of nuclear orientation in the direction perpendicular to that of applied strain ($p < 0.05$) while the only group

which displayed any significant nuclear orientation in the direction of applied strain was in non-mineralized compartment at a physiologically relevant (11%) level of strain ($p < 0.05$). Comparatively, hMSC nuclei in the non-mineralized (aligned) *osteotendinous* scaffold not only had a higher aspect ratio but also displayed a significant ($p < 0.05$) degree of nuclear alignment coincident with the scaffold architecture even in the absence of strain; comparatively nuclei in the mineralized compartment of the *osteotendinous* scaffold showed no organized alignment. As strain increased, increased nuclear alignment in the direction of strain was observed in both compartments of the *osteotendinous* scaffolds (**Figure 5.3.B**). Together with results regarding nuclear aspect ratio, these data suggest that graded microstructural organization within the *osteotendinous* scaffold provides structural cues that preferentially alter hMSC nuclear shape and alignment even in the absence of strain, but that tensile strain and *osteotendinous* scaffold structural organization together contribute to improved hMSC alignment under physiologically-relevant strain conditions.

5.4.5 hMSC cytoskeletal response to tensile strain in multi-compartment scaffolds

Given results regarding changes in nuclear shape and alignment, we next examined the degree of actin alignment for hMSCs in the *layered* versus *osteotendinous* scaffolds using a previously described MATLAB analytical technique [227]. Given the differences in nuclear alignment between *layered* and *osteotendinous* scaffolds in response to strain (**Figure 5.3**), and also the fact that these results were largely unaffected by the level of strain, we compared degree of actin alignment in the mineralized versus non-mineralized compartments of the *layered* (no alignment) versus *osteotendinous* (alignment in the non-mineralized compartment) scaffolds by combining data for all strained conditions (**Figure 5.4**). Consistent with nuclear data, hMSCs in *layered*

scaffolds showed no significant alignment in the direction of strain in either compartment. However, hMSCs in the *osteotendinous* scaffolds showed significant ($p < 0.05$) alignment in the direction of strain in both the non-mineralized and mineralized compartments (**Figure 5.4**). Together this data suggests that while tensile strain can induce changes in cell alignment on a variety of two-dimensional substrates – often in a direction perpendicular to applied strain [230], in fully three-dimensional porous scaffolds applied tensile strain affects cell alignment in a more complex manner that is largely dependent on microstructural features of the underlying scaffold.

5.5: Discussion

A major focus in the field of orthopedic tissue engineering has been development of biomaterial systems that explore the effect of biomolecular cues [116, 231, 232], biophysical cues [110, 233], or mechanical stimulation cues [234-238] on mesenchymal stem cell fate, though often exploring these cues singly. However, in vivo a constellation of cues is presented and assimilated by cells. Although some research has begun to explore how matrix stiffness can sensitize stem cells to biomolecular cues [101, 129, 239, 240], our understanding of how cells incorporate a multitude of signals from different sources is still lacking, but is especially relevant when considering the design of functionally graded biomaterials with the goal of inducing regeneration of complex tissues such as those found in orthopedic interfaces (*e.g.*, osteochondral, osteotendinous).

Here we report the manner in which graded microstructural cues within a scaffold under development for osteotendinous repair applications alters the local response of hMSCs to applied tensile strain. We have previously reported the nature of the graded interface between the mineralized and non-mineralized scaffold regions as being on the order of 100's of microns for

both the layered [69, 145] and osteotendinous scaffold variants [144]. For this work, however, we kept our analyses away from the interfacial region so as to examine bulk cell response within the mineralized and non-mineralized zones. Overall, we find that *osteotendinous* scaffolds, which contain transitions in matrix alignment and mineral content, induced a much stronger degree of cellular alignment than *layered* scaffolds, which contain only a transition in mineral content. hMSC alignment was enhanced in the absence of applied strain in the (aligned) non-mineralized region of the *osteotendinous* scaffold, with increased nuclear aspect ratio, and significant nuclear and actin orientation in the direction of alignment (**Figure 5.3**). Contrastingly, we found hMSCs in the *layered* scaffolds, that did not contain any structural alignment cues, showed a random distribution of nuclear and actin alignment.

Under tensile strain, hMSC nuclear alignment increased but only in the *osteotendinous* scaffolds where anisotropy was initially present. Interestingly, hMSCs in the mineral compartment of the *osteotendinous* scaffold also elicited an increased nuclear aspect ratio, but only after application of strain and even though that scaffold did not present significant degree of pore alignment (**Table 5.2**). Both actin alignment and nuclear orientation were significantly increased in the direction of applied strain in the *osteotendinous* scaffolds (**Figure 5.3, 5.4**). In contrast, hMSCs in the *layered* scaffolds remained randomly oriented under no strain and primarily aligned in a direction perpendicular to that of applied strain, consistent with earlier reports of cell behavior on two-dimensional surfaces where cells attempt to minimize the perceived strain [230, 241].

Together, these results suggest that pore architecture dictates initial cellular response more than applied strain; an intriguing finding that may inform design of biomaterial-bioreactor systems.

These findings also suggests potential differences in cell response to tensile strain in fibrous scaffolds versus in hydrogel constructs, where *Hsieh et al* reported a general increase in alignment in tenocytes in response to static strain [209]. Observed differences in hMSC alignment and response to applied strain found here may be particularly important for osteotendinous regeneration applications. Previous literature has suggested that aligned tissue environments are a key design rule in monolithic (single compartment) biomaterials to enable culture and transcriptomic stability of primary tenocytes [160, 216, 242, 243], and similarly for inducing early pro-tenogenic differentiation events in MSCs [218]. However, recent literature also suggests anisotropic (aligned) biomaterials may be of added benefit for bone regeneration and tissue ingrowth [244-247], making it important to further expand on our finding that hMSCs in the mineralized compartment of the osteotendinous scaffold also exhibited increased alignment with applied strain. Additional characterization of the stress-relaxation characteristics of the mineralized compartment of the osteotendinous scaffold may provide valuable insight into altered cellular alignment profiles observed in these biomaterials in response to tensile strain.

Given the essential nature of mechanotransduction pathway activation in MSC lineage specification events for range of musculoskeletal, and osteotendinous lineages in particular [238, 241, 248, 249], it is essential to improve methods to fully describe relationships between mechanical stimulation, biophysical properties of a three-dimensional biomaterial, and resultant MSC bioactivity. In our study, we examined changes in MSC response to a graded scaffold environment in response to static strain. However, recent work from a range of investigators, including our own lab, have demonstrated the particular advantage of cyclic tensile strain for tendon and ligament tissue engineering [144, 250-253]. New challenges therefore motivate

ongoing and future efforts building on the work described here. First, as we have already shown, anisotropic scaffolds selectively activate ROCK1 mechanotransduction pathways [218]; ongoing efforts are characterizing local changes in MSC response as a function of position within the scaffold at the signal transduction, gene expression, and protein levels in response to strain. Anisotropic pores are already aligned, and thus cells adhered within the scaffold network may experience a greater degree of strain than isotropic variants. MSCs adhered to scaffold struts not aligned in the direction of strain, and thus not truly experiencing a direct increase in strain, may not experience any stimuli which would elicit a cellular response. Second, dynamic analysis of changes in MSC morphology and subsequent lineage specification would offer an exciting capacity to establish changes in MSC fate as a function of local scaffold biophysical properties and cyclic tensile strain. Our evidence here that MSCs are highly responsive to scaffold architecture and applied tensile strain motivate such ongoing efforts in our laboratory. Thirdly, scaffolds containing a graded transition between compartments offer an ability to examine not only bulk cellular response as we report here, but also the opportunity to monitor local response across the interfacial zone, with ongoing efforts concentrating on modifying the width and shape of the interfacial zone as well as on dynamically monitoring cell response within the interfacial zone explicitly.

5.6: Conclusions

In this work, we describe a method to examine changes in the morphology and alignment of hMSCs (nuclear aspect ratio, nuclear orientation, actin alignment) within a three-dimensional collagen biomaterial as a function of both applied strain and local changes in scaffold mineral content and structural alignment. Overall, we found that mesenchymal stem cells within these graded collagen scaffolds respond more strongly to structural alignment cues than applied static

strain, suggesting that local control over scaffold pore architecture may be particularly important in the design of biomaterials for musculoskeletal tissue engineering applications. Our results also suggest that a scaffold variant that includes both a transition in mineral content and structural alignment may be of particular interest for applications in osteotendinous insertion repair.

5.7: Figures and Tables

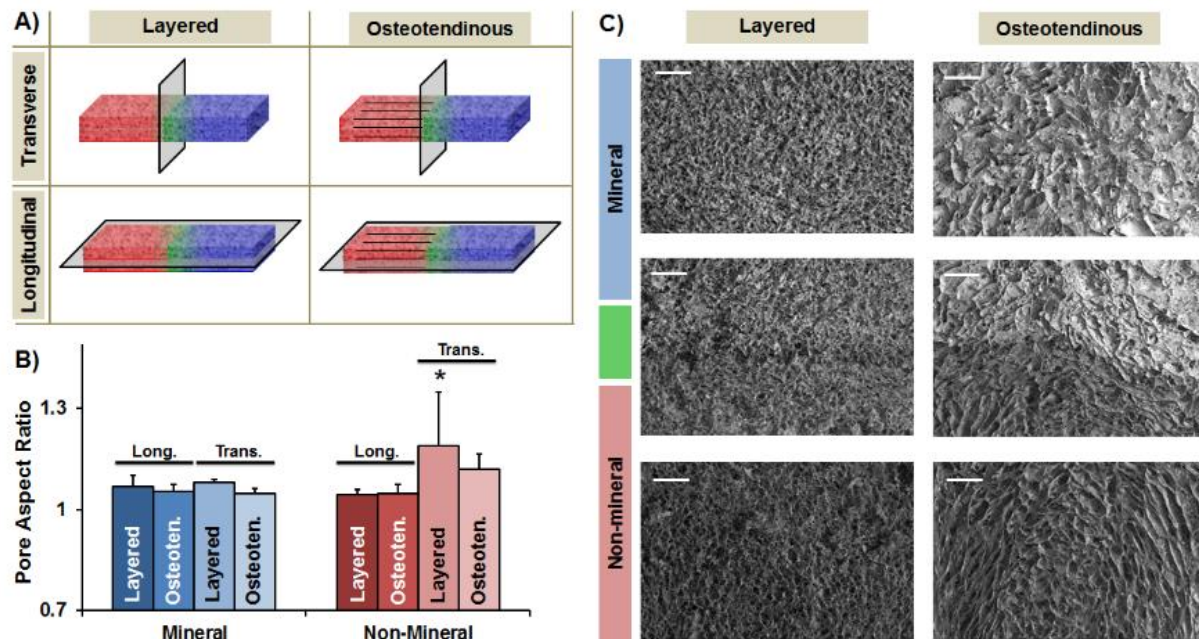
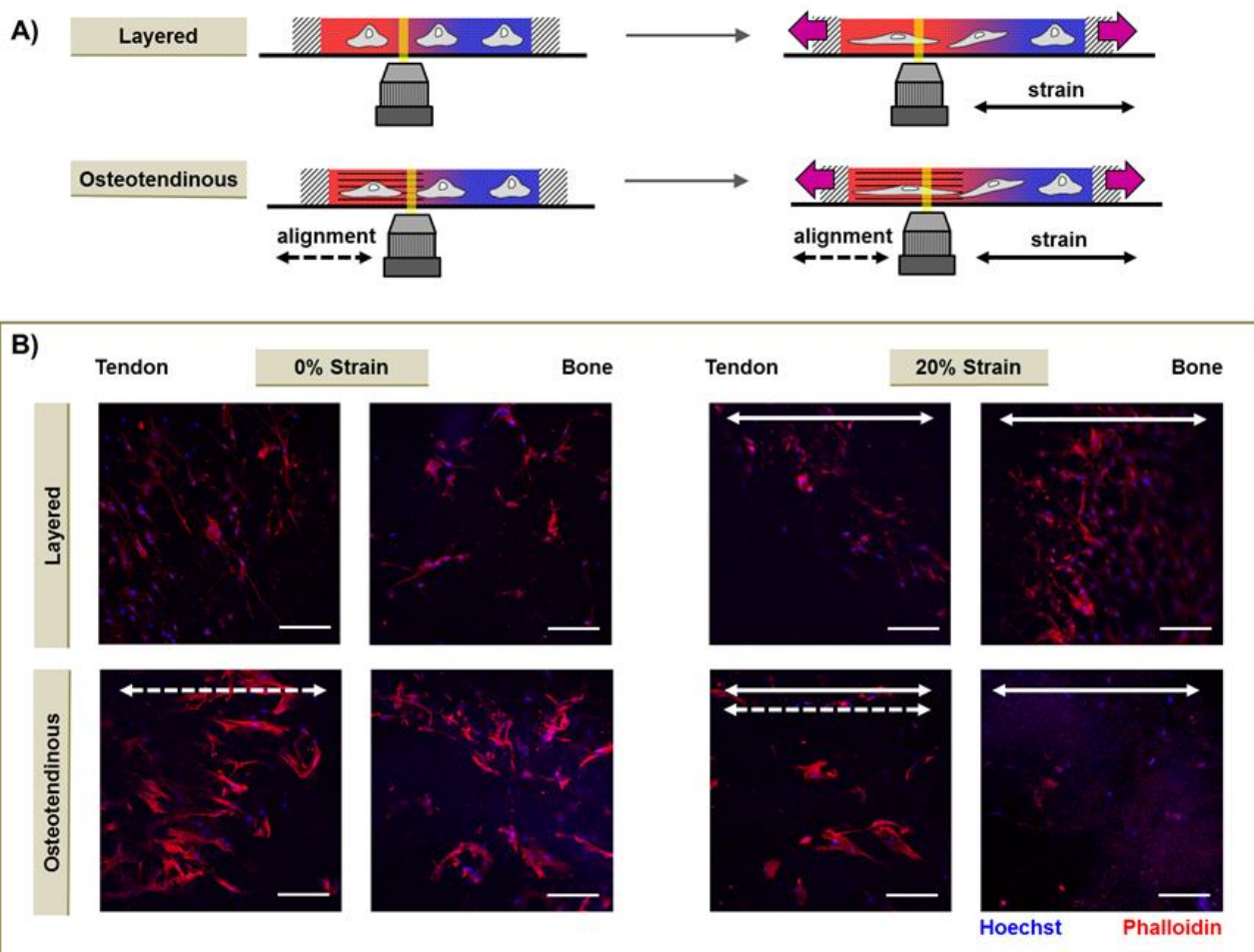
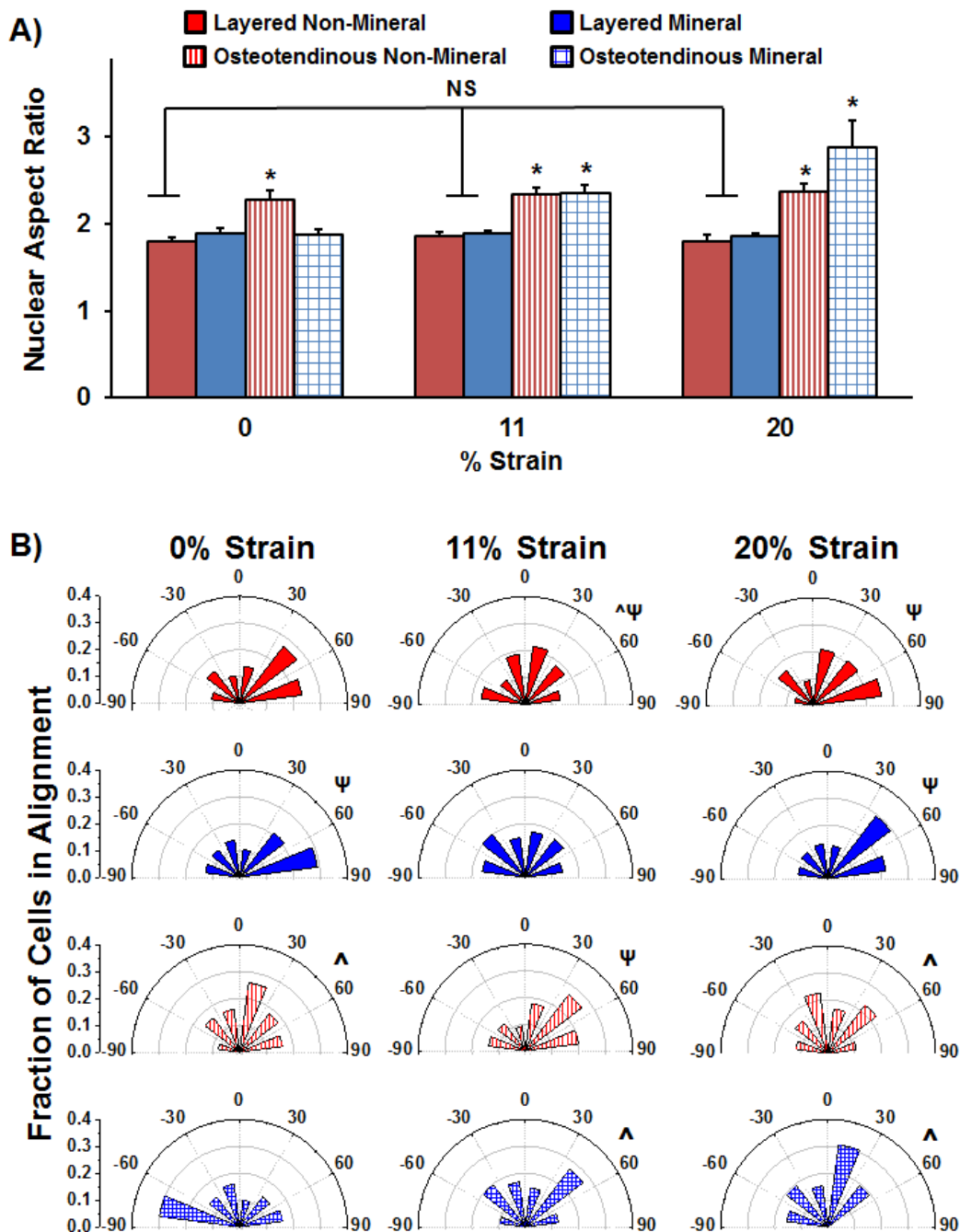


Figure 5.1 Pore architecture of layered and osteotendinous scaffold variants. A) Schematic of histology slices relative to whole scaffolds (left: osteotendinous; right: layered; top: transverse; bottom: longitudinal) *B)* Transverse and longitudinal pore aspect ratio in layered and osteotendinous scaffolds. *: significantly greater than all other values ($p<0.05$) *C)* Scanning electron microscope images of pore architecture at the in discrete mineral (top) and non-mineral (bottom) compartments, in addition to the interface where both compartments meet (middle). Images are displayed for both layered (left) and osteotendinous (right) scaffolds. Cell orientation was not quantified at the insertion between compartments (green). Scale bar: 500 μ m



*Figure 5.2 Schematic of experimental design and representative images acquired from non-mineralized (tendon) and mineralized (bone) regions of the layered vs. osteotendinous scaffold variants under applied strain. **A)** Layered scaffolds (containing a mineralized and non-mineralized regions but no microstructural alignment) and osteotendinous scaffolds (containing mineralized and structurally-aligned non-mineralized regions) were seeded with MSCs then cultured overnight in the presence of discrete levels of applied strain (0%, 11%, 20%). Scaffolds were stained with Hoechst (nuclei) and/or Phalloidin (actin), then viewed on a confocal microscope to quantify cell response (nuclear and cytoskeletal alignment) as a function of local scaffold properties. **B)** Representative images of actin (phalloidin) and nuclear (Hoechst) staining on hMSCs seeded on multi-compartment scaffolds with or without alignment and with increasing strain. Scale bar: 100 μ m.*



*Figure 5.3 Cellular response to scaffold structural variation and increasing strain. A) Overnight strain impacts nuclear aspect ratio in osteotendinous scaffolds, but has no effect in layered scaffold variants. *: significantly greater than layered counter-part ($p < 0.05$) B) Nuclear orientation in (top to bottom) layered and osteotendinous scaffolds with increasing strain. In layered scaffolds, significant nuclear alignment perpendicular to the applied strain was found consistently; in osteotendinous scaffolds, significant nuclear alignment in the direction of applied strain was found consistently. ^: significantly aligned with strain (0 degrees; $p < 0.05$); Ψ: significantly aligned perpendicular to strain (90 degrees; $p < 0.05$)*

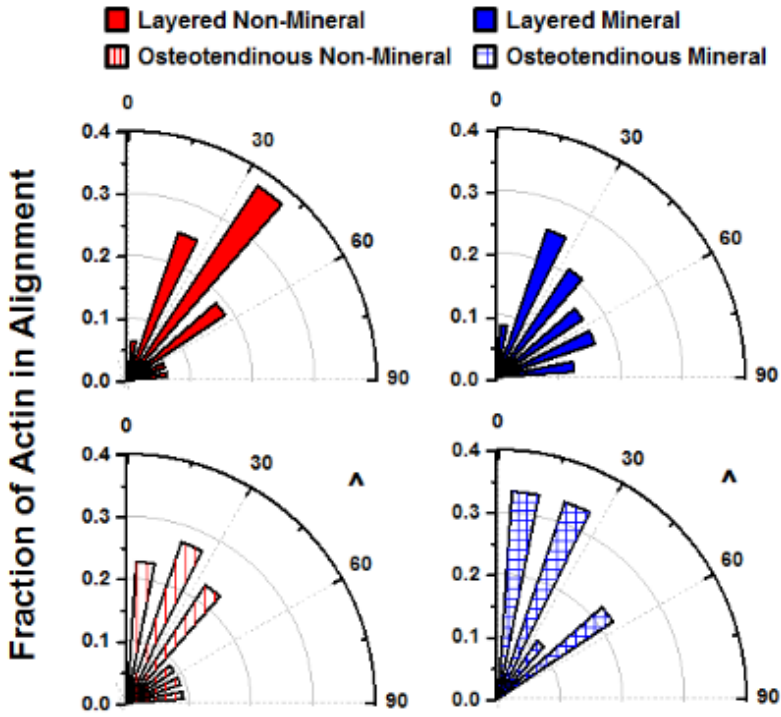


Figure 5.4 Actin alignment in layered and osteotendinous scaffolds after strain. Actin fibers were significantly oriented in the direction of applied strain only in the osteotendinous scaffold variants. ^: significantly aligned with strain (0 degrees; $p < 0.05$)

Table 5.1 Mean scaffold pore size for both layered and osteotendinous scaffolds. Pore sizes are reported as mean \pm standard deviation for both the transverse and longitudinal planes within each scaffold compartment.

Scaffold Variant	Compartment	Transverse Pore Size [μm]	Longitudinal Pore Size [μm]
Layered	Mineral	166 \pm 33.7	256 \pm 64.7
	Non-Mineral	175 \pm 27.6	227 \pm 37.9
Osteotendinous	Mineral	183 \pm 10.6	182 \pm 39.1
	Non-Mineral	125 \pm 18.1	137 \pm 10.9

Table 5.2 Mean scaffold pore aspect ratio within layered and osteotendinous scaffolds. Pore aspect ratios are reported as mean \pm standard deviation for both the transverse and longitudinal planes within each scaffold compartment.

Scaffold Variant	Compartment	Transverse Pore Aspect Ratio	Longitudinal Pore Aspect Ratio
Layered	Mineral	1.05 \pm 0.02	1.07 \pm 0.03
	Non-Mineral	1.05 \pm 0.02	1.04 \pm 0.01
Osteotendinous	Mineral	1.10 \pm 0.03	1.08 \pm 0.02
	Non-Mineral	1.12 \pm 0.04	1.19 \pm 0.16

CHAPTER 6: CONCLUSIONS AND FUTURE WORK

6.1: Conclusions

The tendon bone junction (TBJ) is a primary example of tissue injury and poor native healing in the musculoskeletal system. In TBJ repair, surgical techniques often fail to provide better functional outcomes, which has motivated efforts to create a biomaterial platform which promotes a regenerative response at the injury site. While tissue engineering efforts have often exhibited success when the outcomes have focused on a single tissue, regenerating multiple tissues in parallel has remained a challenge. We proposed a range of important cellular cues (stiffness, composition, pore structure, mechanical stimulation, biomolecular cues; **Chapter 1**), which have been well characterized independently, and proceeded to incorporate these cues in both combinatorial and spatially-selective formats within a single biomaterial (**Chapters 2-5**). The research reported herein has focused on novel methods to develop and characterize heterogeneous biomaterials, with specific focus on overcoming conventional biomaterial design trade-offs and exploring synergies between multiple structural, mechanical, and biomolecular cues. This work further expands the toolbox of multi-tissue biomaterials for the purpose of repair of insertional zones within musculoskeletal tissues, but has implications for the design of biomaterials to address repair of a wider range of multi-tissue structures.

The need to balance biomechanical and bioactivity requirements in the fabrication of biomaterials for multi-tissue regeneration applications requires a new set of design criteria. We explored two bioinspired strategies to create a mechanically robust biomaterial (*polymer fiber reinforcement*, **Chapters 2-3**; *interfacial interdigitation*, **Chapter 4**) while retaining the native bioactivity of a collagen-GAG (CG) scaffold. In **Chapter 2**, we described a composite design

that integrates arrays of ABS fibers with tailorable, but homogeneous mechanical properties generated via 3D printing into a CG scaffold with high bioactivity. We demonstrated that the fiber array significantly enhances the biomaterial mechanical properties, but also provides a pathway to integrate biomolecular cues (growth factors) delivered via the fibers themselves, in a manner orthogonal to the design of the CG scaffold itself. This paradigm describes a novel departure from current methods to address bioactivity-biomechanical trade-offs in biomaterials and offers an approach to locally tune stress-strain behavior of a CG-fiber composite.

In **Chapter 3**, we expanded upon the ideas presented in **Chapter 2**, moving from a homogeneous ABS fiber design to the use of spatially-variable fiber architectures and the use of biocompatible PLA chemistry to create scaffold-fiber composites. This effort explicitly addresses the need to locally alter mechanical performance of a biomaterial implant designed for the interface between mechanically-mismatched tissues such as tendon and bone. This composite design provides the ability to tune both bulk and now local mechanical properties, features vital for the incorporation of mechanically-sensitive cells into the scaffold and to ensure that proper mechanical stimulation conditions are met, but not exceeded. We demonstrated a significant tradeoff between samples containing an increased overall stiffness while simultaneously displaying higher local strain gradients and samples containing a lower overall stiffness but displaying comparatively lower local strain gradients, which elucidates the need for a thorough understanding of the local mechanical effects of incorporating mechanically dissimilar materials into a single construct. We also demonstrated a paradigm under which shifting regions of high strain gradients away from the interface via incorporation of a graded transitional region in fiber reinforcements causes a concentration of high strain gradients in regions of the composite further

removed from the interface. This work clearly illustrates the complexity of key design criteria in local mechanics within dual multi-compartment and composite biomaterials.

In **Chapter 4**, we continue to focus on strategies to dissipate stress concentrations found at the interface between mechanically dissimilar materials, a key challenge in designing multi-compartment biomaterial for orthopedic tissue regeneration. We developed a novel method to create geometric interdigitations at the interface between mechanically dissimilar scaffold compositions. Exploring a homologous series of interdigitation designs, we showed a defined subset of interdigitation designs, particularly interdigitation angles between 14° and 27° , can increase the bulk mechanical behavior of the scaffold under tension. We developed a route to increase the mechanical toughness of the insertional zone, resulting in local strain analysis suggesting a mechanism (dissipation of the regions of high strain gradients and stress concentrations away from the insertion into the scaffold bulk) for this toughening. In contrast to **Chapter 3**, where a gradual transition zone created by fiber reinforcement shifted the location of high strain gradients, interdigitated multi-compartment scaffolds dispersed strain more equally across the whole construct, displaying a fundamentally different local strain pattern. Successfully interdigitated samples regularly displayed bulk mechanical properties consistent with the strongest material from which it was comprised, compared to a traditional flat interface, which regularly displayed bulk mechanical properties consistent with the weakest material from which it was comprised. This work lays the foundation for the use of interdigitation designs as a toughening strategy for multi-compartment scaffolds, particularly as it applies to multi-tissue orthopedic regeneration.

In **Chapter 5**, we shift our focus from local mechanical response and examine cellular response within multi-compartment scaffolds. In this work, we describe a method to examine changes in the morphology and alignment of hMSCs (nuclear aspect ratio, nuclear orientation, actin alignment) within CG biomaterial as a function of both applied strain and local changes in scaffold mineral content and structural alignment. Overall, we found that mesenchymal stem cells within these graded collagen scaffolds respond more strongly to structural alignment cues than applied static strain, suggesting that local control over scaffold pore architecture may be particularly important in the design of biomaterials for musculoskeletal tissue engineering applications. Our results also suggest that a scaffold variant that includes both a transition in mineral content and structural alignment may be of particular interest for applications in osteotendinous insertion repair.

The ultimate goal of this research project was to develop a mechanically strong, spatially distinct (biophysical and biomolecular) CG biomaterials to regenerate the TBJ, with a particular focus on local mechanical and cellular behavior. Our approach is unique in that it recognizes the complexity and heterogeneity of microstructural, mechanical, and biomolecular cues across the native rotator cuff and uses strategies to prune these cues down to a fundamental set of design criteria for multi-tissue biomaterials. While there is a wide field of research being conducted on the mechanical behavior of homogeneous materials, and how single cues influence cellular behavior, we have a unique platform on which we can vary a multitude of heterogeneous signals within a single construct. By leveraging different strategies to combine multiple microenvironmental cues, we have discovered novel mechanical trade-offs and synergies which are influential in directing stem cell fate across a large construct. The design criteria described

within this work are imperative to create robust, heterogeneous constructs for orthopedic tissue regeneration.

6.2: Future Work

The work reported herein describes multiple ways to create and characterize heterogeneous biomaterials and cellular sub-populations for multi-tissue regeneration. Although the work thus far describes a frame-work for combinatorial approaches to incorporate multiple cues into a single biomaterial in a spatially selective manner, future work must focus on combining these approaches to create a single biomaterial with a minimum set of signals to direct stem cell fate appropriately.

6.2.1 Combining multiple mechanically robust strategies

Chapters 2-5 proposed strategies to increase the bulk and local mechanical properties, and local biophysical properties (*pore shape, composition*), of a single biomaterial through the incorporation of a fiber-reinforced paradigm (**Chapters 2-3**), an interdigitating interfacial geometry between two distinct compositions (**Chapter 4**), and the incorporation of anisotropy into one compartment of two distinct compositions (**Chapter 5**). These strategies were extremely successful to increase the bulk mechanical properties of a biomaterial, and developed individual platforms to transmit local biophysical cues to direct stem cell fate.

Important future opportunities exist in the area of developing new methods to combine the fiber and interdigitation designs into a single construct. While fiber reinforcement should be individually compatible with anisotropic pore creation or geometric interfacial interdigitation creation, the two former methods are challenging to incorporate with one another. This is

primarily due to the orientation in which they are formed during lyophilization. Anisotropic pores must be formed in an aligned direction perpendicular to the freeze-dryer shelf, as they are caused by unidirectional heat transfer from the shelf to the bottom of the mold. The osteotendinous scaffolds (incorporating anisotropy into one compartment of a multi-compartment scaffold) discussed within this work are currently created by layering one composition of collagen suspension on top of another, in a direction parallel to the force of gravity (scaffolds are formed in a vertical orientation). Interfacial geometries are created by removing a divider in between two discrete compositions of collagen suspensions, and therefore require the interface to be parallel to both the shelf and to the force of gravity (scaffolds are formed in a horizontal orientation). In either situation, fiber reinforcements may be incorporated independent of the orientation of the shelf or the direction of gravity. In order to truly combine all three of these approaches to create a single biomaterial which can incorporate pore alignment, fiber reinforcement, and interfacial interdigitations, their individual dependence on the orientation of gravity and shelf position must either be decoupled or shifted such that they can all be created in the same orientation. We propose that this may be most easily realized by rotating the orientation of unidirectional heat transfer from the shelf to the bottom of the mold, such that anisotropic pores are created from the side, as opposed to the bottom, of the mold. Thus, all methods are compatible for creation in a horizontal orientation. This will enable the creation of a single biomaterial with both powerful biophysical cues (*pore shape, compositions*) to direct stem cell fate and robust, tunable bulk mechanical properties, which are equally important for the regeneration of a mechanically dynamic and compositionally discrete tissue such as the TBJ.

6.2.2 Characterizing cellular response at the microscale

Although **Chapter 5** characterized cellular response in a compartment-specific manner utilizing an image analysis technique, adapting traditionally bulk techniques to local cellular responses (*gene expression, protein expression*) to a specific biomaterial region is often difficult. While we performed local cellular characterization to link cell morphology to scaffold compartment in **Chapter 5**, future work will develop more robust techniques to characterize a wider variety of local cell behavior and in response to dynamic strain profiles.

Significant future opportunities exist in the area of applying high-content, quantitative imaging strategies to examine local cell response. Technologies such as Laser Scanning Cytometry, which can generate tiled images of large two-dimensional sampled (*e.g.*, fixed, cut, mounted, and stained histology section) provide a first pathway to explore local cellular behavior. This technique is exceptionally powerful for biomaterial applications via its combination of traditional flow cytometry based quantitative analysis of large number of individual cells with the ability to localize specific cellular markers to an anatomical position within the sample. This technique has the ability to image multiple fluorescent and chromatic dyes in unison, and characterize events (positive areas of fluorescent or chromatic stains) in a spatially selective manner [254-256]. As we improve our ability to create biomaterials which present multiple cues in a specified location, we must shift our focus from biomaterial characterization to characterizing cell behavior within the material. This remains a challenge in spatially selective biomaterials for the purpose of orthopedic regeneration, where cells must not simply receive, but respond to distinct signals within their microenvironment, in the appropriate manner and the appropriate location. Such quantitative imaging tools are expected to be a primary area for immediate exploration.

6.2.3 Linking local cellular response to fundamentally different local mechanical profiles

This work has demonstrated our ability to characterize not only the bulk mechanical properties of our multi-compartment materials, but also the local mechanical properties. Current work within our lab has looked at compartment-specific cellular response to cyclic strain within a custom designed bioreactor system [257]. Future work must combine the ability to characterize local strain profiles with the ability to characterize local cellular responses, using a mechanically dynamic culture system such as a bioreactor. The ability to characterize both of these properties in unison allows us to truly characterize cell response at the interface between materials, where local strain gradients were previously unrealized. The characterization of the interfacial zone between tendon and bone is a principle challenge in the field of orthopedic enthesis regeneration, and bulk techniques lack the ability to characterize local mechanical and cellular behavior. However, utilizing local characterization techniques, we have the ability to make major contributions to this field.

6.3: Perspective

Mammalian tissues have developed extremely complex and hierarchal structures over millions of years. Researchers are still discovering new micro-level organization and mechanisms behind the development of highly ordered tissues [4, 258-260]. While the field of tissue engineering is building the ability to start tackling more complicated and complex problems, it is unrealistic to expect scientists and engineers to recreate over a short time scale what took millennia to develop naturally. However, by deriving inspiration from nature, we have the ability to design complex biomaterials from functional principles which have been tried and tested before. The work reported here repeatedly demonstrates that novel designs in biomaterials which incorporate

paradigms from nature (*fiber reinforcement, interdigitation, mineral content, anisotropy*) are surprisingly successful. We should interpret this success as positive reinforcement and continue to recapitulate the paradigms we observe in nature to create more robustly functional biomaterials. As our understanding of these paradigms grows, these naturally inspired designs may prove even more powerful than we currently know.

In the field of orthopedic tissue regeneration, the most successful biomaterials have been homogeneous materials for single tissue regeneration. While promising for a sub-class of tissue defects, the field is moving towards the more complex challenge of incorporating heterogeneities into biomaterials. One of the key challenges is pruning the wide array of “what-is-possible” to “what-is-pragmatic”. While our work has focused on building more and more complex combinations of signals into a single biomaterial, we have made efforts to streamline these efforts into a single, elegant design. We have specifically avoided needless complications, and tend to gravitate towards biophysical and biochemical cues which can be utilized in more than one respect (mineral content: increased stiffness, biomolecular signal; alignment: biophysical cue, alignment cue; interdigitation: dissipating stress concentrations, more even distribution of cyclic strain, wider interfacial zone). We have also delved into the complex characterization of local material and cellular properties, which are often difficult to obtain and interpret. However, these are also the most important characterizations as we move towards the regeneration of multiple, heterogeneous tissues in parallel. While there are still many areas of research to explore, this work has developed a wide tool-box for the development and characterization of heterogeneous biomaterials for orthopedic tissue regeneration.

APPENDIX A: MATERIAL CREATION PROTOCOLS

A.1: CG Suspension Preparation Protocol

Reference: Yannas, Lee et al. 1989; O'Brien, Harley et al. 2004; Caliarì and Harley 2011

Reagents

- Collagen from bovine Achilles tendon (Sigma-Aldrich C9879); store at 4°C
- Chondroitin sulfate sodium salt from shark cartilage (Sigma-Aldrich C4384); store at 4 °C
- Glacial acetic acid (Sigma-Aldrich 71251)
- Ethylene glycol (VWR BDH1125-4LP)
- Deionized water

Equipment and Supplies

- Recirculating chiller (Fisher Isotemp Model 900)
- Rotor-stator (IKA 0593400)
- Disperser S-25N-18G (IKA 0593400)
- Disperser S-25N-25G-ST (IKA 4447500)
- 250 mL Jacketed beaker
- Freeze-dryer (VirTis Genesis)
- Beakers
- Parafilm
- Spatula
- Tweezers

Procedure

*This procedure describes how to make 200 mL (maximum batch size) of 0.5% CG suspension. Scale collagen and glycosaminoglycan (GAG) content appropriately to create different volumes of suspension.

1. Fill recirculating chiller with a 50/50 mix of ethylene glycol and deionized water, making sure that the cooling coils are completely immersed in the liquid. Set the recirculating chiller to 4 °C.
2. Attach recirculating chiller to 250 mL jacketed beaker so that the coolant enters at the jacketed beaker's base and exits at the beaker's top. Allow for the temperature to equilibrate to 4 °C, about 30 minutes. Maintaining this temperature is important, as it will prevent the collagen from denaturing during the blending process.
3. Prepare a 0.05 M solution of acetic acid by adding 0.58 mL of glacial acetic acid to 200 mL of deionized water.
4. Weigh 1.0 g of collagen and add to the jacketed beaker.

5. Pour 170 mL of the 0.05 M acetic acid into the jacketed beaker.
6. Assemble the rotor-stator and S-25N-25G-ST disperser (check diagrams for correct configuration of disperser). The disperser should be hand tight and not over torqued. Attach the disperser to the rotor-stator and verify the disperser is seated correctly by checking the line at the top of the disperser element prior to securing. Lower the rotor-stator into the suspension. The rotor-stator should be vertical and off-center in the beaker.
7. Blend the suspension at 12,000 rpm maximum until blended (approximately 30 min) at 4 °C. The blender should always be started with the rpm at the lowest possible setting and then slowly ramped up. If abnormal noises such as grinding occur the blender should be slowed all the way down and turned off before the dispersing element is taken apart and inspected. The height of the rotor-stator may need to be adjusted via the platform during the blending process: If the rotor-stator is positioned too high, the holes on its side will be visible; if it is too low, the suspension will bubble excessively. Periodically check to see if the rotor-stator is clogged with collagen; remove clogs with a spatula or tweezers as needed. The blender should be operated with constant supervision.
8. Remove the S-25N-25G-ST disperser and replace with S-25N-18G (check diagrams for correct configuration of disperser). The disperser should be hand tight and not over torqued. Attach the disperser to the rotor-stator and verify the disperser is seated correctly by checking the line at the top of the disperser element prior to securing.
9. Add 30 mL of 0.05 M acetic acid to a 50 mL centrifuge tube. Weigh out 0.0887 g of chondroitin sulfate (GAG) and add to the centrifuge tube. Vortex until the GAG is fully dissolved. Let the GAG solution rest in the refrigerator (4 °C) for at least 10 minutes.
10. Add the GAG solution drop-wise to the collagen suspension while it is being mixed at 12,000 rpm maximum at 4 °C. Periodically manually stir in any GAG that remains on the surface of the suspension using a spatula. It may be necessary to stop and unclog the rotor-stator with a spatula during this process.
11. Once all of the GAG solution has been added, blend at 12,000 rpm maximum at 4 °C until blended (approx. 30 min?). Periodically check to ensure the rotor-stator is lowered to the correct depth, as the suspension will gradually become less viscous and creep up the sides of the jacketed beaker. Adjust platform height as needed. Periodically check to see if the rotor-stator is clogged; remove clogs with a spatula or tweezers as needed.
12. Store the suspension for at least 18-22 hours at 4 °C.
13. Degas the suspension to remove any air bubbles prior to use. It is recommended to degas approximately 20 mL at a time, until the solution starts to boil. To minimize suspension loss during the degassing process, cover the beaker with slit Parafilm.
14. Store the suspension at 4 °C. Periodically check the CG suspension; if not homogenous, re-blend at 12,000 rpm for at least 30 min at 4 °C.

A.2: CGCaP Suspension Preparation

Reference: Harley, Lynn et al. 2010; Lynn, Best et al. 2010; Process Record No. PR OM-004 Preparation of Mineralized Slurry, BioUetikon and OrthoMimetics, Process Record No. PR OM-001 Preparation of 0.1456M Phosphoric Acid/0.037M Calcium Hydroxide, BioUetikon and OrthoMimetics.

Reagents

- Collagen from bovine Achilles tendon (Sigma-Aldrich C9879); store at 4 °C
- Chondroitin sulfate sodium salt from shark cartilage (Sigma-Aldrich C4384); store at 4 °C
- 0.1456M phosphoric acid / 0.037M calcium hydroxide buffer solution
 - 5.904 mL 85% phosphoric acid (Sigma-Aldrich P5811)
 - 570 mL deionized water
 - 1.644 g calcium hydroxide (Sigma-Aldrich 31219)
 - Add acid to water, then calcium hydroxide. Bring volume to 600 mL and adjust pH to 2.0-2.4. Solution is good for 3 months.
- Calcium hydroxide (Sigma-Aldrich, 31219)
- Calcium Nitrate Tetrahydrate (Sigma-Aldrich, 31218)
- Ethylene glycol (VWR BDH1125-4LP)
- Deionized water

Supplies and equipment

- Recirculating chiller (Fisher Isotemp Model 900)
- Rotor-stator (IKA 0593400)
- Disperser S-25N-18G (IKA 0593400)
- Disperser S-25N-25G-ST (IKA 4447500)
- 250 mL Jacketed beaker
- Freeze-dryer (VirTis Genesis)
- pH meter
- Beakers
- Transfer pipets
- Centrifuge tubes
- Parafilm
- Spatula
- Tweezers

Procedure

*This procedure describes how to make 200 mL of 40 wt% CGCaP suspension. Scale collagen and GAG content appropriately to create different volumes of suspension.

1. Setup the jacketed vessel, setting the water temperature to 4 °C.
2. Add 3.8644 g collagen to the jacketed vessel. Then add 161.41 mL of phosphate acid / calcium hydroxide buffer to the collagen. Assemble the rotor-stator and S-25N-25G-ST disperser (check diagrams for correct configuration of disperser). The disperser should be hand tight and not over torqued. Attach the disperser to the rotor-stator and verify the disperser is seated correctly by checking the line at the top of the disperser element prior to securing. Lower the rotor-stator into the suspension. The rotor-stator should be vertical and off-center in the beaker.
3. Blend the suspension at 12,000 rpm maximum until blended (approximately 30 min) at 4 °C. The blender should always be started with the rpm at the lowest possible setting and then slowly ramped up. If abnormal noises such as grinding occur the blender should be slowed all the way down and turned off before the dispersing element is taken apart and inspected. The height of the rotor-stator may need to be adjusted via the platform during the blending process: If the rotor-stator is positioned too high, the holes on its side will be visible; if it is too low, the suspension will bubble excessively. Periodically check to see if the rotor-stator is clogged with collagen; remove clogs with a spatula or tweezers as needed. The blender should be operated with constant supervision.
4. Allow the collagen to hydrate for 18-22 hours in the cooled jacketed vessel at 4 °C. This mixture will become very viscous and difficult to blend. Remove the S-25N-25G-ST disperser
5. Measure out 1.677 g of chondroitin sulfate and add it to 28.63 mL of phosphate acid / calcium hydroxide buffer in a beaker. Then mix the buffer and the chondroitin (GAG solution), using a magnetic stirring bar, until fully dissolved.
6. Measure out 1.28 g calcium hydroxide and 0.78 g calcium nitrate tetrahydrate and place both in a 50 mL centrifuge tube. Add 10 mL of deionized water to the tube using a pipette. Then mix (vortex/shake) the solution to suspend the salts in the water.
7. Set-up the rotator stator and the S-25N-18G disperser (check diagrams for correct configuration of disperser). The disperser should be hand tight and not over torqued. Attach the disperser to the rotor-stator and verify the disperser is seated correctly by checking the line at the top of the disperser element prior to securing.
8. Set the blender to 12,000 rpm and blend the hydrated collagen made in step 3 until fully blended.
9. Add the GAG solution prepared in step 5 to the hydrated collagen solution prepared in step 3 drop wise while mixing at 12,000 rpm, stirring with a spatula often to prevent any clumping of the collagen/GAG. With the additional volume, the slurry will mix better.
10. Blend this GAG / hydrated collagen solution at 12,000 rpm until fully blended (approximately 30 minutes).
11. Blend the collagen / GAG mixture at 200-800 rpm while adding the salts to maximize dispersion. Using a pipette, add the salt solution at a rate of 5mL/min to the collagen / GAG mixture, allowing time for blending after each volume. Then blend the slurry at 12,000 rpm until fully blended.
12. Store the slurry for 18-22 hours at 2-8 °C before use. Periodically check the CG suspension; if not homogenous, re-blend at 12,000 rpm until well blended (approximately 30 minutes) at 4 °C.

A.3: Layered and Interdigitated Scaffold Preparation

Reference: Martin, Caliri, et al. 2011; Gonnerman, McGregor, et al. 2012; O'Brien, Harley et al. 2004; Mozdzen et al. *In Preparation*.

Reagents

- CG and CGCaP suspension; store at 4 °C (**Appendices A.1, A.2**)
- Welch DirecTorr Gold synthetic pump oil (Fisher 01-184-105)

Supplies and equipment

- Freeze-dryer (VirTis Genesis)
- Aluminum tray molds
- Aluminum or 3D printed ABS mold dividers
- Beakers
- Parafilm
- Aluminum foil

Procedure

*This procedure describes the fabrication of 3 mm tall scaffold sheets. Check that oil is clean (clear, not yellowed) before and after each freeze-dryer run, replacing when necessary. It is easiest to replace the oil just after a run, when the oil is still warm.

1. Degas the CG an/or CGCaP suspension in a beaker (covered in Parafilm with small slits) by pulling vacuum inside freeze-dryer. Degas just to the boiling point to remove all air bubbles. Make sure the condenser is at least -50 °C or cooler before degassing.
2. For homogenous scaffolds, add 24.25 mL of CG or CGCaP suspension to a 3" x 3" tray mold (or 2.7 mL/in² for other mold sizes), ensuring that the suspension reaches the corners. Push any bubbles or unblended collagen to the edge using tweezers.
3. For layered or interdigitated scaffolds, place aluminum or ABS divider in the center of the mold. Pipette half the total suspension (CG) into one half of the mold and pipette the other half of the total suspension (CGCaP) into the other half of the mold. Dividers can be made in any desired geometry using a 3D printer (Appendix A.5).
4. Open freeze- dryer door, place mold on center of shelf. Remove the divider for layered or interdigitated scaffolds quickly and steadily in the vertical direction, and close the freeze-dryer door.
5. Run the program 'Tf-xx No Hold' where xx is the desired freezing temperature (-10, -40, or -60 °C). A typical schedule is shown below for the constant cooling fabrication method with a final freezing temperature of -10 °C.

Step	Temperature °C	Time, min	Ramp/Hold	Vacuum level, torr	PCM
Freezing hold	20	5	H	~600	N/A
Freezing ramp	-10	30	R	~600	N/A
Freezing hold	-10	120	H	~600	N/A
Drying ramp	0	10	R	0.2	150
Drying hold	0	5	H	0.2	1
Extra drying	0	60	H	0.2	0
Storage ramp	20	20	R	0.2	0
Storage hold	20	indefinite	H	0.2	0

PCM refers to the minimum reading difference between the Pirani and capacitance manometer pressure gauges that must be achieved before the program proceeds to the next step. In Pirani gauges, a filament in the gauge is heated so that it is at a constant temperature at a given pressure. As the pressure increases or decreases, the amount of gas molecule collisions with the filament will change accordingly. More collisions remove more heat from the filament, which lowers the temperature and changes the resistance of the filament. This change in resistance is converted to an output pressure. Pirani gauges are accurate to within around 7-8%. Capacitance manometers operate on the principle of a diaphragm held at a very low reference pressure (10⁻⁷ mbar) that is deflected by changing pressure. This deflection changes the capacitance between the diaphragm and an electrode. This change is converted to pressure. These gauges are extremely accurate (1%). These gauges will read different pressures because they operate on very different principles. The capacitance manometer is more accurate because it reads pressure independent of the type of gas present. In contrast, the temperature of the filament in the Pirani gauge is affected by the thermal conductivity of the colliding gas molecules. For example, the thermal conductivity of water vapor is higher than that of air, so for an equal number of water vapor and air molecules colliding with the filament the water vapor will remove more heat, causing the Pirani gauge to read a higher pressure than the true pressure. Once all of the water vapor is removed the differential between the two gauges should read about the same, indicating that the scaffolds are dry.

6. Once the program has reached the storage hold stage, the program can be cancelled and the array can be removed from the freeze-dryer.
7. Gently remove scaffold by lifting from corner with tweezers. Place scaffold in puffed aluminum pouch. Label pouch with name, collagen type, collagen concentration, freeze date, freeze temperature, and any other relevant notes. Clean mold by rubbing with soapy water; use 0.05 M acetic acid to remove collagen residue. Do not use cleaning brushes.

A.4: Osteotendinous Scaffold Preparation

Reference: Caliari and Harley 2011; Caliari, Ramirez et al. 2011

Reagents

- CG and CGCaP suspension; store at 4 °C (**Appendices A.1, A.2**)
- Welch DirecTorr Gold synthetic pump oil (Fisher 01-184-105)

Supplies and equipment

- Freeze-dryer (VirTis Genesis)
- PTFE-copper freeze-drying mold
- Beakers
- Parafilm
- Aluminum foil

Procedure

*This procedure describes the fabrication of 15 mm tall aligned multi-compartment scaffolds. Check that oil is clean (not yellow) before and after each freeze-dryer run, replacing when necessary.

1. Degas CG and CGCaP suspension in Parafilm-covered beaker by pulling vacuum inside freeze-dryer to remove all air bubbles. Make sure the condenser is at least -50 °C or cooler before degassing.
2. Begin to cool freeze-dryer shelves by running 'Tf = xx C shelf cool' program, where xx is the desired freezing temperature (-10, -40, or -60 °C).
3. If making scaffold-membrane composites, cut membranes to size, roll, and place in PTFE-copper freeze-drying mold holes.
4. Pipette a total of 540 µL (6 mm diameter holes) of suspension into each hole in PTFE-copper freeze-drying mold. Carefully pipet the first suspension (e.g. CG suspension, 360 µL) into mold wells. Then, add the second suspension (e.g. CGCaP suspension, 180 µL) carefully on top of the first suspension, taking care not to mix the two layers. Following pipetting, place entire mold on Kimwipe and allow to interdiffuse for 15-30 min at 4 °C.
5. Cancel shelf cool program and place freeze-dryer mold on the pre-cooled shelf. Shut the freeze-dryer door and run program 'Aligned Tf = xx' where xx is the desired freezing temperature (-10, -40, or -60 °C). A typical freeze-drying schedule is shown for the fabrication of an aligned -60°C scaffold:

Step	Temperature °C	Time, min	Ramp/Hold	Vacuum level, torr	PCM
Freezing hold	-60	60	H	~600	N/A
Drying ramp	0	60	R	0.2	150
Drying hold	0	5	H	0.2	1
Extra drying	0	60	H	0.2	0
Storage ramp	20	20	R	0.2	0
Storage hold	20	indefinite	H	0.2	0

PCM refers to the minimum reading difference between the Pirani and capacitance manometer pressure gauges that must be achieved before the program proceeds to the next step. In Pirani gauges, a filament in the gauge is heated so that it is at a constant temperature at a given pressure. As the pressure increases or decreases, the amount of gas molecule collisions with the filament will change accordingly. More collisions remove more heat from the filament, which lowers the temperature and changes the resistance of the filament. This change in resistance is converted to an output pressure. Pirani gauges are accurate to within around 7-8%. Capacitance manometers operate on the principle of a diaphragm held at a very low reference pressure (10⁻⁷ mbar) that is deflected by changing pressure. This deflection changes the capacitance between the diaphragm and an electrode. This change is converted to pressure. These gauges are extremely accurate (1%). These gauges will read different pressures because they operate on very different principles. The capacitance manometer is more accurate because it reads pressure independent of the type of gas present. In contrast, the temperature of the filament in the Pirani gauge is affected by the thermal conductivity of the colliding gas molecules. For example, the thermal conductivity of water vapor is higher than that of air, so for an equal number of water vapor and air molecules colliding with the filament the water vapor will remove more heat, causing the Pirani gauge to read a higher pressure than the true pressure. Once all of the water vapor is removed the differential between the two gauges should read about the same, indicating that the scaffolds are dry.

6. Once the program has reached the storage hold stage, the program can be cancelled and scaffolds can be removed from the freeze-dryer.
7. Allow scaffolds to sit in mold at room temperature for at least 1 hour before carefully removing them with forceps and placing in an aluminum foil pouch. Label pouch with name, collagen type, collagen concentration, freeze date, freeze temperature, and any other relevant notes.

A.5: Fabrication of ABS/PLA Constructs via 3D Printing

Reference: Mozdzen et al. 2016

Reagents

- D-Limonene (GreenTerpene, Miami, FL)
- Acetone
- ABS filament (1.75mm / 1.8 mm) (Makerbot Industries, Brooklyn, NY)
- MakerBot dissolvable filament/polystyrene filament (1.75mm / 1.8 mm) (Makerbot Industries, Brooklyn, NY)
- PLA filament (1.75mm / 1.8 mm) (Makerbot Industries, Brooklyn, NY)

Supplies and equipment

- MakerBot Replicator 2X (Makerbot Industries, Brooklyn, NY)
- SD card
- Beakers
- Flasks
- 50 mL centrifuge tubes
- Forceps
- Spatula
- Pipettes (transfer or graduated)
- Razor blades

Software

- AutoDesk or Google Sketchup
- Makerware

Procedure

1. Initial construct designs were created using AutoDesk and exported as a .STL file.
2. AutoDesk .STL files were imported into Makerware and manipulated to the desired size and position onto the build plate.
3. Makerware files were then exported to the Makerbot SD card (using a card reader if necessary) using the desired resolution (100-300 μm ; recommendation: 200 μm), infill (10%-100%; recommendation: 10%), and shell (recommendation: 2) options. If printing a design with sharp overhangs or extrusions, the option of printing with supports should be selected.
4. Additionally, extruder speed, extruder temperature, and build plate temperature are customizable within the software. The extruder speed, extruder temperature, and build plate temperature should be adjusted depending on the polymer which is being printed.
 - a. Dual ABS/Dissolvable print
 - i. extruder speed: 90 mm/s
 - ii. extruder temperature ABS 230 °C; Dissolvable 250 °C

- iii. Build plate temperature: 110 °C
 - b. Dual PLA/Dissolvable print
 - i. extruder speed: 25 mm/s
 - ii. extruder temperature ABS 210 °C; Dissolvable 250 °C
 - iii. Build plate temperature: 55°C
 - iv. Chamber doors should be raised to increase the cooling rate
- 5. The options presented within steps 3-4 are completely customizable within the software.
- 6. The SD card with the exported file should be inserted into the Makerbot SD slot. Alternatively, the exported file can be read directly from the computer if it is attached to the Makerbot through a USB cable.
- 7. Before printing, a slurry consisting of a small amount of ABS dissolved in acetone is typically spread across the glass build plate to provide more adhesion to the build plate if necessary, and is recommended.
- 8. After 3D printing, any dissolvable filament supports were subsequently dissolved in D-Limonene until only the ABS or PLA remains (typically 3-8 hours)
- 9. The constructs were washed multiple times with deionized water, and then dried before use.

*Notes: Typically, resolution was limited to approximately 600 µm, and x-y resolution is typically better than z resolution. For troubleshooting or maintenance, MakerBot Industries has an extensive support website and forums associated with the equipment. However, some trouble shooting procedures can be found below.

Printing Troubleshooting

- If using a glass or otherwise smooth build plate, mixing a small amount of acetone and ABS into a milk like solution and applying in a thin layer to build plate minimizes warping and dragging of build or raft components. Pipette solution on to build plate and thin with the side of the pipette tip. It may be useful to store a small amount of this solution in a bottle. Discarded objects, failed prints and removed rafts (ABS) are a good source of the plastic component of the solution.
- For clogged extruders, let cool, clean extruder tip with small amount of acetone and kimwipe, feed and unfeed filament in clogged extruder multiple times as per the MakerBot manual instructions.
- Re-level as build plate as needed.
- Store filament in sealed packages until immediately before use to prevent size changes due to humidity
- Adjust printing speed in the advanced tabs when preparing to export files. Slower movement speed generally results in less jerky motion and better fidelity. The default setting is usually adequate but for finer detail a speed of 50mm/s may be more appropriate.

A.6: Fabrication of ABS/PLA-Scaffold Composite Scaffolds via Lyophilization

Reference: Mozdzen et al. 2016; O'Brien et al. 2004; Harley et al. 2007

Reagents

- 3D printed ABS or PLA fibers (**Appendix A.5**)
- CG suspension; store at 4 °C
- Welch DirecTorr Gold synthetic pump oil (Fisher 01-184-105)

Supplies and equipment

- Freeze-dryer (VirTis Genesis)
- Aluminum tray molds
- Beakers
- Parafilm
- Aluminum foil

Procedure

*This procedure describes the fabrication of 7.6" x 2" scaffold composites. Check that oil is clean (clear, not yellowed) before and after each freeze-dryer run, replacing when necessary. It is easiest to replace the oil just after a run, when the oil is still warm.

1. Degas the CG suspension in a beaker (covered in Parafilm with small slits) by pulling vacuum inside freeze-dryer. Degas just to the boiling point to remove all air bubbles. Make sure the condenser is at least -50 °C or cooler before degassing.
2. Add 3D printed ABS or PLA fibers to the mold in which it was designed. Fibers should typically be a few mm smaller than the mold to ensure easy removal after freeze drying.
3. Add 8.8 mL of CG suspension to a 7.6" x 2" tray mold (or a scaled volume to a different size mold), ensuring that the suspension reaches the corners. Push any bubbles or unblended collagen to the edge using tweezers.
4. Open freeze- dryer door, place mold on center of shelf maintained initially at 20 °C. Close the freeze-dryer door and run the program 'Tf-xx No Hold' where xx is the desired freezing temperature (typically -40, with additional options at -10 or -60 °C). A typical lyophilization cycle can be seen in Appendix A.3. Briefly, the shelf temperature is ramped down to the desired freezing temperature (i.e. -40 °C) at a rate of 1 °C/min, followed by a 1 hour hold at that temperature (-40 °C) to ensure complete solidification. Following freezing, the shelf temperature was ramped up to 0 °C at a rate of 1 °C/min, after which a 200 mTorr vacuum was maintained overnight to remove ice crystals via sublimation, leaving behind the porous CG scaffold impregnated with ABS or PLA fibers.
5. Once the program has reached the storage hold stage, the program can be cancelled and the array can be removed from the freeze-dryer.
6. Gently remove scaffold by lifting from corner with tweezers. Place scaffold in puffed aluminum pouch. Label pouch with name, collagen type, collagen concentration, freeze

date, freeze temperature, and any other relevant notes. Clean mold by rubbing with soapy water; use 0.05 M acetic acid to remove collagen residue. Do not use cleaning brushes.

APPENDIX B: MATERIAL PROCESSING AND FUNCTIONALIZATION

PROTOCOLS

B.1: EDC Cross-linking Protocol

Reference: Olde Damink, Dijkstra et al. 1996; Harley, Leung et al. 2007; Caliarì, Ramirez et al. 2011

Reagents

- 1-ethyl-3-[3-dimethylaminopropyl]carbodiimide hydrochloride (EDC, Sigma-Aldrich E7750); store at -20 °C
- N-hydroxysulfosuccinimide (NHS, Sigma-Aldrich H7377); store in desiccator
- Sterile phosphate-buffered saline (PBS)
- Sterile water
- 100% ethanol

Supplies and equipment

- 6-well plates (Fisher 08-772-1B)
- 50 mL centrifuge tubes (Fisher 14-432-22)
- Syringe and syringe filter (Fisher 148232A)
- MTS 2/4 digital microtiter shaker (IKA 3208001)
- Dual range balance (Mettler Toledo XS105)
- Razor blades
- Biopsy punch (Fisher 12-460-413)
- Scaffolds (**Appendices A.3, A.4**)

Procedure

* Note: all steps should be performed in the laminar flow hood unless otherwise noted.

1. Cut scaffold samples to be cross-linked to desired sample size using a razor blade or biopsy punch.
2. Transfer scaffold pieces to sterile centrifuge tube, remove from laminar flow hood, and weigh pieces on dual range balance.
3. Hydrate scaffolds in 100% ethanol overnight.
4. Rinse scaffolds several times in PBS and then let soak in PBS for 24 hours before cross-linking.
5. Determine the EDC and NHS concentrations to be used in cross-linking solution. The sample calculations in this protocol are done with a 5:2:1 EDC:NHS:COOH molar ratio where COOH is carboxylic acid groups in CG material based on a conversion factor of 1.2 mmol COOH per gram of collagen (Olde Damink, Dijkstra et al. 1996). The mass of EDC and NHS required can be calculated as follows:

$$M_{EDC} = M_{Scaffold} \left(0.0012 \frac{mol_{COOH}}{g_{collagen}} \right) \left(\frac{5mol_{EDAC}}{1mol_{COOH}} \right) \left(\frac{191.7g_{EDAC}}{1mol_{EDAC}} \right) \quad \text{(Equation A.1)}$$

$$M_{NHS} = M_{Scaffold} \left(0.0012 \frac{mol_{COOH}}{g_{collagen}} \right) \left(\frac{2mol_{NHS}}{1mol_{COOH}} \right) \left(\frac{191.7g_{NHS}}{1mol_{NHS}} \right) \quad \text{(Equation A.2)}$$

6. Mix the EDC and NHS in sterile water. Approximately 1 mL of solution will be needed per scaffold (6-8 mm diameter, 3-5 mm thick)
7. In the laminar flow hood, sterile filter the solution and add to 6-well plates such that each scaffold is exposed to an equal amount of the EDC solution.
8. Add scaffolds in cross-linking solution and place well plate on digital microtiter shaker in incubator at 37 °C. Allow scaffolds to cross-link under moderate shaking for 30-120 min. Cross-linking time should be increased for less permeable constructs such as membranes and high solids content scaffolds.
9. Remove EDC/NHS solution and rinse scaffolds in sterile PBS under moderate shaking for 10-15 min.
10. Remove first PBS wash solution and rinse scaffolds in fresh PBS under moderate shaking for an additional 30-45 min. Store in fresh sterile PBS until use.

B.2: Functionalization of ABS Constructs with Biomolecules

Reference: Mozdzen et al. 2016; Ma et al. 2005

Reagents

- Biomolecule of interest (i.e. BSA, PDGF)
- 3D printed ABS construct (**Appendix A.5**)
- 1-ethyl-3-[3-dimethylaminopropyl] carbodiimide hydrochloride (EDC)
- N-hydroxysulfosuccinimide (NHS)
- Phosphate Buffered Saline (PBS)

Supplies and equipment

- Plasma cleaner (PDC-32G, Harrick Plasma, Ithaca, NY)
- Plate shaker
- Fluorescence spectrophotometer (infinite M200 Pro, Tecan, Switzerland)
- Fluorescent microscope (Leica DMI 4000B)
- HCImage camera

Procedure

* This protocol can be adapted to functionalize PLA fibers by skipping the oxygen plasma treatment

1. If immobilizing a biomolecule of interest to ABS, place the ABS construct into the oxygen plasma cleaner (no gas flow, high RF, <0.3 torr, 5 min per side) in order to expose carboxylic acid groups on the ABS surface.
2. Place either PLA constructs or plasma-cleaned ABS constructs into the presence of the biomolecule of interest (i.e. BSA-Alexafluor-594 conjugate at 100 µg/mL; PDGF at 1 µg/mL) in the presence of a solution of 1-ethyl-3-[3-dimethylaminopropyl] carbodiimide hydrochloride (EDC) (5 mg/mL) and N-hydroxysulfosuccinimide (NHS) (5 mg/mL) for 1 hour while gently shaking to catalyze the formation of covalent crosslinks between the PLA or the plasma cleaned ABS and the biomolecule of interest.
3. If quantifying the degree of fluorescently labeled biomolecular attachment, create a standard using serial dilutions, starting with the maximum concentration of the fluorescent biomolecule intended to be used for functionalization.
4. Collect the supernatant after biomolecular functionalization for each of 4 experimental groups to quantify against the standard:
 - a. Negative control (no fluorescent biomolecule, no plasma cleaning, and no carbodiimide crosslinker)
 - b. Fluorescent biomolecule added with carbodiimide crosslinker but without plasma cleaning
 - c. Fluorescent biomolecule added after plasma cleaning but without the carbodiimide crosslinker

- d. Fluorescent biomolecule added with carbodiimide crosslinker after plasma cleaning.
5. The amount of unattached fluorescent biomolecule remaining in the supernatant was quantified against a known standard via a fluorescence spectrophotometer (infinite M200 Pro, Tecan, Switzerland), and the amount immobilized to the fiber was taken as the amount unobserved in the supernatant.
6. To qualitatively observe the amount of fluorescent functionalization onto the ABS or PLA construct, image the construct with a fluorescent microscope using a camera with a constant exposure time (i.e. 0.1 s) against controls.

B.3: Sectioning Collagen-Based Scaffolds via Cryostat

Reference: Leica_CM3050_S Manual

(http://www.igb.illinois.edu/sites/default/files/upload/core/PDF/Leica_CM3050_S_Manual_EN.pdf)

Reagents:

- Formalin
- PBS
- Tissue-Tek O.C.T. Compound

Supplies and equipment:

- Leica CM3050S
- Samples to be sectioned
- Superfrost™ Plus Gold Adhesion Slides (Cat # 10143351)
- Scaffolds (**Appendices A.3, A.4**)

Procedure

1. Fix samples in formalin for at least 1 hour.
2. After fixing, serially wash samples in PBS to ensure freezing in subsequent steps.
3. Turn the cryostat on if it is not already. Typical chamber settings are -30 to -40 °C. Wait until it has reached the temperature set point to continue. While waiting, change out the microtome razor blade to ensure even, sharp cutting.
4. Embed samples in the plastic sample holders provided next to the cryostat using Tissue-Tek OCT mounting media, ensuring the sample is aligned properly.
5. Place the sample within the cryostat until it is mostly frozen.
6. Place a small amount of Tissue-Tek OCT mounting compound on the sample block holder, and use this to mount your sample to the sample block holder, ensuring alignment of the sample with respect to the sample holder.
7. Load the sample holder onto the microtome and set the appropriate sample temperature (Typically between -18 and -25 °C). Wait a few minutes for freezing to complete before cutting.
8. Set the microtome cutting step-size.
9. Slowly use the coarse and fine controls to align the sample with the razor blade mounted to the microtome. When the sample has approached and begins to cut, continue cutting until the full width of the sample is cutting evenly.
10. After a desirable sample section is produced, pick it up using the functionalized side of the adhesion slides, label, and set aside.
11. After the desired samples are obtained, let the sample holder and sample block holder partially thaw until the remaining mounting media can be disposed of. Clean the inside of the microtome area of frozen mounting media shavings
12. Store slides in a slide at -20 °C until further use.

B.4: Scaffold Glycolmethacrylate Embedding Protocol

Reference: O'Brien, Harley et al. 2004; O'Brien, Harley et al. 2005; Caliarì and Harley 2011

Reagents

- JB-4 embedding solution A (100 mL); store at 4 °C for up to 1 week
 - 100 mL JB-4 embedding solution A (monomer) (Polysciences 0226A-800)
 - 1.25 g JB-4 catalyst (benzoyl peroxide, plasticized) (Polysciences 02618-12);
- JB-4 embedding solution B (accelerator) (Polysciences 0226B-30)
- 100% ethanol

Supplies and equipment

- Polyethylene molding cup trays (Polysciences 16643A-1)
- JB-4 plastic block holders (Polysciences 15899-50)
- DryFast vacuum pump (Welch Vacuum 2014B-01)
- Pyrex desiccator (Fisher 08-626B)
- Serological pipettes (Fisher 13-678-14B)
- 6-well plates (08-772-1B)
- Chemical fume hood (Lab Fabricators Company)
- Razor blades
- Scaffolds (**Appendices A.3, A.4**)

Procedure

1. Cut scaffold pieces to be analyzed using a razor blade, no longer than 5 mm in each direction Both transverse and longitudinal sections should be cut for analysis.
2. Place samples in 6-well plates and hydrate in 100% ethanol under vacuum inside desiccator for 24 hours.
3. Add hydrated samples to JB-4 embedding solution A (see reagent list for instructions to make solution A) under vacuum inside desiccator at 4 °C. After 24 hours, replace with fresh JB-4 embedding solution A and hold under vacuum inside desiccator at 4 °C for an additional 48 hours.
4. Mix 25 mL of JB-4 embedding solution A with 1 mL of JB-4 B solution and pipette ~3.5 mL into each well of the plastic embedding mold.
5. Place each sample into a well. The JB-4 mixture will polymerize quickly (~30 min) so make sure the samples stay in the proper orientation.
6. Place one labeled plastic stub in each well once the JB-4 mixture has become sufficiently viscous that the stubs don't completely sink.
7. Keep embedding mold at 4 °C overnight to allow polymerization to complete. Store samples at 4 °C until use.

APPENDIX C: MATERIAL VISUALIZATION, CHARACTERIZATION, AND ANALYSIS PROTOCOLS

C.1: Scanning Electron Microscope Imaging

Reference: Caliari et al, 2011

Supplies and equipment

- Sample (collagen scaffold variant)
- Freeze dryer (VirTis Genesis, Gardiner, NY)
- Scanning electron microscope (JEOL JSM-6060LV, JEOL USA)
- Razor blade
- Black carbon tape
- Tweezers
- Scaffolds or scaffold composites (**Appendices A.3, A.4, A.6**)

Procedure

1. In order to visualize the scaffold without considering edge effects, cut transverse or longitudinal sections (depending on area of interest) through the scaffold to expose the interior structure.
2. Secure sample with black carbon tape, with the area of interest facing upwards and load the sample into the vacuum chamber of the SEM.
3. After SEM calibration, set the chamber to low vacuum (10 Pa)
4. Take SEM images of the sample at desired magnification (20X to 200X). A combination of secondary and backscatter electron detection were found to produce the best images with minimal charging, typically at 20kV, 10 Pa, and spot size of 40-50.
5. If necessary, repeat these steps, using tweezers to peel off carbon tape between samples.

C.2: Scaffold Pore Size Analysis: Aniline Blue Staining, Image Acquisition, and Linear

Intercept Analysis Protocol

Reference: O'Brien, Harley et al. 2004; O'Brien, Harley et al. 2005; Caliari and Harley 2011; Weisgerber 2015

Reagents

- Aniline blue solution (100 mL)
 - 2.5 g aniline blue (Fisher AC40118-0250)
 - 2 mL glacial acetic acid (Sigma-Aldrich 71251)
 - 100 mL deionized water
 - Mix well, filter before use
- 1% Acetic acid (100 mL)
 - 1 mL glacial acetic acid (Sigma-Aldrich 71251)
 - 99 mL deionized water
- Permunt mounting medium (Fisher SP15-100)
- 95%, 100% ethanol

Supplies and equipment

- Optical microscope with camera (Leica Microsystems DMIL LED with DFC295 camera)
- Panoramic Tools graphic user interface (PTgui)
- MATLAB
- Beakers
- Cover slips

Aniline blue staining procedure

1. Obtain slides of serially sectioned embedded scaffolds (5 μm thick) from histologist or cut from independently on a microtome (both longitudinal and transverse if desired).
2. Dip slides in aniline blue solution for 2-4 min. Analyze in groups of 12-18 slides.
3. Place slides in 1% acetic acid for 1 min.
4. Dip each slide several times in 95% ethanol until most of background staining goes away.
5. Dip each slide several times in 100% ethanol to complete rinse and allow slides to dry.
6. Mount each sample with 1 drop of Permunt per slide section. Firmly press cover slip onto slide so as not to introduce any air bubbles. Allow slides to dry for 24 hours before further analysis.

Image acquisition procedure

1. Visualize embedded, sectioned, and stained scaffold samples using optical microscope.
2. If spatial resolution across a large area is required, acquire serial images at low magnification (i.e. 10x) an optical microscope and mosaically stitch images together using Panoramic Tools graphical user interface (PTgui) software to produce a single high

resolution image of each scaffold section. If using a mosaically stitched image, ensure that at least 10% of the sample was represented for further calculations.

3. If spatial resolution is not required, acquire three images for each transverse section and two images for each smaller longitudinal section can be directly acquired using the camera.

Linear intercept analysis procedure

1. Transfer images for analysis to a single folder, open MATLAB, and set this folder as the working directory.
2. Grayscale images were converted to binary images using Ostu's method, which minimizes intra-class variance and is a built-in function in MATLAB.
3. The binary images were further analyzed using a linear intercept script in MATLAB. The script calculated a best-fit ellipse representation of the average pore in each histology section and gave fitting parameters to determine pore size and aspect ratio, the ratio of the major and minor axes of the best-fit ellipse.
4. After the linear intercept script in MATLAB is run, the calculated data will be exported to an excel spreadsheet. The MATLAB script calculates the average distance between struts to a best-fit ellipse and calculates linear intercept coefficients C0, C1, and C2 for the ellipse, as well as the minor (*a*) and major (*b*) axes of best-fit ellipse using the following equations:

$$a = \frac{1}{\sqrt{C_0 + \sqrt{C_1^2 + C_2^2}}} \quad \text{(Equation C.1)}$$

$$b = \frac{\sqrt{\frac{C_1^2 + C_2^2}{C_0 + \sqrt{C_1^2 + C_2^2}}}}{\sqrt{C_0 + \sqrt{C_1^2 + C_2^2} - C_1^2}} \quad \text{(Equation C.2)}$$

$$\text{Aspect Ratio} = \frac{b}{a} \quad \text{(Equation C.3)}$$

5. The mean pore size (*d*) is also calculated from values of the major and minor axes of the best-fit ellipse. To account for the fact that pores were not sectioned through their maximal cross-section the mean pore size is corrected by a factor of 1.5. To convert the pore radius to diameter the mean pore size is additionally multiplied by 2 for a total correction factor of 3:

$$d = 3 \sqrt{\frac{a^2 + b^2}{2}} \quad \text{(Equation C.4)}$$

6. The following script may be used in MATLAB to perform the above calculations.

Linear Intercept Script (MATLAB)

```
close all
clear
```

```

clc
list_input=dir;
list_output=cell(1, 1);
list_output(1) = [];
for i = 3: length(list_input)
    input_string = getfield(list_input(i), 'name');
    if ~isempty(input_string)
        if sum(input_string(length(input_string) - 3:length(input_string)) == '.tif') == 4
            list_output{length(list_output) + 1} = input_string;
        end
    end
end
end
for ii=1:length(list_output);
    filename=list_output{ii};
    image=imread(filename);
    SETleft=0;
    SETwidth=1;
    SETtop=0;
    SETheight=1;
    AspectRatio=1;

    %scale = 347 for 4X mag and scale = 867 for 10X
    scale=867;
    width=round(size(image,2)*SETwidth);
    top=round(size(image,1)*SETtop);
    height=round(size(image,1)*SETheight);
    left=round(size(image,2)*SETleft);
    MLxSTART=left+1;
    MLxEND=left+width;
    MLySTART=top+1;
    MLyEND=top+height;
    image=image(MLySTART:MLyEND,MLxSTART:MLxEND);

    %Using MATLABs built in thresholding function
    level=graythresh(image);
    binary=im2bw(image,level);

    clear image
    if width<height
        MinDim=width;
    else
        MinDim=height;
    end
    ThetaStep=pi/36;
    rUser1=0*ones(36,1);
    rUser2=rUser1;

```

```

for j=0:1:35
    LineSum=0;
    Intercepts=0;
    x1=left;
    y1=top;
    Theta=j*ThetaStep;
    nx=10*sin(Theta)*width/height;
    ny=10*abs(cos(Theta));
    for i=0:1:nx
        if Theta==0
            x1=left;
            x2=x1+width;
        else
            x1=left+(width*i/(nx+1))+width/(2*(nx+1));
            x2=x1+(height*cos(Theta)/sin(Theta));
        end
        y2=top+height;
        if x2>=left+width
            x2=left+width;
            y2=y1+(x2-x1)*sin(Theta)/cos(Theta);
        elseif x2<left
            x2=left;
            if Theta>pi/2
                y2=y1+(x2-x1)*sin(Theta)/cos(Theta);
            end
        end
        plength=sqrt((x2-x1)^2+((y2-y1)/AspectRatio)^2);
        valx=x1;
        valy=y1;
        dx=(x2-x1)/plength;
        dy=(y2-y1)/plength;
        switchh=true;
        if plength>=MinDim
            LineSum=LineSum+(plength/scale);
            for k=0:1:plength
                if round(y1+k*dy+1)<=size(binary,1) && round(x1+k*dx+1)<=size(binary,2)
                    if binary(round(y1+k*dy+1),round(x1+k*dx+1))>0
                        indicator=true;
                    else
                        indicator=false;
                    end
                end
            end
            if switchh==true && indicator==true
                Intercepts=Intercepts+1;
                switchh=false;
            end
        end
    end
end

```

```

        if indicator==false
            switchh=true;
        end
    end
end
end
for i=1:1:ny
    if Theta<=pi/2
        x1=left;
        x2=left+width;
    else
        x1=left+width;
        x2=left;
    end
    y1=top+height*i/(ny+1);
    y2=y1+(width*sin(Theta)/abs(cos(Theta)));
    if y2>top+height
        y2=top+height;
        x2=x1+((y2-y1)*cos(Theta)/sin(Theta));
    end
    plength=sqrt((x2-x1)^2+((y2-y1)/AspectRatio)^2);
    valx=x1;
    valy=y1;
    dx=(x2-x1)/plength;
    dy=(y2-y1)/plength;
    switchh=true;
    if plength>=MinDim
        LineSum=LineSum+(plength/scale);
        for k=0:1:plength
            if round(y1+k*dy+1)<=size(binary,1) && round(x1+k*dx+1)<=size(binary,2)
                if binary(round(y1+k*dy+1),round(x1+k*dx+1))>0
                    indicator=true;
                else
                    indicator=false;
                end
            end
        end
        if switchh==true && indicator==true
            Intercepts=Intercepts+1;
            switchh=false;
        end
        if indicator==false
            switchh=true;
        end
    end
end
end
end
end

```

```

    IntLength=LineSum/Intercepts;
    rUser1(j+1)=180*Theta/pi;
    rUser2(j+1)=IntLength*1000;
end
maxdim=0;
for i=1:1:36
    if rUser2(i)>maxdim
        maxdim=rUser2(i);
    end
end
width1=400;
height1=400;
pscale=0.8*(width1+height1)/(2*maxdim);
for i=1:1:36
    dx1=pscale*0.5*rUser2(i)*cos(rUser1(i)*pi/180);
    dy1=pscale*0.5*rUser2(i)*sin(rUser1(i)*pi/180);
    if i<36
        dx2=pscale*0.5*rUser2(i+1)*cos(rUser1(i+1)*pi/180);
        dy2=pscale*0.5*rUser2(i+1)*sin(rUser1(i+1)*pi/180);
    else
        dx2=-pscale*0.5*rUser2(1)*cos(rUser1(1)*pi/180);
        dy2=-pscale*0.5*rUser2(1)*sin(rUser1(1)*pi/180);
    end
end
end
n=36;
sumX=0;
sumY=0;
sumZ=0;
sumXY=0;
sumYZ=0;
sumXZ=0;
sumZsqr=0;
sumXsqr=0;
for i=1:1:n
    Y=1/((rUser2(i)/2)^2);
    X=cos(2*pi*rUser1(i)/180);
    Z=sin(2*pi*rUser1(i)/180);
    sumX=sumX+X;
    sumY=sumY+Y;
    sumZ=sumZ+Z;
    sumXY=sumXY+X*Y;
    sumYZ=sumYZ+Y*Z;
    sumXZ=sumXZ+X*Z;
    sumZsqr=sumZsqr+Z^2;
    sumXsqr=sumXsqr+X^2;
end

```

```

C1=((sumXY*sumZsqr)-(sumXZ*sumYZ))/((sumXsqr*sumZsqr)-sumXZ^2);
C2=((sumYZ*sumXsqr)-(sumXY*sumXZ))/((sumXsqr*sumZsqr)-sumXZ^2);
C0=(sumY/n)-C1*(sumX/n)-C2*(sumZ/n);
a=1/sqrt(C0+sqrt(C1^2+C2^2));
b=sqrt(sqrt(C1^2+C2^2)/(C0*sqrt(C1^2+C2^2)+C2^2-C1^2));
d=1.5*2*sqrt((a^2+b^2)/2);
results(ii+1,:)= { filename,level,C1,C2,C0,a,b,b/a,d };
end
results(1,:)= { 'filename','level','C1','C2','C0','a','b','pore aspect ratio','diameter' };
time=clock;
xlswrite(['PoreSizeAnalysis_' int2str(time(1)) '_' int2str(time(2)) '_' int2str(time(3)) '_'
int2str(time(4)) '_' int2str(time(5))],results);

```

C.3: Bulk Mechanical Characterization

Reference: Mozdzen, et al 2016

Reagents:

- PBS
- ABS

Supplies and equipment

- House air line
- Instron 5943 Mechanical Testing System
- 100 N electromechanical load frame
- 5 N electromechanical load frame
- pneumatic grips (tension)
- compression platen (compression)
- 3D printed ABS end-blocks (*optional*, **Appendix A.5**)
- Tweezers
- Caliper
- Bluehill software
- Instron biobath

Procedure

*Note: this procedure describes uniaxial tension testing. In order to test in compression, use the compression platen in place of the pneumatic grips, do not embed samples in end-blocks, and set mechanical safeties such that the plates do not crash into each other.

1. Create samples such that the anticipated gauge length is twice as long as the width of the sample which will undergo mechanical testing. This typically requires the sample to contain extra length, which are used to grip the sample.
2. If desired, endblocks were 3D printed to prevent the grips during mechanical testing from unduly crushing, and damaging, the sample. The end-blocks are meant to hold PDMS, which will infiltrate into the porous sample to undergo mechanical testing and provide a sturdy region for the pneumatic grips to clamp while keeping the ends of the sample undamaged. PDMS was prepared in a 3:1 (monomer: catalyst) ratio, poured into the 3D printed end-blocks, and allowed to cure at room temperature for 60 minutes before scaffolds were placed within the end-blocks. If necessary, additional PDMS was added to the end-blocks to prevent pull-out during mechanical testing.
3. Install the correct load cell (100N or 5N), being especially careful not to jar the load cell, as this can damage the sensitive load cells (especially 5N).
4. Install the pneumatic grips, ensuring both grips are aligned with one another for uniaxial tensile strain. (If performing compression, install the compression platen).
5. For mechanical testing of hydrated samples, set up the bio bath and fill with the correct level of PBS such that during testing, the sample will be completely submerged.

6. The Instron 5943 Mechanical Testing System frame was turned on, and a period of 2 minutes was allowed to pass before calling the Bluehill software.
7. Calibrate the load cell if desired (recommended when there is significant drift in the load reading)
8. Using the hand-held interface, slowly move the pneumatic grips (or platen) to the desired gauge length, checking this length with the calipers for accuracy. After this length is set, zero the extension on the Bluehill software.
9. Set the mechanical safeties such that the top grip cannot crash into the top of the load frame (alternatively, that the platen cannot crash into each other).
10. Load the mechanical testing protocol from the Bluehill software (or create a new protocol if necessary. See software tutorial if needed). *Note: if raw data is desired, ensure that the export raw data box is checked within the protocol, otherwise raw data will not be saved.
11. Load sample evenly between the grips, ensuring the sample is centered in both the vertical and horizontal directions, and is completely vertical.
12. Once sample is lined up, manually tighten the grips until the sample is held in place as desired. Finally, press the foot pedal which controls the pneumatic grips twice (first pedal actuation closes the top grip, second pedal actuation closes the bottom grip). *Note: if pneumatic grips release on their own, check the air line and make sure the air is hooked up to the pneumatic grips, the house air is on, and the actuator connected to the house air is open.
13. Begin mechanical test. Ensure the load is balanced (typically, a standard protocol balances the load before each test) Typical test settings for tensile straining are a 1 mm/min strain rate until a 40% drop in load which indicates failure.
14. After the test, remove the sample before allowing the cross-head to return to avoid the load cell crashing into a potentially stiff sample.
15. Repeat steps 9-12 until all samples are tested.
16. End the test in Bluehill and save data as necessary.
17. To calculate bulk mechanical properties, stress strain curves must be generated. Stress is calculated as the load divided by the cross-sectional area of the sample prior to testing. Strain is calculated as the extension divided by the gauge length, and is typically reported as either a fraction or a percent.
 - a. Elastic modulus is calculated as the slope of the linear elastic region of the stress-strain curve.
 - b. Failure load (also known as peak stress) was taken as the peak load (or stress) the sample experienced before failure.
 - c. Failure mode should be recorded (if desired) with an image.

C.4: Local Mechanical Characterization via Digital Image Correlation

Reference: Elizabeth Jones 2015 <http://www.mathworks.com/matlabcentral/fileexchange/12413>; Mozdzen et al *In Preparation*

Reagents

- India Ink (Blick Art Materials, Galesburg, Illinois)
- Heterogeneous sample (i.e. multi-compartment scaffold **Appendices A.3, A.4**; composite scaffold **Appendix A.6**)
- 3D printed ABS end-blocks (*optional*, **Appendix A.5**)
- PDMS (Hisco-Schaumburg Incorporated, Schaumburg, Illinois) (*optional*)

Supplies and equipment

- MATLAB
- MATLAB Toolboxes (Image Processing Toolbox, Parallel Computing Toolbox, Statistics and Machine Learning Toolbox)
- Airbrush (nozzle: 0.3 mm; gravity feed, hooked to house air)
- Mechanical tester (Instron 4200 series)
- Camera with camera lens (Cannon EOS 5D with Cannon 100 mm Macro Lens EF)
- Tine Lapse Remote (Canon TC-80N3 Timer/Remote Controller)
- Tripod
- LED light source

Sample Preparation Procedure

1. If desired, endblocks were 3D printed to prevent the grips during mechanical testing from unduly crushing, and damaging, the sample, using the Fabrication of ABS/PLA Constructs via 3D Printing Protocol.
2. If desired, samples were embedded into 3D printed end-blocks using PDMS. PDMS was prepared in a 3:1 (monomer: catalyst) ratio, poured into the 3D printed end-blocks (10 mm height x 20 mm width x 30 mm length), and allowed to cure at room temperature for 60 minutes before scaffolds were placed within the end-blocks.
3. Samples were then speckle patterned using an airbrush filled with waterproof india ink attached to house air. Best speckle patterns were found when the house air was minimally open, and the airbrush was held approximately 6 inches away from the sample being sprayed.
4. Airbrush was rinsed, taken apart if necessary. If a clog occurred, india ink is dissolvable in ethylene glycol.

Sample Straining and Image Capture Procedure

1. Camera was setup on the tripod, with the sample centered in the field of view. Be careful to avoid the sample reaching the edge of the camera's field of view, as these areas are more prone to visual distortion.

2. To ensure consistency between pictures, the camera was set to Av mode, which uses auto-focus but allows the user to set aperture, ISO, flash, and other settings.
3. Take a sample picture to ensure setting quality before mechanical test. Once settings are confirmed, take one more image to set the focus for the first image.
4. The time lapse remote was plugged into the camera and set to a specific time. Typically, longest and shortest test samples are run to measure the length of time a typical mechanical test takes. The time lapse can take a maximum of 99 images continuously, so set the timer to allow the mechanical test to be set in this time frame (typically at a rate of 1 picture every 1 or 2 seconds).
5. Samples were strained according to the Bulk Mechanical Straining Protocol (Appendix C.3), where the mechanical test and the time lapse remote were started simultaneously. This simultaneous start does not need to be exact, only approximate, as the bulk mechanical analysis and the image analysis are independent.

Digital Image Correlation Procedure using MATLAB

Configuration (This step needs to be set up only once)

1. Place the DIC Matlab files in one folder, and add the folder to the Matlab search path, directly below the default folder. This needs to be done only once, when you first install the code.
 - a. In Matlab 2012b, go to the “Home tab”. In the “Environment” box, click on “Set Path”. Click on “Add Folder...”, and navigate to the folder containing the DIC Matlab files. Move this folder directly below the default folder (usually “...\Documents\MATLAB”).
 - b. In earlier versions of Matlab, “Set Path” is under “File”.
2. Change the Image Processing Toolbox preferences to display axes on images when using “imshow.”
 - a. In Matlab 2012b and 2014b, type “iptprefs” in the command window. Check the box for “IMSHOW Display - Axes visible.”
 - b. Alternatively, type `iptsetpref('ImshowAxesVisible','on')` in the Command Window. You only need to do this once. The preference will be remembered.
3. If the images to be correlated are too large to be displayed at 100 % magnification on the computer screen, the warning “Warning: Image is too big to fit on screen; displaying at 67%.” may be displayed. This warning does not affect the correlation results. To turn off the warning, type `warning('off','images:initSize:adjustingMag')` in the Command Window of Matlab. Matlab should remember the setting for the future.
4. Check to see if the message catalog “menu.xml” exists in the following location (or equivalent location): C:\Program Files\MATLAB\R2012b\resources\MATLAB\en\uistringnmenu.xml. If the folder “uistring” does not exist, create a folder called “uistring” within the “en” folder. Then place the “menu.xml” file, included in the DIC files in this FileExchange, into the “uistring” folder. If the folder “uistring” exists and contains the “menu.xml”_le, then you do not need to do anything.
5. Some Mac users may encounter an error, similar to the one found below, when running the code in parallel mode:
`>> matlabpool open`

Error using matlabpool (line 134)
Java exception occurred:
java.lang.NullPointerException
at java.util.logging.Logger.demandLogger(Logger.java:286)
at java.util.logging.Logger.getLogger(Logger.java:321)

Image Preparation

1. Set up the images to be correlated.
 - a. Place all images to be processed in one folder.
 - b. Set the working directory in Matlab to the folder containing the images (double click on the folder on the left-hand side of the MATLAB interface).
 - c. Run image setup GUI to prepare the images (type 'image_setup_GUI' and press enter)
 - d. Select the appropriate file extension (*i.e.* *.jpg*), and set 'image skip' to 1 in order to correlate all images within the folder.
 - e. Press 'setup images', and allow conversion to grayscale if prompted.
2. Determine if displacements are large enough to require an initial guess.
 - a. Run correlate images GUI (type 'correlate_images_GUI' and press enter). Run images in parallel, correlate full image, do not use reduced data, and define a full new grid. Sample settings (subset size of 21 pixels; a threshold of 0.2-0.5, and a search zone to 2 to 3).
 - b. MATLAB will then run the matlabpool.
 - c. When prompted, select the first image of the series (reference image) to open. Click the top left corner and the bottom right corner to define the region of interest. Choose a step size of 50-75 for images about 1000x1000 pixels (or 100 for 4000x6000 pixels), considered a sparse grid, which reduces computation time.
 - d. Run visualize data GUI (type 'visualize_data_GUI' and press enter). Visualize the full data and select 'filled contour plot' to view data. In order to visualize all data, keep 'image skip' set to 1.
 - e. If the entire region of interest correlated well (there are no large areas of missing data where there are large displacements), then displacements are small enough that no initial guess is required, and the reduced-size images do not need to be correlated. Proceed to step 4.
 - f. If the images did not correlate well in regions where displacements are large, then you need to generate initial guesses for the displacements by correlating reduced-size images. Proceed to step 3.
3. If necessary, generate initial guesses for displacements by correlating reduced-size images.
 - a. Run correlate images GUI, and correlate reduced-size images only. Use approximately 100-200 grid points. (For 4000 x 6000 pixel images, a reduction size of 7-11, threshold between 0.2 and 0.5, and search zone between 3 and 4 were found to work well for most images) Multiple iterations may be necessary if images do not correlate well with reductions of 7-11 Run visualize data GUI and evaluate the results.
 - b. If the correlation of the reduced images did not capture the large displacements, adjust one or more of three parameters until satisfactory results are obtained:

- i. Change the subset size.
 - ii. Change the image reduction factor.
- c. Iterate the correlation of the reduced images, using the results from the previous correlation of reduced images as initial guesses for the current correlation of reduced images. (iterations 6-11, until images correlate well at the edges)
4. Determine the optimal subset size for the correlation of the full-sized images. (*Optional*)
 - a. Run correlate images GUI (type 'correlate_images_GUI' and press enter) and correlate full-sized images only, using results from the correlation of the reduced-size images as initial guesses as necessary, and using a sparse grid (step size of about 100 pixels for images about 4000x6000 pixels).
 - b. Run visualize data GUI (type 'visualize_data_GUI' and press enter) and evaluate the results.
 - c. If there are very few points that did not correlate, then run correlate images GUI again, using a smaller subset size.
 - d. Repeat this process until the subset size is too small to provide a good correlation. Note the smallest subset size that provided a good correlation, and use this in the final correlation.

Image Correlation

1. Run final correlation.
 - a. Run correlate images GUI (type 'correlate_images_GUI' and press enter).
 - b. Correlate full-size images only.
 - c. Use results from the correlation of reduced-size images if necessary.
 - d. Use the optimal subset size found in the previous step.
 - e. Create a new, dense grid (step size of approximately 5-10 pixels for images about 1000x1000 pixels or 23-27 pixels for 4000x6000 pixel images).
2. Delete regions of poorly-correlated data. (*Optional*)
 - a. Run visualize data GUI (type 'visualize_data_GUI' and press enter).
 - b. Determine if there are regions where data did not correlate well.
 - c. Run delete data GUI.
 - d. Select a single image to preview, and choose regions of data to delete. Data will be deleted for all the images.
3. Smooth displacements and calculate strains.
 - a. Run compute data GUI (type 'compute_data_GUI' and press enter).
 - b. If desired, enter the scale of your images (must be determined separately, using a known length, i.e. using the measure feature in ImageJ).
 - c. Choose a smoothing kernel size and the number of smoothing passes (i.e. 11 and 3).
 - d. Choose finite element used in the interpolation of displacements and subsequent strain calculations. The author recommends always using cubic elements.
 - e. Compute the deformed grid if desired.
 - f. Run visualize data GUI (type 'visualize_data_GUI' and press enter) to view the smoothed displacements and strains. Line scans of displacements and of strains are particularly useful to judge the effectiveness of the smoothing.

- g. Re-run compute data GUI (type 'compute_data_GUI' and press enter), adjusting the smoothing parameters as necessary until smoothed displacements and strains are satisfactory.

Data Visualization

1. Visualize results.
 - a. Run visualize data GUI (type 'visualize_data_GUI' and press enter)
 - b. Save plots as desired (as MATLAB '.fig' files). Typically, contour maps of local strains in the E_{xx} direction for horizontally strained images are saved, as well as line scans across the sample at various levels (see Export Data section)
 - c. Run movie GUI. Make a time-lapsed movie of the contour plot if desired.
(Optional)

Export Data

Export additional line scan data using the following MATLAB script to excel if desired using the following matlab function

1. Prepare line scans by using the "visualize_data_GUI", creating and saving line scans (typically horizontal regions of interest from 0.1 to 0.9 with a step size of 0.1 (i.e. 0.1, 0.2, ... 0.8, 0.9) saving line scans as .fig files with the title "Line Scan .#.fig" where # is the fractional region of interest)
2. This exports data to excel in order to find maximum slope for each line scan

MATLAB Script to Export Data to Excel

%This code extracts data from a line graph in MATLAB

%First, open the .fig file you would like to extract from

clear all;

for i=1:9

open(['Line Scan .' num2str(i) '.fig']); %name of matlab .fig file. Can be changed

h = gcf; %current figure handle

axesObjs = get(h, 'Children'); %axes handles

dataObjs = get(axesObjs, 'Children'); %handles to low-level graphics objects in axes

objTypes = get(dataObjs, 'Type'); %type of low-level graphics object

xdata = get(dataObjs, 'XData'); %data from low-level graphics objects

ydata = get(dataObjs, 'YData');

%finally, export data to excel, in an excel spreadsheet named "Line Scan"

filename='Linescan';

%get values from cell arrays

x_values=xdata{1};

y_values=cell2mat(ydata);

```
%transpose
x_values=x_values';
y_values=y_values';

%first column is x, rest is y
values_xandy=[x_values y_values];

    xlswrite(filename, values_xandy,i);
end

close all;
```

APPENDIX D: CELL CULTURE, ASSAYS, AND STAINING PROTOCOLS

D.1: hMSC and pMSC Culture Protocol

Reference: Protocols from Matt Wheeler group and Jennie P. Mather

Reagents

- Complete hMSC media (500 mL); store at 4 °C
 - 445 mL low glucose DMEM (Based on Fisher SH30022.FS, order from Sandy at SCS Media Facility); store at 4 °C
 - 50 mL MSC-validated fetal bovine serum (Invitrogen); store at -20 °C
 - 5 mL antibiotic-antimycotic (Invitrogen 15140-122); store at -20 °C
- Trypsin-EDTA (Invitrogen 25300-062); store at -20 °C
- Trypan blue (Sigma-Aldrich T8154)
- DMSO (Fisher D128-500)
- Sterile phosphate-buffered saline without Ca^{2+} or Mg^{2+} (PBS)

Supplies and equipment

- Hausser phase contrast hemacytometer (Fisher 02-671-5)
- Tabletop centrifuge (VWR 53513-812)
- Optical microscope (Leica Microsystems DMIL LED)
- Water bath (37 °C, Fisher 15-474-35)
- Sterile filters
- Sterile pipettes (5, 10, 25 mL)
- T75 tissue culture flasks

Procedure

*Note: all steps should be performed in the laminar flow hood unless otherwise noted.

MSC thawing procedure

1. Place complete MSC media in water bath and warm to 37 °C.
2. Thaw frozen cell vials in 37 °C water bath for about 2 min.
3. Transfer the thawed cells and freezing media to a 15 mL centrifuge tube. Add complete MSC media until the cerulean effect has dissipated, then bring the volume up to 9 mL.
4. Remove a 10 μL cell suspension aliquot for counting. Gently re-suspend the cells in the diluted media and pellet the cells at 600 g for 5 min.
5. While cells are spinning down, mix the 10 μL cell suspension aliquot with 10 μL of Trypan blue. Pipette several times to mix the stain and cell suspension.
6. Place a cover slip on the hemocytometer and pipette 10 μL of the stain/cell suspension into the hemocytometer.

7. Cell counts are performed in as many of the nine separate regions of the hemocytometer as is feasible. Average number of cells per region is used to calculate the total cell population. For this calculation, the dilution factor is typically 2 (1:1 ratio of cell suspension to Trypan blue).

$$\text{Total Cell Population} = (\text{Mean Cells/Region}) * \text{Dilution} * 10,000 * (\text{Cell Suspension Volume})$$

8. Seed the cells at the required density (usually 5,000-6,000 cells/cm²). Use around 10-12 mL media for a 100 mm dish, 12-14 mL for a T75, or 7-8 mL for a T25.
9. Place the flask(s) into the incubator. Check the confluence every 24 hours and feed cells twice a week. Cells are usually confluent after 7-9 days. Do not use past passage 6.

MSC feeding procedure

1. Warm complete MSC media in water bath to 37 °C.
2. When the media is warm, wipe dry with paper towel and spray with 70% ethanol before placing in the sterile hood.
3. Remove all old media from each flask or well plate, taking care not to scrape the cells with the pipette tip.
4. Add appropriate volume of media. Return the flasks or well plates to the incubator and feed every twice a week. Adjust volume of media accordingly for different sized containers.

MSC passaging procedure

1. Warm complete MSC media, sterile PBS, and 3 mL trypsin-EDTA per T75 flask to be passaged in water bath to 37 °C.
2. When the media, PBS and trypsin are warm, wipe them dry with paper towel and spray with 70% ethanol before placing in the sterile hood.
3. Remove all old media from each T75 flask, taking care not to scrape the cells with the pipette tip.
4. Add 10 mL of PBS per T75 flask and leave the PBS in the flask to rinse the cells for 30 s. Swirl gently to remove any excess media from the cells. Adjust volumes of PBS, media, and trypsin accordingly for different sized flasks.
5. Remove the PBS and add 3 mL of trypsin per T75 flask. Return the flasks to the incubator for 8 min to allow for the cells to detach from the tissue culture plastic (allow the cells to sit for 3-4 additional min in the incubator if they do not detach after 6 min). Slap flasks a few times to detach cells.
6. Add 6 mL of complete MSC media to each flask to neutralize the trypsin and to flush cells off of the tissue culture plastic.
7. Remove the trypsin, additional media, and cells from the flask and put into a conical tube. Remove a 10 µL cell suspension aliquot for counting. Centrifuge the cells at 600 g for 5 min.
8. While cells are spinning down, mix the 10 µL cell suspension aliquot with 10 µL of Trypan blue. Pipette several times to mix the stain and cell suspension.

9. Place a cover slip on the hemocytometer and pipette 10 μ L of the stain/cell suspension into the hemocytometer.
10. Cell counts are performed in as many of the nine separate regions of the hemocytometer as is feasible. Average number of cells per region is used to calculate the total cell population. For this calculation, the dilution factor is typically 2 (1:1 ratio of cell suspension to Trypan blue).

$$\text{Total Cell Population} = (\text{Mean Cells/Region}) * \text{Dilution} * 10,000 * (\text{Cell Suspension Volume})$$

11. Aspirate off the media supernatant and add new media to dilute cells to desired concentration.
12. Seed the cells at the required density (usually 5,000-6,000 cells/cm²). Use around 10-12 mL media for a 100 mm dish, 12-14 mL for a T75, or 7-8 mL for a T25.
13. Place the flask(s) into the incubator. Check the confluence every 24 hours and feed cells twice a week.

MSC freezing procedure

1. Grow cells to confluence and replace media the day before freezing.
2. Warm complete MSC media, sterile PBS, and 3 mL trypsin-EDTA per T75 flask to be passaged in water bath to 37 °C.
3. When the media, PBS and trypsin are warm, wipe them dry with paper towel and spray with 70% ethanol before placing in the sterile hood.
4. Remove all old media from each flask, taking care not to scrape the cells with the pipette tip.
5. Add 10 mL of PBS per T75 flask and leave the PBS in the flask to rinse the cells for 30 s. Swirl gently to remove any excess media from the cells. Adjust volumes of PBS, media, and trypsin accordingly for different sized flasks.
6. Remove the PBS and add 3 mL of trypsin per T75 flask. Return the flasks to the incubator for 8 min to allow for the cells to detach from the tissue culture plastic (allow the cells to sit for 3-4 additional min in the incubator if they do not detach after 6 min). Slap flasks a few times to detach cells.
7. Add 6 mL of complete MSC media to each flask to neutralize the trypsin and to flush cells off of the tissue culture plastic.
8. Remove the trypsin, additional media, and cells from the flask and put into a conical tube. Remove a 10 μ L cell suspension aliquot for counting. Centrifuge the cells at 600 g for 5 min.
9. While cells are spinning down, mix the 10 μ L cell suspension aliquot with 10 μ L of Trypan blue. Pipette several times to mix the stain and cell suspension.
10. Place a cover slip on the hemocytometer and pipette 10 μ L of the stain/cell suspension into the hemocytometer.
11. Cell counts are performed in as many of the nine separate regions of the hemocytometer as is feasible. Average number of cells per region is used to calculate the total cell population. For this calculation, the dilution factor is typically 2 (1:1 ratio of cell suspension to Trypan blue).

$$\text{Total Cell Population} = (\text{Mean Cells/Region}) * \text{Dilution} * 10,000 * (\text{Cell Suspension Volume})$$

12. Aspirate off the media supernatant and calculate volume of freezing media needed to re-suspend $1-10 \times 10^6$ cells per mL (freezing media: 50% complete MSC media, 40% FBS, 10% DMSO).
13. Aliquot cells into 1 mL cryogenic tubes and place in $-20\text{ }^{\circ}\text{C}$ freezer for 1 hour.
14. Place cryogenic tubes in $-80\text{ }^{\circ}\text{C}$ freezer. Cells can be stored here for up to 6 months. For longer-term storage, keep cells at $-80\text{ }^{\circ}\text{C}$ for at least 24 hours and then carefully move to liquid nitrogen storage in IGB.

D.2: Cell Seeding on Scaffold Variants

Reference: Caliari and Harley 2011; Caliari, Ramirez et al. 2011, Mozdzen et al 2016

Reagents

- Complete media (see **Appendix D.1** for recipe); store at 4 °C
- Trypsin-EDTA (Invitrogen 25300-062); store at -20 °C
- Trypan blue (Sigma-Aldrich T8154)
- Sterile phosphate-buffered saline without Ca^{2+} or Mg^{2+} (PBS)

Supplies and equipment

- Ultra-low attachment 6-well plates (Fisher 07-200-601)
- Hausser phase contrast hemacytometer (Fisher 02-671-5)
- Tabletop centrifuge (VWR 53513-812)
- Optical microscope (Leica Microsystems DMIL LED)
- Water bath (37 °C, Fisher 15-474-35)
- Sterile pipettes (5, 10, 25 mL)
- Kimwipes
- Scaffold variant (EDC crosslinked, **Appendices A.3, A.4, A.6, B.1**)

Procedure

*Note: all steps should be performed in the laminar flow hood unless otherwise noted. For growth factor supplemented studies, use tendon cell media without serum.

1. Warm complete media, sterile PBS, and 3 mL trypsin-EDTA per T75 flask to be passaged in water bath to 37 °C.
2. Place hydrated scaffold pieces in fresh media for at least 30 min.
3. Carefully remove excess media from scaffolds with a Kimwipe and place 3-4 scaffolds in each well of Ultra-low attachment 6-well plates. If scaffolds are larger, place fewer scaffolds in each well plate. Do not overdry scaffolds (especially CGCaP scaffolds) as this will lead to reduced viability.
4. When the media, PBS and trypsin are warm, wipe them dry with paper towel and spray with 70% ethanol before placing in the sterile hood.
5. Remove all old media from each flask, taking care not to scrape the cells with the pipette tip.
6. Add 10 mL of PBS per T75 flask and leave the PBS in the flask to rinse the cells for 30 s. Swirl gently to remove any excess media from the cells. Adjust volumes of PBS, media, and trypsin accordingly for different sized flasks.
7. Remove the PBS and add 3 mL of trypsin per flask. Return the flasks to the incubator for 6-8 min to allow for the cells to detach from the tissue culture plastic (allow the cells to sit for 3-4 additional min in the incubator if they do not detach after 6 min). Slap flasks a few times to detach cells.

8. Add 6 mL of complete tendon cell media to each flask to neutralize the trypsin and to flush cells off of the tissue culture plastic.
9. Remove the trypsin, additional media, and cells from the flask and put into a conical tube. Remove a 10 μ L cell suspension aliquot for counting. Centrifuge the cells at 600 g for 5 min.
10. While cells are spinning down, mix the 10 μ L cell suspension aliquot with 10 μ L of Trypan blue. Pipette several times to mix the stain and cell suspension.
11. Place a cover slip on the hemocytometer and pipette 10 μ L of the stain/cell suspension into the hemocytometer.
12. Cell counts are performed in as many of the nine separate regions of the hemocytometer as is feasible. Average number of cells per region is used to calculate the total cell population. For this calculation, the dilution factor is typically 2 (1:1 ratio of cell suspension to Trypan blue).

$$\text{Total Cell Population} = (\text{Mean Cells/Region}) * \text{Dilution} * 10,000 * (\text{Cell Suspension Volume})$$

13. Aspirate off the media supernatant and add new media to dilute cells to desired concentration. For 5 mm x 5 mm x 15 mm rectangular scaffolds, seed approximately 3×10^5 cells per scaffold (dilute cell suspension to approximately 1×10^5 per 10-20 μ L media)
14. Add 10 μ L of cell suspension to each scaffold, typically placing 3 aliquots evenly along the length of the scaffold. Place scaffolds in incubator for 15-30 min.
15. Remove scaffolds from incubator, flip over, add additional 3 aliquots of 10 μ L of cell suspension to the other side of each scaffold, and return to incubate for additional 2-3 hours.
16. Carefully add 6 mL complete media (or media with growth factors but without serum) to each well. Change media every 3 days over the course of the experiment.

D.3: AlamarBlue Metabolic Activity Protocol

Reference: Tierney, Jaasma et al. 2009; Caliari and Harley 2011; Caliari, Ramirez et al. 2011

Reagents

- Complete media (see **Appendix D.1** for recipe); store at 4 °C
- AlamarBlue (Invitrogen DAL1100); store at 4 °C

Supplies and equipment

- 24-well plates (Fisher 08-772-1)
- 96-well plates (Fisher 12-565-369)
- MTS 2/4 digital microtiter shaker (IKA 3208001)
- Water bath (37 °C, Fisher 15-474-35)
- Fluorescence spectrophotometer (Tecan)

Procedure

*Note: all steps should be performed in the laminar flow hood unless otherwise noted. The volumes of reagents used are correct for 8 mm diameter, 5 mm thick scaffold pieces. Use identical media to that being used for experiment.

Generating standard curve procedure

1. Warm media and alamarBlue in water bath to 37 °C.
2. Before starting an experiment, generate a standard curve with a known number of cells. The standard should have at least eight sample points: one well with just media, one well with media and alamarBlue, and six wells with media, alamarBlue, and a different number of cells. An example standard setup is shown:

	Well 1	Well 2	Well 3	Well 4	Well 5	Well 6	Well 7	Well 8
Media	1000 µL	900 µL	895 µL	890 µL	885 µL	880 µL	860 µL	840 µL
Cell suspension	0 µL	0 µL	5 µL	10 µL	15 µL	20 µL	40 µL	60 µL
AlamarBlue	0 µL	100 µL	100 µL	100 µL	100 µL	100 µL	100 µL	100 µL

Well 1 is a negative control, well 2 is a background control, and the other wells are used to make the standard curve.

3. Incubate at 37 °C under gentle (~50 rpm) shaking for 1.5-5.5 hours. During this time healthy cells convert the active ingredient in alamarBlue (resazurin) to the highly fluorescent resorufin. Longer incubation times are necessary for smaller cell concentrations, but make sure not to incubate cells too long or all of the resazurin will be reduced to resorufin.

4. After incubation, pipette 100 μ L in triplicate from each sample well into a clear 96-well plate.
5. Measure fluorescence (excitation: 540 nm, emission: 580 nm) on the spectrophotometer in RAL using the program 'AlamarBlue F200'. Remember to reserve the F200 machine on the Google Calendar prior to use. For each data point, adjust the fluorescence reading by subtracting the reading from well 2 (background control). The standard curve is created by plotting cell number as a function of adjusted fluorescent intensity.

Quantifying metabolic activity on scaffolds procedure

1. For measuring cell metabolic activity on scaffolds, pipette 900 μ L media into each well (one well for each scaffold piece plus the two control wells). Add 100 μ L alamarBlue to each well except for one negative control well. Adjust volumes for smaller/larger materials accordingly, keeping the 9:1 media: alamarBlue® ratio constant.
2. Remove scaffolds to be assayed and rinse in sterile PBS to remove excess media and unattached/dead cells. Add scaffolds to experimental wells and incubate at 37 °C under gentle (~50 rpm) shaking for 1.5-5.5 hours. The incubation time should be identical to the time used to make the standard curve.
3. After incubation, pipette 100 μ L in triplicate from each sample well into a 96-well plate.
4. Measure fluorescence (excitation: 540 nm, emission: 580 nm) on the spectrophotometer in RAL 299 using the program 'AlamarBlue F200'. Remember to reserve the F200 machine on the Google Calendar prior to use. Subtract the background control from the data points and extrapolate adjusted fluorescent intensity on the standard curve to give metabolic activity.
5. This assay is non-destructive, so scaffolds can continue to be cultured and analyzed at later time points.

D.4: DNA Quantification (Hoechst Dye) Protocol

Reference: Kim, Sah et al. 1988; Caliari and Harley 2011; Caliari, Ramirez et al. 2011

Reagents

- Hoechst dye buffer (500 mL); store at 4 °C for up to 3 months
 - 400 mL deionized water
 - 58.44 g sodium chloride
 - 0.605 g Tris base
 - 0.185 g disodium EDTA (Sigma-Aldrich E5134)
 - Adjust pH to 7.4, bring total volume to 500 mL, sterile filter before use
- Papain buffer (100 mL); store at 4 °C
 - 100 mL PBS
 - 1 mL 0.5 M EDTA (pH = 8.0, Sigma-Aldrich EDS); store at 4 °C
 - 79 mg cysteine-HCl (Sigma-Aldrich 00320)
- Hoechst 33258 dye solution (1 mL); store at 4 °C for up to 6 months
 - 1 mL sterile water
 - 1 mg Hoechst 33258 dye (Invitrogen H1398); store at 4 °C
- Papain from Carica papaya (Sigma-Aldrich 76218); store at -20 °C
- Sterile phosphate-buffered saline without Ca₂₊ or Mg₂₊ (PBS)

Supplies and equipment

- 96-well plates (Fisher 12-565-369)
- Vortex (Fisher 02-215-365)
- Water bath (60°C, Fisher 15-460-2SQ)
- Fluorescence spectrophotometer (Tecan, Room 299 RAL)
- Microcentrifuge tubes (1.5 mL)

Procedure

*Note: Some steps should be performed in the laminar flow hood when requiring sterile conditions or while working with live cells. These steps are noted throughout this protocol.

Generating standard curve procedure

*Note: steps 1-2 should be performed in the laminar flow hood.

1. At the beginning of each experiment, a standard curve should be generated with a known number of cells. To make a standard curve spanning 5×10^3 to 1.5×10^6 million cells, make up active papain enzyme solution by dissolving 18-20 mg papain in 15 mL papain buffer in the 60 °C water bath.

2. Spin down two aliquots of 2 million cells each. Remove supernatant and add 12 mL papain enzyme solution to one tube and 400 μ L to the other tube. Allow to digest for 24 hours in the 60 °C water bath.
3. After 24 hours, vortex tubes thoroughly. For the 12 mL tube, add cell lysate to labeled microcentrifuge tubes in 30 μ L intervals (starting from a blank control) up to 300 μ L. Bring all volumes to 300 μ L with blank papain buffer. For the 400 μ L tube, add cell lysate to labeled microcentrifuge tubes in 2 μ L intervals (starting from a blank control) up to 30 μ L. Bring all volumes to 30 μ L with blank papain buffer.
4. Prepare Hoechst working dye solution by adding 1 μ L dye solution to 10 mL Hoechst dye buffer. Vortex thoroughly. Add working dye solution to each tube to bring total volume to 630 μ L. Vortex thoroughly. The Hoechst dye fluorescently binds to double-stranded DNA from the lysed cells, allowing quantification of DNA and thus cell number.
5. Pipette 200 μ L from each tube in triplicate into a black 96-well plate.
6. Measure fluorescence (excitation: 360 nm, emission: 465 nm) on the spectrophotometer in RAL 299. Use the 'DNA F200' program and remember to reserve the F200 machine on the Google Calendar prior to use. For each data point, adjust the fluorescence reading by subtracting the reading from the blank control. The standard curve is created by plotting cell number as a function of adjusted fluorescent intensity.

Quantifying cell number on scaffolds procedure

*Note: step 2 should be performed in the laminar flow hood.

1. For measuring cell number on scaffolds, pipette 300 μ L of papain enzyme solution into microcentrifuge tubes (one for each scaffold plus two controls: one tube with just papain enzyme solution as a negative control and one tube containing a blank scaffold with no seeded cells as a background control).
2. Remove scaffolds to be assayed and rinse in sterile PBS to remove excess media and unattached/dead cells. Add scaffolds to microcentrifuge tubes and incubate in 60 °C water bath for 24 hours. Vortex occasionally to facilitate digestion of scaffold.
3. After incubation, pipette 600 μ L Hoechst working dye solution in microcentrifuge tubes.
4. Remove samples from water bath and vortex thoroughly. Add 30 μ L from each tube to its corresponding tube containing working dye solution. Vortex thoroughly.
5. Pipette 200 μ L from each tube in triplicate from each sample well into a 96-well plate.
6. Measure fluorescence (excitation: 360 nm, emission: 465 nm) on the spectrophotometer in RAL 299. Use the 'DNA F200' program and remember to reserve the F200 machine on the Google Calendar prior to use. For each data point, adjust the fluorescence reading by subtracting the reading from the background control. Adjusted fluorescent intensity can be extrapolated on the standard curve to give a cell number.

D.5: BOSE System Multi-Compartment Scaffold Straining

Reference: Legerlotz et al. 2011

Reagents:

- Complete media (see **Appendix D.1** for recipe); store at 4 °C
- CG-CGCaP scaffolds (hydrated and seeded with cells, **Appendices A.3, A.4, D.2**)

Supplies and equipment:

- BOSE loading frame (BOSE Corporation, Eden, Prairie, Minnesota, USA)
- Custom made loading chambers
- Custom cut spacers (4 and 7 mm thick)
- Incubator (37 °C)
- Water bath (37 °C, Fisher 15-474-35)
- Micropipette
- Sterile pipette tips (100-1000 µL)
- Sterile blunt-nosed tweezers
- Small screw driver

Procedure

*Note: all steps should be performed in the laminar flow hood unless otherwise noted.

1. Autoclave all tools before starting (tweezers, screw driver, custom chambers and spacers)
2. Warm media in water bath (37 °C) for 20 minutes or until warm.
3. Remove seeded scaffolds from the incubator (37 °C) and place in laminar flow hood along with autoclaved materials and warmed media.
4. Disassemble chambers, taking care not to lose any small parts.
5. Secure non-mineralized compartment of the scaffold to the moveable upper grip. Tighten screws such that they will hold the scaffold, but not so tight that they tear the scaffold upon movement.
6. Carefully insert the moveable upper grip into the chamber and gently pull the scaffold into the chamber. Attach the mineralized compartment of the scaffold to the bottom, stationary grip. Tighten screws such that they will hold the scaffold, but not so tight that they tear the scaffold upon movement. Note that load chambers provide a 10 mm gauge length.
7. Pipette warmed complete media into the chamber as it lies horizontally. Slide the glass chamber over the main chamber to create a water-tight seal.
8. Carefully slide the custom made spacers to the desired strain (0, 7, 11, 15, or 20 percent strain) using small spacers (0.4 mm and 0.7 mm).
9. Place chambers in the incubator for desired time.
10. Image samples as described in **Appendix D.6**.

D.6: Confocal Imaging Protocol

Reference: Martin et al. 2010

Reagents

- Formalin solution, 10% formaldehyde in neutral buffer (Polysciences 08379-3.75)
- Sterile phosphate-buffered saline without Ca^{2+} or Mg^{2+} (PBS)
- AlexaFluor® 555-phalloidin (Invitrogen A34055); store at -20°C
- Hoechst 33342 stock (Invitrogen H3570) store at 4°C

Supplies and equipment

- 6-well plates
- Kimwipes
- Tweezers
- Leica TCS SP2 laser scanning confocal microscope (Leica Microsystems GmbH, Wetzlar, Germany)
- ImageJ analysis software

Procedure

Nuclei/Actin staining procedure

1. Rinse samples in PBS to remove dead/unattached cells and then place samples in formalin. Store at 4°C overnight, replace formalin, and store at 4°C until next step.
2. Wash scaffolds in PBS for 1 min (3x).
3. Incubate scaffolds in 0.1% Triton X100 in PBS for 15 min.
4. Wash scaffolds in PBS for 1 min (3x).
5. Dilute 25 μL of AlexaFluor® 555-phalloidin dye methanolic stock solution per 1 mL PBS.
6. Incubate scaffolds in solution for 30 min. Keep samples in the dark.
7. Wash scaffolds in PBS for 1 min (3x).
8. Dilute 1 μL of DAPI or Hoechst stock per 800 μL PBS and incubate scaffolds in solution for 5 min.
9. Wash scaffolds in PBS for 1 min (3x).
10. Store scaffolds in PBS in the dark at 4°C until imaging.

Confocal imaging procedure

*Note: This procedure was performed in the Screen Lab at Queen Mary University of London. The IGB core facility has a confocal with slightly different imaging procedures.

1. Reserve time on confocal microscope using google calendar.
2. Turn on PC
3. Turn scanner on (on microscope tower)

4. Turn on all fans and let them equilibrate for approximately 20 minutes.
5. Turn Ar/ArKr laser to start, hold, release (458 nm, 476 nm, 488 nm, 496 nm, and 514 nm wavelength capabilities)
6. Turn HeNe laser on (543 nm and 633 nm capabilities)
7. Turn on mercury bulb (note: if mercury bulb is turned off, the bulb must cool for 30 minutes before it is turned back on).
8. Turn UV laser on (switch is located on a black box below the computer, with an additional switch next to the microscope. Both must be turned on)
9. Log into windows using QMUL id and password.
10. Turn on microscope.
11. After microscope has initialized, open Leica No MP on desktop, accept “Personal” and click start.
12. To look through the visual binoculars, make sure the port is marked as VIS, the filters are not blocked (the rod is pulled out), and the magnification is 1X. The filter wheel is marked as 1) UV for DAPI or Hoechst 2) Red emission for TRITC or Alexa-594 3) Green emission for GFP, FITC, or Alexa-488 and 4) Scan for confocal.
13. On the Leica software, load profile.
14. Pick the objective to use (20X)
15. Adjust image. For CG scaffolds stained with Hoechst and phalloidin Alexa-555 the offset was typically around 2 and the gain was approximately 500-700. For phalloidin Alexa-555, the excitation wavelength was 543 and collected between 560-700 nm. For Hoechst, the UV laser collected between 370-535 nm using a filter of ND50. If the image is not clear enough, the filter can be reduced.
16. When finished, turn everything off in the reverse order of what was turned on. Leave the fans running for approximately 20-30 minutes.
17. Analyze images on personal computer using ImageJ software.

D.7: Nuclei and Actin Orientation Analysis

Reference: Thévenaz et al. 2011; Mozdzen et al. 2016

Supplies and equipment:

- Computer
- ImageJ analysis software
- Ovuscul plugin for ImageJ
- Images to be analyzed (preferably in .tiff format)

Procedure

1. Obtain images as **Appendix D.6** using Leica TCS SP2 laser scanning confocal microscope (Leica Microsystems GmbH, Wetzlar, Germany)

Nuclei Orientation and Aspect Ratio Procedure

1. Load nuclei stained image in ImageJ.
2. Go to Image -> Adjust -> Threshold and pick a consistent threshold over which to analyze the images. Note that it is easier to visually check ovuscul's yellow oval against a black background, but any consistent degree of thresholding is acceptable.
3. Open Ovuscul (Plug-ins -> ovuscul).
4. Manually drag the yellow oval around the first cell nuclei.
5. Press "space" on the keyboard or press the play button on the toolbar.
6. Visually check that the yellow oval has converged around the cell nuclei. If it has not, repeat steps 4 and 5.
7. Press "enter" or save on the toolbar to save the data.
8. Repeat process for every nuclei in the image
9. Copy and paste the data output into excel or save as a text file.

Actin Orientation Procedure

1. Load each group of actin images into the work path of MATLAB and run the following code. *Note that all MATLAB code was provided by Stephen Thorpe.

Actin Orientation MATLAB Scripts

MainActinOrient.m

% Script for running actin alignment for Laura's actin images

```
close all;  
clear all;  
clc
```

```
XLfilename = 'ResultsMain.xlsx'; %Filename for results output
```

```

Resultlist = {'Filename','Fibre angle','Coalignment ratio','Angle deviation',...
'Analysed fibre area'};
l = 2; %line to start results output in excel sheet

% Set number of characters to ignore at start of figure name for output
% name
beginning = 0; % 13;

% Main Algorithm
filenames = dir('*.tif'); %read in file names in directory
s = numel(filenames);
for p = 1:s
    fname = filenames(p).name;
    OutName = fname(beginning+1:end-9);
    Resultlist{1,1} = OutName; %Image name for results list

    IR = imread(fname);

    [IRDir IRCR IRAD AnArea] = FibreOrient4(IR); %Call actin function FibreOrient4
    Resultlist{1,2} = IRDir; % Mean fibre orientation
    Resultlist{1,3} = IRCR; % Mean coalignment ratio for fibre orientation
    Resultlist{1,4} = IRAD; % Mean angle deviation for fibre orientation
    Resultlist{1,5} = AnArea; % Area analysed/Total area (less removed edges)

    l = l+1; % Increment line number
end
xlswrite(XLfilename,Resultlist); %Output excel sheet with result list

FibreOrient4.m
%close all;
%clear all;
% clc
function [IRDir, IRCR, IRAD, AnArea] = FibreOrient4(I)

% Imagefile = uigetfile('*.tif','Select the .tif file for analysis');
% I = double(imread(Imagefile));
if size(I,3) == 3
    I = I(:, :, 1); %Select channel: 1 for red, 2 for green, 3 for blue
end

%Image average smoothening by (i)th times
I2 = double(I);
h = fspecial('average');
for i = 1:4
    I2 = imfilter(I2,h);

```

```

end
[T1] = ThreshMode2(I2);
[IRT] = ApplyThresh(I2,T1);

IRT1 = IRT;
% Speckle removal
[cluster_mat, cluster_num] = bwlabeln(IRT1); %Cluster each group of pixels
for i=1:cluster_num
    [row,col] = find(cluster_mat == i);
    if length(row) < 10; %Find small clusters, i.e. speckles
        for l=1:length(row)
            IRT1(row(l),col(l))=0; %Make zero
        end
    end
end
end

% Dilate and erode
se90 = strel('line', 2, 90); %Morphological structuring elements for dialtion
se0 = strel('line', 2, 0);
seD = strel('disk',1); %Morphological structuring element disk of radius 1
IRT2 = imdilate(IRT1,[se90 se0]); %Each border pixel is turned into a 3x3 cross
IRT3 = imerode(IRT2,seD);

% Reduce image size
I3 = I2.*IRT3;
IR = imresize(I3,0.5); %Reduce image size by factor

%IR = I;

s = 3; %Mask size
sigma = 3; %Area of influence of the mask
hx = zeros(s);
hy = zeros(s);
for i = 1:2*s+1
    for j = 1:2*s+1
        m = i-s-1;
        n = j-s-1;
        hx(j,i) = (2*m/sigma^2)*exp(-(m^2+n^2)/sigma^2); %x directed mask
        hy(j,i) = (2*n/sigma^2)*exp(-(m^2+n^2)/sigma^2); %y directed mask
    end
end
end
Gx = conv2(IR,hx,'valid');
Gy = conv2(IR,hy,'valid');
G = sqrt(Gx.^2+Gy.^2); %Gradient magnitude
IntGrad = -atan(Gy./Gx); %Intensity grad
PhiLocalrad = IntGrad+pi/2; %Local direction of orientation

```

```

PhiLocal = PhiLocalrad*180/pi; %Convert from radians to degrees

IR1 = IR(s+1:(length(IR)-s),s+1:(length(IR)-s));
IThresh = 0.4*mean(mean(IR1)); %Threshold for whether region is analysed
m = 25; %Subimage side length
numw = (floor(length(G)/m))^2; %Number of subregions
A = zeros(180,numw); %Accumulator bins for each subregion
CR = zeros(180,numw);
Pix = zeros(180,numw);
AD = zeros(numw);
w = 1; %Subregion number
nan = isnan(PhiLocal);
for p = 1:floor(length(G)/m) %Loop through each sub region
    pstart = (p-1)*m+1;
    pend = p*m;
    for q = 1:fix(length(G)/m)
        qstart = (q-1)*m+1;
        qend = q*m;
        M = IR1(pstart:pend,qstart:qend);
        M = M(:);
        Mnan = nan(pstart:pend,qstart:qend);
        Mnan = Mnan(:);
        PhiM = PhiLocal(pstart:pend,qstart:qend);
        PhiM = PhiM(:);
        PhiM(Mnan==1) = [];
        GM = G(pstart:pend,qstart:qend);
        GM = GM(:);
        GM(Mnan==1) = [];
        if mean(M) > IThresh
            for theta = 1:180 % For each angle bin from 0 to 180 degrees
                AnglWt = exp(2*cosd(2*(theta-PhiM)))/exp(2); % Angle weighting
                Aw = GM.*AnglWt; % Angle bin value weighted to gradient magnitude
                A(theta,w) = sum(Aw); %Angle weighting
                CR(theta,w) = sum(AnglWt)/length(AnglWt); %Coalignment ratio
            end
            AD(w) = std(PhiM); %Angle deviation
            Pix(w) = length(PhiM); %Number non-thresholded pixels
            w = w+1;
        else
            IR1(pstart:pend,qstart:qend) = 255;
        end
    end
end
end
A = A(:,1:w-1); %Trim matrices to remove space from below threshold regions
CR = CR(:,1:w-1);
Pix = Pix(1:w-1);

```



```

AD = AD(1:w-1);
% Predominant orientation of each reion given by Dirw90 from 0 to 180
[C Dirw90] = max(A);
Dirw0 = zeros(numel(Dirw90,1)); % Convert angles to -90 to +90
for i = 1:numel(Dirw90)
    if Dirw90(i) > 90
        Dirw0(i) = abs(Dirw90(i)-180);
    else
        Dirw0(i) = Dirw90(i);
    end
end
bins = 2.5:5:87.5; % Bins of 5 degrees
H = hist(Dirw0,bins); % Histogram of number of regions in each angle bin
[C IndDir] = max(H); % Cell's fibre orientation is orientation of max bin
IRDir = bins(IndDir); % Output fibre orientation
% Mean of coalignment ratios for each drection in regions principle
% direction
IRCR = mean(CR(Dirw90));
IRAD = mean(AD); % Mean or region angle deviations
% Fraction of total pixels analysed. i.e. above threshold and in region
% above threshold.
AnArea = sum(Pix)/numel(IR1);

```

ApplyThresh.m

```
function [IThresh] = ApplyThresh(I,T)
```

```

%%%%%%%%%%%%%%%%%%%%%%%%%%%%%%%%%%%%%%%%%%%%%%%%%%%%%%%%%%%%%%%%%%%%%%%%
%%%%%%%%%%%%%%%%%%%%%%%%%%%%%%%%%%%%%%%%%%%%%%%%%%%%%%%%%%%%%%%%%%%%%%%%
%This function receive the image to be thresholded and the threshold value.
%This function then produce a thresholded image.
%I: image to be thresholded
%T: threshold value
%%%%%%%%%%%%%%%%%%%%%%%%%%%%%%%%%%%%%%%%%%%%%%%%%%%%%%%%%%%%%%%%%%%%%%%%
%%%%%%%%%%%%%%%%%%%%%%%%%%%%%%%%%%%%%%%%%%%%%%%%%%%%%%%%%%%%%%%%%%%%%%%%

```

```
clear row column int S sizerow sizecolumn R C
```

```

[row,column,int] = find(I>T);
S = length(row);
[sizerow,sizecolumn] = size(I);
IThresh = zeros(sizerow,sizecolumn);
for i = 1:S
    R = row(i,1);
    C = column(i,1);
    IThresh(R,C) = 1;
end

```

ThreshMode2.m

```
function [Thresh] = ThreshMode2(I)
```

```
% This function receives an image and uses a unimodal threshold selection  
% algorithm adapted from the k-means clustering algorithm. This has been  
% proven to converge at a local minimum, such that a different initial  
% threshold may give a different final result
```

```
T1 = uint8(mean(mean(I))); %Get initial threshold value
```

```
c = false; %for convergence
```

```
i = 0;
```

```
while c == false
```

```
    G1 = I(I<=T1); %All pixels less than threshold
```

```
    G2 = I(I>T1); %All pixels above threshold
```

```
    m1 = mean(G1); %Average pixel value below threshold
```

```
    m2 = mean(G2); %Average pixel value above threshold
```

```
    T2 = uint8((m1+m2)/2); %New threshold
```

```
    if T1 == T2 %when old and new thresholds equal, convergence reached
```

```
        Thresh = T2;
```

```
        c = true;
```

```
    else
```

```
        T1 = T2;
```

```
    end
```

```
    i = i + 1; %To ensure it doesn't run forever if no valley
```

```
    if i > 10000
```

```
        Thresh = 0;
```

```
        return
```

```
    end
```

```
end
```

REFERENCES

- [1] Genin GM, Kent A, Birman V, Wopenka B, Pasteris JD, Marquez PJ, et al. Functional Grading of Mineral and Collagen in the Attachment of Tendon to Bone. *Biophysical Journal* 2009;97:976-85.
- [2] Galatz LM, Sandell LJ, Rothermich SY, Das R, Mastny A, Havlioglu N, et al. Characteristics of the rat supraspinatus tendon during tendon-to-bone healing after acute injury. *Journal of Orthopaedic Research* 2006;24:541-50.
- [3] Liu Y, Ramanath HS, Wang D-A. Tendon tissue engineering using scaffold enhancing strategies. *Trends in Biotechnology* 2008;26:201-9.
- [4] Schwartz AG, Pasteris JD, Genin GM, Daulton TL, Thomopoulos S. Mineral Distributions at the Developing Tendon Enthesis. *PLoS ONE* 2012;7.
- [5] Yamaguchi K, Ditsios K, Middleton WD, Hildebolt CF, Galatz LM, Teefey SA. The Demographic and Morphological Features of Rotator Cuff Disease A Comparison of Asymptomatic and Symptomatic Shoulders. *The Journal of Bone & Joint Surgery* 2006;88:1699-704.
- [6] Barber FA, Drew OR. A Biomechanical Comparison of Tendon-Bone Interface Motion and Cyclic Loading Between Single-Row, Triple-Loaded Cuff Repairs and Double-Row, Suture-Tape Cuff Repairs Using Biocomposite Anchors. *Arthroscopy: The Journal of Arthroscopic & Related Surgery* 2012;28:1197-205.
- [7] Denard PJ, Lädermann A, Jiwani AZ, Burkhart SS. Functional Outcome After Arthroscopic Repair of Massive Rotator Cuff Tears in Individuals With Pseudoparalysis. *Arthroscopy: The Journal of Arthroscopic & Related Surgery* 2012;28:1214-9.
- [8] Jackson M, Tétreault P, Allard P, Begon M. Optimal shoulder immobilization postures following surgical repair of rotator cuff tears: a simulation analysis. *Journal of Shoulder and Elbow Surgery*.
- [9] Killian ML, Cavinatto L, Shah SA, Sato EJ, Ward SR, Havlioglu N, et al. The effects of chronic unloading and gap formation on tendon-to-bone healing in a rat model of massive rotator cuff tears. *Journal of Orthopaedic Research* 2014;32:439-47.
- [10] Medicine AOSfS. Rotator Cuff Tears. *OrthoInfo: American Academy of Orthopaedic Surgeons*; 2011.
- [11] Reuther KE, Thomas SJ, Sarver JJ, Tucker JJ, Lee C-S, Gray CF, et al. Effect of return to overuse activity following an isolated supraspinatus tendon tear on adjacent intact tendons and glenoid cartilage in a rat model. *Journal of Orthopaedic Research* 2012:n/a-n/a.
- [12] Chuang T-Y, Ho W-P, Chen C-H, Lee C-H, Liao J-J, Huang C-H. Arthroscopic Treatment of Rotator Cuff Tears With Shoulder Stiffness A Comparison of Functional Outcomes With and Without Capsular Release. *Am J Sports Med* 2012;40:2121-7.
- [13] Galatz LM, Ball CM, Teefey SA, Middleton WD, Yamaguchi K. The outcome and repair integrity of completely arthroscopically repaired large and massive rotator cuff tears. *The Journal of Bone & Joint Surgery* 2004;86:219-24.
- [14] Lubowitz JH, Provencher MT, Poehling GG. Single- Versus Double-Row Arthroscopic Rotator Cuff Repair: The Complexity Grows. *Arthroscopy: The Journal of Arthroscopic & Related Surgery* 2012;28:1189-92.
- [15] Ramirez MA, Ramirez J, Murthi AM. Reverse Total Shoulder Arthroplasty for Irreparable Rotator Cuff Tears and Cuff Tear Arthropathy. *Clinics in Sports Medicine* 2012;31:749-59.

- [16] van der Meijden OA, Wijdicks CA, Gaskill TR, Jansson KS, Millett PJ. Biomechanical Analysis of Two Tendon Posterosuperior Rotator Cuff Tear Repairs: Extended Linked Repairs and Augmented Repairs. *Arthroscopy: The Journal of Arthroscopic & Related Surgery* 2013;29:37-45.
- [17] Atesok K, Fu FH, Wolf MR, Ochi M, Jazrawi LM, Doral MN, et al. Augmentation of Tendon-to-Bone Healing. *J Bone Joint Surg Am* 2014;96:513-21.
- [18] Chiou GJ, Crowe C, McGoldrick R, Hui K, Pham H, Chang J. Optimization of an Injectable Tendon Hydrogel: The Effects of Platelet-Rich Plasma and Adipose-Derived Stem Cells on Tendon Healing In Vivo. *Tissue Engineering Part A* 2015;21:1579-86.
- [19] Ely EE, Figueroa NM, Gilot GJ. Biomechanical Analysis of Rotator Cuff Repairs With Extracellular Matrix Graft Augmentation. *Orthopedics* 2014;37:608-14.
- [20] Hernigou P, Lachaniette CHF, Delambre J, Zilber S, Duffiet P, Chevallier N, et al. Biologic augmentation of rotator cuff repair with mesenchymal stem cells during arthroscopy improves healing and prevents further tears: a case-controlled study. *International Orthopaedics (SICOT)* 2014;38:1811-8.
- [21] Chung SW, Park H, Kwon J, Choe GY, Kim SH, Oh JH. Effect of Hypercholesterolemia on Fatty Infiltration and Quality of Tendon-to-Bone Healing in a Rabbit Model of a Chronic Rotator Cuff Tear Electrophysiological, Biomechanical, and Histological Analyses. *Am J Sports Med* 2016;0363546515627816.
- [22] Gumucio JP, Davis ME, Bradley JR, Stafford PL, Schiffman CJ, Lynch EB, et al. Rotator cuff tear reduces muscle fiber specific force production and induces macrophage accumulation and autophagy. *Journal of Orthopaedic Research* 2012;30:1963-70.
- [23] Reuther KE, Sarver JJ, Schultz SM, Lee CS, Sehgal CM, Glaser DL, et al. Glenoid cartilage mechanical properties decrease after rotator cuff tears in a rat model. *Journal of Orthopaedic Research* 2012;30:1435-9.
- [24] Goutallier D. Comments on: “Arthroscopic treatment of rotator cuff tear in the over-60s: Repair is preferable to isolated acromioplasty-tenotomy in the short term,” by C. Dezaly, F. Sirveaux, R. Philippe, F. Wein-Remy, J. Sedaghatian, O. Roche and D. Molé, published in *Orthop Traumatol Surg Res* 2011;97S:S125–30. *Orthopaedics & Traumatology: Surgery & Research* 2012;98:618-9.
- [25] Mather IIIRC, Koenig L, Acevedo D, Dall TM, Gallo P, Romeo A, et al. The Societal and Economic Value of Rotator Cuff Repair. *The Journal of Bone & Joint Surgery* 2013;95:1993-2000.
- [26] Plate JF, Brown PJ, Walters J, Clark JA, Smith TL, Freehill MT, et al. Advanced Age Diminishes Tendon-to-Bone Healing in a Rat Model of Rotator Cuff Repair. *Am J Sports Med* 2014.
- [27] Miller BS, Downie BK, Kohen RB, Kijek T, Lesniak B, Jacobson JA, et al. When Do Rotator Cuff Repairs Fail? Serial Ultrasound Examination After Arthroscopic Repair of Large and Massive Rotator Cuff Tears. *Am J Sports Med* 2011;39:2064-70.
- [28] Gelse K. Collagens—structure, function, and biosynthesis. *Advanced Drug Delivery Reviews* 2003;55:1531-46.
- [29] Place ES, Evans ND, Stevens MM. Complexity in biomaterials for tissue engineering. *Nature Materials* 2009;8:457-70.
- [30] Davies JA. Extracellular matrix. *eLS* 2001.
- [31] Listen to Bone Quality: How Ultrasound Helps to Reveal Microstructure and Elastic Function in Bone.

- [32] Harley BA, Lynn AK, Wissner-Gross Z, Bonfield W, Yannas IV, Gibson LJ. Design of a multiphase osteochondral scaffold. II. Fabrication of a mineralized collagen–glycosaminoglycan scaffold. *Journal of Biomedical Materials Research Part A* 2010;92A:1066-77.
- [33] Hortensius RA, Harley BA. The use of bioinspired alterations in the glycosaminoglycan content of collagen-GAG scaffolds to regulate cell activity. *Biomaterials* 2013;34:7645-52.
- [34] O'Brien F. Influence of freezing rate on pore structure in freeze-dried collagen-GAG scaffolds. *Biomaterials* 2004;25:1077-86.
- [35] Caliari SR, Harley BAC. The effect of anisotropic collagen-GAG scaffolds and growth factor supplementation on tendon cell recruitment, alignment, and metabolic activity. *Biomaterials* 2011;32:5330-40.
- [36] O'Brien FJ, Harley BA, Yannas IV, Gibson L. Influence of freezing rate on pore structure in freeze-dried collagen-GAG scaffolds. *Biomaterials* 2004;25:1077-86.
- [37] Caliari SR, Harley BAC. Composite growth factor supplementation strategies to enhance tenocyte bioactivity in aligned collagen-GAG scaffolds. *Tissue Eng Pt A* 2013;19:1100-12.
- [38] Yannas IV, Tzeranis DS, Harley BA, So PTC. Biologically active collagen-based scaffolds: advances in processing and characterization. *Philosophical Transactions of the Royal Society A: Mathematical, Physical and Engineering Sciences* 2010;368:2123-39.
- [39] Caliari SR, Weisgerber DW, Ramirez MA, Kelkhoff DO, Harley BAC. The influence of collagen–glycosaminoglycan scaffold relative density and microstructural anisotropy on tenocyte bioactivity and transcriptomic stability. *J Mech Behav Biomed* 2012;11:27-40.
- [40] Zhao J, Wang S, Bao J, Sun X, Zhang X, Zhang X, et al. Trehalose maintains bioactivity and promotes sustained release of BMP-2 from lyophilized CDHA scaffolds for enhanced osteogenesis in vitro and in vivo. *PLoS ONE* 2013;8.
- [41] O'Brien FJ, Harley BA, Waller MA, Yannas IV, Gibson LJ, Prendergast PJ. The effect of pore size on permeability and cell attachment in collagen scaffolds for tissue engineering. *Technology and Health Care* 2007;15:3-17.
- [42] Gibson LJ, Ashby MF, Harley BA. *Cellular Materials in Nature and Medicine*: Cambridge University Press; 2010.
- [43] McCoy RJ, Jungreuthmayer C, O'Brien FJ. Influence of flow rate and scaffold pore size on cell behavior during mechanical stimulation in a flow perfusion bioreactor. *Biotechnology and Bioengineering* 2012;109:1583-94.
- [44] Zeltinger J, Sherwood JK, Graham DA, Mueller R, Griffith LG. Effect of pore size and void fraction on cellular adhesion, proliferation, and matrix deposition. *Tissue Engineering* 2001;7:557-72.
- [45] Weisgerber DW, Kelkhoff DO, Caliari SR, Harley BAC. The impact of discrete compartments of a multi-compartment collagen–GAG scaffold on overall construct biophysical properties. *Journal of the Mechanical Behavior of Biomedical Materials* 2013;28:26-36.
- [46] Caliari SR, Mozdzen LC, Armitage O, Oyen ML, Harley BAC. Award Winner in the Young Investigator Category, 2014 Society for Biomaterials Annual Meeting and Exposition, Denver, Colorado, April 16–19, 2014: Periodically perforated core–shell collagen biomaterials balance cell infiltration, bioactivity, and mechanical properties. *J Biomed Res A* 2014;102:917-27.
- [47] Fan J, Jia X, Huang Y, Fu BM, Fan Y. Greater scaffold permeability promotes growth of osteoblastic cells in a perfused bioreactor. *Journal of Tissue Engineering and Regenerative Medicine* 2013;n/a-n/a.

- [48] Murphy CM, Haugh MG, O'Brien FJ. The effect of mean pore size on cell attachment, proliferation and migration in collagen–glycosaminoglycan scaffolds for bone tissue engineering. *Biomaterials* 2010;31:461-6.
- [49] O'Brien FJ, Harley BA, Yannas IV, Gibson LJ. The effect of pore size on cell adhesion in collagen-GAG scaffolds. *Biomaterials* 2005;26:433-41.
- [50] Nehrer S, Breinan HA, Ramappa A, Young G, Shortkroff S, Louie LK, et al. Matrix collagen type and pore size influence behaviour of seeded canine chondrocytes. *Biomaterials* 1997;18:769-76.
- [51] Zhang Q, Lu H, Kawazoe N, Chen G. Pore size effect of collagen scaffolds on cartilage regeneration. *Acta Biomaterialia* 2014;10:2005-13.
- [52] Gonnerman EA, Kelkhoff DO, McGregor LM, Harley BAC. The promotion of HL-1 cardiomyocyte beating using anisotropic collagen-GAG scaffolds. *Biomaterials* 2012;33:8812-21.
- [53] Yao X, Peng R, Ding J. Effects of aspect ratios of stem cells on lineage commitments with and without induction media. *Biomaterials* 2013;34:930-9.
- [54] Caliri SR, Harley BAC. Collagen-GAG scaffold biophysical properties bias MSC lineage choice in the presence of mixed soluble signals. *Tissue Eng Pt A* 2014.
- [55] Kilian KA, Bugarija B, Lahn BT, Mrksich M. Geometric cues for directing the differentiation of mesenchymal stem cells. *Proceedings of the National Academy of Sciences* 2010;107:4872-7.
- [56] McBeath R, Pirone DM, Nelson CM, Bhadriraju K, Chen CS. Cell shape, cytoskeletal tension, and RhoA regulate stem cell lineage commitment. *Dev Cell* 2004;6:483-95.
- [57] Engler AJ, Sen S, Sweeney HL, Discher DE. Matrix elasticity directs stem cell lineage specification. *Cell* 2006;126:677-89.
- [58] Chaudhuri O, Mooney DJ. Stem-cell differentiation: anchoring cell-fate cues. *Nat Mater* 2012;11:568-9.
- [59] Murphy CM, Matsiko A, Haugh MG, Gleeson JP, O'Brien FJ. Mesenchymal stem cell fate is regulated by the composition and mechanical properties of collagen–glycosaminoglycan scaffolds. *J Mech Behav Biomed* 2012;11:53-62.
- [60] Trappmann B, Gautrot JE, Connelly JT, Strange DGT, Li Y, Oyen ML, et al. Extracellular-matrix tethering regulates stem-cell fate. *Nat Mater* 2012;11:642-9.
- [61] Greiner A, Wendorff JH. Electrospinning: A Fascinating Method for the Preparation of Ultrathin Fibers. *Angewandte Chemie International Edition* 2007;46:5670-703.
- [62] Thorpe CT, Stark RJ, Goodship AE, Birch HL. Mechanical properties of the equine superficial digital flexor tendon relate to specific collagen cross-link levels. *Equine Vet J* 2010;42 Suppl 38:538-43.
- [63] Thorpe CT, Udeze CP, Birch HL, Clegg PD, Screen HRC. Specialization of tendon mechanical properties results from interfascicular differences. *J R Soc Interface* 2012;9:3108-17.
- [64] Moore TLA, Gibson LJ. Modeling modulus reduction in bovine trabecular bone damaged in compression. *Journal of Biomechanical Engineering-Transactions of the Asme* 2001;123:613-22.
- [65] Michel MC, Guo XDE, Gibson LJ, McMahon TA, Hayes WC. Compressive Fatigue Behavior of Bovine Trabecular Bone. *Journal of Biomechanics* 1993;26:453-63.
- [66] Wopenka B, Kent A, Pasteris JD, Yoon Y, Thomopoulos S. The tendon-to-bone transition of the rotator cuff: a preliminary Raman spectroscopic study documenting the gradual mineralization across the insertion in rat tissue samples. *Appl Spectrosc* 2008;62:1285-94.

- [67] Harley B, Leung J, Silva E, Gibson L. Mechanical characterization of collagen–glycosaminoglycan scaffolds. *Acta Biomater* 2007;3:463-74.
- [68] Caliri SR, Grier WK, Weisgerber DW, Mahmassani Z, Boppart MD, Harley BAC. Collagen scaffolds incorporating coincident patterns of instructive structural and biochemical cues for osteotendinous junction engineering. *Advanced healthcare materials* 2015;4:831-7.
- [69] Weisgerber DW, Kelkhoff DO, Caliri SR, Harley BAC. The impact of discrete compartments of a multi-compartment collagen-GAG scaffold on overall construct biophysical properties. *J Mech Behav Biomed Mater* 2013;28:26-36.
- [70] Keays SL, Bullock-Saxton JE, Keays AC, Newcombe PA, Bullock MI. A 6-Year Follow-up of the Effect of Graft Site on Strength, Stability, Range of Motion, Function, and Joint Degeneration After Anterior Cruciate Ligament Reconstruction Patellar Tendon Versus Semitendinosus and Gracilis Tendon Graft. *Am J Sports Med* 2007;35:729-39.
- [71] Mathew AP, Oksman K, Pierron D, Harmand M-F. Biocompatible Fibrous Networks of Cellulose Nanofibres and Collagen Crosslinked Using Genipin: Potential as Artificial Ligament/Tendons. *Macromolecular Bioscience* 2012;n/a-n/a.
- [72] Caliri SR, Ramirez MA, Harley BAC. The development of collagen-GAG scaffold-membrane composites for tendon tissue engineering. *Biomaterials* 2011;32:8990-8.
- [73] Levingstone TJ, Matsiko A, Dickson GR, O'Brien FJ, Gleeson JP. A biomimetic multi-layered collagen-based scaffold for osteochondral repair. *Acta Biomaterialia* 2014;10:1996-2004.
- [74] Kanungo BP, Silva E, Vliet KV, Gibson LJ. Characterization of mineralized collagen–glycosaminoglycan scaffolds for bone regeneration. *Acta Biomaterialia* 2008;4:490-503.
- [75] Ferreira AM, Gentile P, Chiono V, Ciardelli G. Collagen for bone tissue regeneration. *Acta Biomaterialia* 2012;8:3191-200.
- [76] Capito RM, Spector M. Collagen scaffolds for nonviral IGF-1 gene delivery in articular cartilage tissue engineering. *Gene therapy* 2007;14:721-32.
- [77] Harley BA, Freyman TM, Wong MQ, Gibson LJ. A New Technique for Calculating Individual Dermal Fibroblast Contractile Forces Generated within Collagen-GAG Scaffolds. *Biophysical Journal* 2007;93:2911-22.
- [78] Olde Damink LHH, Dijkstra PJ, Van Luyn MJA, Van Wachem PB, Nieuwenhuis P, Feijen J. Cross-linking of dermal sheep collagen using a water-soluble carbodiimide. *Biomaterials* 1996;17:765-73.
- [79] Liu X, Wu H, Byrne M, Krane S, Jaenisch R. Type III collagen is crucial for collagen I fibrillogenesis and for normal cardiovascular development. *Proceedings of the National Academy of Sciences* 1997;94:1852-6.
- [80] Kikuchi M, Itoh S, Ichinose S, Shinomiya K, Tanaka J. Self-organization mechanism in a bone-like hydroxyapatite/collagen nanocomposite synthesized in vitro and its biological reaction in vivo. *Biomaterials* 2001;22:1705-11.
- [81] Smith LJ, Deymier AC, Boyle JJ, Li Z, Linderman SW, Pasteris JD, et al. Tunability of collagen matrix mechanical properties via multiple modes of mineralization. *Interface Focus* 2016;6:20150070.
- [82] Giannoni P, Lazzarini E, Ceseracciu L, Barone AC, Quarto R, Scaglione S. Design and characterization of a tissue-engineered bilayer scaffold for osteochondral tissue repair. *Journal of Tissue Engineering and Regenerative Medicine* 2012;n/a-n/a.
- [83] Baud'huin M, Solban N, Cornwall-Brady M, Sako D, Kawamoto Y, Liharska K, et al. A soluble bone morphogenetic protein type IA receptor increases bone mass and bone strength. *Proceedings of the National Academy of Sciences* 2012;109:12207-12.

- [84] Screen HRC, Shelton JC, Bader DL, Lee DA. Cyclic tensile strain upregulates collagen synthesis in isolated tendon fascicles. *Biochemical and Biophysical Research Communications* 2005;336:424-9.
- [85] Liang M-S, Koobatian M, Lei P, Swartz DD, Andreadis ST. Differential and synergistic effects of mechanical stimulation and growth factor presentation on vascular wall function. *Biomaterials* 2013;34:7281-91.
- [86] Qiu Y, Lei J, Koob TJ, Temenoff JS. Cyclic tension promotes fibroblastic differentiation of human MSCs cultured on collagen-fibre scaffolds. *Journal of Tissue Engineering and Regenerative Medicine* 2014:n/a-n/a.
- [87] Santos E, Hernández RM, Pedraz JL, Orive G. Novel advances in the design of three-dimensional bio-scaffolds to control cell fate: translation from 2D to 3D. *Trends Biotechnol* 2012;30:331-41.
- [88] Caliari SR, Harley BA. Composite growth factor supplementation strategies to enhance tenocyte bioactivity in aligned collagen-GAG scaffolds. *Tissue Eng Part A* 2013;19:1100-12.
- [89] Borselli C, Storrie H, Benesch-Lee F, Shvartsman D, Cezar C, Lichtman JW, et al. Functional muscle regeneration with combined delivery of angiogenesis and myogenesis factors. *Proc Natl Acad Sci U S A* 2010;107:3287-92.
- [90] Tan S-L, Ahmad RE, Ahmad TS, Merican AM, Abbas AA, Ng WM, et al. Effect of growth differentiation factor 5 on the proliferation and tenogenic differentiation potential of human mesenchymal stem cells in vitro. *Cells Tissues Organs* 2012;196:325-38.
- [91] Cheng X, Tsao C, Sylvia VL, Cornet D, Nicolella DP, Bredbenner TL, et al. Platelet-derived growth-factor-releasing aligned collagen–nanoparticle fibers promote the proliferation and tenogenic differentiation of adipose-derived stem cells. *Acta Biomater* 2014;10:1360-9.
- [92] Park A, Hogan MV, Kesturu GS, James R, Balian G, Chhabra AB. Adipose-derived mesenchymal stem cells treated with growth differentiation factor-5 express tendon-specific markers. *Tissue Eng Pt A* 2010;16:2941-51.
- [93] Aigner A, Butscheid M, Kunkel P, Krause E, Lamszus K, Wellstein A, et al. An FGF-binding protein (FGF-BP) exerts its biological function by parallel paracrine stimulation of tumor cell and endothelial cell proliferation through FGF-2 release. *International Journal of Cancer* 2001;92:510-7.
- [94] Lee MH, Adams CS, Boettiger D, DeGrado WF, Shapiro IM, Composto RJ, et al. Adhesion of MC3T3-E1 cells to RGD peptides of different flanking residues: Detachment strength and correlation with long-term cellular function. *Journal of Biomedical Materials Research Part A* 2007;81A:150-60.
- [95] Odedra D, Chiu LLY, Shoichet M, Radisic M. Endothelial cells guided by immobilized gradients of vascular endothelial growth factor on porous collagen scaffolds. *Acta Biomater* 2011;7:3027-35.
- [96] Madl CM, Mehta M, Duda GN, Heilshorn SC, Mooney DJ. Presentation of BMP-2 mimicking peptides in 3D hydrogels directs cell fate commitment in osteoblasts and mesenchymal stem cells. *Biomacromolecules* 2014;15:445-55.
- [97] Hu W-W, Wang Z, Krebsbach PH. Virus immobilization on biomaterial scaffolds through biotin–avidin interaction for improving bone regeneration. *J Tissue Eng Regen M* 2013:n/a-n/a.
- [98] Hudalla GA, Murphy WL. Immobilization of peptides with distinct biological activities onto stem cell culture substrates using orthogonal chemistries. *Langmuir* 2010;26:6449-56.
- [99] Culver JC, Hoffmann JC, Poché RA, Slater JH, West JL, Dickinson ME. Three-dimensional biomimetic patterning in hydrogels to guide cellular organization. *Adv Mater* 2012;24:2344-8.

- [100] Martin TA, Caliri SR, Williford PD, Harley BA, Bailey RC. The generation of biomolecular patterns in highly porous collagen-GAG scaffolds using direct photolithography. *Biomaterials* 2011;32:3949-57.
- [101] Banks JM, Mozden LC, Harley BAC, Bailey RC. The combined effects of matrix stiffness and growth factor immobilization on the bioactivity and differentiation capabilities of adipose-derived stem cells. *Biomaterials* 2014;35:8951-9.
- [102] Sathy BN, Mony U, Menon D, Bhaskaran V, Mikos AG, Nair S. Bone tissue engineering with multi-layered scaffolds - Part I: An approach for vascularizing engineered constructs in vivo. *Tissue Engineering Part A* 2015.
- [103] Sathy BN, Watson BM, Kinard LA, Spicer PP, Dahlin RL, Mikos AG, et al. Bone tissue engineering with multi-layered scaffolds - Part II: Combining vascularization with bone formation in critical sized bone defect. *Tissue Engineering Part A* 2015.
- [104] Ghezzi CE, Marelli B, Donelli I, Alessandrino A, Freddi G, Nazhat SN. Multilayered dense collagen-silk fibroin hybrid: a platform for mesenchymal stem cell differentiation towards chondrogenic and osteogenic lineages. *Journal of Tissue Engineering and Regenerative Medicine* 2015:n/a-n/a.
- [105] Levingstone TJ, Thompson E, Matsiko A, Schepens A, Gleeson JP, O'Brien FJ. Multi-layered collagen-based scaffolds for osteochondral defect repair in rabbits. *Acta Biomaterialia* 2016;32:149-60.
- [106] Levingstone TJ, Ramesh A, Brady RT, Brama PAJ, Kearney C, Gleeson JP, et al. Cell-free multi-layered collagen-based scaffolds demonstrate layer specific regeneration of functional osteochondral tissue in caprine joints. *Biomaterials* 2016;87:69-81.
- [107] Qu J, Thoreson AR, Chen Q, An K-N, Amadio PC, Zhao C. Tendon gradient mineralization for tendon to bone interface integration. *Journal of Orthopaedic Research* 2013:n/a-n/a.
- [108] Lipner J, Liu W, Liu Y, Boyle J, Genin GM, Xia Y, et al. The mechanics of PLGA nanofiber scaffolds with biomimetic gradients in mineral for tendon-to-bone repair. *Journal of the Mechanical Behavior of Biomedical Materials* 2014;40:59-68.
- [109] Liu W, Lipner J, Xie J, Manning CN, Thomopoulos S, Xia Y. Nanofiber Scaffolds with Gradients in Mineral Content for Spatial Control of Osteogenesis. *ACS Appl Mater Interfaces* 2014;6:2842-9.
- [110] Kim TH, An DB, Oh SH, Kang MK, Song HH, Lee JH. Creating stiffness gradient polyvinyl alcohol hydrogel using a simple gradual freezing-thawing method to investigate stem cell differentiation behaviors. *Biomaterials* 2015;40:51-60.
- [111] Tseng P, Di Carlo D. Substrates with patterned extracellular matrix and subcellular stiffness gradients reveal local biomechanical responses. *Adv Mater* 2014;26:1242-7.
- [112] Xie J, Li X, Lipner J, Manning CN, Schwartz AG, Thomopoulos S, et al. "Aligned-to-random" nanofiber scaffolds for mimicking the structure of the tendon-to-bone insertion site. *Nanoscale* 2010;2.
- [113] Lu J, Zou X, Zhao Z, Mu Z, Zhao Y, Gu Z. Cell Orientation Gradients on an Inverse Opal Substrate. *ACS Appl Mater Interfaces* 2015;7:10091-5.
- [114] Akar B, Jiang B, Somo SI, Appel AA, Larson JC, Tichauer KM, et al. Biomaterials with persistent growth factor gradients in vivo accelerate vascularized tissue formation. *Biomaterials* 2015;72:61-73.

- [115] Almodóvar J, Crouzier T, Selimović Š, Boudou T, Khademhosseini A, Picart C. Gradients of physical and biochemical cues on polyelectrolyte multilayer films generated via microfluidics. *Lab on a Chip* 2013;13.
- [116] Min HK, Oh SH, Lee JM, Im GI, Lee JH. Porous membrane with reverse gradients of PDGF-BB and BMP-2 for tendon-to-bone repair: In vitro evaluation on adipose-derived stem cell differentiation. *Acta Biomaterialia* 2014;10:1272-9.
- [117] Mahadik BP, Wheeler TD, Skertich LJ, Kenis PJA, Harley BAC. Microfluidic Generation of Gradient Hydrogels to Modulate Hematopoietic Stem Cell Culture Environment. *Advanced Healthcare Materials* 2014;3:449-58.
- [118] Almodóvar J, Guillot R, Monge C, Vollaire J, Selimović Š, Coll J-L, et al. Spatial patterning of BMP-2 and BMP-7 on biopolymeric films and the guidance of muscle cell fate. *Biomaterials* 2014;35:3975-85.
- [119] Alsop AT, Pence JC, Weisgerber DW, Harley BAC, Bailey RC. Photopatterning of vascular endothelial growth factor within collagen-glycosaminoglycan scaffolds can induce a spatially confined response in human umbilical vein endothelial cells. *Acta Biomaterialia* 2014;10:4715-22.
- [120] Grim JC, Marozas IA, Anseth KS. Thiol-ene and photo-cleavage chemistry for controlled presentation of biomolecules in hydrogels. *Journal of Controlled Release* 2015;219:95-106.
- [121] Xu H, Ling XY, van Bennekum J, Duan X, Ludden MJW, Reinhoudt DN, et al. Microcontact Printing of Dendrimers, Proteins, and Nanoparticles by Porous Stamps. *Journal of the American Chemical Society* 2009;131:797-803.
- [122] Gibson LJ, Ashby MF, Karam GN, Wegst U, Shercliff HR. The mechanical-properties of natural materials 2. Microstructures for mechanical efficiency. *Philos Trans R Soc Lond A* 1995;450:141-62.
- [123] Karam GN, Gibson LJ. Biomimicking of animal quills and plant stems - natural cylindrical-shells with foam cores. *Mater Sci Eng C Biomim Mater Sens Syst* 1994;2:113-32.
- [124] Song J, Ortiz C, Boyce MC. Threat-protection mechanics of an armored fish. *Journal of the Mechanical Behavior of Biomedical Materials* 2011;4:699-712.
- [125] Lin YS, Wei CT, Olevsky EA, Meyers MA. Mechanical properties and the laminate structure of Arapaima gigas scales. *Journal of the Mechanical Behavior of Biomedical Materials* 2011;4:1145-56.
- [126] Yang W, Chen IH, Gludovatz B, Zimmermann EA, Ritchie RO, Meyers MA. Natural Flexible Dermal Armor. *Advanced Materials* 2013;25:31-48.
- [127] Krauss S, Monsonego-Ornan E, Zelzer E, Fratzl P, Shahar R. Mechanical Function of a Complex Three-Dimensional Suture Joining the Bony Elements in the Shell of the Red-Eared Slider Turtle. *Advanced Materials* 2009;21:407-12.
- [128] Li Y, Ortiz C, Boyce M. Stiffness and strength of suture joints in nature. *Physical Review E* 2011;84.
- [129] Zouani OF, Kalisky J, Ibarboure E, Durrieu M-C. Effect of BMP-2 from matrices of different stiffnesses for the modulation of stem cell fate. *Biomaterials* 2013;34:2157-66.
- [130] Tan S, Fang JY, Yang Z, Nimni ME, Han B. The synergetic effect of hydrogel stiffness and growth factor on osteogenic differentiation. *Biomaterials* 2014;35:5294-306.
- [131] Subramony SD, Dargis BR, Castillo M, Azeloglu EU, Tracey MS, Su A, et al. The guidance of stem cell differentiation by substrate alignment and mechanical stimulation. *Biomaterials* 2013;34:1942-53.

- [132] Banks JM, Mozdzen LC, Harley BAC, Bailey RC. The combined effects of matrix stiffness and growth factor immobilization on the bioactivity and differentiation capabilities of adipose-derived stem cells. *Biomaterials*.
- [133] Lamplot JD, Angeline M, Angeles J, Beederman M, Wagner E, Rastegar F, et al. Distinct Effects of Platelet-Rich Plasma and BMP13 on Rotator Cuff Tendon Injury Healing in a Rat Model. *Am J Sports Med* 2014;42:2877-87.
- [134] Gomes M. Tendon regeneration: understanding tissue physiology and development to engineer functional substitutes. Boston, MA: Elsevier; 2015.
- [135] Thomopoulos S. Variation of biomechanical, structural, and compositional properties along the tendon to bone insertion site. *Journal of Orthopaedic Research* 2003;21:413-9.
- [136] Caliari S, Harley B. Collagen scaffolds incorporating coincident gradations of structural and biochemical instructive cues for osteotendinous junction engineering,. In Preparation 2014.
- [137] James R, Kesturu G, Balian G, Chhabra AB. Tendon: biology, biomechanics, repair, growth factors, and evolving treatment options. *J Hand Surg Am* 2008;33:102-12.
- [138] Xu Y, Murrell GA. The basic science of tendinopathy. *Clin Orthop Relat Res* 2008;466:1528-38.
- [139] Liu Y, Ramanath HS, Wang DA. Tendon tissue engineering using scaffold enhancing strategies. *Trends Biotechnol* 2008;26:201-9.
- [140] O'Brien FJ, Harley BA, Yannas IV, Gibson LJ. The effect of pore size on cell adhesion in collagen-GAG scaffolds. *Biomaterials* 2005;26:433-41.
- [141] Chamberlain LJ, Yannas IV, Hsu H-P, Strichartz G, Spector M. Collagen-GAG substrate enhances the quality of nerve regeneration through collagen tubes up to level of autograft. *Exper Neurol* 1998;154:315-29.
- [142] Freyman TM, Yannas IV, Pek YS, Yokoo R, Gibson LJ. Micromechanics of fibroblast contraction of a collagen-GAG matrix. *Exp Cell Res* 2001;269:140-53.
- [143] Harley BA, Kim HD, Zaman MH, Yannas IV, Lauffenburger DA, Gibson LJ. Microarchitecture of three-dimensional scaffolds influences cell migration behavior via junction interactions. *Biophys J* 2008;95:4013-24.
- [144] Caliari SR, Grier WK, Weisgerber DW, Mahmassani Z, Boppart MD, Harley BAC. Collagen scaffolds incorporating coincident gradations of instructive structural and biochemical cues for osteotendinous junction engineering. *Advanced healthcare materials* 2015;4:831-7.
- [145] Harley BA, Lynn AK, Wissner-Gross Z, Bonfield W, Yannas IV, Gibson LJ. Design of a multiphase osteochondral scaffold III: fabrication of layered scaffolds with continuous interfaces. *J Biomed Mater Res A* 2010;92:1078-93.
- [146] Quinlan E, Partap S, Azevedo MM, Jell G, Stevens MM, O'Brien FJ. Hypoxia-mimicking bioactive glass/collagen glycosaminoglycan composite scaffolds to enhance angiogenesis and bone repair. *Biomaterials* 2015;52:358-66.
- [147] Lyons FG, Gleeson JP, Partap S, Coghlan K, O'Brien FJ. Novel microhydroxyapatite particles in a collagen scaffold: a bioactive bone void filler? *Clin Orthop Relat Res* 2014;472:1318-28.
- [148] Weisgerber DW, Caliari SR, Harley BAC. Mineralized collagen scaffolds induce hMSC osteogenesis and matrix remodeling. *Biomater Sci* 2015;3:533-42.
- [149] McCoy RJ, Widaa A, Watters KM, Wuerstle M, Stallings RL, Duffy GP, et al. Orchestrating osteogenic differentiation of mesenchymal stem cells—identification of placental growth factor as a mechanosensitive gene with a pro-osteogenic role. *STEM CELLS* 2013;31:2420-31.

- [150] Mullen LM, Best SM, Ghose S, Wardale J, Rushton N, Cameron RE. Bioactive IGF-1 release from collagen-GAG scaffold to enhance cartilage repair in vitro. *J Mater Sci Mater Med* 2015;26:5325.
- [151] Miyagi Y, Chiu LL, Cimini M, Weisel RD, Radisic M, Li RK. Biodegradable collagen patch with covalently immobilized VEGF for myocardial repair. *Biomaterials* 2011;32:1280-90.
- [152] Alsop AT, Pence JC, Weisgerber DW, Harley BAC, Bailey RC. Photopatterning of VEGF within collagen-GAG scaffolds can induce a spatially confined response in human umbilical vein endothelial cells. *Acta Biomater* 2014;10:4715-22.
- [153] Banks JM, Mozdzen LC, Harley BAC, Bailey RC. The combined effects of matrix stiffness and growth factor immobilization on the bioactivity and differentiation capabilities of adipose-derived stem cells. *Biomaterials* 2014;35:8951-9.
- [154] Hortensius RA, Becraft JR, Pack DW, Harley BAC. The effect of glycosaminoglycan content on polyethylenimine-based gene delivery within three-dimensional collagen-GAG scaffolds. *Biomater Sci* 2015;3:645-54.
- [155] Murphy CM, Haugh MG, O'Brien FJ. The effect of mean pore size on cell attachment, proliferation and migration in collagen-glycosaminoglycan scaffolds for bone tissue engineering. *Biomaterials* 2010;31:461-6.
- [156] Gibson LJ, Ashby MF, Harley BA. *Cellular materials in nature and medicine*. Cambridge, U.K.: Cambridge University Press; 2010.
- [157] Yannas IV, Lee E, Orgill DP, Skrabut EM, Murphy GF. Synthesis and characterization of a model extracellular matrix that induces partial regeneration of adult mammalian skin. *Proc Nat Acad Sci* 1989;86:933-7.
- [158] Harley BA, Leung JH, Silva EC, Gibson LJ. Mechanical characterization of collagen-glycosaminoglycan scaffolds. *Acta Biomater* 2007;3:463-74.
- [159] Ma Z, He W, Yong T, Ramakrishna S. Grafting of Gelatin on Electrospun Poly(caprolactone) Nanofibers to Improve Endothelial Cell Spreading and Proliferation and to Control Cell Orientation. *Tissue Engineering* 2005;11:1149-58.
- [160] Caliar SR, Weisgerber DW, Ramirez MA, Kelkhoff DO, Harley BAC. The influence of collagen-glycosaminoglycan scaffold relative density and microstructural anisotropy on tenocyte bioactivity and transcriptomic stability. *J Mech Behav Biomed Mater* 2012;11:27-40.
- [161] Kim D, Monaco E, Maki A, de Lima AS, Kong HJ, Hurley WL, et al. Morphologic and transcriptomic comparison of adipose- and bone-marrow-derived porcine stem cells cultured in alginate hydrogels. *Cell Tissue Res* 2010;341:359-70.
- [162] Tierney CM, Jaasma MJ, O'Brien FJ. Osteoblast activity on collagen-GAG scaffolds is affected by collagen and GAG concentrations. *J Biomed Mater Res A* 2009;91A:92-101.
- [163] Kim YJ, Sah RLY, Doong JYH, Grodzinsky AJ. Fluorometric assay of DNA in cartilage explants using Hoechst 33258. *Analytical biochemistry* 1988;174:168-76.
- [164] Maganaris CN, Paul JP. In vivo human tendon mechanical properties. *J Physiol* 1999;521 Pt 1:307-13.
- [165] Baker BM, Shah RP, Silverstein AM, Esterhai JL, Burdick JA, Mauck RL. Sacrificial nanofibrous composites provide instruction without impediment and enable functional tissue formation. *Proc Natl Acad Sci U S A* 2012;109:14176-81.
- [166] Mironov V, Boland T, Trusk T, Forgacs G, Markwald RR. Organ printing: computer-aided jet-based 3D tissue engineering. *Trends Biotechnol* 2003;21:157-61.
- [167] Serra T, Planell JA, Navarro M. High-resolution PLA-based composite scaffolds via 3-D printing technology. *Acta Biomater* 2013;9:5521-30.

- [168] Speck T, Burgert I. Plant stems: functional design and mechanics. *Ann Rev Mater Res* 2011;41:169-93.
- [169] Maganaris CN, Paul JP. In vivo human tendinous tissue stretch upon maximum muscle force generation. *J Biomech* 2000;33:1453-9.
- [170] Lichtwark GA, Wilson AM. In vivo mechanical properties of the human Achilles tendon during one-legged hopping. *Journal of Experimental Biology* 2005;208:4715-25.
- [171] Abrahams M. Mechanical behaviour of tendon *In vitro*. *Medical and Biological Engineering* 1967;5:433-43.
- [172] Maganaris CN, Paul JP. In vivo human tendon mechanical properties. *J Physiol* 1999;521:307-13.
- [173] Killian ML, Cavinatto L, Galatz LM, Thomopoulos S. Recent advances in shoulder research. *Arthritis Research & Therapy* 2012;14.
- [174] Li X, Xie J, Lipner J, Yuan X, Thomopoulos S, Xia Y. Nanofiber Scaffolds with Gradations in Mineral Content for Mimicking the Tendon-to-Bone Insertion Site. *Nano Letters* 2009;9:2763-8.
- [175] Weisgerber DW, Caliri SR, Harley BAC. Mineralized collagen scaffolds induce hMSC osteogenesis and matrix remodeling. *Biomater Sci* 2015;3:533-42.
- [176] Mozdzen LC, Rodgers R, Banks JM, Bailey RC, Harley BAC. Increasing the strength and bioactivity of collagen scaffolds using customizable arrays of 3D-printed polymer fibers. *Acta Biomaterialia*.
- [177] Lionello G, Sirieix C, Baleani M. An effective procedure to create a speckle pattern on biological soft tissue for digital image correlation measurements. *Journal of the Mechanical Behavior of Biomedical Materials* 2014;39:1-8.
- [178] Chandrashekar N, Slauterbeck J, Hashemi J. Effects of cyclic loading on the tensile properties of human patellar tendon. *The Knee* 2012;19:65-8.
- [179] Jones E. Improved Digital Image Correlation (DIC). 2013.
- [180] Szabo B, Babuska I. Finite Element Analysis. New York: John Wiley and Sons; 1991.
- [181] Zienkiewicz OC. The Finite Element Method. 3rd ed. New York: McGraw-Hill; 1977.
- [182] Abd Elhady AA. Stress and strain concentration factors for plate with small notch subjected to biaxial loading – Three dimensional finite element analysis. *Ain Shams Engineering Journal* 2010;1:139-45.
- [183] Marino M, Vairo G. Stress and strain localization in stretched collagenous tissues via a multiscale modelling approach. *Comput Methods Biomech Biomed Engin* 2014;17:11-30.
- [184] Sano H, Hatta T, Yamamoto N, Itoi E. Stress Distribution Within Rotator Cuff Tendons With a Crescent-Shaped and an L-Shaped Tear. *Am J Sports Med* 2013;41:2262-9.
- [185] Pu J, Komvopoulos K. Mechanical properties of electrospun bilayer fibrous membranes as potential scaffolds for tissue engineering. *Acta Biomaterialia* 2014;10:2718-26.
- [186] Serra T, Planell JA, Navarro M. High-resolution PLA-based composite scaffolds via 3-D printing technology. *Acta Biomaterialia* 2013;9:5521-30.
- [187] Mozdzen LC, Harley BAC. Multi-compartment collagen scaffolds with geometric interdigitations across the interface to dissipate stress concentrations. 2016, *In Preparation*.
- [188] Atesok K, Doral MN, Karlsson J, Egol KA, Jazrawi LM, Coelho PG, et al. Multilayer scaffolds in orthopaedic tissue engineering. *Knee Surg Sports Traumatol Arthrosc* 2014:1-9.
- [189] Chen S, Nakamoto T, Kawazoe N, Chen G. Engineering multi-layered skeletal muscle tissue by using 3D microgrooved collagen scaffolds. *Biomaterials* 2015;73:23-31.

- [190] Farnebo S, Woon CY, Kim M, Pham H, Chang J. Reconstruction of the Tendon–Bone Insertion With Decellularized Tendon–Bone Composite Grafts: Comparison With Conventional Repair. *The Journal of Hand Surgery* 2014;39:65-74.
- [191] Chaudhuri O, Gu L, Klumpers D, Darnell M, Bencherif SA, Weaver JC, et al. Hydrogels with tunable stress relaxation regulate stem cell fate and activity. *Nature Materials* 2016;15:326-34.
- [192] Foolen J, Janssen-van den Broek MWJT, Baaijens FPT. Synergy between Rho signaling and matrix density in cyclic stretch-induced stress fiber organization. *Acta Biomaterialia* 2014;10:1876-85.
- [193] Caliari SR, Weisgerber DW, Grier WK, Mahmassani Z, Boppart MD, Harley BAC. Collagen Scaffolds Incorporating Coincident Gradations of Instructive Structural and Biochemical Cues for Osteotendinous Junction Engineering. *Advanced Healthcare Materials* 2015:n/a-n/a.
- [194] Armitage OE, Oyen ML. Hard-Soft Tissue Interface Engineering. In: Bertassoni LE, Coelho PG, editors. *Engineering Mineralized and Load Bearing Tissues*: Springer International Publishing; 2015. p. 187-204.
- [195] Bunker DLJ, Ilie V, Ilie V, Nicklin S. Tendon to bone healing and its implications for surgery. *Muscles Ligaments Tendons J* 2014;4:343-50.
- [196] Liu Y, Birman V, Chen C, Thomopoulos S, Genin GM. Mechanisms of Bimaterial Attachment at the Interface of Tendon to Bone. *J Eng Mater Technol* 2011;133.
- [197] Lu HH, Thomopoulos S. Functional Attachment of Soft Tissues to Bone: Development, Healing, and Tissue Engineering. *Annual Review of Biomedical Engineering* 2013;15:201-26.
- [198] Lynn AK, Best SM, Cameron RE, Harley BA, Yannas IV, Gibson LJ, et al. Design of a multiphase osteochondral scaffold. I. Control of chemical composition. *Journal of Biomedical Materials Research Part A* 2010;92A:1057-65.
- [199] He J, Zhang W, Liu Y, Li X, Li D, Jin Z. Design and fabrication of biomimetic multiphased scaffolds for ligament-to-bone fixation. *Materials Science and Engineering: C* 2015;50:12-8.
- [200] Chainani A, Hippensteel KJ, Kishan A, Garrigues NW, Ruch DS, Guilak F, et al. Multilayered Electrospun Scaffolds for Tendon Tissue Engineering. *Tissue Engineering Part A* 2013;19:2594-604.
- [201] Hu Y, Birman V, Deymier-Black A, Schwartz Andrea G, Thomopoulos S, Genin Guy M. Stochastic Interdigitation as a Toughening Mechanism at the Interface between Tendon and Bone. *Biophysical Journal* 2015;108:431-7.
- [202] Harley BA, Lynn AK, Wissner-Gross Z, Bonfield W, Yannas IV, Gibson LJ. Design of a multiphase osteochondral scaffold III: Fabrication of layered scaffolds with continuous interfaces. *Journal of Biomedical Materials Research Part A* 2010;92A:1078-93.
- [203] Dunlop JWC, Weinkamer R, Fratzl P. Artful interfaces within biological materials. *Materials Today* 2011;14:70-8.
- [204] Kim Y-t, Haftel VK, Kumar S, Bellamkonda RV. The role of aligned polymer fiber-based constructs in the bridging of long peripheral nerve gaps. *Biomaterials* 2008;29:3117-27.
- [205] Chew SY, Mi R, Hoke A, Leong KW. Aligned Protein–Polymer Composite Fibers Enhance Nerve Regeneration: A Potential Tissue-Engineering Platform. *Advanced functional materials* 2007;17:1288-96.

- [206] Kapoor A, Caporali EHG, Kenis PJA, Stewart MC. Microtopographically patterned surfaces promote the alignment of tenocytes and extracellular collagen. *Acta Biomater* 2010;6:2580-9.
- [207] Chaubaroux C, Perrin-Schmitt F, Senger B, Vidal L, Voegel J-C, Schaaf P, et al. Cell Alignment Driven by Mechanically Induced Collagen Fiber Alignment in Collagen/Alginate Coatings. *Tissue Engineering Part C: Methods* 2015;21:881-8.
- [208] Younesi M, Islam A, Kishore V, Anderson JM, Akkus O. Tenogenic Induction of Human MSCs by Anisotropically Aligned Collagen Biotextiles. *Advanced Functional Materials* 2014;24:5762-70.
- [209] Hsieh H-Y, Camci-Unal G, Huang T-W, Liao R, Chen T-J, Paul A, et al. Gradient static-strain stimulation in a microfluidic chip for 3D cellular alignment. *Lab on a Chip* 2013;14:482-93.
- [210] Jacques P, Lambrecht S, Verheugen E, Pauwels E, Kollias G, Armaka M, et al. Proof of concept: enthesitis and new bone formation in spondyloarthritis are driven by mechanical strain and stromal cells. *Ann Rheum Dis* 2014;73:437-45.
- [211] Legerlotz K, Jones GC, Screen HRC, Riley GP. Cyclic loading of tendon fascicles using a novel fatigue loading system increases interleukin-6 expression by tenocytes. *Scand J Med Sci Sports* 2013;23:31-7.
- [212] Saber S, Zhang AY, Ki SH, Lindsey DP, Smith RL, Riboh J, et al. Flexor tendon tissue engineering: bioreactor cyclic strain increases construct strength. *Tissue Engineering Part A* 2010;16:2085-90.
- [213] Maeda E, Hagiwara Y, Wang JHC, Ohashi T. A new experimental system for simultaneous application of cyclic tensile strain and fluid shear stress to tenocytes in vitro. *Biomed Microdevices* 2013;15:1067-75.
- [214] Anssari-Benam A, Bader DL, Screen HRC. Anisotropic time-dependant behaviour of the aortic valve. *Journal of the Mechanical Behavior of Biomedical Materials* 2011;4:1603-10.
- [215] Tseng L-F, Mather PT, Henderson JH. Shape-memory-actuated change in scaffold fiber alignment directs stem cell morphology. *Acta Biomaterialia* 2013;9:8790-801.
- [216] Caliarì SR, Harley BAC. The effect of anisotropic collagen-GAG scaffolds and growth factor supplementation on tendon cell recruitment, alignment, and metabolic activity. *Biomaterials* 2011;32:5330-40.
- [217] Caliarì SR, Harley BAC. Collagen-GAG scaffold biophysical properties bias MSC lineage selection in the presence of mixed soluble signals. *Tissue Eng A* 2014;20:2463-72.
- [218] Caliarì SR, Harley BAC. Structural and biochemical modification of a collagen scaffold to selectively enhance MSC tenogenic, chondrogenic, and osteogenic differentiation. *Advanced healthcare materials* 2014;3:1086-96.
- [219] Lee JC, Pereira CT, Ren X, Huang W, Weisgerber DW, Yamaguchi DT, et al. Optimizing collagen scaffolds for bone engineering: effects of crosslinking and mineral content on structural contraction and osteogenesis. *J Craniofac Surg* 2015;26:1992-6.
- [220] Ren X, Bischoff D, Weisgerber DW, Lewis MS, Tu V, Yamaguchi DT, et al. Osteogenesis on nanoparticulate mineralized collagen scaffolds via autogenous activation of the canonical BMP receptor signaling pathway. *Biomaterials* 2015;50:107-14.
- [221] Spillmann D, Lindahl U. Glycosaminoglycan-protein interactions: a question of specificity. *Current Opinion in Structural Biology* 1994;4:677-82.
- [222] O'Brien FJ, Harley BA, Yannas IV, Gibson L. Influence of freezing rate on pore structure in freeze-dried collagen-GAG scaffolds. *Biomaterials* 2004;25:1077-86.

- [223] Legerlotz K, Jones GC, Screen HRC, Riley GP. Cyclic loading of tendon fascicles using a novel fatigue loading system increases interleukin-6 expression by tenocytes. *Scand J Med Sci Sports* 2013;23:31-7.
- [224] Anssari-Benam A, Gupta HS, Screen HR. Strain transfer through the aortic valve. *J Biomech Eng* 2012;134:061003.
- [225] Screen HRC, Demirci T, Lynn A, Blackney A, Patel D, Bryant SJ. Fiber composite scaffolds uniquely regulate fibroblast response to cyclic tensile strain. *Int J Exp Pathol* 2011;92:A11-A2.
- [226] Thévenaz P, Delgado-Gonzalo R, Unser M. The Ovuscul. *IEEE Transactions on Pattern Analysis and Machine Intelligence* 2011;33:382-93.
- [227] Karlson WJ, Hsu P-P, Li S, Chien S, McCulloch AD, Omens JH. Measurement of orientation and distribution of cellular alignment and cytoskeletal organization. *Annals of Biomedical Engineering* 1999;27:712-20.
- [228] Berens P. CircStat: a MATLAB toolbox for circular statistics. *J Stat Softw* 2009;31:1-21.
- [229] Screen HR, Lee DA, Bader DL, Shelton JC. An investigation into the effects of the hierarchical structure of tendon fascicles on micromechanical properties. *Proc Inst Mech Eng H* 2004;218:109-19.
- [230] Wei Z, Deshpande VS, McMeeking RM, Evans AG. Analysis and interpretation of stress fiber organization in cells subject to cyclic stretch. *J Biomech Eng* 2008;130:031009.
- [231] Matsiko A, Levingstone TJ, Gleeson JP, O'Brien FJ. Incorporation of TGF-Beta 3 within Collagen-Hyaluronic Acid Scaffolds Improves their Chondrogenic Potential. *Advanced Healthcare Materials* 2015;4:1175-9.
- [232] Halper J. Advances in the Use of Growth Factors for Treatment of Disorders of Soft Tissues. In: Halper J, editor. *Progress in Heritable Soft Connective Tissue Diseases*: Springer Netherlands; 2014. p. 59-76.
- [233] Gershlak JR, Resnikoff JI, Sullivan KE, Williams C, Wang RM, Black LD, 3rd. Mesenchymal stem cells ability to generate traction stress in response to substrate stiffness is modulated by the changing extracellular matrix composition of the heart during development. *Biochem Bioph Res Co* 2013;439:161-6.
- [234] Youngstrom DW, Rajpar I, Kaplan DL, Barrett JG. A bioreactor system for in vitro tendon differentiation and tendon tissue engineering. *Journal of Orthopaedic Research* 2015;33:911-8.
- [235] Popov C, Burggraf M, Kreja L, Ignatius A, Schieker M, Docheva D. Mechanical stimulation of human tendon stem/progenitor cells results in upregulation of matrix proteins, integrins and MMPs, and activation of p38 and ERK1/2 kinases. *BMC Mol Biol* 2015;16.
- [236] Xu Y, Wang Q, Li Y, Gan Y, Li P, Li S, et al. Cyclic Tensile Strain Induces Tenogenic Differentiation of Tendon-Derived Stem Cells in Bioreactor Culture. *Biomed Res Int* 2015;2015:790804.
- [237] Wang T, Lin Z, Ni M, Thien C, Day RE, Gardiner B, et al. Cyclic mechanical stimulation rescues achilles tendon from degeneration in a bioreactor system. *Journal of Orthopaedic Research* 2015:n/a-n/a.
- [238] Hao J, Zhang Y, Jing D, Shen Y, Tang G, Huang S, et al. Mechanobiology of mesenchymal stem cells: Perspective into mechanical induction of MSC fate. *Acta Biomaterialia* 2015;20:1-9.
- [239] Wen JH, Vincent LG, Fuhrmann A, Choi YS, Hribar KC, Taylor-Weiner H, et al. Interplay of matrix stiffness and protein tethering in stem cell differentiation. *Nature Materials* 2014;13:979-87.

- [240] Allen JL, Cooke ME, Alliston T. ECM stiffness primes the TGF β pathway to promote chondrocyte differentiation. *Mol Biol Cell* 2012;23:3731-42.
- [241] Kurpinski K, Chu J, Hashi C, Li S. Anisotropic mechanosensing by mesenchymal stem cells. *Proc Natl Acad Sci U S A* 2006;103:16095-100.
- [242] Kapoor A, Caporali EH, Kenis PJ, Stewart MC. Microtopographically patterned surfaces promote the alignment of tenocytes and extracellular collagen. *Acta Biomater* 2010;6:2580-9.
- [243] Caporali E, Kapoor A, Kenis PA, Stewart MC. TGF- β and microtopographical cues promote expression of tenogenic marker genes and tenocyte alignment. *Proceedings of the 36th Annual Conference of the Veterinary Orthopedic Society* 2009.
- [244] Joly P, Duda GN, Schone M, Welzel PB, Freudenberg U, Werner C, et al. Geometry-driven cell organization determines tissue growths in scaffold pores: consequences for fibronectin organization. *PLoS One* 2013;8:e73545.
- [245] Kopf J, Petersen A, Duda GN, Knaus P. BMP2 and mechanical loading cooperatively regulate immediate early signalling events in the BMP pathway. *BMC Biol* 2012;10:37.
- [246] Davidenko N, Gibb T, Schuster C, Best SM, Campbell JJ, Watson CJ, et al. Biomimetic collagen scaffolds with anisotropic pore architecture. *Acta Biomater* 2012;8:667-76.
- [247] Li J, You F, Li Y, Zuo Y, Li L, Jiang J, et al. Bone regeneration and infiltration of an anisotropic composite scaffold: an experimental study of rabbit cranial defect repair. *J Biomater Sci Polym Ed* 2016;27:327-38.
- [248] Xu B, Song G, Ju Y, Li X, Song Y, Watanabe S. RhoA/ROCK, cytoskeletal dynamics, and focal adhesion kinase are required for mechanical stretch-induced tenogenic differentiation of human mesenchymal stem cells. *J Cell Physiol* 2012;227:2722-9.
- [249] Marolt D, Augst A, Freed LE, Vepari C, Fajardo R, Patel N, et al. Bone and cartilage tissue constructs grown using human bone marrow stromal cells, silk scaffolds and rotating bioreactors. *Biomaterials* 2006;27:6138-49.
- [250] Qiu Y, Lei J, Koob TJ, Temenoff JS. Cyclic tension promotes fibroblastic differentiation of human MSCs cultured on collagen-fibre scaffolds. *J Tissue Eng Regen Med* 2014.
- [251] Paxton JZ, Hagerty P, Andrick JJ, Baar K. Optimizing an intermittent stretch paradigm using ERK1/2 phosphorylation results in increased collagen synthesis in engineered ligaments. *Tissue Eng Part A* 2012;18:277-84.
- [252] Morita Y, Watanabe S, Ju Y, Xu B. Determination of optimal cyclic uniaxial stretches for stem cell-to-tenocyte differentiation under a wide range of mechanical stretch conditions by evaluating gene expression and protein synthesis levels. *Acta of bioengineering and biomechanics / Wroclaw University of Technology* 2013;15:71-9.
- [253] Screen HRC, Byers SR, Lynn AD, Nguyen V, Patel D, Bryant SJ. Characterization of a novel fiber composite material for mechanotransduction research of fibrous connective tissues. *Adv Funct Mater* 2010;20:738-47.
- [254] Nombela-Arrieta C, Pivarnik G, Winkel B, Canty KJ, Harley B, Mahoney JE, et al. Quantitative Imaging of Hematopoietic Stem and Progenitor Cell localization and hypoxic status in the Bone Marrow microenvironment. *Nat Cell Biol* 2013;15:533-43.
- [255] Park S-Y, Wolfram P, Canty K, Harley B, Nombela-Arrieta C, Pivarnik G, et al. Focal Adhesion Kinase Regulates the Localization and Retention of Pro-B Cells in Bone Marrow Microenvironments. *J Immunol* 2013;190:1094-102.
- [256] Lin Y, Richards FM, Krippendorff BF, Bramhall JL, Harrington JA, Bapiro TE, et al. Paclitaxel and CYC3, an aurora kinase A inhibitor, synergise in pancreatic cancer cells but not bone marrow precursor cells. *Br J Cancer* 2012;107:1692-701.

- [257] Grier WK, Moy AS, Harley BAC. Design and application of a cyclic-tensile strain bioreactor to enhance tenogenesis of hMSCs on 3D collagen-glycosaminoglycan scaffolds. 2016, *In Preparation*.
- [258] Potter R, Havlioglu N, Thomopoulos S. The developing shoulder has a limited capacity to recover after a short duration of neonatal paralysis. *Journal of Biomechanics* 2014;47:2314-20.
- [259] Tatara AM, Lipner JH, Das R, Kim HM, Patel N, Ntouvali E, et al. The Role of Muscle Loading on Bone (Re)modeling at the Developing Enthesis. *PLoS ONE* 2014;9.
- [260] Zelzer E, Blitz E, Killian ML, Thomopoulos S. Tendon-to-Bone Attachment: From Development to Maturity. *Birth Defects Res C Embryo Today* 2014;102:101-12.